Imperial College London
Department of Civil and Environmental Engineering

Metal 3D printed bolted connections

Xi Guo

December 2022

A thesis submitted for the degree of

Doctor of Philosophy

Statement of Originality

I confirm that this thesis 'Metal 3D printed bolted connections' is my own work and that any material from published or unpublished work from others is appropriately referenced. This thesis is submitted to Imperial College London for the degree for Doctor of Philosophy and has not been submitted for a degree of any other qualification at another university.

Xi Guo

June 2023, London

Copyright Declaration

The copyright of this thesis rests with the author. Unless otherwise indicated, its contents are licensed under a Creative Commons Attribution-Non Commercial 4.0 International Licence (CC BY-NC). Under this licence, you may copy and redistribute the material in any medium or format. You may also create and distribute modified versions of the work. This is on the condition that: you credit the author and do not use it, or any derivative works, for a commercial purpose. When reusing or sharing this work, ensure you make the licence terms clear to others by naming the licence and linking to the licence text. Where a work has been adapted, you should indicate that the work has been changed and describe those changes. Please seek permission from the copyright holder for uses of this work that are not included in this licence or permitted under UK Copyright Law.'

Abstract

Additive manufacturing (AM) is receiving increasing attention in the construction industry, owing to its potential to bring enhanced automation and sustainability. In order to achieve wider integration, this thesis is aimed at providing fundamental underpinning experimental data for wire arc additively manufactured (WAAM) steel bolted connections, including single- and double-lap shear bolted connections and T-stub connections. The applicability of current design specifications is also evaluated.

A series of material tensile coupon tests on the WAAM steel is presented. A total of 27 coupons, featuring two nominal thicknesses, two surface conditions (i.e. as-built and machined) and three print layer orientations, were tested. Advanced measuring techniques, namely 3D Laser scanning and Digital Image Correlation, were employed in the tests. Negative influences of surface undulations were evidenced while the differences between the different print layer orientation were found to be small.

A total of 120 WAAM single- and double-lap shear tests, 60 of each, with different thicknesses, print layer orientations and geometric configurations, were conducted using advanced measuring techniques. Conventional failure modes were observed and analysed, while several unique failure modes were also highlighted. The test results were compared against the design predictions of current design specifications and their accuracies were assessed.

Finally, tests on 80 T-stub bolted connections with different printing strategies, bolt arrangements and geometric configurations were carried out. A new method was introduced for the determination of the failure mode and key points on the load-deformation response of T-stub connections. The structural response of the WAAM T-stubs generally followed the anticipated trends, though the geometric irregularities and printing strategies were shown to have clear influences on the load-carrying capacity. Comparisons between the test results and the capacity predictions yielded by existing design equations were subsequently made; overall, reasonable agreement was achieved.

The work presented in this thesis has highlighted the feasibility and sound structural performance of connections produced through WAAM. Future research needs include the assessment of optimisation and structural reliability of WAAM connections.

Acknowledgements

It was on 22nd February 2013,10 years ago, that I boarded on the plane from Beijing to Paris. Young and naïve as I was, the boarding gate seemed like a wardrobe to Narnia to me, which I didn't really understand where it would take me to. My last glance to the city from the sky, where the sunset reddened the clouds and buildings, and the lamps lightened the alleys and streets, still lingers in my mind. I am often asked how much I miss my hometown. I, too, often ask myself the same question but always fail to answer. Maybe staying here for too long has blurred my definition of hometown. Trading seconds to hours, growing seasons to years, time can change a lot of things, such as building a child to a grown-up man, filling an empty mind with knowledge, or making an ungrateful person less so.

Lucky I was, I met Professor Leroy Gardner three years ago, who was willing to give me a chance and has since been putting more faith in me than I have ever had in myself. Patient and kind, he has been not only directing me towards the path I should go, but also encouraging me to release all my power and potential. I can never thank him enough for the help he has provided to me during these years, and also for the days to come.

People describe the path for seeking knowledge as a lane that is full of thistles and thorns. While waving my sword and trying to fight a way out, I have never been alone because Dr Pinelopi Kyvelou has always been fighting with me, side by side. Whenever a hard challenge stumbled me, she has never hesitated to jump right into it, lending me her wisdom, correcting my mistakes and tolerating my stupidity. Also, she is admirably self-disciplined. Any of this spirit one can find on me is just my clumsy imitation, but from which I can still benefit for a lifetime.

As much as life is sometimes seemed to be full of difficulties, I have always been surrounded by friends and warmth. Dr Xin Meng has always been a big brother to me, helped me with my questions, not only regarding the work, but also the daily life. Dr Ruizhi Zhang has been rather kind to tolerate the childishly naughty version of me for these years, though I am afraid that she might have to tolerate me for a little bit longer. The same is the case for Ben Weber and Athina Spinasa, my good friends in another office, whose company I really enjoyed. My appreciation also goes to my dear friends and colleagues – Jing Zhang, Lyn Li, Yong Zhu, Yin Zhang, Dr Shiying Zheng, Dr Xiang Yun, Dr Fiona Walport, Dr Luke Lapira, Prof Ahmer

Wadee, Dr Jun Ye, Dr Cheng Huang, Harry Slack, Zichang Yang, Zexu Shao, Yufei Zhu, Ziyou Wang, the technicians who contributed to my project – Gordon Herbert, Les Clark, Paul Crudge, Alfredo Olivo, Trevor Stickland, and whoever has generously helped me, accompanied me and brought joy to my life. Particularly, Dr Yunan Zuo, my dearest friend since high school, whom I haven't met for more than four years, has been there for me during those years as if we had never been apart. There must be a lot of names I haven't managed to mention, and which if I had, the list of names would be as long as this thesis. 'Differences of habit and language are nothing at all if our aims are identical and our hearts are open.' It is because of all of you that I am so optimistic to every day that I have spent, and will spend here.

Several months ago, I heard the heartbreaking news, that my primary school teacher passed away at an age where she should be shining in her domain and having a wonderful life with her husband and son. How unfair the universe is, letting morons like me idle their life everyday, while robbing time from honourable people like her. Thoughts that I should have thanked her have not only once, but countless times slipped my mind, leaving nothing but faded memories to be treasured and endless regret.

The other day, my mother made a video call to me, showing my father lying on a bed in a hospital. He was smiling to me with an aged and tired face, telling me that it was nothing but a small surgery, and blaming my mother for bothering me for such a tiny matter. I looked at him, trying to match his face to the one from my childhood memories, where it was so energetic and dashing, as when he gave speeches on stages, and as when he held my hand walking along the riverside. The one thing, however that stayed the same was the way he looked at me: full of love and pride. I joked, 'people said one may lose hair for studying too hard. I thought I might be an exception. It turns out that you are taking this burden for me.' He laughed as delighted and gratified. I, too, laughed, but with my heart burning. I can't ask for a better life than I have right now, as I can't image better parents than them. Watching them ageing is the most heartbreaking thing which, unfortunately, I must endure. There is no one who wants to stay still with them more than me. But I can't. I must move forward and fight hard, so that I might be able to outspeed their growing old, and, finally, prove them and tell them in person that I haven't wasted their effort and years, and that I very much deserve their love.

I fear to be stuck to a square inch in this life, like being caged in the bottom of an ocean, knowing I might ultimately leave nothing behind but a handful of ash. I fear to become nobody in this terrifyingly enormous world, with no place left for me to stand, to breath or even to

regret. I fear that time and the burden of life may eventually crash me, bend my knees and force me to accept to be characterless, and all chance of valour has gone beyond recall or desire. Among all these fears, the one I fear the very most is to let people that I care for down, to not keep my promises to them. I sincerely appreciate these who care about me, who have supported or are supporting me, who embraced me with their warm heart, and who let me be a part of their delightful lives.

People chase the happiness like waiting for several fleeting moments where the aurora dancing in the dark sky, while being willing to bear with the endless nights and exhausting cold. Sometimes, as hopeless as it seems to be, there are these stubborn ones that would never give up. My given name, ‘hope’, as a precious gift from my parents implying their best wishes to me, has guided me to travel through time, and over mountains and seas. As the last object hidden at the bottom of Pandora’s box, as the hardship and struggle being the very nature of life that I have since long ago realised, and as the life is an audience-less path that is often surrounded by loneliness, with all the mentioned as well as the non-mentioned names, I shall be more brave, more wise and more unstoppable to chase the hope that I may never reach but, since born, I have been bounded to.

Contents

Statement of Originality 1
Copyright Declaration 2
Abstract 3
Acknowledgements 4
Contents 7
List of Figures 10
List of Tables 14
1. Introduction 16
1.1. Background 16
1.2. Bolted connections 19
1.3. Aims and objectives 21
1.4. Thesis outline 22
2. Literature Review 23
2.1. Introduction 23
2.2. Additive manufacturing 23
2.2.1. Overview of additive manufacturing 23
2.2.2. Applications 24
2.2.3. Current research 28
2.3. Bolted lap shear connections 29
2.3.1. Development 30
2.3.2. Current design rules for bolted lap connections 33
2.4. T-stub connections 33
2.4.1. The component method and Eurocode 3 33
2.4.2. Relevant research into T-stub connections 35
2.5. Concluding remarks 36

3. WAAM Single-Lap Shear Bolted Connections 37
3.1. Introduction 37
3.2. Manufacturing and geometric measurements of test specimens 37
3.3. Material tests 43
3.4. Lap shear connection tests 46
3.4.1. Test setup 46
3.4.2. Failure modes 47
3.4.3. Transition between failure modes 55
3.4.4. Influence of print orientation 57
3.5. Ultimate loads and load-deformation responses 58
3.6. Existing design equations 69
3.6.1. AISI S100 69
3.6.2. AISC 360 70
3.6.3. Eurocode 3 70
3.6.4. AS/NZS 4600 71
3.6.5. Design equations proposed in the literature 71
3.7. Comparisons between test results and existing design equations 72
3.7.1. Net section tension failure 75
3.7.2. Shear-out (and end-splitting) failure 76
3.7.3. Localised tearing and curl-bearing failures 78
3.8. Conclusions 79
4. WAAM Double-Lap Shear Bolted Connections 81
4.1. Introduction 81
4.2. Manufacturing and geometric measurements of test specimens 81
4.3. Double-lap shear lap tests 86
4.3.1. Test setup 86
4.3.2. Failure modes 87
4.3.3. Ultimate loads and load-deformation responses 94
4.3.4. Influence of print layer orientation 103
4.4. Available design equations 105
4.4.1. Eurocode 3 105
4.4.2. AISI S100 105
4.4.3. AISC 360 106
4.4.4. AS/NZS 4600 106
4.4.5. Summary of design specifications 106

4.4.6. Proposed equations in the literature 106
4.5. Comparisons between test and predicted capacities 106
4.6. Comparisons with WAAM lap connections in single shear 113
4.7. Conclusions 116
5. WAAM T-Stub Bolted Connections 118
5.1. Introduction 118
5.2. Manufacturing and T-stub specimen geometry 118
5.3. Test setup 124
5.4. Test results 125
5.4.1. Load-displacement curves 125
5.4.2. Determination of plastic hinges in the flanges and yielding of bolts 140
5.4.3. Determination of plastic resistance and identification of failure mode 149
5.5. Influence of printing strategy 153
5.6. Design equations 155
5.6.1. Yield line pattern and effective length 155
5.6.2. Plastic collapse load predictions 158
5.7. Comparisons between test results and design equations 158
5.7.1. T-stubs with two bolts in a row 159
5.7.2. T-stubs with four bolts in a row 160
5.7.3. Yielding at the web-to-flange conjunction 160
5.8. Conclusions 161
6. Conclusions and Future Research 163
6.1. Conclusions 163
6.2. Suggestions for future research 165
6.2.1. Different steel grade and type 165
6.2.2. Dynamic tests on WAAM bolted connections 165
6.2.3. Numerical analysis and parametric study 165
6.2.4. Topological optimisation 166
References 167

List of Figures

Figure 1.1*:* Numbers of publications related to AM, PBF and DED, reproduced from (Kanyilmaz et al., 2022).....17
Figure 1.2: SuperDracos rocket engine by SpaceX (https://www.flickr.com/photos/spacex/16789102495/in/photolist-rzAxfp-AVPiao/) 17
Figure 1.3: Relativity Space 3D printed rocket engine.....18
Figure 1.4: Tank of the rocket Terran 1 18
Figure 1.5: Connection failure in Hyatt Regency walkway collapse (https://www2.engineering.com/Library/ArticlesPage/tabid/85/articleType/ArticleView/ArticleID) 20
Figure 1.6: Lap shear bolted connections (double-lap shear connection) 20
Figure 1.7: Beam (with haunch) connected to column flange through end-plate (equivalent T-stub connection) (https://resources.scia.net/en/factsheets/steel/steeldesigner_connectionsframe-rigid.htm).....21
Figure 2.1: 3D printed injector (left) and chamber (right) (https://www.nasa.gov/centers/marshall/news/releases/2015/nasa-tests-methane-powered-engine-components-for-next-generation-landers.html) 25
Figure 2.2: Optimisation of welding jig element (Schuh et al., 2020).....25
Figure 2.3: Models of traditional nodes and two optimised AM nodes (Galjaard et al., 2015) 26
Figure 2.4: Overall view of MX3D bridge (Gardner et al., 2020).....27
Figure 2.5: WAAM bridge on the campus of Technische Universität Darmstadt (Feucht et al., 2020) 27
Figure 2.6: WAAM tubular cantilever truss (Ye et al., 2021) 27
Figure 2.7: Optimised WAAM beam-to-column connection (Lange, Feucht & Erven, 2020) 28

Figure 2.8: Optimised WAAM beam-to-beam connection (Lange, Feucht & Erven, 2020) ..28
Figure 2.9: Conventional failure modes for bolted connections 30
Figure 2.10: Position of different shear planes 31
Figure 2.11: Position of the shear plane proposed by Kamtekar (2012) 32
Figure 2.12: Beam-to-column bolted joint 34
Figure 2.13: Plastic failure mechanisms of T-stubs with 2 bolts in a row, as defined in EN 1993-1-8 35
Figure 2.14: Plastic failure mechanisms defined in (Demonceau et al., 2010) 36
Figure 3.1: WAAM oval tubes from which test specimens were cut 39
Figure 3.2: Specimens cut from the flat sides of the tubes using a water jet cutter 39
Figure 3.3: Basic geometry of test specimens 40
Figure 3.4: Orientation of tensile coupons and lap specimens extracted from WAAM plates relative to print layer orientation 40
Figure 3.5: Typical test specimen: (a) following sandblasting, (b) digital model from laser scan and (c) after testing 43
Figure 3.6: Stress-strain curves obtained from tensile coupon tests 45
Figure 3.7: Experimental setup for lap shear connection tests 46
Figure 3.8: Typical failure modes: (a) shear-out and (b) net section tension 50
Figure 3.9: Localised tearing failure 50
Figure 3.10: Specimen (S8-117-80-90) failing by localised tearing 51
Figure 3.11: Strain fields at different loading levels for a specimen (specimen S8-65-39-90) failing by net section tension 52
Figure 3.12: Schematic view of bolt tilting and bolt head either penetration or avoiding plate in single-lap shear connections 53
Figure 3.13: Close-up view of bolt head penetrating into plate – curl-bearing failure (Specimen S3-145-104-90) 54
Figure 3.14: Strain fields at different loading levels for a specimen (specimen S8-117-48-90) failing by end-splitting 55
Figure 3.15: Failure mode transition from net section tension to end-splitting and shear-out failure 56
Figure 3.16: Failure mode transition from shear-out to end-splitting and localised tearing failure 56
Figure 3.17: Failure mode transition from shear-out to localised tearing failure 57

Figure 3.18: (a) Localised tearing in specimen S3-105-33-90 and (b) shear-out failure in specimen S3-105-33-0 57
Figure 3.19: Load-displacement curves of lap shear test specimens 65
Figure 3.20: Load-displacement curves of pairs of specimens with $\theta = 0°$ and $\theta = 90°$ exhibiting: (a) shear-out, (b) net section tension, (c) localised tearing, (d) end-splitting and (e) curl-bearing failure 66
Figure 3.21: Influence of width b and end distance e_1 on load-displacement curves of typical test specimens in comparison groups 67
Figure 3.22: Comparison of experimental results and design equations for bearing and net section tension, where net section tension and bearing failure, as described by the considered design codes, are indicated 76
Figure 3.23: Comparison of experimental results and design equations for shear-out and bearing, where shear-out and bearing failure, as described by the considered design codes, are indicated 77
Figure 4.1: Preparation process of typical specimen 82
Figure 4.2: Real specimen and digital models 83
Figure 4.3: Experimental setup for double-lap shear tests 87
Figure 4.4: Typical failure modes: (a) shear-out, (b) net section tension and (c) bearing failure 90
Figure 4.5: Shear-out and end-splitting failures of specimens with b = 65 mm and (a) θ = 0° and (b) θ = 90° 91
Figure 4.6: Specimens failing in incidental block shear (a) Specimen D3-65-43.2-90 and (b) Specimen D3-65-43.2-0 93
Figure 4.7: Load-displacement curves of double-lap shear test specimens 101
Figure 4.8: Typical load-displacement curves of specimens exhibiting: (a) shear-out, (b) net section tension, (c) bearing and (d) end-splitting failure 102
Figure 4.9: Load-displacement curves of specimens failing in shear-out (D3-65-21.6-90) and end-splitting (D3-65-21.6-0) 102
Figure 4.10: Influence of print layer orientation on failure modes for different specimen pairs: (a) D3-65-21.6, (b) D3-65-36, (c) D8-90-52 and (d) D8-120-80 103
Figure 4.11: Comparison of experimental results and design equations for shear-out and bearing, where shear-out and bearing failure, as described by the considered design codes, are indicated 109
Figure 5.1. Different printing strategies 119

Figure 5.2. Geometrical configuration of different types of T-stub specimens: (a) continuously printed with rounded corners, (b) with web and flange individually printed with rounded (stepped) corners, (c) with two bolts in a row and (d) with four bolts in a row 121
Figure 5.3. T-stub test setup 125
Figure 5.4. Load-displacement curves of tested T-stub specimens 136
Figure 5.5. Typical load-displacement curves 136
Figure 5.6. Gaps between the T-stub flanges 137
Figure 5.7. Influence of increasing gap size between T-stub flanges on the load-displacement curve of a typical specimen, based on preliminary FE simulations (Specimen T1-70-0.50-C-S) 138
Figure 5.8. Location of virtual strain and displacement gauges on flange outstands of T-stubs with (a) two bolts in a row and (b) four bolts in a row (VSG: virtual strain gauge, VDG: virtual displacement gauge, C: web-to-flange junction, BL: bolt line, B: bolt and E: flange end) 139
Figure 5.9. Load-vertical displacement of the flange end of Specimen T1-120-1.33-C-R, with illustration of key points 140
Figure 5.10. Typical load-strain curves at the web-to-flange conjunction and the bolt line . 141
Figure 5.11. Strain and stress distributions through flange thickness 142
Figure 5.12. Moment-strain curves at critical locations (Specimen T1-160-1.50-C-S) 143
Figure 5.13. Typical load-displacement curves with critical points marked 151
Figure 5.14. Typical specimens failing in (a) Mode 1 and (b) Mode 2 152
Figure 5.15. Ultimate failure of tested T-stubs 153
Figure 5.16. Theoretical yield line patterns: (a) beam, (b) circular with full circle, (c) circular individual end and (d) non-circular 157
Figure 5.17. Improved model recognising the influence of the bolt head size 161

List of Tables

Table 3.1: Chemical composition (% by weight) of feedstock wire, as provided by the manufacturer 38
Table 3.2: Mechanical properties (as welded) of feedstock wire, as provided by the manufacturer 38
Table 3.3: Printing parameters for WAAM material of two nominal thicknesses t_{nom} 38
Table 3.4: Measured geometric properties of test specimens 41
Table 3.5: Measured mechanical properties obtained from machined tensile coupons 44
Table 3.6: Measured effective mechanical properties obtained from as-built tensile coupons 45
Table 3.7: Summary of experimental results (FM = failure mode) 47
Table 3.8: Influence of print layer orientation on ultimate capacity of lap shear connections 68
Table 3.9: Summary of comparisons between the test results and design equations 73
Table 4.1: Measured geometric properties of test specimens 84
Table 4.2: Summary of experimental results 87
Table 4.3: Influence of print layer orientation on ultimate capacity and failure mode of double-lap shear connections 103
Table 4.4: Summary of comparisons between the test results and design equations 107
Table 4.5: Assessment of design methods for net section tension failure 110
Table 4.6: Assessment of design methods for shear-out failure 111
Table 4.7: Assessment of design methods for bearing failure 112
Table 4.8: Assessment of design methods for end-splitting failure using shear-out equations 113
Table 4.9: Comparisons between the single and double shear capacities 115
Table 5.1. Measured geometric properties of T-stubs with two bolts in a row 122
Table 5.2. Measured geometric properties of T-stubs with four bolts in a row 123

Table 5.3. Average mechanical properties obtained from as-built WAAM tensile coupons 141
Table 5.4. Evaluation of M_x relative to the theoretical plastic moment M_{pl} for varying multiples of the yield strain ε_y 143
Table 5.5. Summary of experimental results for T-stubs with two bolts in a row and comparisons with design equations (FM_{Test} = test failure mode and FM_{theo} = theoretical failure mode in brackets if different from the test results) 144
Table 5.6. Summary of experimental results for T-stubs with four bolts in a row and comparisons with design equations (FM_{Test} = test failure mode and FM_{theo} = theoretical failure mode in brackets if different from the test results) 147
Table 5.7. Comparisons between the yield loads of the four different printing strategies 154

1. Introduction

1.1. Background

Additive manufacturing (AM) is a novel process of producing physical objects with successive layers of raw materials based on pre-defined 3D digital models, showing outstanding advantages such as reduced material consumption and enhanced customisation (Kyvelou et al., 2020a; Gardner, 2023). Commonly used printing materials includes metal, polymer and aggregate based materials such as concrete. In 2015, a residential house was first constructed using AM technology by a Chinese commercial company — Winsu. The firm later accomplished a 3D-printed office which was printed in Suzhou and assembled in Dubai. According to the company, construction costs were reduced by approximately 80% and labour costs by approximately 60%, while 60 % less waste was produced compared with the conventional on-site construction (World Economic Forum, 2016). In the economic perspective, the global AM market size was valued at $13.84 billion in 2021 and is expected to keep expanding at a sharp rate (Grand View Research, 2022).

Metal additive manufacturing has made a major contribution to the increase in the market share of AM across the engineering sectors (Liu et al., 2020). Among a variety of types of fabrication process, Power Bed Fusion (PBF) and Directed Energy Deposition (DED) are the generally preferred methods within engineering applications thanks to their ability to print large-scale elements in a time efficient manner. The last decade has witnessed an explosion of research on AM, with the PBF being the most popular topic and the number of publications on DED also rising sharply since 2002 – see Figure 1.1 (Kanyilmaz et al., 2022). Underpinned by extensive research, metal AM has already shone through in many remarkable products. For example, a metal AM engine chamber (Figure 1.2), fabricated by SpaceX, has already accomplished several launch missions; the first entirely 3D-printed rocket fabricated by Relativity Space, the

engine and tank of which was made by PBF and DED respectively, is about to start its maiden voyage – see Figure 1.3 and 1.4.

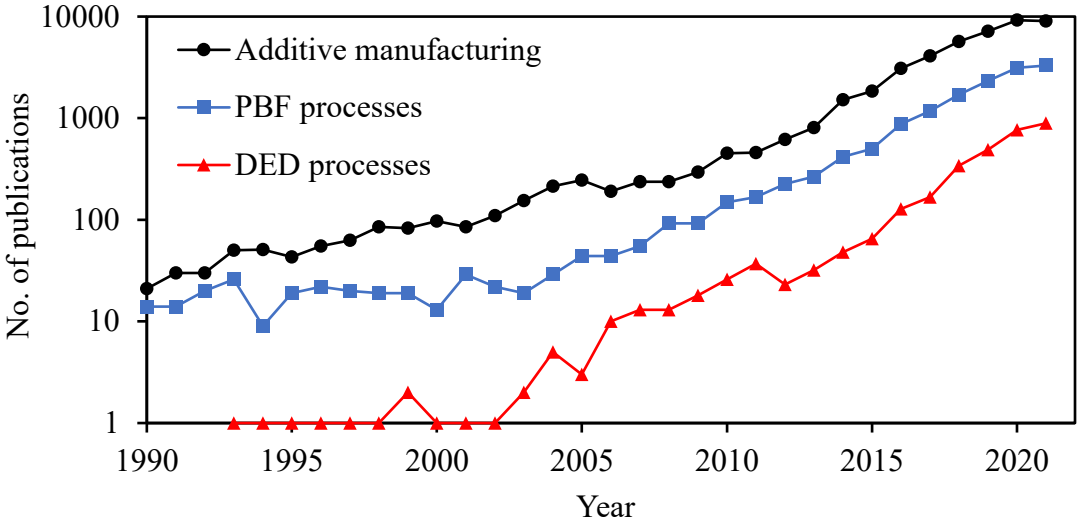


Figure 1.1: Numbers of publications related to AM, PBF and DED, reproduced from (Kanyilmaz et al., 2022)



Figure 1.2: SuperDracos rocket engine by SpaceX (https://www.flickr.com/photos/spacex/16789102495/in/photolist-rzAxfp-AVPiao/)

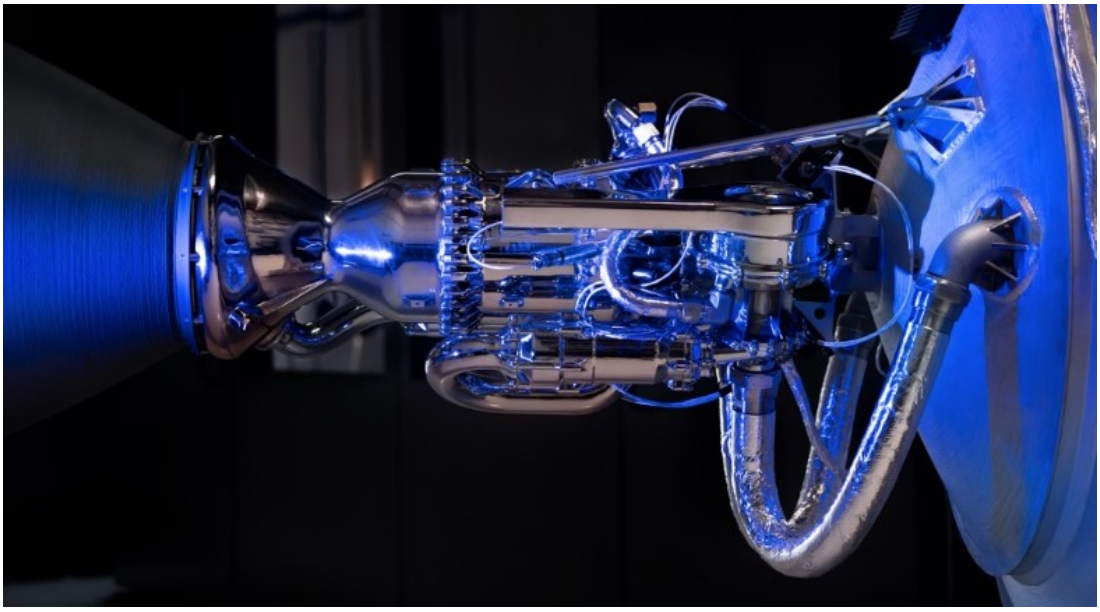


Figure 1.3: Relativity Space 3D printed rocket engine
(https://www.motorbiscuit.com/can-you-3d-print-your-own-rocket-relativity-space-does/)

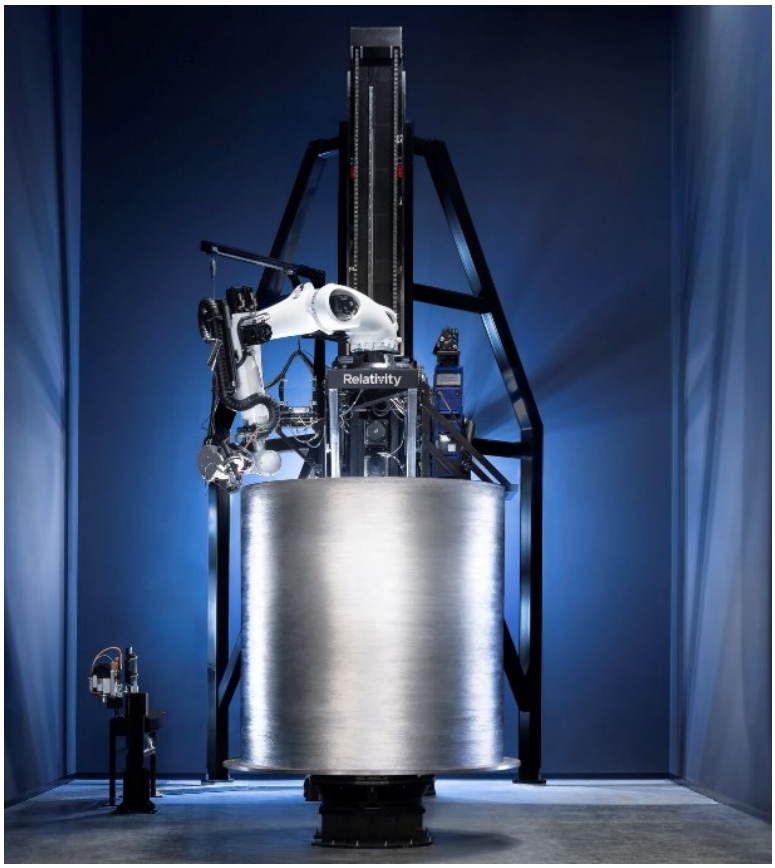


Figure 1.4: Tank of the rocket Terran 1
(https://www.relativityspace.com/rockets)

Wire arc additive manufacturing (WAAM), which belongs to the DED family of methods, can be used to build large scale elements in an efficient manner. WAAM utilises conventional welding equipment, in conjunction with robotic control, to build target components through successive deposition of layers of material. The advantages of this innovative technology over conventional manufacturing methods, which include enhanced geometric versatility, increased automation and reduced material consumption, render WAAM capable of bringing about a step-change to the modus operandi of various engineering industries especially the construction sector.

1.2. Bolted connections

The concept of employing bolts to assemble steel structures dates back to 1934, as proposed by Batho and Bateman. In 1947, the Research Council on Riveted and Bolted Structural Joints was formed for the purpose of investigating the suitability of joints used in various scenarios for structural frames. A preliminary code for the design of bolted connections was issued in Germany in 1956, while a British Standard (BS 3139) for the bolt material was issued in 1959 in the UK (Kulak et al., 1987).

To date, bolted connections feature in most structural steel joints and are preferred over other types of joints due to their low cost and ease of assembly. Since joints are often regarded as the most vulnerable parts in structural frames, special attention should be paid to ensure their safety. Inappropriate design or installation can lead to catastrophic damage, such as the well-known Hyatt Regency walkway collapse, which occurred due to incorrect installation of a connection (Figure 1.5), causing 114 deaths and over 200 injuries.

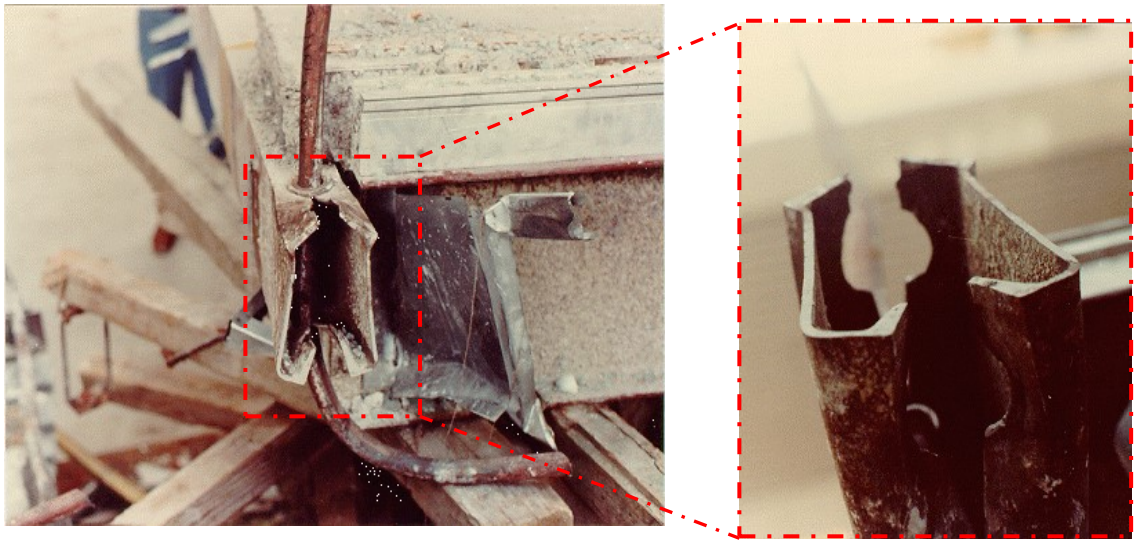


Figure 1.5: Connection failure in Hyatt Regency walkway collapse (https://www2.engineering.com/Library/ArticlesPage/tabid/85/articleType/ArticleView/ArticleID)

Lap shear bolted connections are one of the most common types of connection in steel construction, where the load is transmitted by means of shear in the bolts and bearing in the connected parts. Such connections are often used to connect beams to beams – see Figure 1.6. Beam-to-column connections are also commonly seen in steel structures – see Figure 1.7. These connections feature bolts in shear and bearing, but also in tension. The response of these connections is often investigated through T-stub tests.

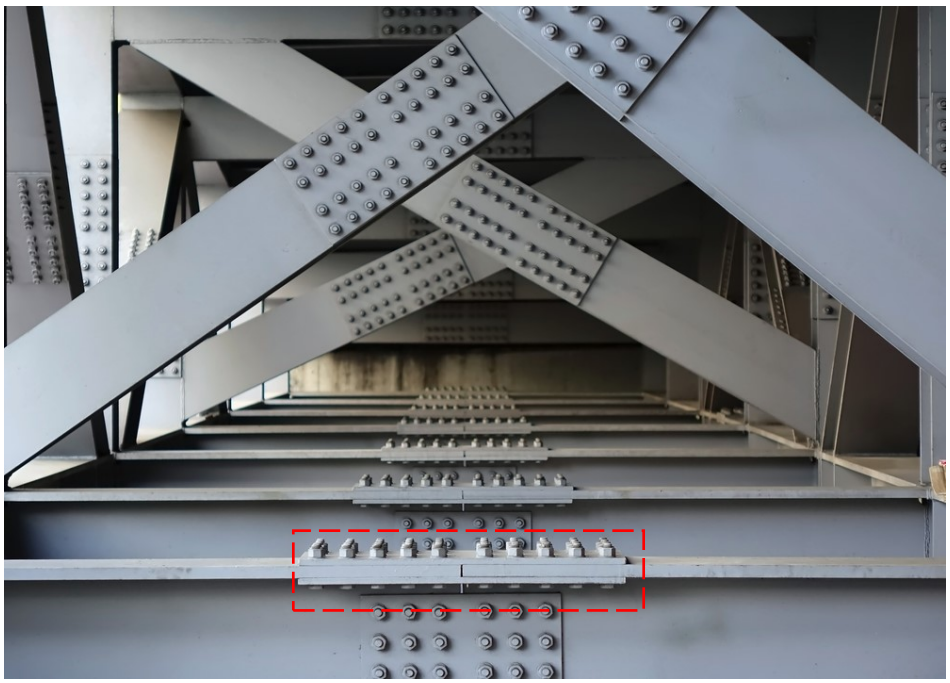


Figure 1.6: Lap shear bolted connections (double-lap shear connection)

(https://www.bhamfast.com/astm-f3125-a325-a490/)

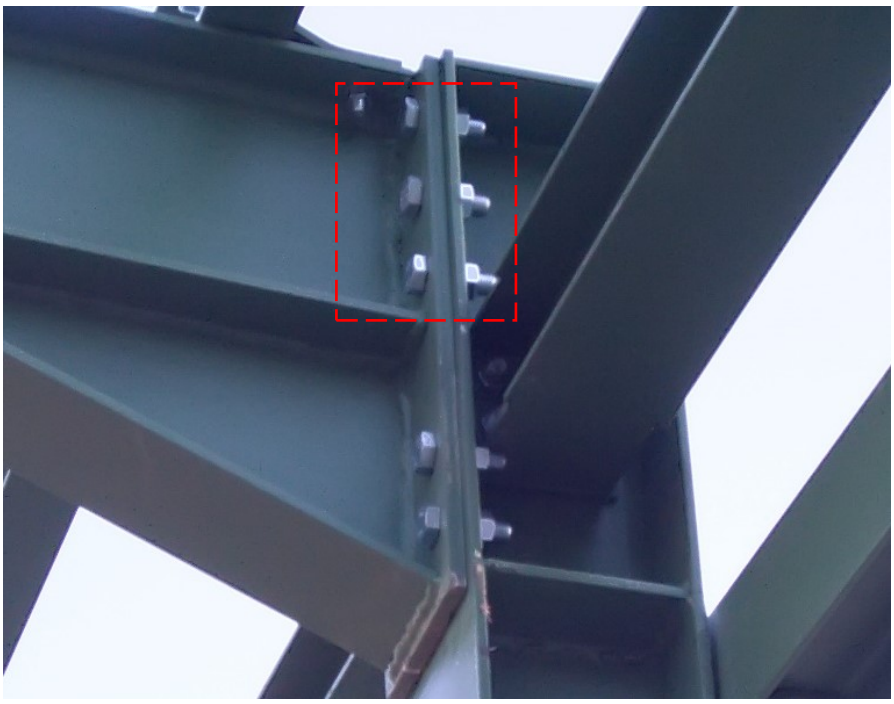


Figure 1.7: Beam (with haunch) connected to column flange through end-plate (equivalent T-stub connection)
(https://resources.scia.net/en/factsheets/steel/steeldesigner_connectionsframe-rigid.htm)

1.3. Aims and objectives

The main focus of this thesis is the experimental investigation of the structural behaviour of WAAM bolted connections, namely single and double-lap shear bolted connections and T-stub connections. Extensive research has been carried out to investigate the structure performance of bolted connections, which has led to the development of several design standards such as Eurocode 3. However, the structural behaviour of such connections made by WAAM has yet to be explored. Therefore, this study aims to investigate the response and load-bearing capacity of these connections and to evaluate the applicability of current design codes. More specifically, the objective includes:

- To examine the mechanical properties of WAAM steels as well as the influence of thickness and printing layer orientation;
- To investigate experimentally the ultimate load-carrying capacities of lap bolted connections subjected to single and double shear;

- To assess the accuracy of existing design codes as well as the equations from the literature for WAAM bolted connections subjected to single and double shear;
- To investigate experimentally the behaviour, failure modes and resistances of T-stub bolted connections under tension;
- To evaluate the applicability of existing design equations in Eurocode 3 and in the literature to WAAM T-stub bolted connections.

1.4. Thesis outline

This introductory chapter provides basic knowledge of additive manufacturing, particularly wire arc additive manufacturing, and bolted connections. The aim of the study was highlighted, and the structure of the thesis was presented.

In Chapter 2, the development of WAAM techniques as well as the relevant applications and the current research are presented through a literature review. The material features of WAAM steel are mentioned and the previous studies into the bolted connections as well as the existing design codes are comprehensively reviewed.

The structural responses of WAAM bolted lap connections subjected to single shear are addressed in Chapter 3, where the examined material properties are also presented. The obtained failure modes are fully discussed, and the test data are used to compare against design equations.

Based on the material tests described in Chapter 3, Chapter 4 presents double-lap shear tests. In addition to the discussion of the obtained failure modes and the evaluation of the design equations based on the results, the differences between single and double shear are analysed.

A new analysis approach to investigate the structural responses of T-stubs in tension based on the experiments conducted is presented in Chapter 5. The determined failure modes and plastic resistances are discussed and the accuracy of the design equations are evaluated.

Finally, Chapter 7 presents the key findings and conclusions of this study. The direction of future research is also pointed out.

2. Literature Review

2.1. Introduction

This chapter presents key concepts and existing research relevant to this thesis with three main topics covered. Firstly, the origin and early developments of additive manufacturing are introduced, followed by its applications in different fields and current research. The second section presents a review of lap shear bolted connections with the investigations into different failure modes being highlighted and different design standards being introduced. Finally, an overview of research conducted on T-stub bolted connections is presented, where the component method and the corresponding design guidance are briefly explained. Additional research and all mentioned design equations are further reviewed in the subsequent individual chapters of this thesis.

2.2. Additive manufacturing

2.2.1. Overview of additive manufacturing

Additive manufacturing, commonly known as 3D printing, is a fabrication method where an element is built layer-by-layer through the addition of raw material. The very origin of the concept of 3D printing can be dated back to 1860s to a process known as photo sculpture, where cross-sections of an object were scanned to be replicated by a specific material (Gao et al., 2015). The first 3D printed part was created in 1983 by Chuck Hull, who is regarded as the inventor of stereolithography. It was then in 1987 that the stereolithography was commercialised and the first AM system was created, opening the age of additive manufacturing (Wohlers & Gornet, 2015). After significant developments in AM techniques being witnessed over the following decades, modern AM techniques are now widely spread and well codified. According to ISO/ASTM 52900 (2017), AM processes can be categorised

based on the fabrication technology, into binder jetting, directed energy deposition, powder bed fusion, material jetting, etc.

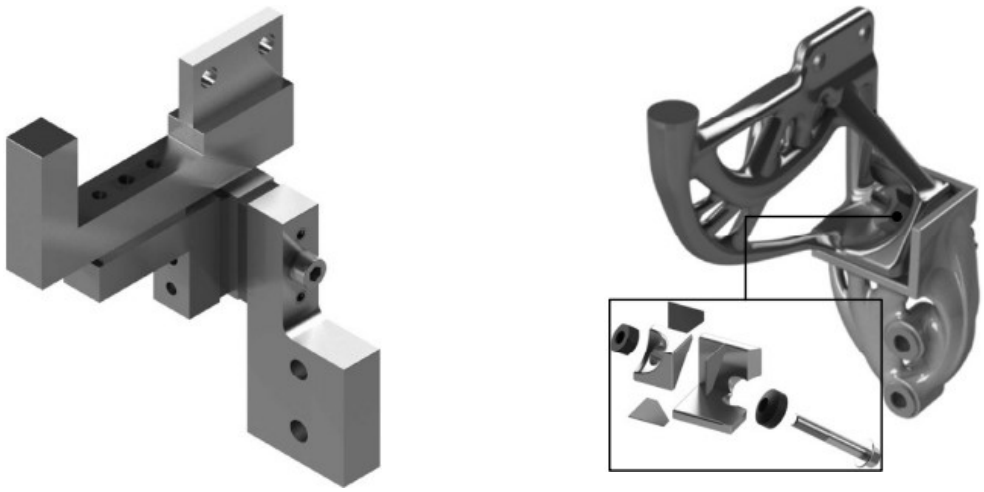
Nowadays, tremendous contributions have been made by AM in a variety of engineering sectors thanks to its reduced material usage, geometric freedom and customisation that allows products with a high level of complexity to be created in a timely efficient manner (Uriondo, Esperon-Miguez & Perinpanayagam, 2015; Buchanan & Gardner, 2019; Gardner, 2023). In addition, when geometries no longer limit the designers, components can be directly built into optimised shapes, which can achieve better performance by utilising less material. Some challenges, on the other hand, remain in various aspects such as the increased effort in design, lack of reliability and consistency of the fabricated parts, and the high production costs (Guo & Leu, 2013). Meanwhile, a universal concern shared by the government, industry and academia is the way to qualify and verify AM elements. Both destructive and non-destructive experiments are required to ensure the safe use of WAAM elements, while the available data pool is currently insufficient. Further exploration is needed to broaden the applications of AM technology.

2.2.2. Applications

Since the commercialization of AM, it has been expanding its application areas and elevating itself to a mainstream technology. In the aerospace industry, for example, the superior ability of AM in producing high-value, high-complexity and highly customised parts has already rendered itself a revolutionary manufacturing method. National Aeronautics and Space Administration (NASA) is engaged in AM in nearly all Centres (Waller et al., 2014), where the research covers improving printing technologies (Gradl et al., 2018), manufacturing superalloys (Soltani-Tehrani et al., 2022) and relevant applications such as the Thrust Chamber Injectors – see Figure 2.1. Meanwhile, the potential of topological optimisation of AM is also favoured by the automotive industry, where AM is regarded as a promising method to realise weight reduction of vehicles (Leal et al., 2017). Figure 2.2 shows a welding jig used in an automotive body before and after topological optimisation, which was eventually fabricated by laser based PBF, reducing more than 50 % of the origin mass while reaching a much more homogenous stress distribution (Schuh et al., 2020).



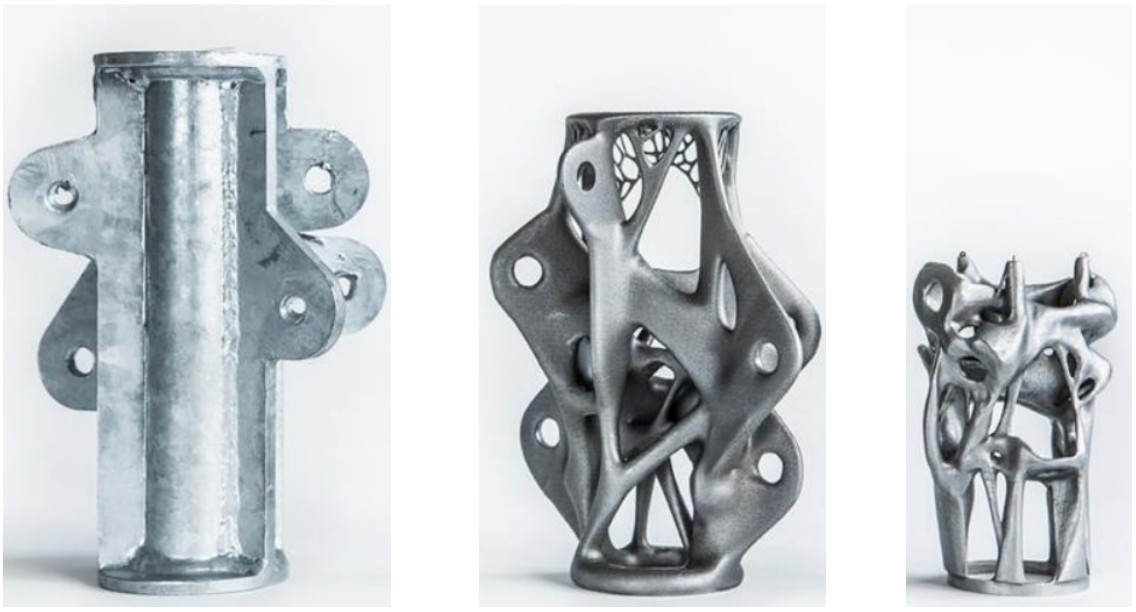
Figure 2.1: 3D printed injector (left) and chamber (right) (https://www.nasa.gov/centers/marshall/news/releases/2015/nasa-tests-methane-powered-engine-components-for-next-generation-landers.html)



(a) Original jig element (b) Topologically optimised jig element

Figure 2.2: Optimisation of welding jig element (Schuh et al., 2020)

When it comes to the construction industry, which is responsible for 40 % of global carbon emission, AM is regarded as an environmental-friendly method to potentially realise a sustainable future (Kanyilmaz et al., 2022; Shah et al., 2023). Figures 2.3(a) and 2.3(b) show a model of a connecting node produced in the traditional way and by PBF respectively, where a 15 % weight reduction was achieved through the optimisation, along with better structural performance (Galjaard, Hofman & Ren, 2015). Followed by this experience, a new model was fabricated by PBF where further optimisation was carried out, which allowed a weight reduction of 75% – see Figure 2.3(c) (Galjaard et al., 2015).



(a) Original node (b) First optimisation (c) Second optimisation

Figure 2.3: Models of traditional nodes and two optimised AM nodes (Galjaard et al., 2015)

Another milestone of metal AM is the MX3D bridge, which has a width of 2.5 m and a span of 10 m, entirely printed by WAAM – see Figure 2.4. Since the metal AM process has not yet been standardised, existing structural design provisions could not be applied directly to the bridge. Extensive research has been conducted to ensure the safety of the AM structure, including the material (Kyvelou et al., 2020), cross-sectional (Kyvelou et al., 2021) and dynamic tests (Wynne et al., 2022) as well as a series of non-destructive tests (Gardner et al., 2020). Inspired by the MX3D bridge, a bridge of 3 m-span was constructed on site in the campus of Technische Universität Darmstadt (Feucht et al., 2020, 2022) – see Figure 2.5. Moreover, the ability of fabricating elements with irregular shapes was demonstrated by the WAAM steel tubular truss presented in Figure 2.6 (Ye et al., 2021), of which the cross-section area varied based on the load distribution. On the other hand, WAAM is considered as a method not just to completely replace the conventional production process, but also to complement it (Buchanan & Gardner, 2019). For example, connections in steel structures with relatively small dimensions but great geometrical variation can be easily fabricated by the WAAM process. Figures 2.7 and 2.8 show optimisation and 3D printing of novel beam-to-column and beam-to-beam connections, respectively. Moreover, the use of metal WAAM has been expanded to concrete construction to fabricate steel bars. By combining metal WAAM with concrete 3D-printing technology, a fully automated manufacturing process can be achieved (Dörrie et al., 2022).



Figure 2.4: Overall view of MX3D bridge (Gardner et al., 2020)



Figure 2.5: WAAM bridge on the campus of Technische Universität Darmstadt (Feucht et al., 2020)

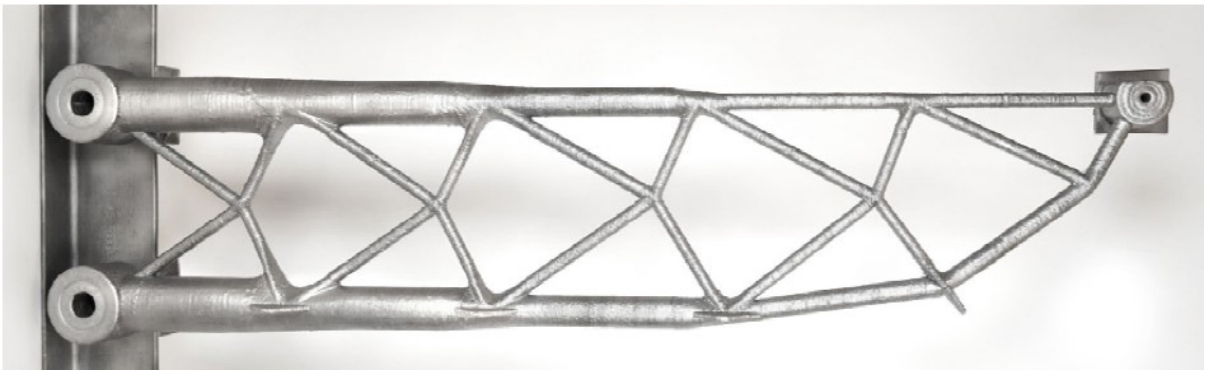
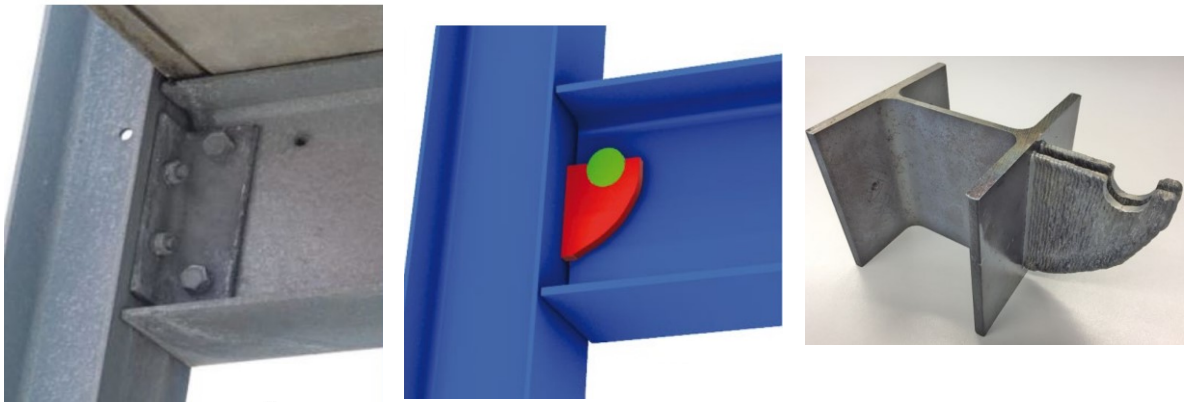


Figure 2.6: WAAM tubular cantilever truss (Ye et al., 2021)

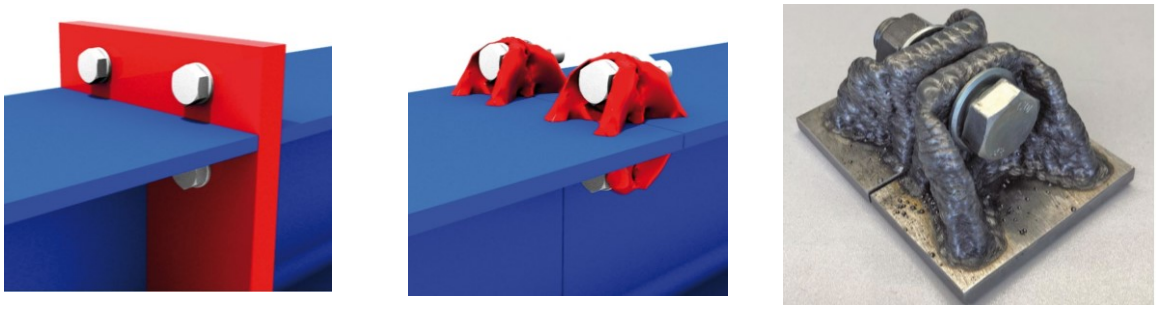


(a) Conventional double angle connection

(b) Beam hook model

(c) WAAM beam hook

Figure 2.7: Optimised WAAM beam-to-column connection (Lange, Feucht & Erven, 2020)



(d) Conventional T-stub end plate

(e) Optimised connection

(f) WAAM connection

Figure 2.8: Optimised WAAM beam-to-beam connection (Lange, Feucht & Erven, 2020)

2.2.3. Current research

Extensive research has been carried out into metal AM to investigate the capability and performance. In the aspect of the manufacturing process, efforts have been made to improve the printing strategies and methods in order to benefit more from the advantages while overcome the limitations (Pragana et al., 2021). On the other hand, for the fabricated elements, methods have been proposed to examine the quality, such as the porosity (du Plessis & Macdonald, 2020; du Plessis, Yadroitsava & Yadroitsev, 2020). Meanwhile, in order to expand the use of metal AM, a range of additively manufactured metallic materials has been studied, including titanium alloys (Alonso et al., 2020; Chi et al., 2020; Ng et al., 2021; Veiga et al., 2020; Attar et al., 2019; Wang et al., 2019a), aluminium alloys (Arana et al., 2022; Horgar et al., 2018; Derekar et al., 2019), inconel alloys (Tanvir et al., 2019; Kumar et al., 2021; Onuike & Bandyopadhyay, 2019), stainless steel (Zhang et al., 2021; Kyvelou et al., 2020) and carbon

steel (Huang et al., 2022a). For WAAM elements, in particular, the unique undulating surface has been investigated (Xiong et al., 2018) and its negative influence on the material stiffness and strength has been revealed (Kyvelou et al., 2020), while the anisotropic behaviour has been described using an orthotropic plane stress material model (Hadjipantelis et al., 2022; Laghi et al., 2021).

The structural response of AM elements has been investigated through experimental investigations. Stainless steel PBF stub columns with square, rectangular and circular hollow sections were tested, and the obtained results were compared with conventionally formed stub column data as well as the current design provisions to evaluate their performances. It was found that the structural behaviour of PBF stub columns generally followed the anticipated trends (Yan et al., 2019; Buchanan et al., 2017; Zhang et al., 2021b). Meanwhile, studies have also been conducted on the WAAM elements subjected to compression (Kyvelou et al., 2021; Laghi et al., 2020; Huang et al., 2022b) and bending (Huang, Meng & Gardner, 2022), the results of which all generally followed the anticipated trends.

Recent works have demonstrated the feasibility as well as benefits of the structural optimisation of AM elements (Kanyilmaz et al., 2022). For example, optimised corrugated stainless steel shells made by PBF have been investigated by Zhang et al., where 40% increase in capacity was achieved by using essentially the same amount of material as normal circular shells (Zhang, Meng & Gardner, 2022; Zhang et al., 2022). Moreover, the WAAM truss illustrated in Figure 2.6 is another example of the marriage between AM and optimisation. Compared with the corresponding reference designs where conventional beams with standard cross-sections were employed, the capacity-to-mass ratio obtained from FE simulations of the optimised design was found to be at least twice that of the conventional steel sections in all investigated loading scenarios (Ye et al., 2021). Physical experiments are currently being undertaken to examine the structural behaviour of the WAAM optimised trusses.

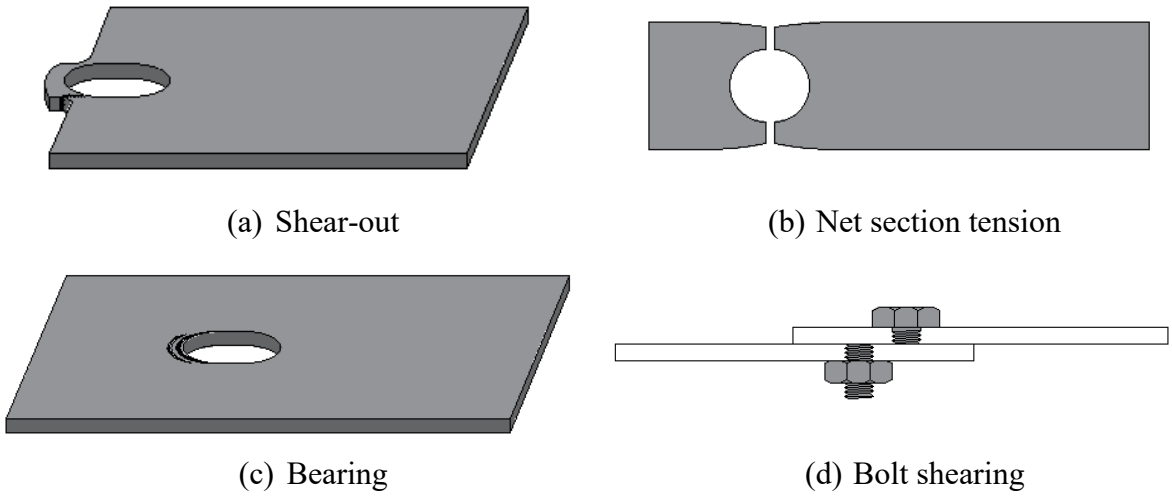
2.3. Bolted lap shear connections

Lap shear connections involve cases where the fasteners are loaded in either concentric or eccentric shear. In the former case, the applied load passes through the centroid of the connection so the fasteners are loaded concentrically (e.g. double-lap shear connections), and in the latter case the applied load does not pass through the centroid, resulting in bending of the fasteners in addition to the shear (e.g. single-lap shear connections).

If the contact between the bolt shank and bolt hole is not established during assembly, the friction at the interface will initially resist the applied load, in which stage the connection is regarded as "friction-type". Once the frictional resistance of the connection is exceeded, slip occurs, the slipping distance of which depends on the bolt hole clearance. Subsequently, the connection shifts into "bearing-type" when the bolt shank and bolt hole come into contact, in which case the load is transmitted by means of shear in the bolts and bearing in the connected parts.

2.3.1. Development

Failure of a lap shear connection, which occurs when the ultimate resistance of either the bolt or the connected part is reached, can be in various modes, and it is important to check each to ensure the structural performance. Failure of a bolted lap shear connection happens due to (1) insufficient distance downstream of the bolt hole to the free end of the plate where the bolt splits out through; (2) the net-section of the connected plate being too narrow to resist the tensile load; (3) excessive deformation developing in the material downstream of the bolt hole or (4) the shear force developed in the bolt exceeding its ultimate shear strength. Winter (1956) conducted 574 tests on bolted connections in cold-formed steel, and first identified four distinct modes of failure: shear-out, bearing, net section tension and bolt shear failure – see Figure 2.9.



(a) Shear-out (b) Net section tension

(c) Bearing (d) Bolt shearing

Figure 2.9: Conventional failure modes for bolted connections

A shear-out failure occurs when two shear planes downstream of the bolt hole fail to resist the shear force. Winter (1956) concluded that the shear-out capacity was related to the yield strength f_y of the plate material, while Dhalla et al. (1971) found that more accurate predictions could be achieved by employing the material ultimate strength f_u. On the other hand, efforts

have been made to identify accurately the shear planes. For single bolted connections, gross shear planes which are measured from the centre of the bolt hole to the end of the plate, and net shear planes which are measured between the edge of the bolt hole to the plate end (Figure 2.10), are the two models generally adopted by researchers and design specifications. A new model was proposed by Kamtekar (2012) who pointed out that the locations of the shear planes depended on the bolt diameter – see Figure 2.11. Meanwhile, the so called 'active' shear plane, which is assumed to lie between the gross and net shear plane, was proposed by Teh & Uz (2015) – see Figure 2.10. The accuracy of the two proposed shear plane models were evaluated against both experimental and numerical results. It was found that the active shear plane provided consistently accurate predictions. In addition, Xing et al. (2020) found that catenary action that arose from large deformations downstream of the bolt hole makes a significant contribution to the shear-out capacity.

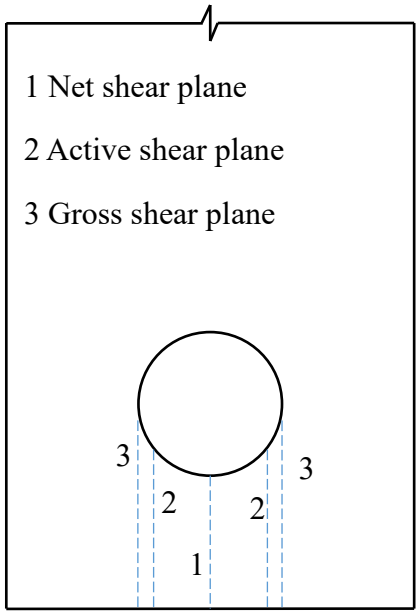


Figure 2.10: Position of different shear planes

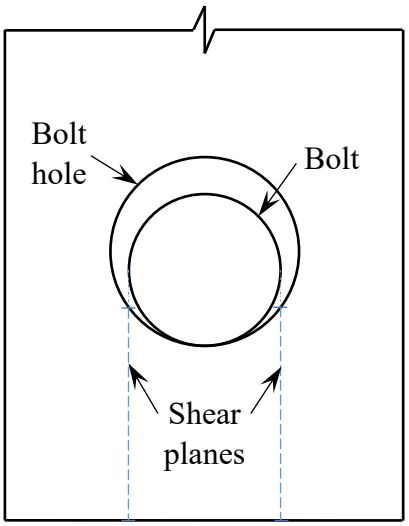


Figure 2.11: Position of the shear plane proposed by Kamtekar (2012)

Research has also been conducted into net section tension failure. Winter (1956) described this failure mode as "transverse tension-tearing across the sheet". LaBoube (1988) commented that bearing failures sometimes can be misidentified as net section tension failures. Consequently, the derived equation for the capacity prediction addressed more than just net section failure. Rogers & Hancock (2000) highlighted the importance of the occurrences of necking across the width and thickness of the specimens in the identification of net section tension failure. More recently, Teh & Gilbert (2012) analysed the reduction factors utilised in the current design standards for computing net section tension capacity, and proposed a new mathematical expression to calculate the reduction factor for connections in cold-reduced steel.

When end distances and widths of specimens are large enough to avoid shear-out and net section tension failures, specimens will eventually fail in bearing. An equation for computing the ultimate bearing capacity was provided by Rogers & Hancock (1999) for mild steel and by Aalberg & Larsen for high strength steel (2001, 2002). Kim & Yura (1999) conducted tests on two different steels with low and high ultimate-to-yield stress ratios and reconfirmed that the bearing strength is proportional to the material ultimate strength. Research has subsequently been carried out to calibrate the proportionality coefficient, namely the bearing factor (Može & Beg, 2014; Wang et al., 2017; Može, 2018). More recently, the effect of material ductility has been investigated by Cho, Teh and Young (2021) by testing specimens composed of mild, high strength and ultra-high strength steels, and respective bearing factors have been proposed.

2.3.2. Current design rules for bolted lap connections

Since bolted lap shear connections are widely used in the construction sector, corresponding design guidance can be found in many design standards. Eurocode 3 part 1.8 (EN 1993-1-8, 2021) for structural steel combines shear-out and bearing failure predictions into one single equation, while having a separate equation for the bearing resistance of single-lap shear connections. Meanwhile, the equation for net section tension failure is specified in Eurocode 3 part 1.1(EN 1993-1-1, 2020).

The American design standard for cold-formed steel members AISI S100 (2016) is used for bolted connections in cold-formed steel with thicknesses less than 4.76 mm. The differences between single and double-lap shear connections are distinguished in the bearing strength prediction by adopting different bearing factors. On the other hand, AISC 360 (2016) which is used for structural steel does not distinguish between single and double-lap shear connections. AS/NZS 4600 (2018) provides the same prediction equations for bearing and net section tension failures as in AISI S100 (2016), while a different equation is specified for shear-out strength.

2.4. T-stub connections

T-stubs are simplified components that represent the behaviour of key parts of joints that are commonly employed in steel structures. This section briefly introduces the development and applications of the component method and relevant research on T-stub connections.

2.4.1. The component method and Eurocode 3

Moment resisting bolted connections such as beam-to-column connections have been investigated by numbers of researchers (Fisher & Struik, 1974; Goverdhan, 1984; Owens & Cheal, 1989). However, due to the complexity and the variety of joints employed in different scenarios, research focusing on each individual joint has been found to be less efficient. After reviewing a number of studies into moment resisting bolted connections, Nethercot and Zandonini (1989) concluded that the most suitable method to assess the structural behaviour of a complex bolted joint was to decompose the joint into simplified mechanical models, which can be analysed separately. Thereafter, the component method, which initially appeared in the Eurocodes 1992, is now specified in Eurocode 3 part 1.8 (2021) and widely adopted as an efficient and reliable approach to the analysis and design of joints (Berrospi Aquino et al.,

2021). Generally, the component method comprises three steps. The first step is to identify all the components that contribute to the rotational deformability. Then, each individual component model should be analysed, and the stiffness and the strength should be determined. Finally, the overall structural response of the joint is derived from the summation of the behaviour of the single components (Weynand, Jaspart & Steenhuis, 1995).

A typical example of applying the component method is shown in Figure 2.12 for the case of a beam-to-column bolted joint, which is normally divided into three main regions, namely tension, compression and shear zones. The model of a T-stub in tension is used to represent the behaviour of the tension zone. The T-stub model is then decomposed into rigid bars and springs to represent the behaviour of T-stub flanges and bolts, respectively. According to Eurocode 3 part 1.8 (EN 1993-1-8, 2021), three modes of failure could occur in T-stub connections, namely Mode 1: Formation of a plastic collapse mechanism in the flange, Mode 2: Bolt failure with yielding of the flange and Mode 3: Bolt failure – see Figures 2.13(a), (b) and (c) respectively.

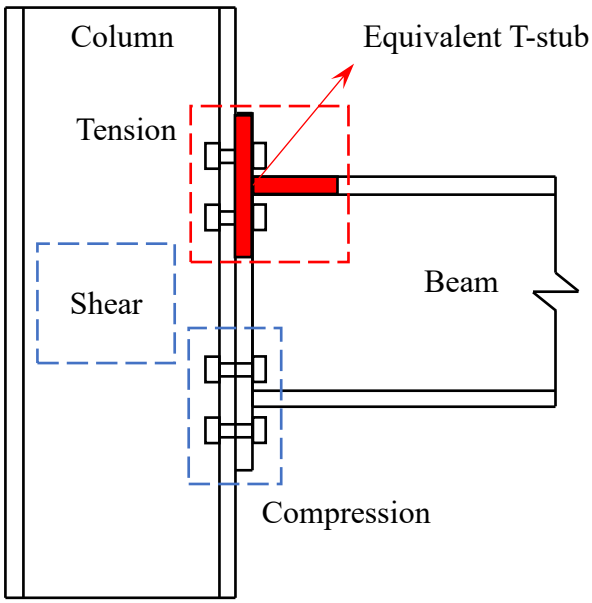
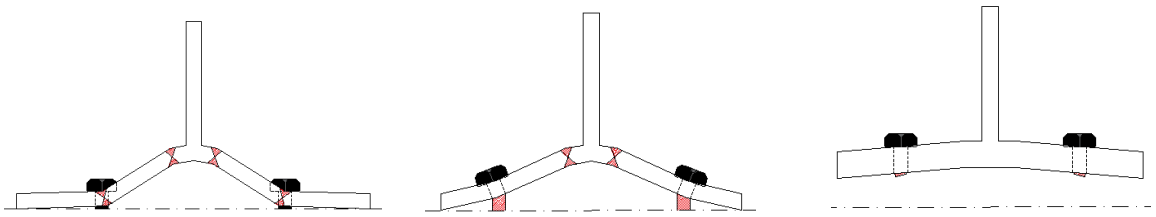


Figure 2.12: Beam-to-column bolted joint



(a) Mode 1 (b) Mode 2 (c) Mode 3

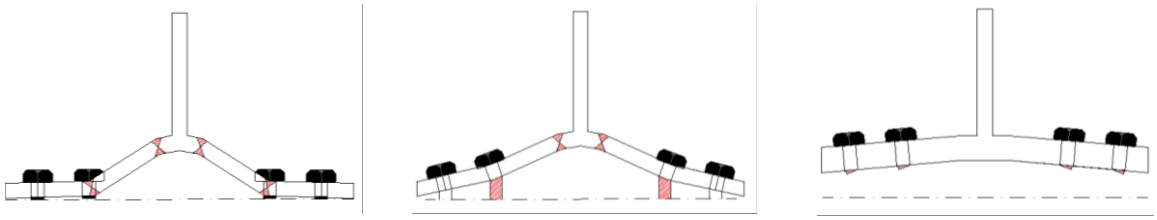
Figure 2.13: Plastic failure mechanisms of T-stubs with 2 bolts in a row, as defined in EN 1993-1-8

2.4.2. Relevant research into T-stub connections

An early investigation carried out by Douty & McGuire covered several types of bolted moment connections, including the T-stub web-to-beam flange, T-stub to column connection, assembled T-stub connection and end plate connection, where design methods for T-stub connections were first proposed (Douty & McGuire, 1965). A series of tests has then been conducted by Zoetemeijer (1974) where the focus was to evaluate the proposed theory of yield line patterns and effective lengths of the yield lines, and to check the applicability of the design method to the analysis of column flanges. Two major failure modes – bolt fracture and flange failure were identified. Packer & Morris (1977) studied the failure modes according to the yield line method, and redefined the failure modes by three mechanisms, namely complete bolt fracture, combined bolt and flange failure, and complete flange yield, which were later adopted by Eurocode 3 (EN 1993-1-8, 2021). The effect of the bolt preload was studied by Faella et al. (1998), where it was found that the preload significantly influences the stiffness of the T-stubs. Coelho et al. (2004) conducted 32 tests on T-stubs made up of welded plates where a number of variables were considered, including the steel grade, weld throat thickness, effective width, etc. T-stubs connected by thread-fixed one-side bolts were investigated by Liu et al. (2017) and Zhang et al. (2020), and the current design method was found to provide reasonable but conservative predictions for such T-stubs. T-stubs undergoing large displacements were investigated by Tartaglia et al. (2020) and Faralli et al. (2021), while the yield line patterns were investigated by Zhao et al. (2021).

In addition to T-stubs with two bolts in a row (i.e. one bolt per flange outstand – see Figure 2.13) which constitute the most commonly employed type of T-stub joint, T-stubs with four bolts in a row (i.e. two bolts per flange outstand) which are not included in Eurocode 3, have been receiving more and more attention (Demonceau et al., 2010; Latour et al., 2014).

According to Demonceau et al.(2010), essentially the same three failure mechanisms described above can also arise in T-stubs with four bolts in a row – see Figure 2.14.



(a) Mode 1 (b) Mode 2 (c) Mode 3

Figure 2.14: Plastic failure mechanisms defined in (Demonceau et al., 2010)

2.5. Concluding remarks

A literature review of additive manufacturing, particularly metal AM, has been presented in this chapter, with the current applications and research being introduced, and its unique features and advantages being highlighted. This was followed by a general overview of bolted lap shear connections where investigations into the ultimate load-bearing capacity corresponding to different failure modes were presented, and the related existing design specifications were introduced. Finally, research into bolted T-stub connections based on the component method has been presented, with the design guidance specified in Eurocode 3 being emphasised.

The presented literature review shows that despite a number of studies on lap shear and T-stub bolted connections having been conducted, investigations into bolted connections made by WAAM steel are yet to be carried out. The thesis aims to fill this gap and provide relevant experimental data and insights.

3. WAAM Single-Lap Shear Bolted Connections

3.1. Introduction

In this chapter, an experimental investigation into structural performance of WAAM steel bolted connections subjected to single shear is presented for the first time. Sixty WAAM specimens of two different nominal thicknesses (3 mm and 8 mm) were manufactured with varying dimensions to obtain four distinct failure modes: net section tension fracture, shear-out, localised tearing and curl-bearing failure. The effects of material anisotropy and of the surface undulations inherent to the WAAM process on the structural response of the examined connections were investigated by testing specimens with two different angles (0° and 90°) between the print layer orientation and the axis of loading. The particular geometric features of all specimens were captured by means of laser scanning, while digital image correlation (DIC) was employed to monitor the surface strain fields during testing. The observed failure modes are discussed herein and the applicability of current steel structure specifications (AISI S100, 2016; AISC 360, 2016; EN 1993-1-8, 2021; EN 1993-1-1, 2020; AS/NZS 4600, 2018) to the design of WAAM connections is assessed.

3.2. Manufacturing and geometric measurements of test specimens

The test specimens were manufactured by MX3D (2021), using their proprietary multi-axis robotic WAAM technology. Oval tubes of 3 mm and 8 mm nominal thickness, which covers the range of thin-to-thick material commonly used in steel construction, as shown in Figure 3.1, were printed using EN ISO 14341-A (2010): G 42 4 M21 3Si1 steel welding wire (equivalent to AWS A5.18: ER 70S-6), which is the most common choice for welding mild steel and can be used for robotic welding. The first letter G indicates gas-shielded metal arc welding; the number 42 denotes a minimum yield strength of 420 MPa, a tensile strength between 500 MPa and 640 MPa and a minimum elongation at fracture of 20%; the number 4 indicates that at a

temperature of -40 °C a minimum average impact energy of 47 J is achieved; the notation M21 is the classification of the shielding gas; and the last notation 3Si1 refers to the chemical composition of the wire electrode (ISO 14341: 2010). The chemical composition and the mechanical properties of the feedstock material, as reported by the manufacturer, are presented in Tables 3.1 and 3.2, respectively, and the printing parameters employed during the WAAM process are reported in Table 3.3. The oval tubes provided a stable build geometry and are more efficient to print. Test specimens were extracted from the flat sides of the tubes using a water jet cutter, as shown in Figure 3.2, and were then sandblasted with glass beads to remove any welding soot from the WAAM process.

Table 3.1: Chemical composition (% by weight) of feedstock wire, as provided by the manufacturer

C	Si	Mn	P	S	Cr	Ni	Mo	Cu	V	Ai	Zr+Ti
0.07	0.85	1.43	0.007	0.006	0.04	0.01	0.01	0.01	0.01	0.01	0.02

Table 3.2: Mechanical properties (as welded) of feedstock wire, as provided by the manufacturer

Yield strength (MPa)	Ultimate tensile strength (MPa)	Elongation A5 (%)	Impact energy at 40 °C (J)
471	580	25	73

Table 3.3: Printing parameters for WAAM material of two nominal thicknesses t_{nom}

Printing parameter	t_{nom}	
	3mm	8 mm
Wire diameter (mm)	0.8	1.2
Travel speed (mm/s)	8	8
Wire feed speed (m/min)	3	4
Welding voltage (V)	14.8	24.8
Welding current (A)	54	130
Gas flow rate (L/min)	14	16
Shielding gas	80% Ar + 20% CO_2	
Welding mode	Short-arc	Pulsed
Dwell time (s)	30	30



Figure 3.1: WAAM oval tubes from which test specimens were cut

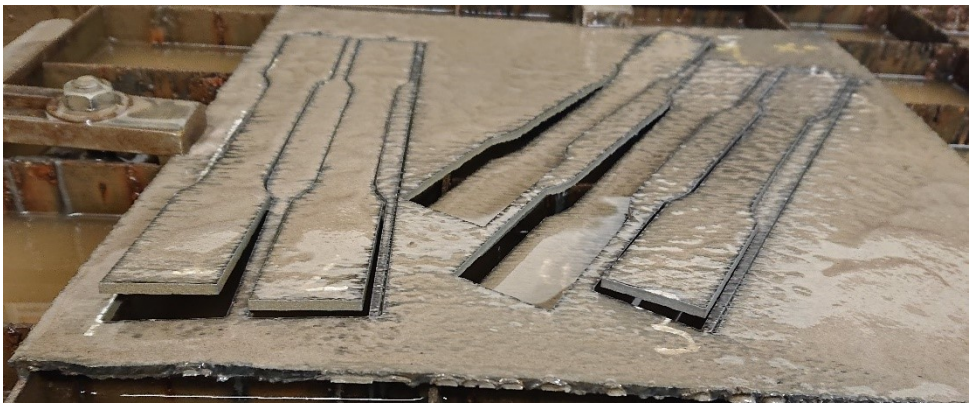


Figure 3.2: Specimens cut from the flat sides of the tubes using a water jet cutter

Sixty WAAM lap shear specimens of two different nominal thicknesses and two print layer orientations were fabricated, the basic configuration of which is shown in Figure 3.3, where d_0 is the bolt hole diameter, e_1 is the end distance between the centre of the bolt hole and the end of the WAAM plate, b is the plate width and x and y represent the directions perpendicular and parallel to the loading direction, respectively. The lengths of the specimens were approximately three times their respective widths, varying from 190 mm to 390 mm.

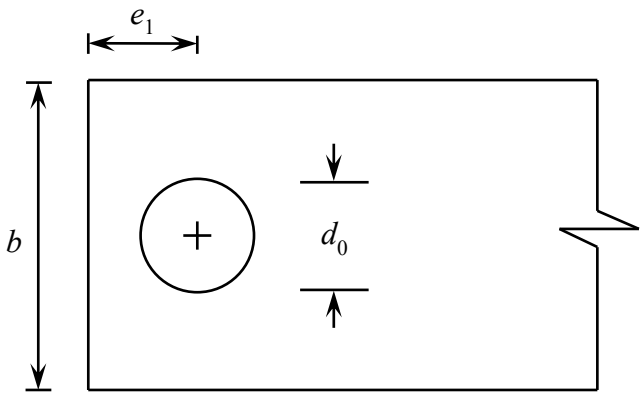


Figure 3.3: Basic geometry of test specimens

The labelling for the test specimens begins with the letter S (for single shear) followed immediately by the nominal thickness in mm, a hyphen, the nominal width b in mm, a second hyphen, the end distance e_1 in mm, a third hyphen and, finally, the angle in degrees between the axis of loading and the print layer orientation – see Figure 3.4. For example, Specimen S3-55-27-90 is a lap shear specimen with nominal values of thickness, width and end distance equal to 3 mm, 55 mm and 27 mm, respectively, with the axis of loading perpendicular to the print layer orientation.

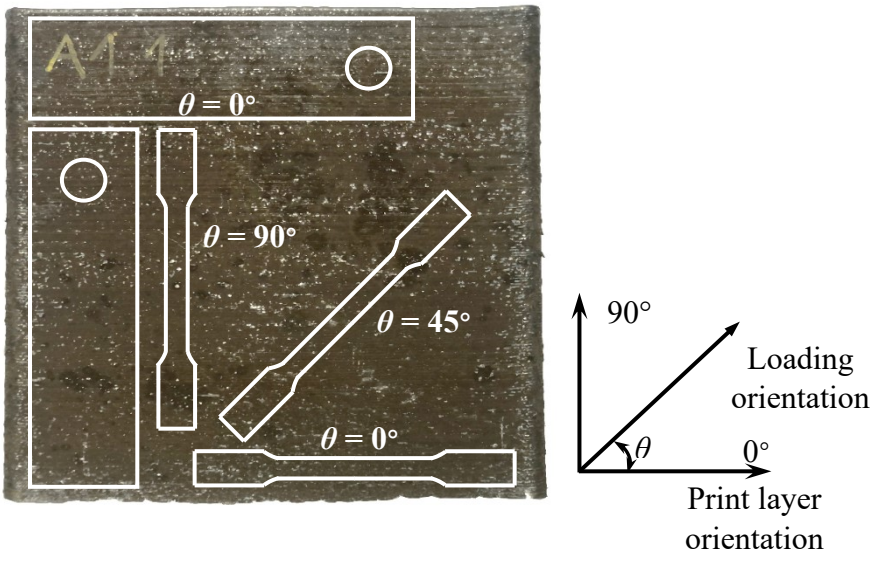


Figure 3.4: Orientation of tensile coupons and lap specimens extracted from WAAM plates relative to print layer orientation

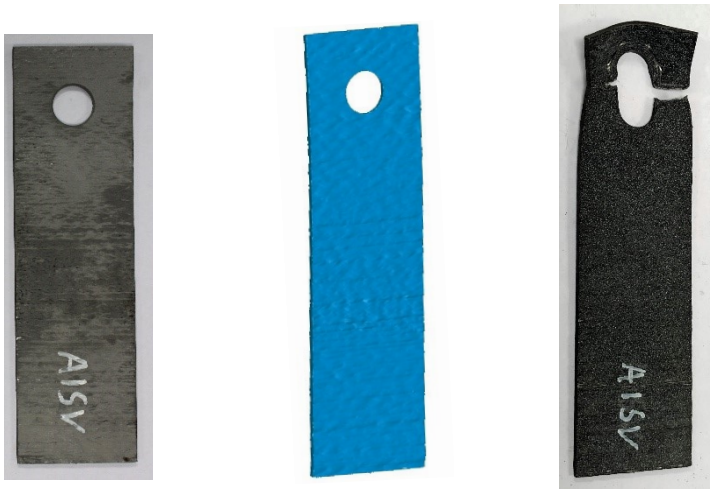
The width b, end distance e_1 and bolt hole diameter d_0 of each test specimen were measured using Vernier callipers; the results are presented in Table 3.4. However, due to the inherent surface undulations of as-built WAAM specimens, thickness measurements taken using conventional tools can be inaccurate (Kyvelou et al., 2021, 2020). Therefore, 3D laser scanning was employed in the present work. A FARO Design ScanArm 2.0, capable of recording 600,000 points per second with an accuracy of 0.075 mm (Faro, 2018), was used to obtain scans of both surfaces of each lap specimen; which were then merged into a single model represented as a point cloud in the software Geomagic Wrap (2017). The point cloud was subsequently inter-connected to form a polygonal mesh and a 3D CAD model, which was then imported into Rhino 3D (2017) as an STL file to determine the average thickness of the specimen (Kyvelou et al., 2021, 2020). The values of the average thickness t of all specimens are given in Table 3.4. Photographs of a typical specimen before and after testing, together with the corresponding 3D CAD model following laser scanning, are shown in Figure 3.5.

Table 3.4: Measured geometric properties of test specimens

Specimen	Bolt type	t (mm)	d_0 (mm)	b (mm)	e_1 (mm)
S3-55-27-0	M16	2.7	18.0	55.1	26.9
S3-45-27-0	M16	3.0	17.8	45.4	27.3
S3-45-36-0	M16	3.0	17.7	45.4	36.3
S3-35-27-0	M16	2.7	17.9	34.8	26.8
S3-65-18-0	M16	2.8	17.8	65.5	18.2
S3-65-21.6-0	M16	2.9	17.8	65.4	21.6
S3-65-27-0	M16	2.9	17.8	65.3	27.0
S3-65-32.4-0	M16	2.8	17.8	65.4	32.5
S3-65-36-0	M16	2.8	17.8	65.5	36.3
S3-85-33-0	M20	2.8	21.8	85.5	33.3
S3-85-44-0	M20	2.7	21.7	85.4	44.3
S3-105-33-0	M20	2.6	22.2	105.0	32.9
S3-105-39.6-0	M20	2.6	22.6	105.0	39.3
S3-105-44-0	M20	2.7	22.2	105.1	44.1
S3-145-44.2-0	M24	2.7	26.2	144.0	43.8
S3-145-78-0	M24	2.7	26.3	143.4	78.2

S3-145-104-0	M24	2.6	26.3	144.2	104.2
S8-45-39-0	M24	7.3	26.4	45.1	38.9
S8-55-39-0	M24	7.5	26.2	55.0	39.1
S8-65-39-0	M24	7.5	26.2	64.7	39.1
S8-75-39-0	M24	7.6	25.9	75.0	39.0
S8-95-26-0	M24	7.5	25.9	95.1	26.1
S8-95-33.8-0	M24	7.6	26.1	95.3	33.9
S8-95-39-0	M24	7.5	25.9	95.3	39.2
S8-95-65-0	M24	7.4	25.9	94.9	65.0
S8-95-78-0	M24	7.4	25.9	94.9	78.3
S8-117-32-0	M30	7.4	32.0	117.2	32.1
S8-117-48-0	M30	7.6	31.7	117.1	47.8
S8-117-80-0	M30	7.5	31.8	117.3	79.9
S8-117-96-0	M30	7.6	31.9	117.3	96.0
S3-55-27-90	M16	2.7	18.1	54.5	26.8
S3-45-27-90	M16	2.9	17.9	45.5	27.4
S3-45-36-90	M16	2.9	17.8	45.3	36.3
S3-35-27-90	M16	2.7	18.1	34.8	26.9
S3-65-18-90	M16	3.0	17.8	65.5	18.3
S3-65-21.6-90	M16	2.9	17.8	65.3	21.8
S3-65-27-90	M16	2.9	17.7	65.3	27.0
S3-65-32.4-90	M16	2.9	17.8	65.3	32.4
S3-65-36-90	M16	2.9	17.8	65.1	36.3
S3-85-33-90	M20	2.8	21.9	85.6	33.4
S3-85-44-90	M20	2.8	21.9	85.6	44.4
S3-105-33-90	M20	2.8	22.2	105.1	33.0
S3-105-39.6-90	M20	2.8	22.1	105.1	39.0
S3-105-44-90	M20	2.8	22.1	104.9	43.6
S3-145-44.2-90	M24	2.7	25.9	144.0	40.8
S3-145-78-90	M24	2.7	26.2	145.1	78.1
S3-145-104-90	M24	2.7	26.2	143.9	103.4
S8-45-39-90	M24	7.4	26.2	44.7	38.8
S8-55-39-90	M24	7.5	26.2	54.9	38.9

S8-65-39-90	M24	7.3	26.2	64.9	39.2
S8-75-39-90	M24	7.5	26.2	75.2	38.9
S8-95-26-90	M24	7.7	25.9	95.2	26.1
S8-95-33.8-90	M24	7.6	26.0	95.2	34.0
S8-95-39-90	M24	7.7	25.9	95.0	39.2
S8-95-65-90	M24	7.7	25.8	95.1	65.1
S8-95-78-90	M24	7.6	25.9	94.9	78.2
S8-117-32-90	M30	7.5	32.0	117.2	32.2
S8-117-48-90	M30	7.5	31.9	117.2	48.3
S8-117-80-90	M30	7.6	31.9	117.2	80.2
S8-117-96-90	M30	7.6	32.0	117.2	96.2



(a) (b) (c)

Figure 3.5: Typical test specimen: (a) following sandblasting, (b) digital model from laser scan and (c) after testing

3.3. Material tests

Twenty nine tensile coupon tests were conducted to determine the mechanical properties of the WAAM material. Anisotropy was investigated by testing coupons extracted from the WAAM plates at angles of 0°, 45° and 90° to the print layer orientation, as illustrated in Figure 3.4. The influence of the undulating as-built geometry on the mechanical response was examined by testing as-built and machined coupons, with the surface undulations of the latter having been

removed using an end mill. Following their extraction from the parent plates using a water jet cutter, the coupons were sandblasted and laser scanned to obtain their average thickness and cross-sectional area.

The material tests were conducted in accordance with EN ISO 6892-1: 2019 (EN ISO 6892-1: 2019), using a 250 kN Instron 8800 testing machine at a constant strain rate of 0.00007 s^{-1}. A four-camera LaVision digital image correlation (DIC) system was employed to accurately monitor the surface strain fields on both sides of each coupon, over the parallel length. The acquired images, recorded at a frequency of 1 Hz, were processed in the software Davis (2017).

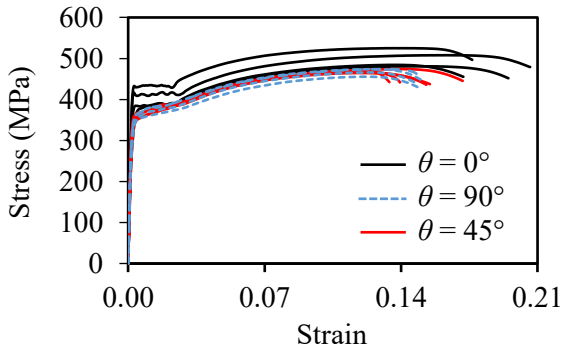
A summary of the average mechanical properties in each loading direction obtained from the machined coupon tests by loading direction (i.e. θ = 0°, 45°, 90°) is presented in Table 3.5, where E is the Young's modulus, f_y is the yield strength defined as the 0.2% proof stress, f_u is the ultimate tensile strength, ε_u is the strain at f_u and ε_f is the fracture strain, determined over a standard gauge length of $5.65\sqrt{A}$, where A is the mean cross-section area along the parallel length (EN ISO 6892-1: 2019). The results from the as-built coupon tests are provided in Table 3.6, where the subscript 'eff' has been added to the variables to reflect the effective nature of the mechanical properties, as influenced by the as-built geometry (Kyvelou et al., 2020). The stress-strain curves of all coupons, grouped by nominal thickness and surface condition (i.e. machined and as-built), are presented in Figure 3.6.

Table 3.5: Measured mechanical properties obtained from machined tensile coupons

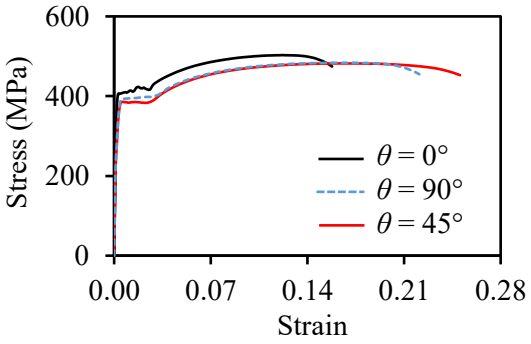
t_{nom} (mm)	θ (°)	E (GPa)	f_y (MPa)	f_u (MPa)	ε_u	ε_f
3	0	211	405	503	0.12	0.26
	45	210	366	482	0.16	0.39
	90	209	372	484	0.16	0.35
8	0	214	292	435	0.22	0.40
	45	212	329	452	0.21	0.38
	90	212	319	446	0.17	0.30

Table 3.6: Measured effective mechanical properties obtained from as-built tensile coupons

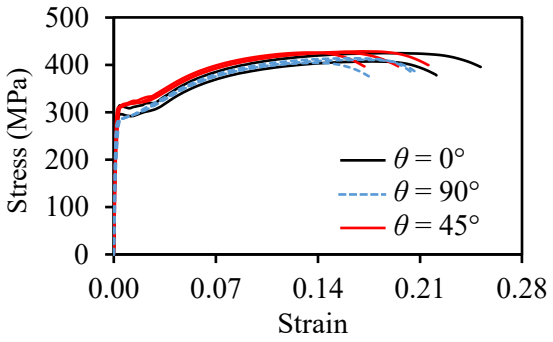
t_{nom} (mm)	θ (°)	E_{eff} (GPa)	$f_{y,eff}$ (MPa)	$f_{u,eff}$ (MPa)	$\varepsilon_{u,eff}$	$\varepsilon_{f,eff}$
3	0	196	407	500	0.15	0.26
	45	194	355	469	0.12	0.24
	90	196	354	467	0.13	0.22
8	0	215	306	416	0.18	0.36
	45	213	304	427	0.15	0.27
	90	218	278	409	0.16	0.24



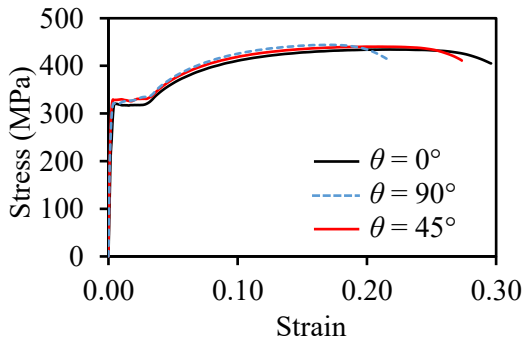
(a) 3 mm thick as-built coupons



(b) 3 mm thick machined coupons



(c) 8 mm thick as-built coupons



(d) 8 mm thick machined coupons

Figure 3.6: Stress-strain curves obtained from tensile coupon tests

The overall stress-strain response of WAAM steel is generally similar to that of hot-rolled steel. The material anisotropy was found to be rather mild compared with WAAM stainless steel, with the variations in the yield and ultimate tensile strengths being within 15% (but has been found to be up to almost 50% for WAAM stainless steel (Kyvelou et al., 2020)). The influence of the surface undulations on the mechanical properties of the examined WAAM material is

evident, with the Young's modulus, yield and ultimate strengths of the as-built coupons being up to 10% lower than those of the machined coupons. The strength of the thicker material, both for the machined and as-built coupons, was found to be consistently lower than the strength of the thinner material, with differences of up to about 40% and 20% for the yield and ultimate tensile strengths, respectively – see Tables 3.5 and 3.6; this is attributed to the slower cooling rate of the thicker material (Huang et al., 2022a).

3.4. Lap shear connection tests

3.4.1. Test setup

An overview of the test setup employed for the lap shear tests is illustrated in Figure 3.7. Each test comprised a WAAM plate (i.e. the test specimen) connected to a conventional high strength steel (HSS) plate by means of a single fully threaded bolt in a 2 mm clearance bolt hole (EN 1993-1-8, 2021). The bolt head and nut were finger-tightened to ensure contact at the interface of the plates, while limiting the influence of friction (Talja & Torkar, 2014). Note that the WAAM and HSS plates were of the same dimensions, ensuring the occurrence of failure within the (weaker) WAAM plate. The size (varying from M16 to M30) and grade (grade 12.9) of the bolts were selected such that shear failure of the bolts would be avoided.

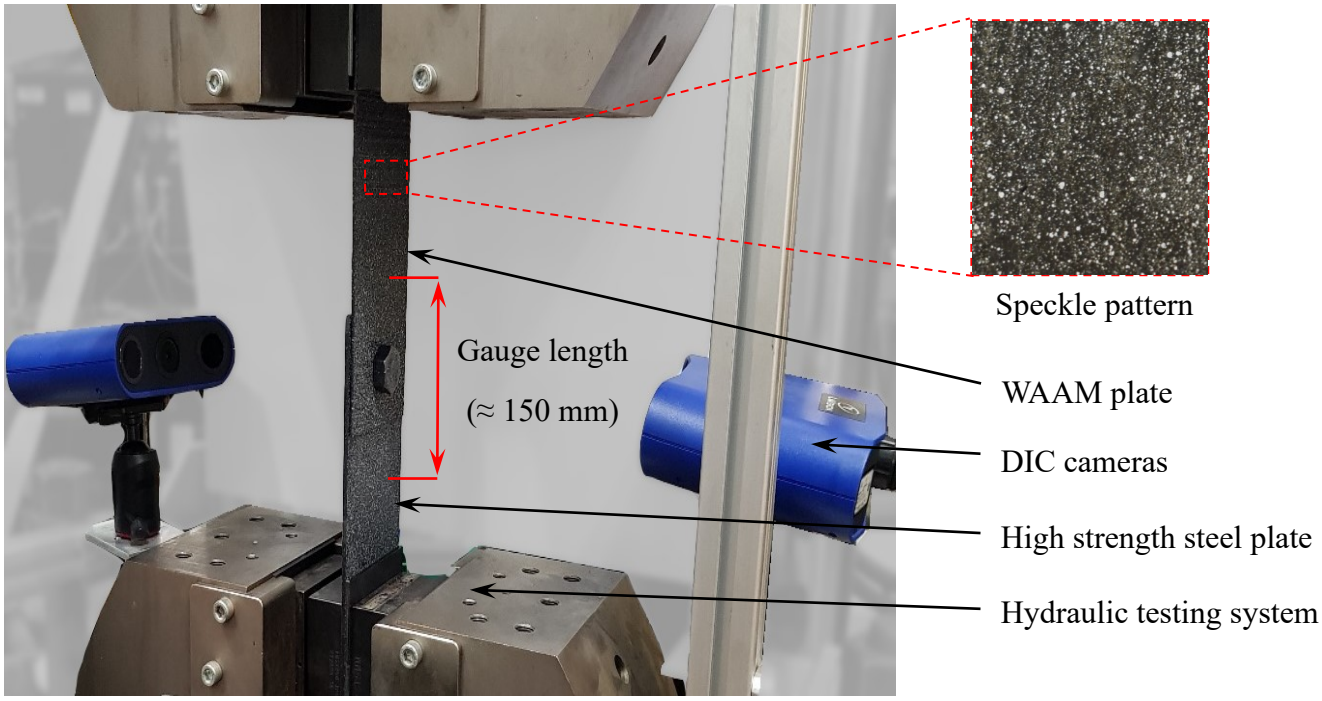


Figure 3.7: Experimental setup for lap shear connection tests

All tests were conducted using a 600 kN Instron testing machine. The specimens were loaded using displacement control at a constant rate of 0.8 mm/min. A four-camera DIC system was employed to record the displacements and strain fields of both sides of the specimens, which were first painted black and then sprayed with a random white speckle pattern prior to testing to provide features for the DIC system to monitor – see Figure 3.7.

3.4.2. Failure modes

The observed failure modes of all tested specimens are reported in Table 3.7, where shear-out, net section tension, localised tearing, end-splitting and curl-bearing (see Section 4.2.4) failures are denoted by SO, NS, LT, ES and CB, respectively.

Table 3.7: Summary of experimental results (FM = failure mode)

Specimen	Test		
	P_u (kN)	FM	Curling
S3-35-27-90	21.44	NS[1]	
S3-35-27-0	21.53	NS	
S3-45-27-90	35.51	NS+LT	✓
S3-45-27-0	37.13	NS+LT	✓
S3-45-36-90	36.12	NS+LT	✓
S3-45-36-0	37.17	NS+LT	✓
S3-55-27-90	36.30	LT	✓
S3-55-27-0	39.28	LT	✓
S3-65-18-90	25.97	SO	
S3-65-18-0	25.08	SO	
S3-65-21.6-90	31.12	SO	
S3-65-21.6-0	31.70	SO	
S3-65-27-90	43.95	LT	✓
S3-65-27-0	42.59	SO	✓
S3-65-32.4-90	44.30	LT	✓
S3-65-32.4-0	43.71	LT	✓
S3-65-36-90	42.50	LT	✓

S3-65-36-0	43.10	LT	✓
S3-85-33-90	42.78	LT	✓
S3-85-33-0	48.88	LT	✓
S3-85-44-90	49.41	LT	✓
S3-85-44-0	50.46	LT	✓
S3-105-33-90	47.54	LT	✓
S3-105-33-0	47.67	SO	✓
S3-105-39.6-90	53.21	LT	✓
S3-105-39.6-0	48.02	LT	✓
S3-105-44-90	50.88	LT	✓
S3-105-44-0	51.12	LT	✓
S3-145-44.2-90	46.30	LT	✓
S3-145-44.2-0	49.32	LT	✓
S3-145-78-90	56.81	CB	✓
S3-145-78-0	57.03	CB	✓
S3-145-104-90	55.88	CB	✓
S3-145-104-0	54.34	CB	✓
S8-45-39-90	62.71	NS	
S8-45-39-0	60.44	NS	
S8-55-39-90	95.75	NS	
S8-55-39-0	101.11	NS	
S8-65-39-90	118.77	NS	
S8-65-39-0	123.78	NS	
S8-75-39-90	133.38	ES	
S8-75-39-0	146.77	ES+SO	
S8-95-26-90	84.56	SO	
S8-95-26-0	88.61	SO	
S8-95-33.8-90	118.04	SO	
S8-95-33.8-0	119.37	SO	
S8-95-39-90	140.86	SO+ES	
S8-95-39-0	135.59	SO+ES	

S8-95-65-90	194.76	LT	✓
S8-95-65-0	174.51	LT	✓
S8-95-78-90	178.62	LT	✓
S8-95-78-0	191.19	LT	✓
S8-117-32-90	102.45	SO	
S8-117-32-0	101.86	SO	
S8-117-48-90	162.28	ES	
S8-117-48-0	168.14	ES	
S8-117-80-90	223.89	LT	✓
S8-117-80-0	210.80	LT	✓
S8-117-96-90	208.02	LT	✓
S8-117-96-0	213.78	LT	✓

[1] NS: net section tension, LT: localised tearing, SO: Shear-out, ES: end-splitting, CB: curl-bearing failure)

3.4.2.1 Shear-out, net section tension and bearing failures

As expected, shear-out failures developed in the specimens with short end distances e_1 and large plate widths b – see Figure 3.8(a), while net section tension failures occurred in the specimens with larger end distances and narrower widths – see Figure 3.8(b). Purely bearing failures did not occur in the single-shear lap tests because of the tilting of the bolt and the curling of the plate. Instead, localised tearing or curl-bearing failure developed where the end distance and the width of the plate were sufficiently large.



(a) (b)

Figure 3.8: Typical failure modes: (a) shear-out and (b) net section tension

3.4.2.2 Localised tearing failure

The failure mode shown in Figure 3.9, which is associated with fracture away from the minimum net section (i.e. at the centre of the bolt hole) combined with significant out-of-plane deformations, is referred to as localised tearing and was first identified by Rogers and Hancock (2000). Localised tearing develops in elements made of ductile mild steel and can be viewed as a characteristic of localised bearing stress (Rogers & Hancock, 2000). Note that particular attention is required to distinguish localised tearing from net section tension failure. Rogers and Hancock (2000) pointed out that a lack of necking across the net section, which is characteristic of a net section tension failure, is an indication of a localised tearing failure.

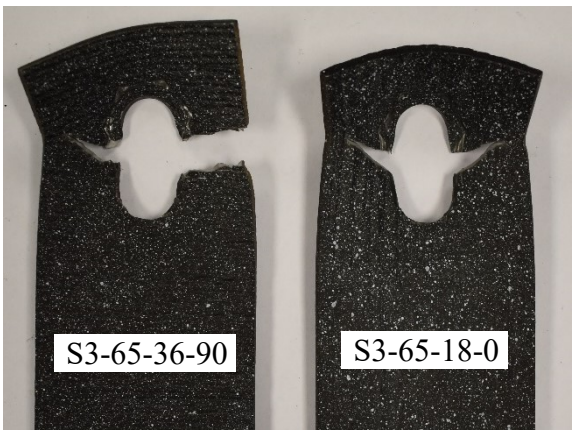
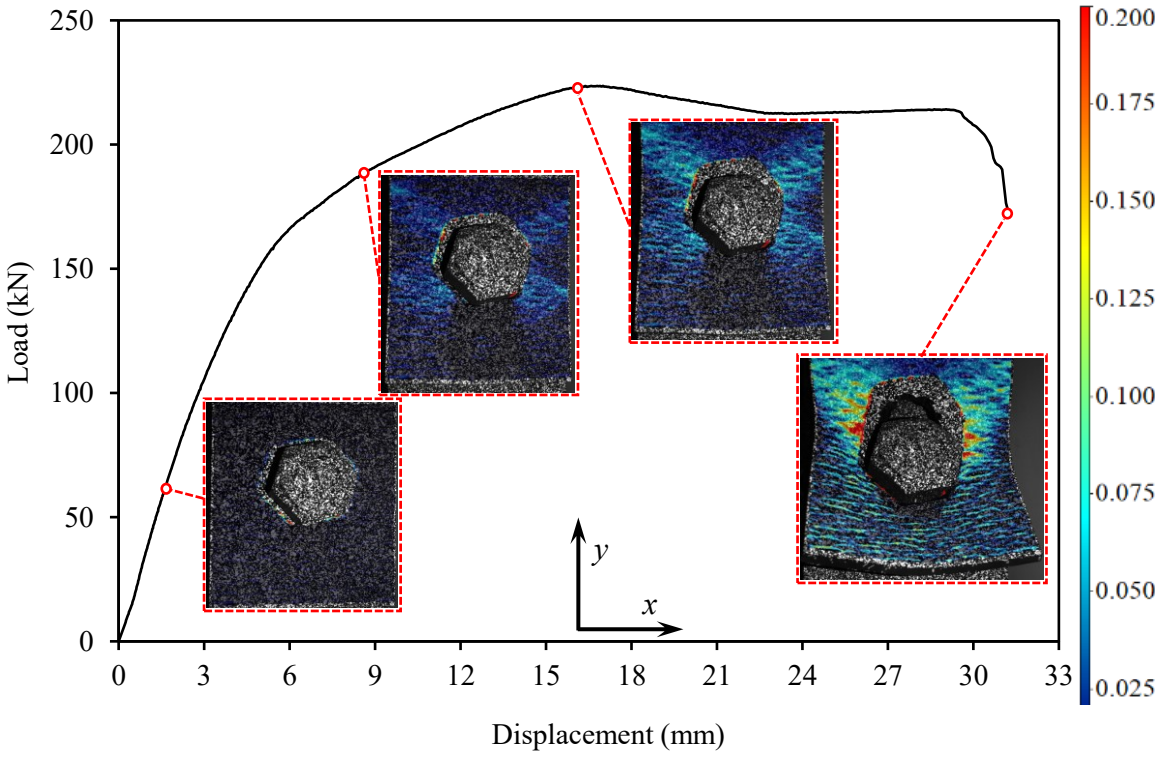


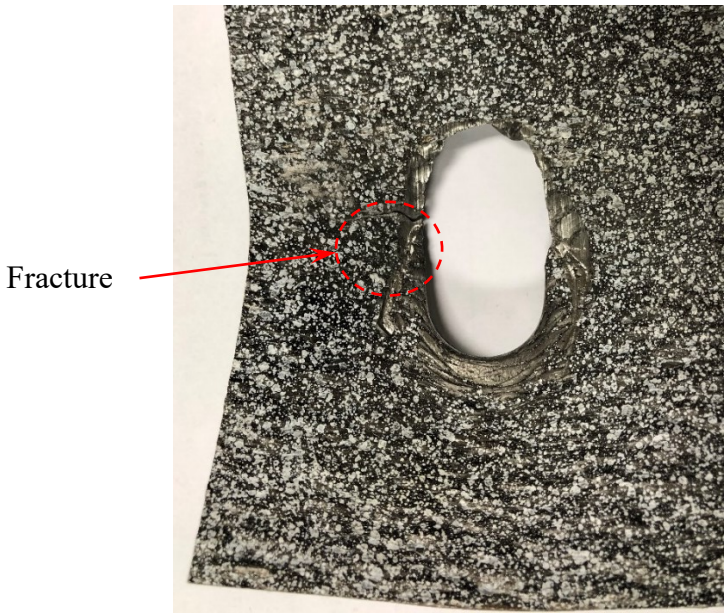
Figure 3.9: Localised tearing failure

The evolution of tensile strain fields in typical cases of localised tearing and of net section tension failures are presented in Figures 3.10 and 3.11, respectively. In Figure 3.10(a), a

butterfly shaped strain distribution can be observed at the later stages of loading, eventually leading to fracture away from the minimum net section, as shown in Figure 3.10(b). In Figure 3.11, where a typical case of net section tension failure is shown, the butterfly shaped strain distribution was only partially developed when necking and subsequently rupture took place at the minimum net section, as shown in Figure 3.8(b).



(a) Strain fields at different loading levels for the specimen



(b) Close-up view of the fracture

Figure 3.10: Specimen (S8-117-80-90) failing by localised tearing

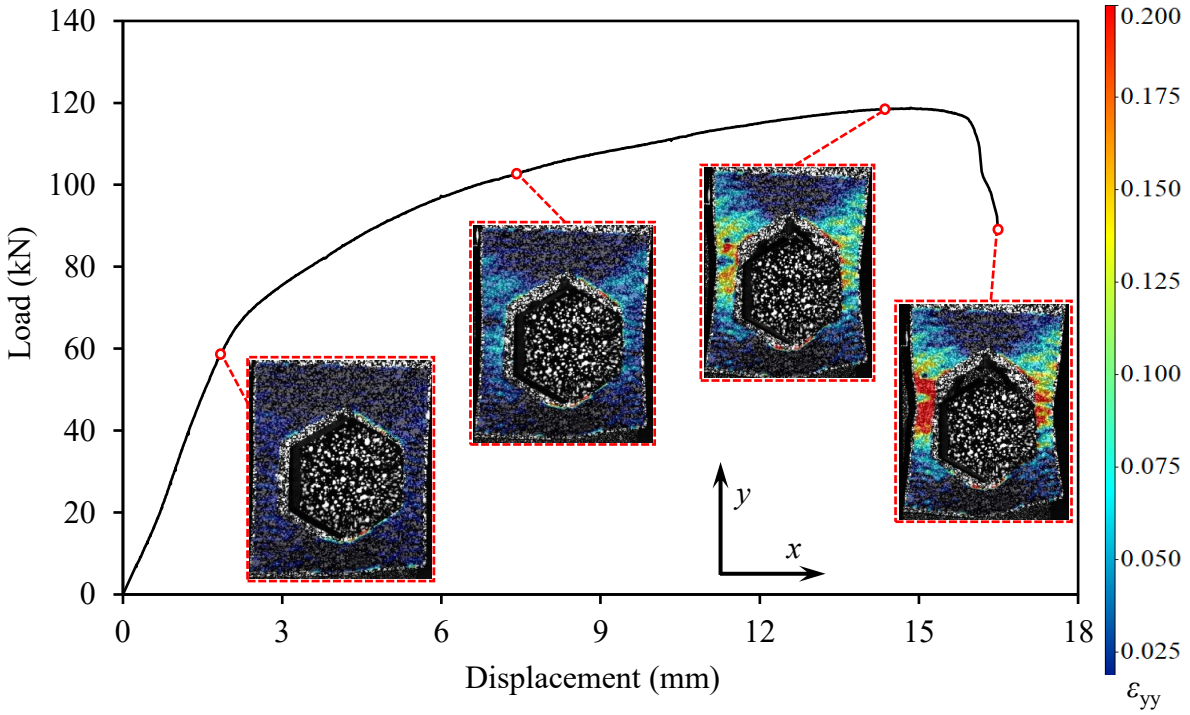
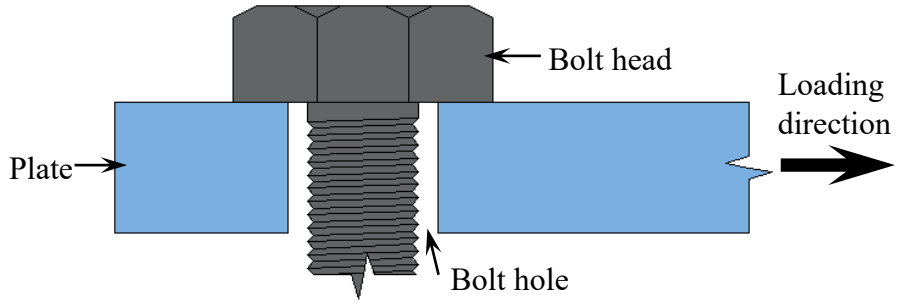


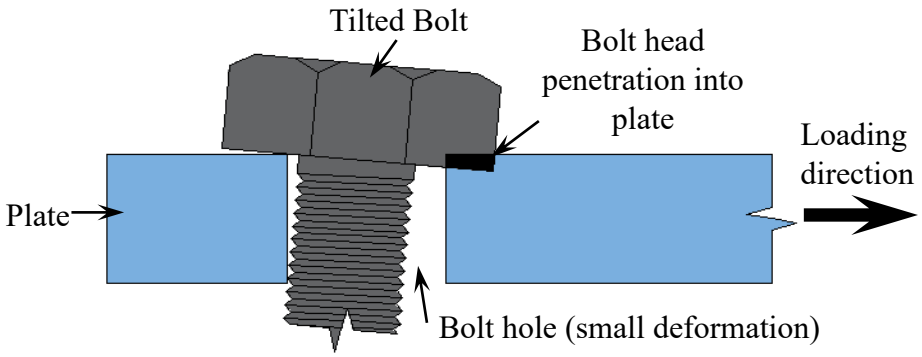
Figure 3.11: Strain fields at different loading levels for a specimen (specimen S8-65-39-90) failing by net section tension

3.4.2.3 Tilt-bearing failure

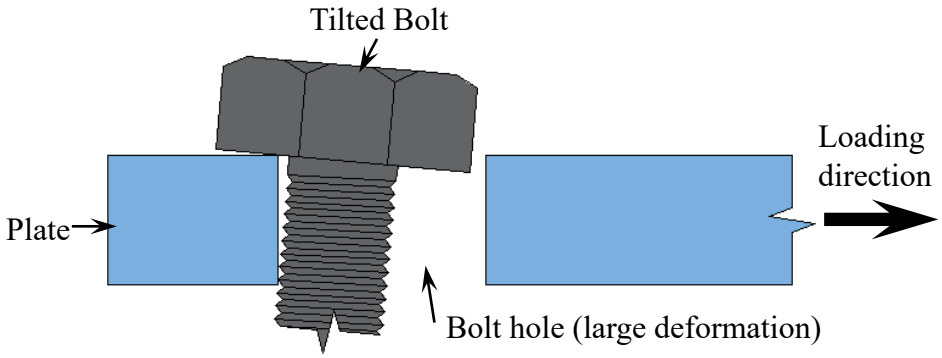
Tilt-bearing (Teh & Uz, 2017) is a mode of failure characterised by tilting of the bolt head or nut, which punches through the plate on the upstream side of the bolt hole, typically developing in lap tests under single shear when washers are not used – see Figure 3.12(b). Although tilting of the bolts was observed in the tested specimens, tilt-bearing failure did not occur. This outcome is attributed to the configuration of the test specimens and the good ductility of the studied WAAM steel, resulting in large deformations of the bolt hole and thus avoiding the bolt head (or nut) punching through the upstream side of the connected sheet – see Figure 3.12 (c).



(a) Unloaded configuration



(b) Bolt head penetrating into plate during loading



(c) Bolt head avoiding penetration into plate because of large deformation of bolt hole during loading

Figure 3.12: Schematic view of bolt tilting and bolt head either penetration or avoiding plate in single-lap shear connections

3.4.2.4 Curling and curl-bearing failure

The out-of-plane deformation mode known as curling (as distinct from curl-bearing failure, although this failure mode must be accompanied by curling) was observed for most specimens. As expected, curling was more pronounced in the thinner (i.e. 3 mm thick) plates. Although,

in most cases, curling was not the direct cause of failure, in the tests of the thin plates where the end distances were extremely large, severe curling resulted in the bolt head penetrating into the lap plate downstream of the bolt hole – see Figure 3.13. This failure mode is referred to as curl-bearing failure herein, and to the author's knowledge, has not been previously defined in the literature. In a sense, the curl-bearing failure mode is the "mirror" mode of the tilt-bearing failure mode, which involves the bolt head punching through the connected plate upstream as the bolt tilts backwards. They therefore share a similar fracture mechanism.

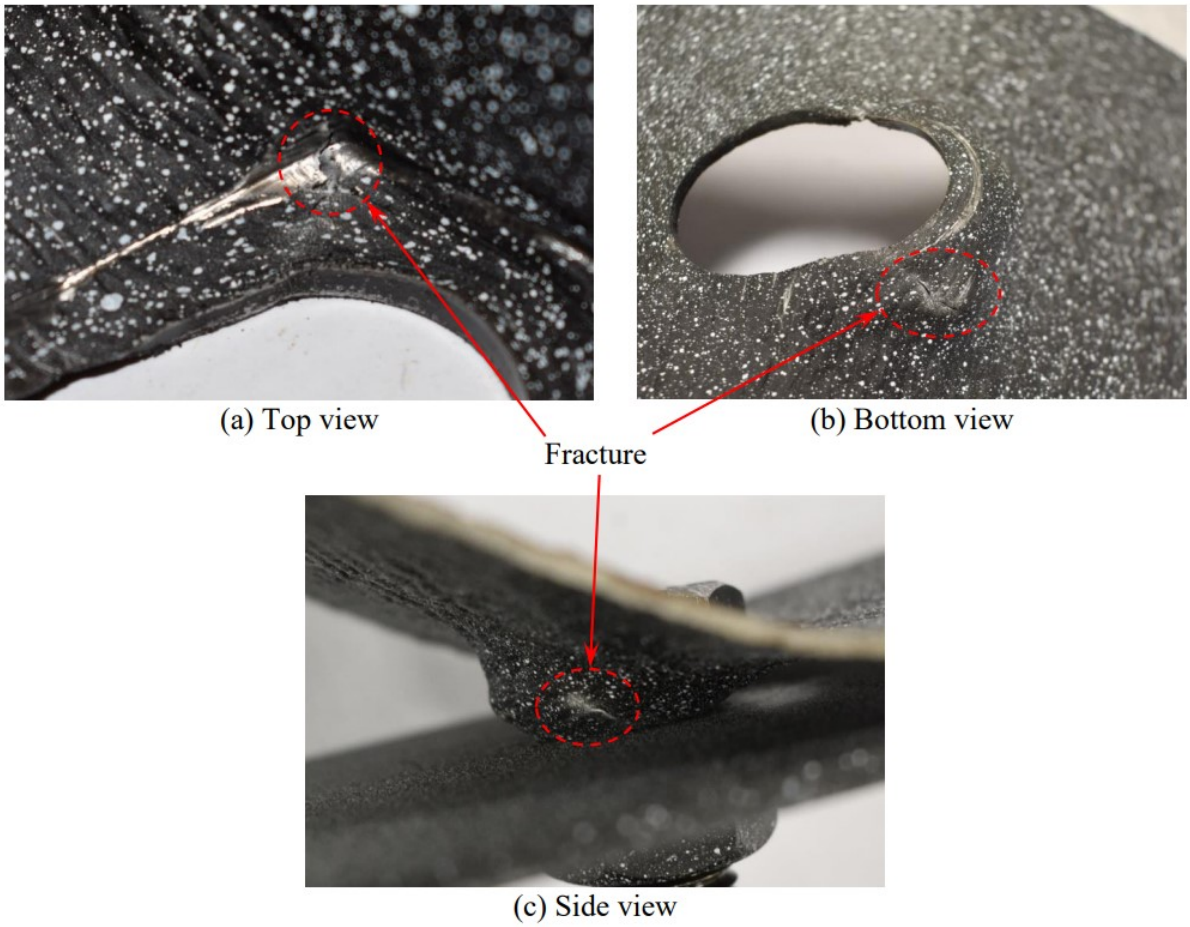


Figure 3.13: Close-up view of bolt head penetrating into plate – curl-bearing failure (Specimen S3-145-104-90)

3.4.2.5 End-splitting failure

End-splitting failure is characterised by in-plane bending and transverse tensile fracture at the specimen end. This mode of failure has been reported by several researchers (Može & Beg, 2010; Wang, Lyu & Li, 2018; Xing et al., 2020b; Wang et al., 2017; Rex & Easterling, 2003; Može & Beg, 2014) and was also observed among the specimens tested herein. It has been

shown that the occurrence of either shear-out or end-splitting failure can be sensitive to the method used to cut the connected steel sheets (Xing et al., 2020b; Rex & Easterling, 2003).

The strain fields recorded by the DIC system for a specimen (specimen S8-117-48-90) that displayed end-splitting failure are illustrated in Figure 3.14, where ε_{yy} and ε_{xx} denote the longitudinal and the transverse tensile strains, respectively. It can be observed that this failure mode is characterised by high localised transverse tensile strains ε_{xx} downstream of the bolt hole leading to tensile fracture at the plate end.

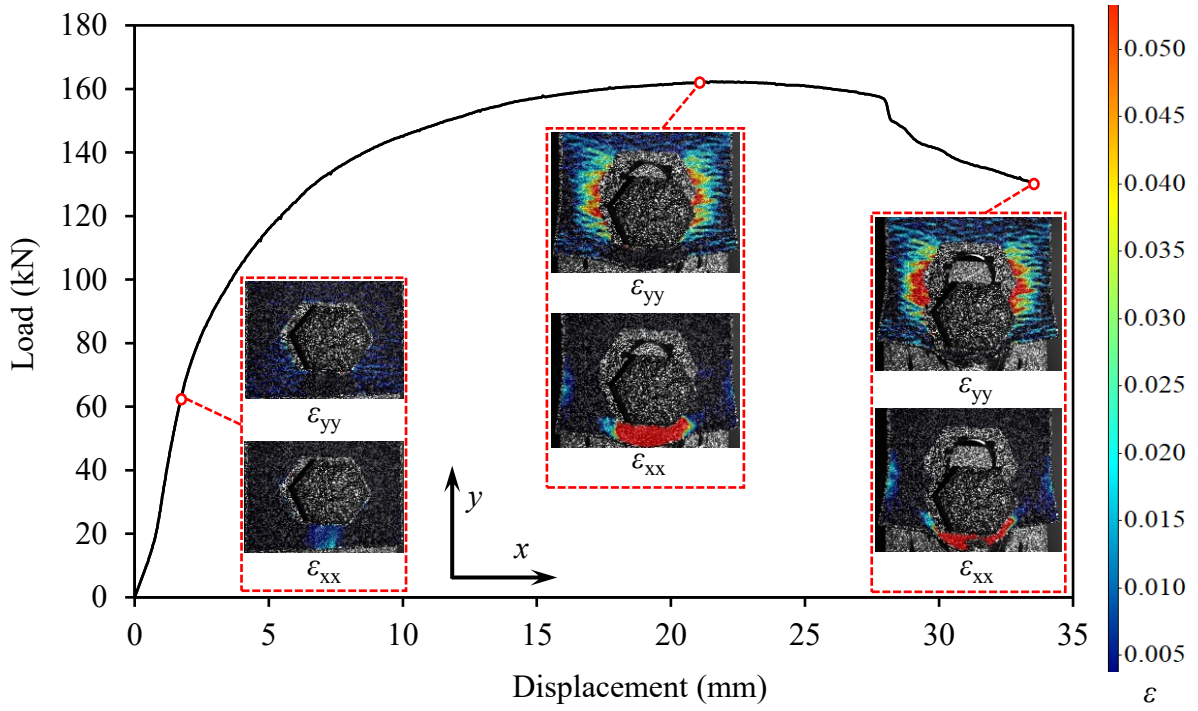


Figure 3.14: Strain fields at different loading levels for a specimen (specimen S8-117-48-90) failing by end-splitting

3.4.3. Transition between failure modes

The transition between the different failure modes has been examined herein by varying the geometric proportions of the test specimens and carefully inspecting the exhibited failure mechanisms. As shown in Figure 3.15, increasing the plate width b while keeping the end distance e_1 constant resulted in a transition from net section tension failure to end-splitting and, eventually, shear-out failure. Similarly, as shown in Figures 3.16 and 3.17, increasing the end distance e_1 for specimens with the same width b led to a failure mode transition from shear-out to end-splitting and, then, to localised tearing failure.



Figure 3.15: Failure mode transition from net section tension to end-splitting and shear-out failure



Figure 3.16: Failure mode transition from shear-out to end-splitting and localised tearing failure

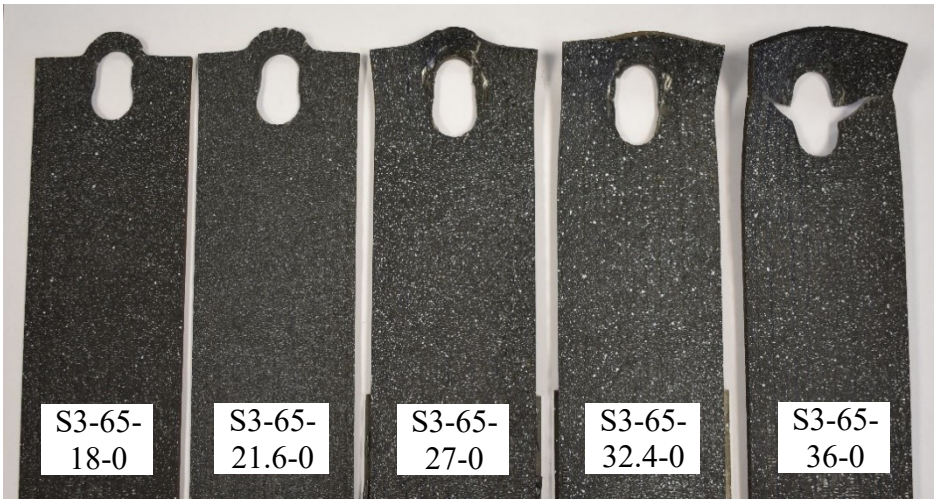


Figure 3.17: Failure mode transition from shear-out to localised tearing failure

3.4.4. Influence of print orientation

The angle θ between the axis of loading and the print layer orientation was not found to have a significant influence on the failure modes of most specimens, as shown in Figures 3.8 and 3.9. However, some specimens of the same nominal dimensions but of different print layer orientations (i.e. $\theta = 0°$ and 90°), failed in different modes and fractured at different locations. A typical example is shown in Figure 3.18, where it can be observed that the $\theta = 90°$ specimens failed by localised tearing while the $\theta = 0°$ specimen failed in shear-out, combined with significant curling. This is attributed to the fracture lines developing along the interface of adjoining print layers.

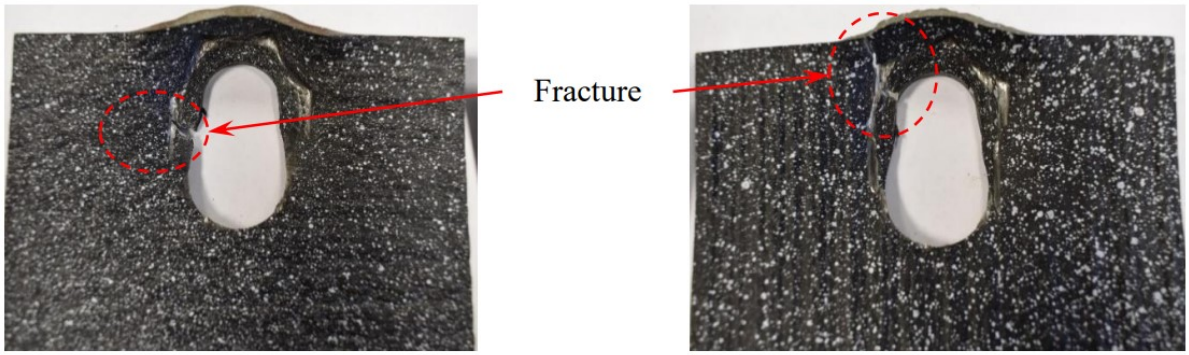
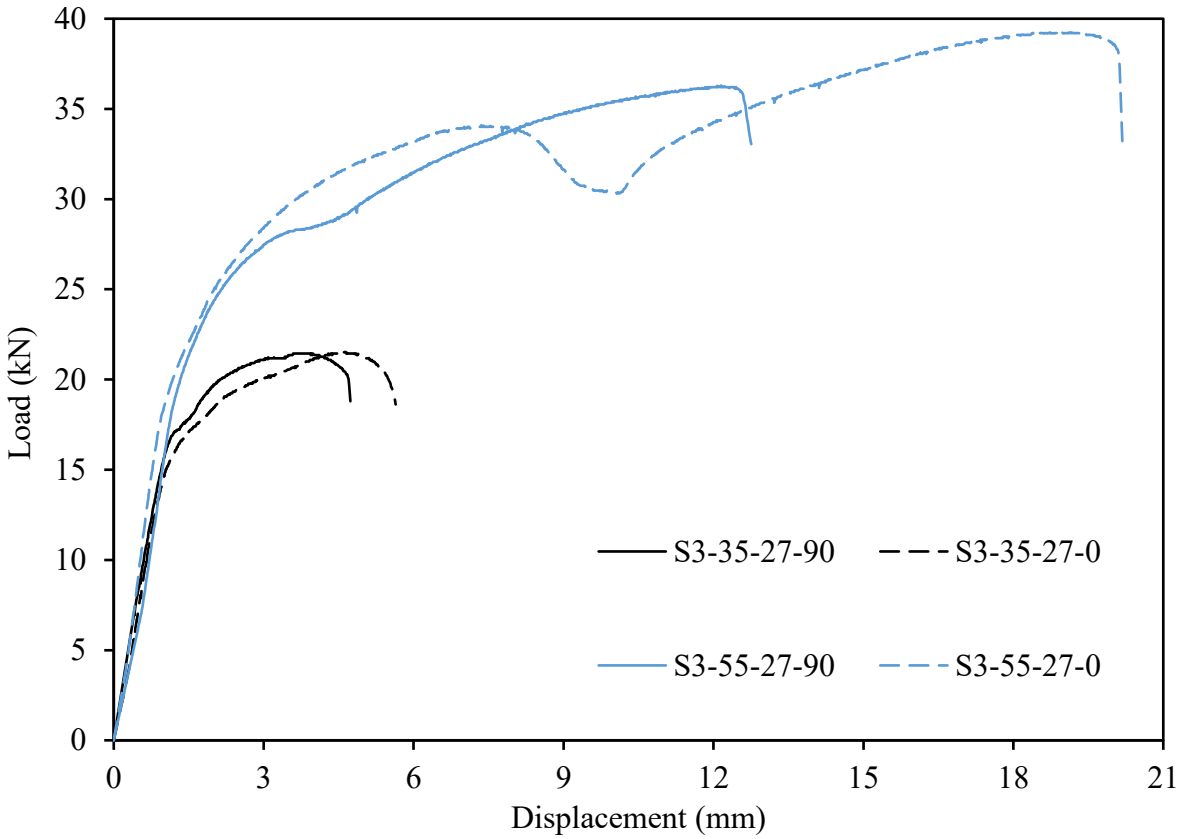


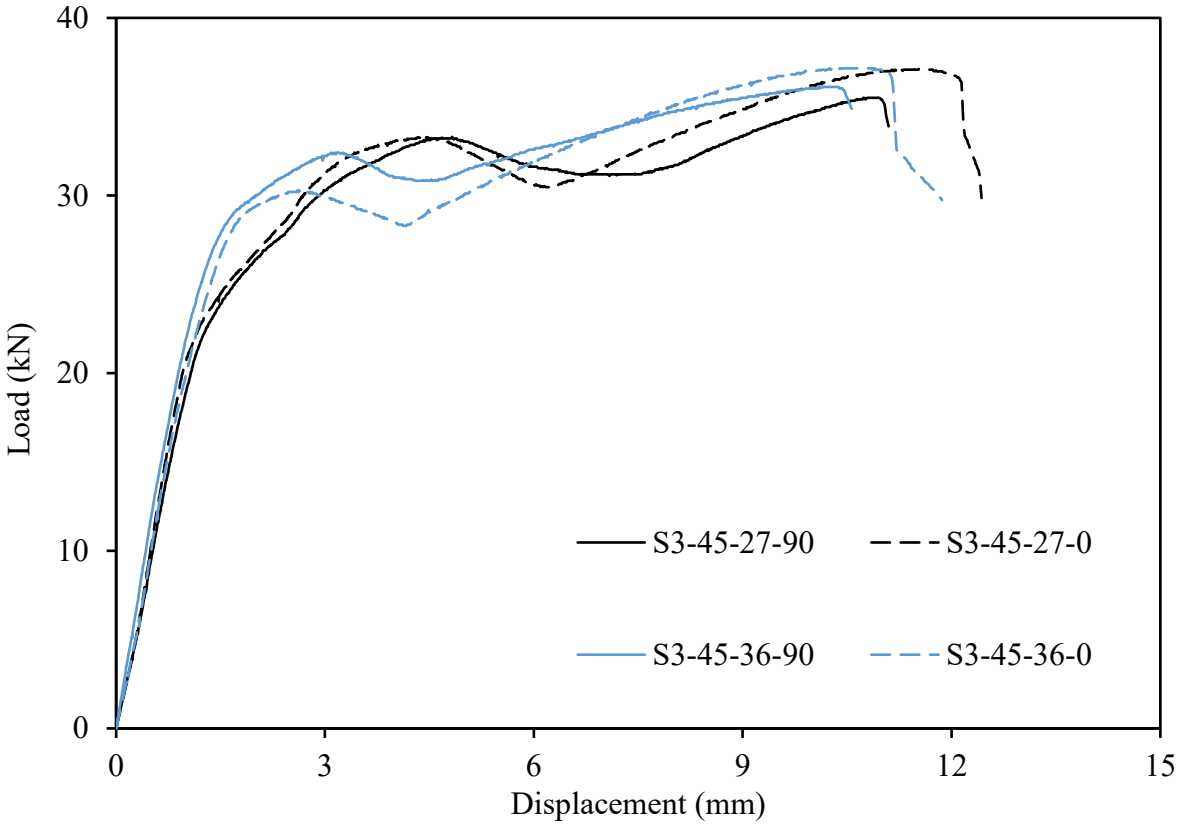
Figure 3.18: (a) Localised tearing in specimen S3-105-33-90 and (b) shear-out failure in specimen S3-105-33-0

3.5. Ultimate loads and load-deformation responses

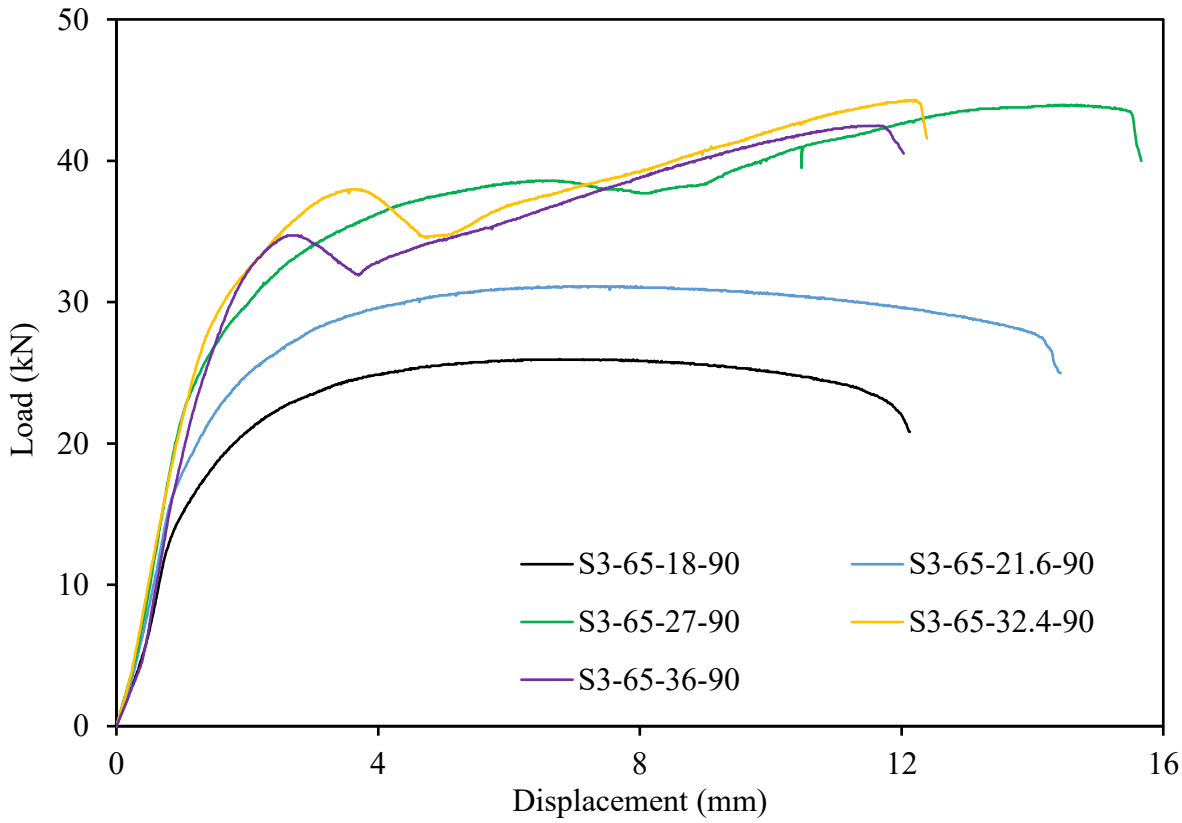
The ultimate loads P_u attained by all specimens are summarised in Table 3.7, while the load-displacement curves, all of which demonstrate good ductility, are plotted in Figure 3.19. Note that the displacements (averaged from the two sides of the specimens) were measured over a gauge length of about 150 mm – see Figure 3.7. Typical load-displacement curves of specimens exhibiting shear-out, net section tension, localised tearing, end-splitting and curl-bearing failures are presented in Figure 3.20. It can be observed that, while the curves corresponding to specimens failing by shear-out, net section tension and end-splitting have one distinct peak, the curves of specimens failing by localised tearing and curl-bearing have two peaks. This phenomenon is associated with the occurrence of curling, which, as observed during the tests, corresponded to the initial drop in load (i.e. the first peak). Once significant curling had developed, the resistance increased until the attainment of the second peak triggered by localised fracture.



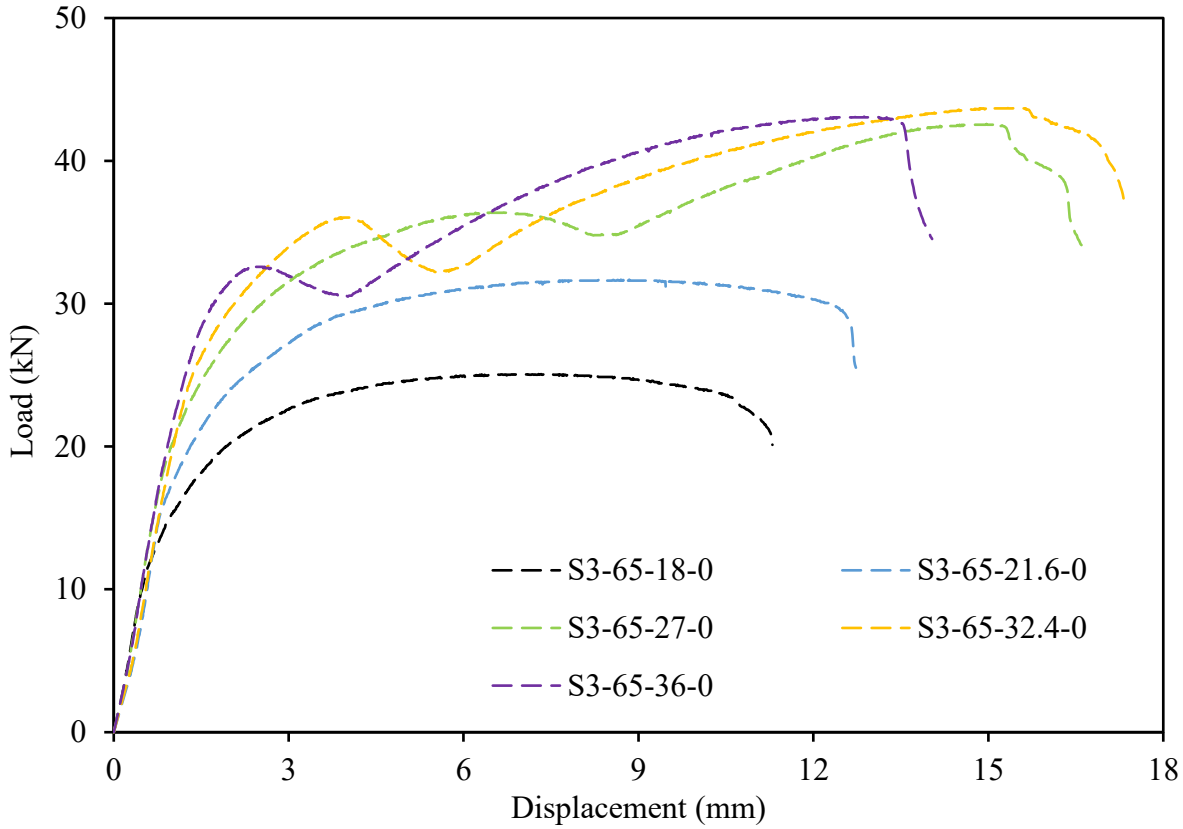
(a) $t = 3$ mm, $\theta = 0°$ or $90°$, $b = 35$ or 55 mm and $e_1 = 27$ mm



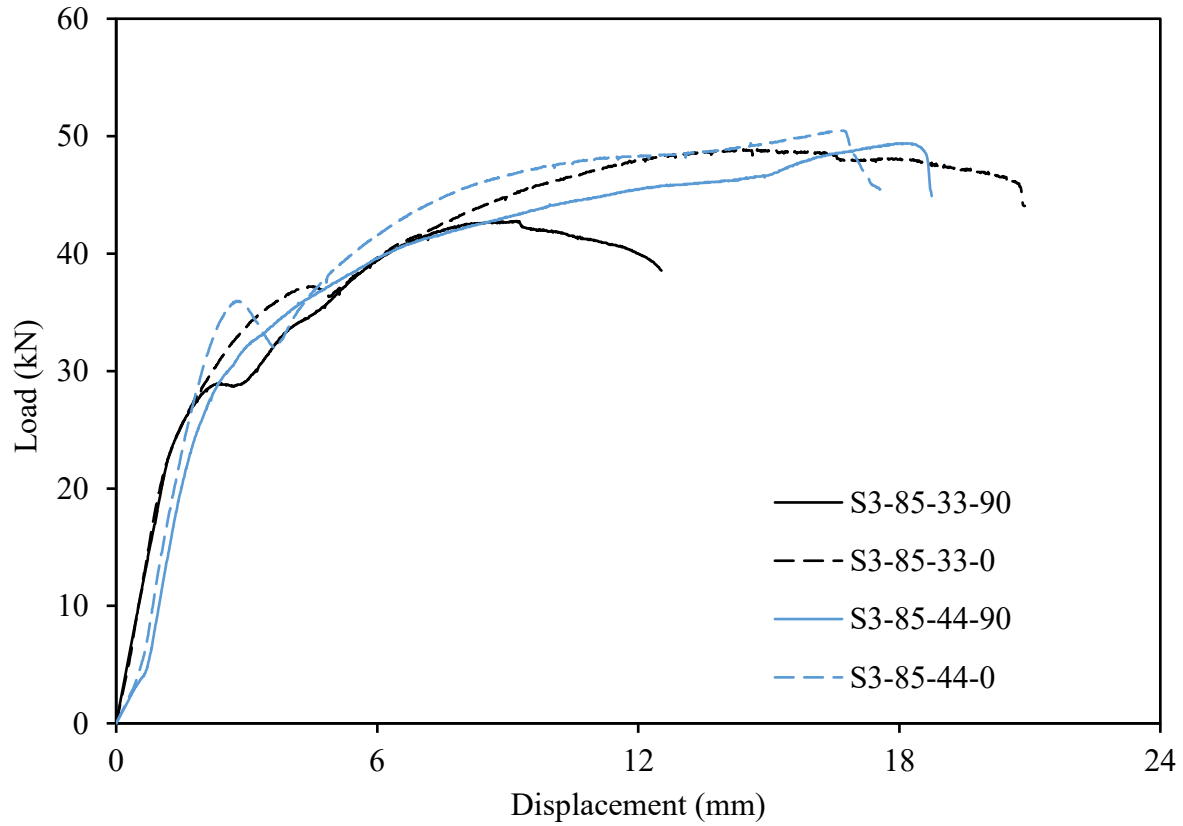
(b) $t = 3$ mm, $\theta = 0°$ or $90°$, $b = 45$ mm and $e_1 = 27$ or 36 mm



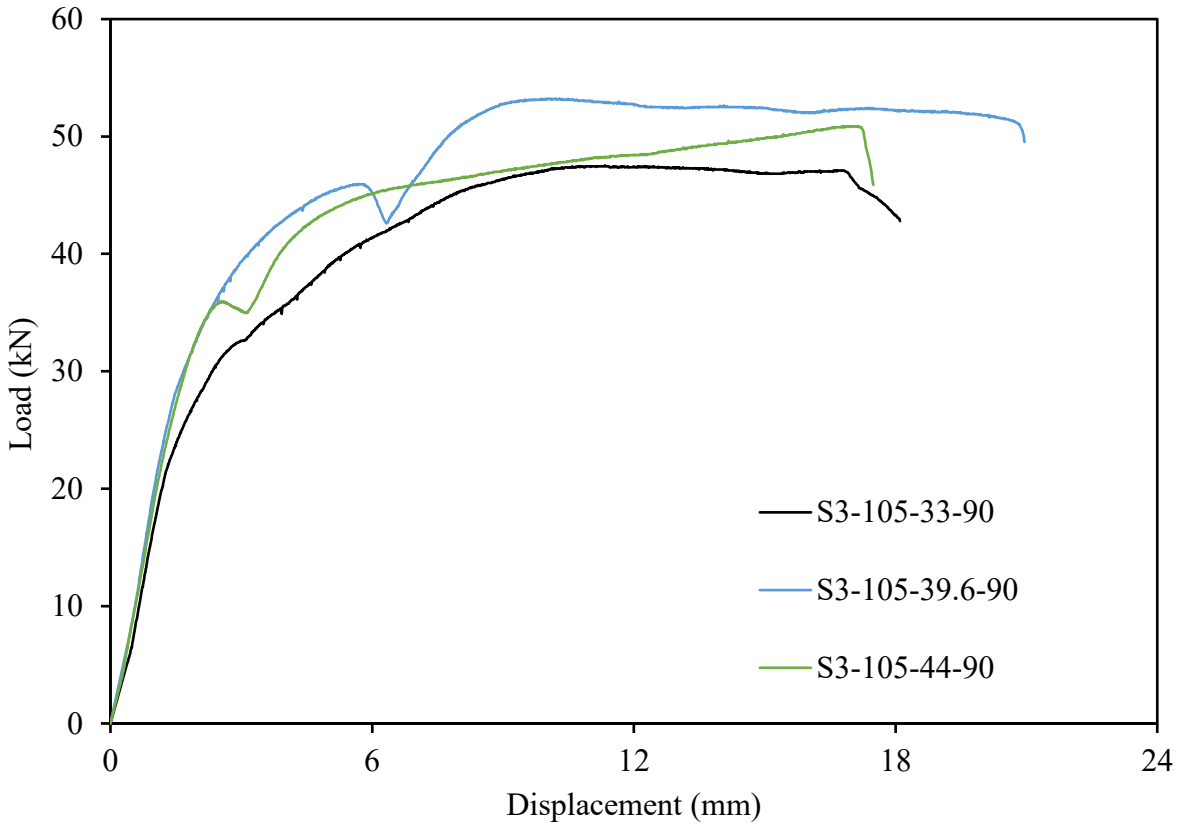
(c) $t = 3$ mm, $\theta = 90°$, $b = 65$ mm and e_1 varying from 18 to 36 mm



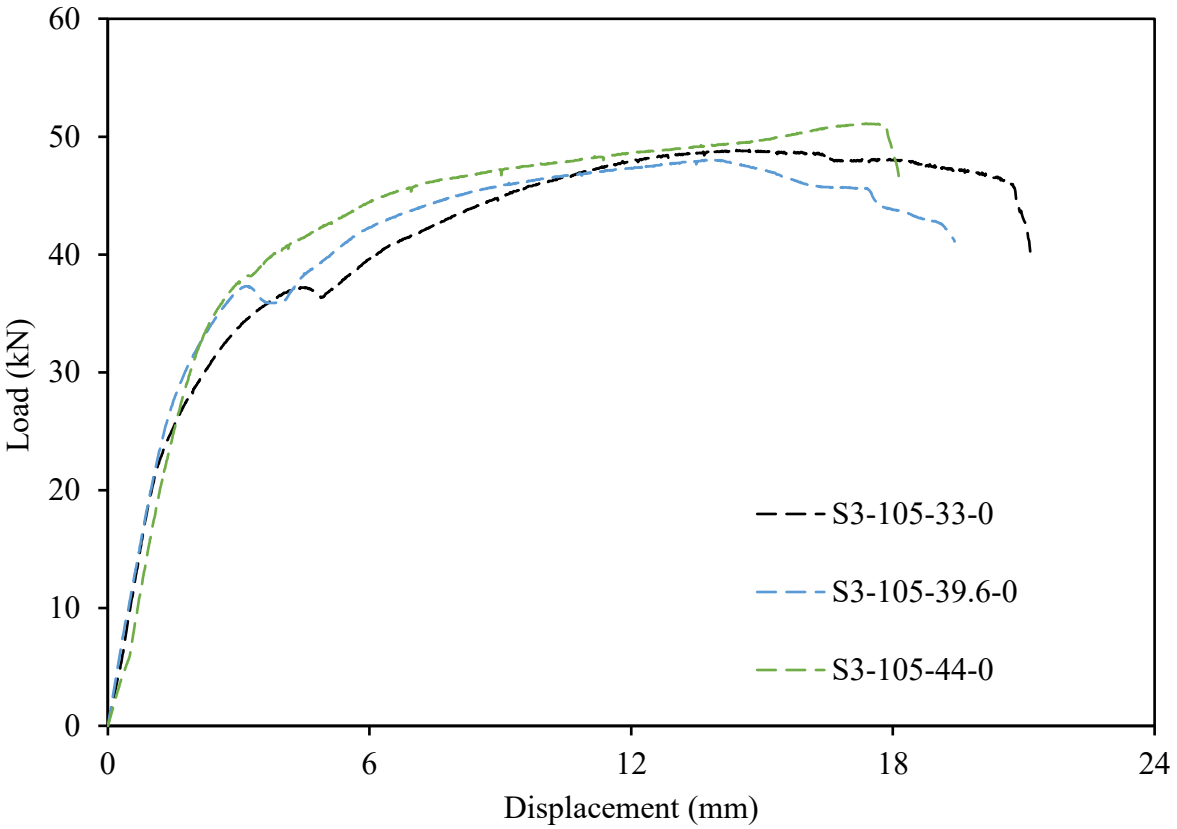
(d) $t = 3$ mm, $\theta = 0°$, $b = 65$ mm and e_1 varying from 18 to 36 mm



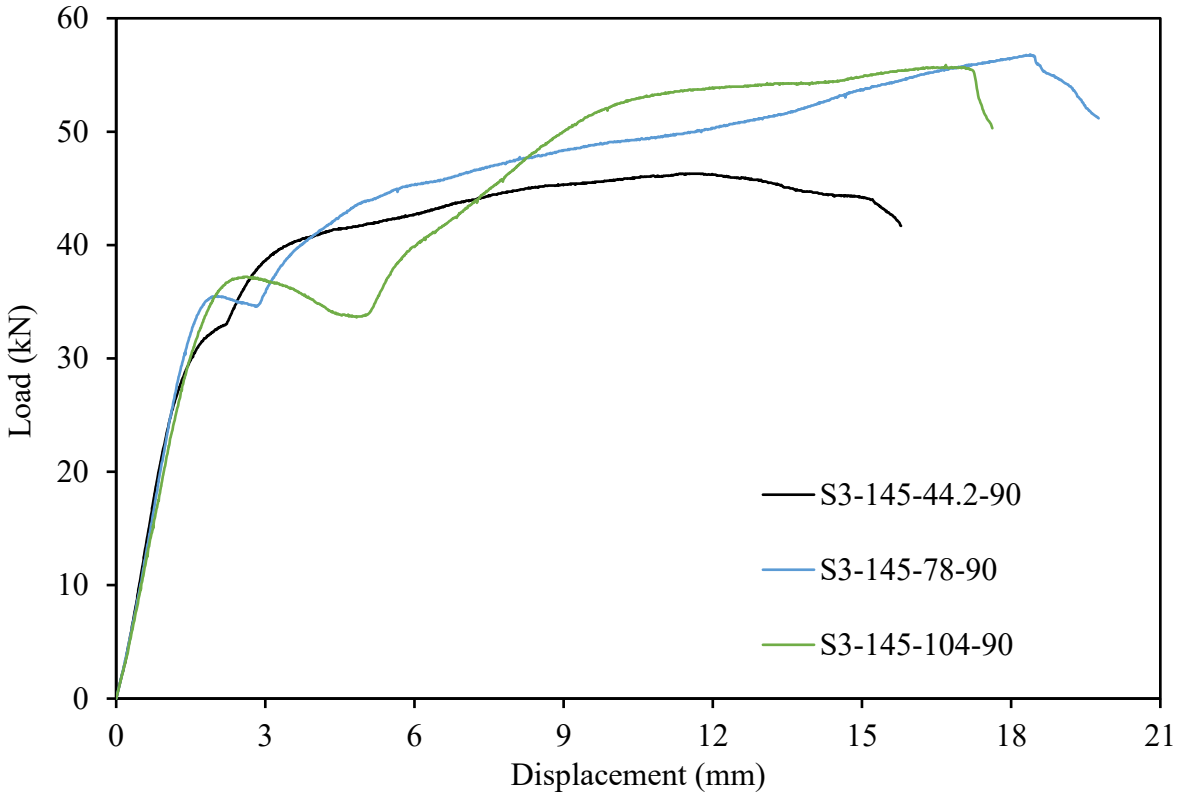
(e) $t = 3$ mm, $\theta = 0°$ or $90°$, $b = 85$ mm and $e_1 = 33$ or 44 mm



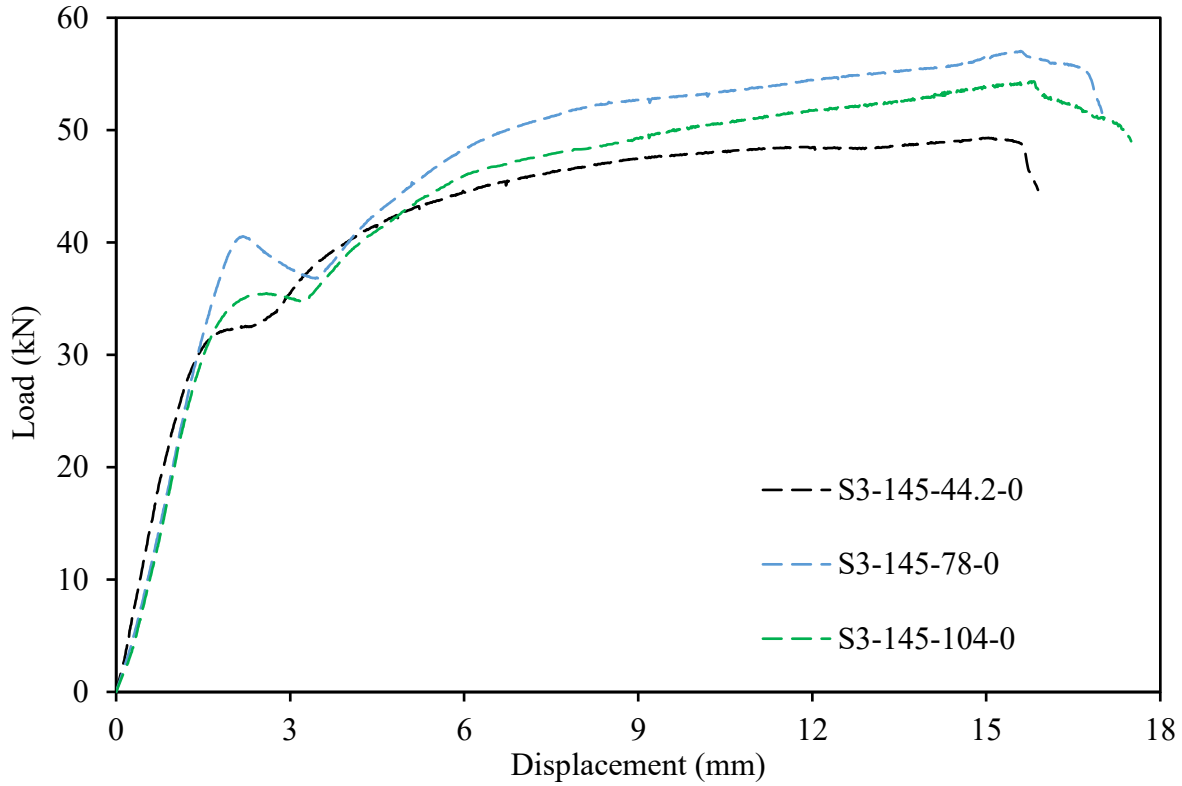
(f) $t = 3$ mm, $\theta = 90°$, $b = 105$ mm and e_1 varying from 33 to 44 mm



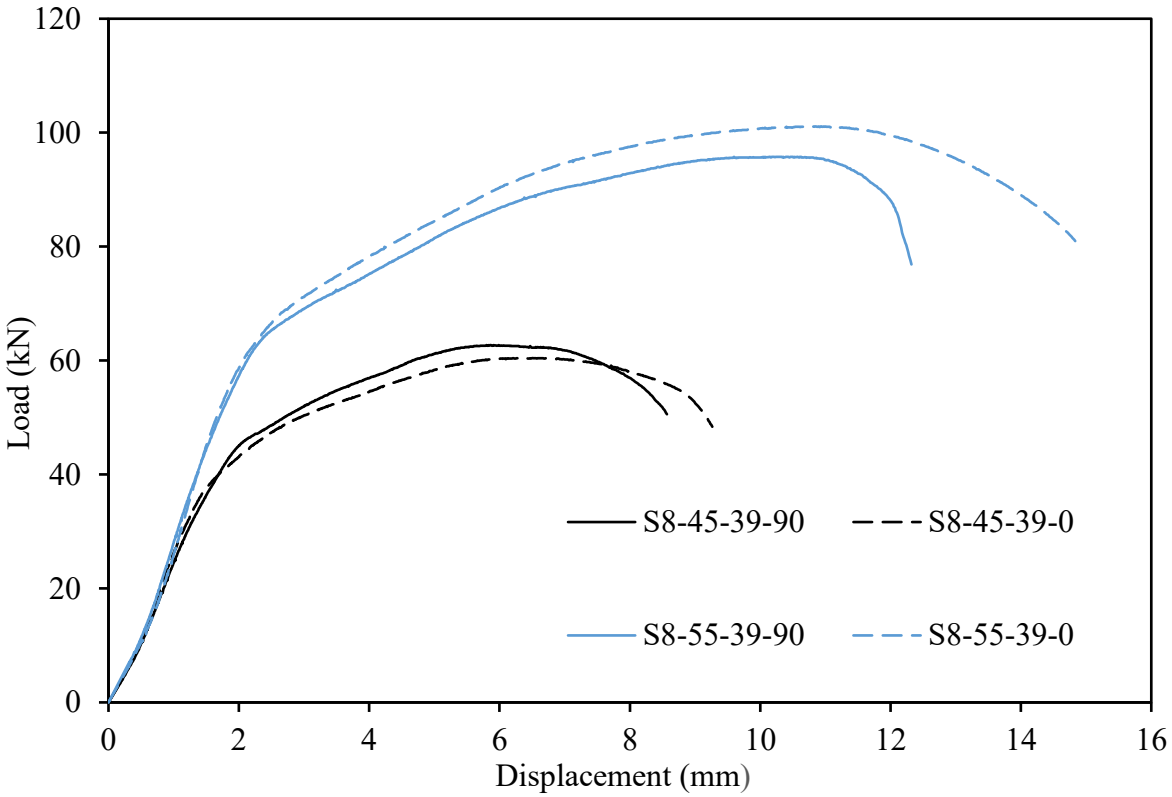
(g) t = 3 mm, θ = 0°, b = 105 mm and e1 varying from 33 to 44 mm



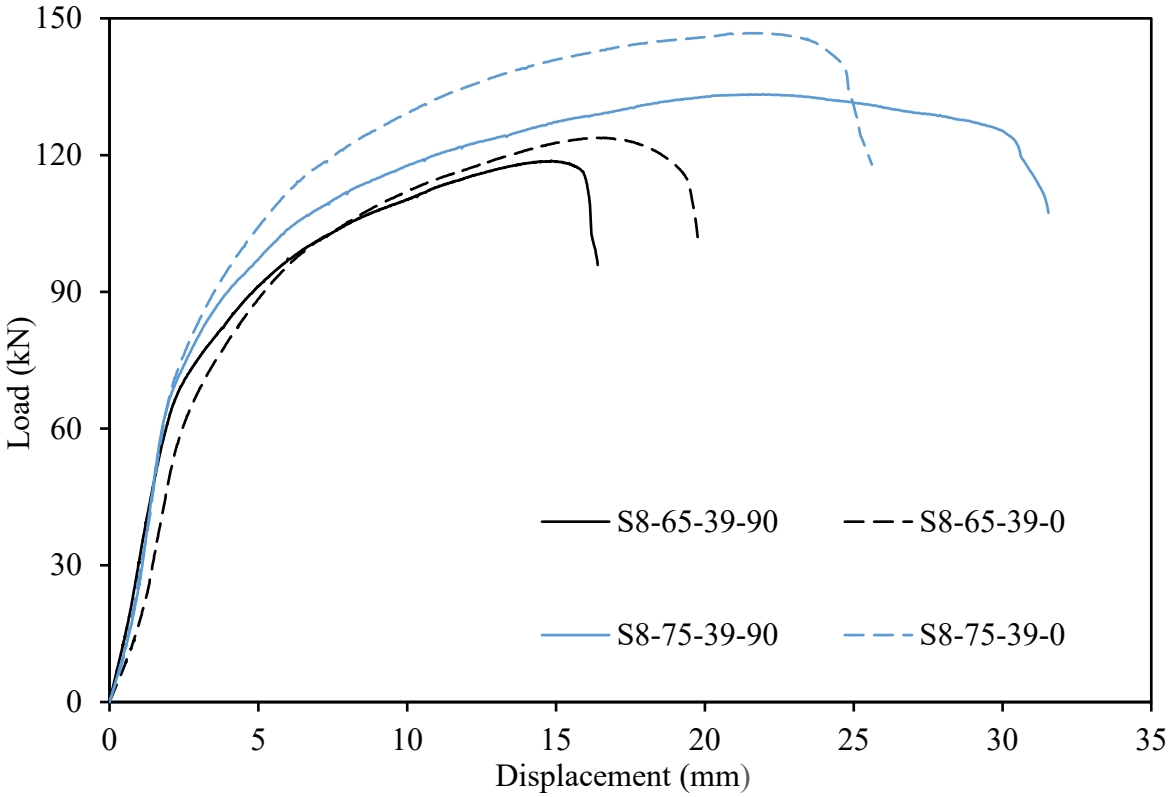
(h) t = 3 mm, θ = 90°, b = 145 mm and e_1 varying from 44.2 to 104 mm



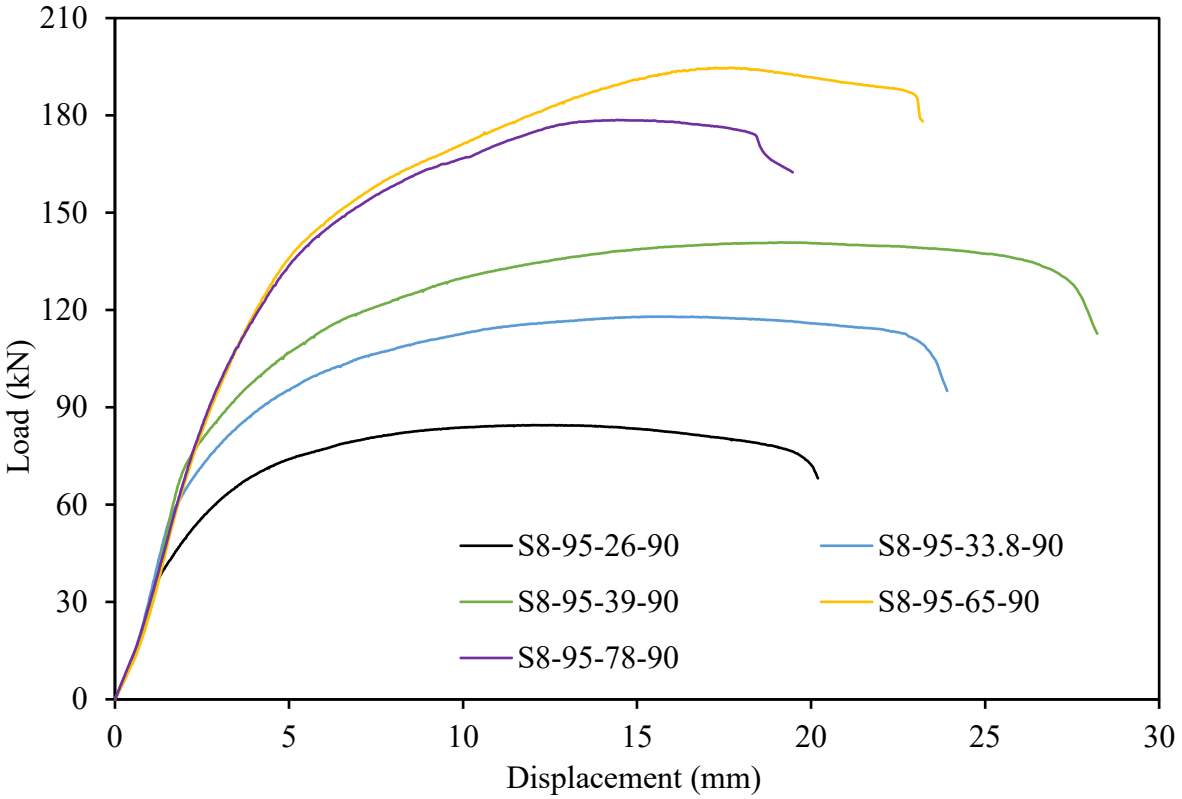
(i) t = 3 mm, θ = 0°, b = 145 mm and e_1 varying from 44.2 to 104 mm



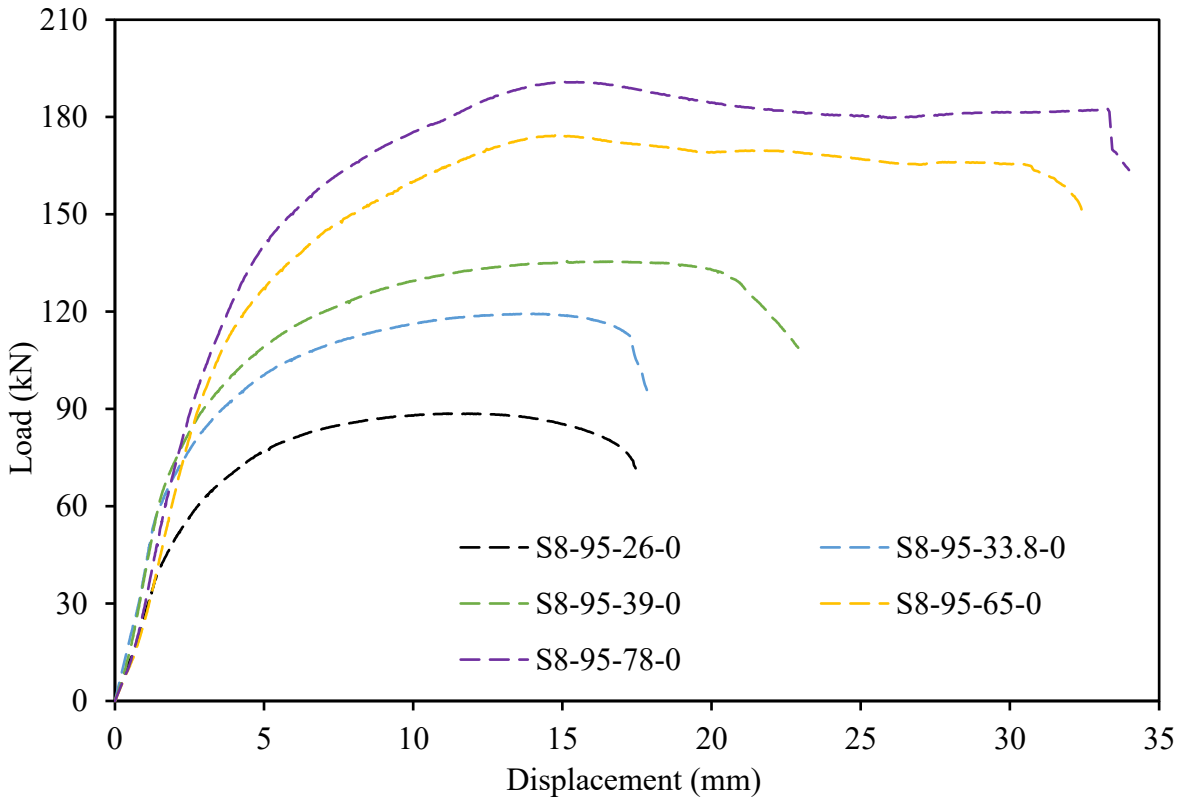
(j) t = 8 mm, θ = 0° and 90°, b = 45 or 55 mm and e_1 = 39 mm



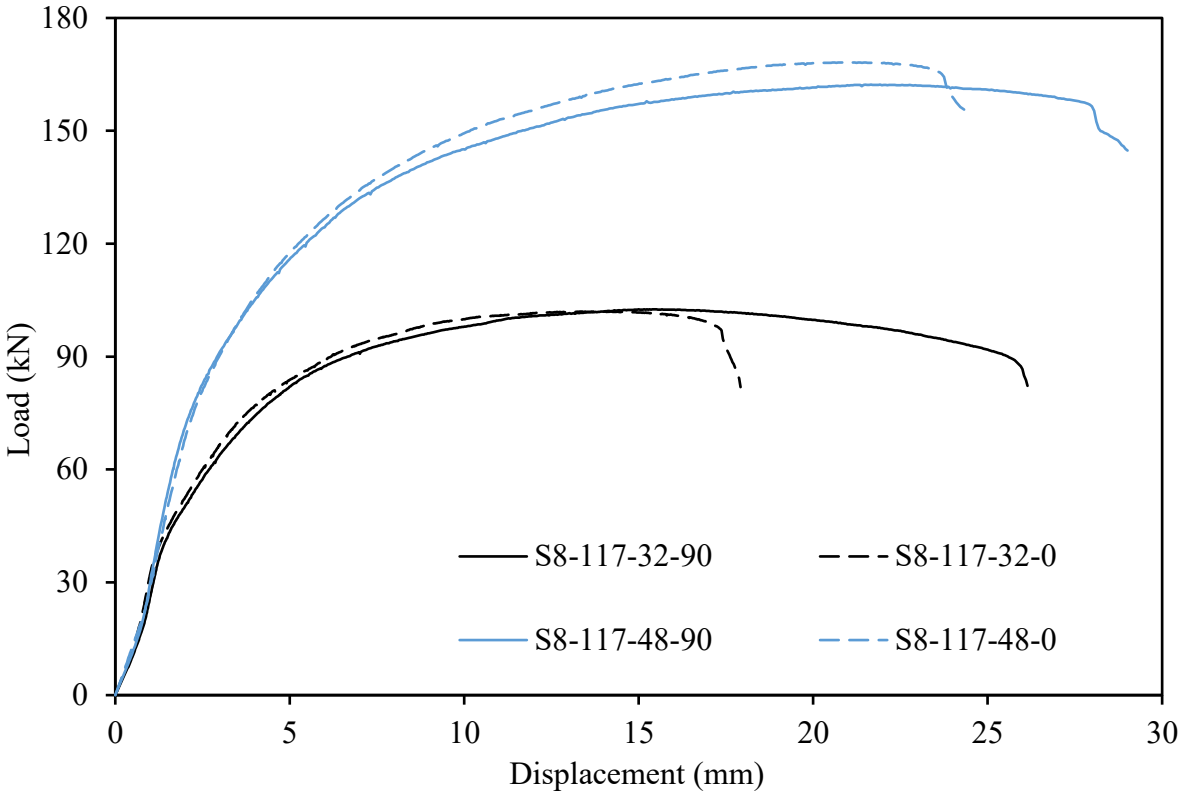
(k) t = 8 mm, θ = 0° and 90°, b = 65 or 75 mm and e_1 = 39 mm



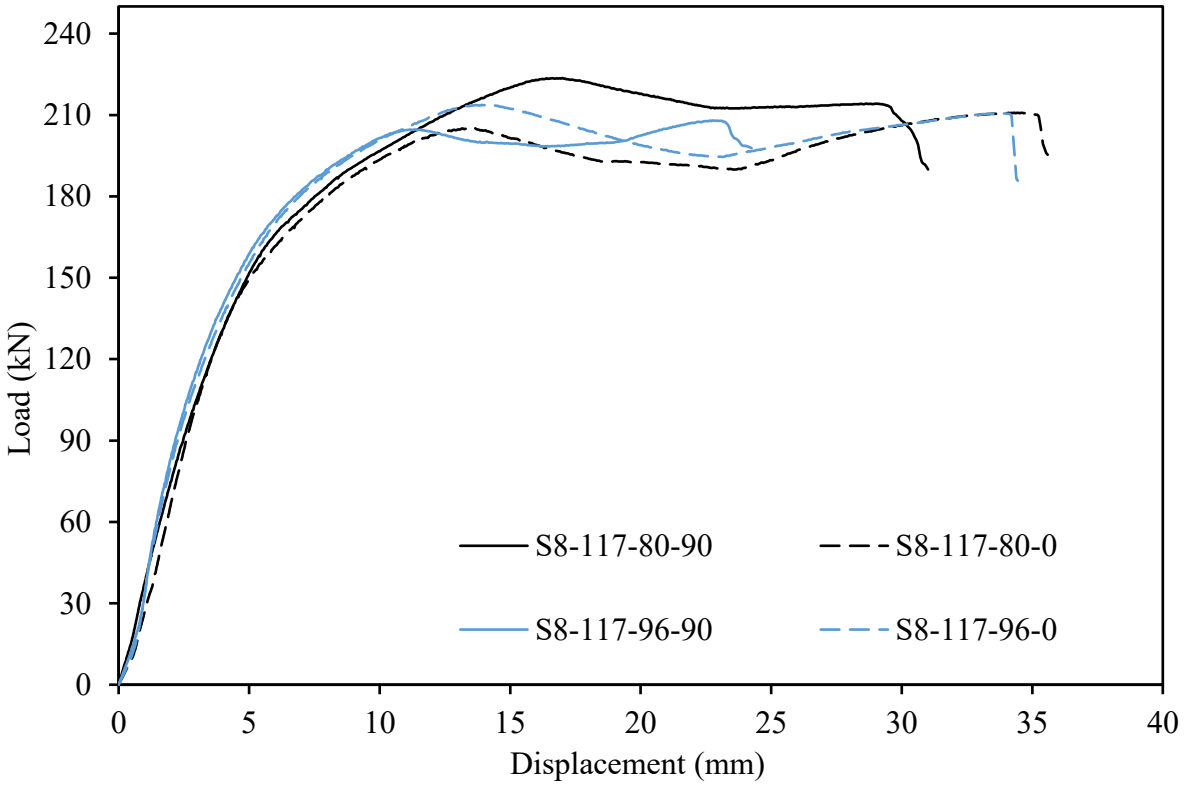
(l) $t = 8$ mm, $\theta = 90°$, $b = 95$ mm and e_1 varying from 26 to 78 mm



(m)$t = 8$ mm, $\theta = 0°$, $b = 95$ mm and e_1 varying from 26 to 78 mm

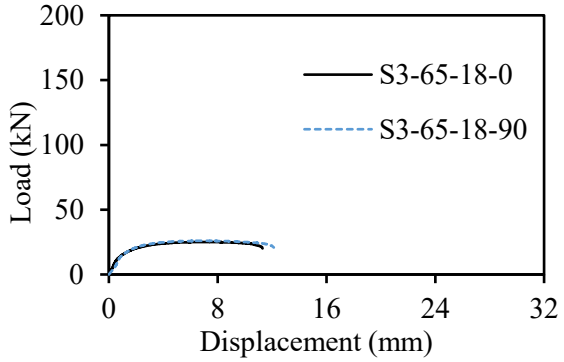


(n) t = 8 mm, θ = 0 or 90°, b = 117 mm and e_1 = 32 or 48 mm

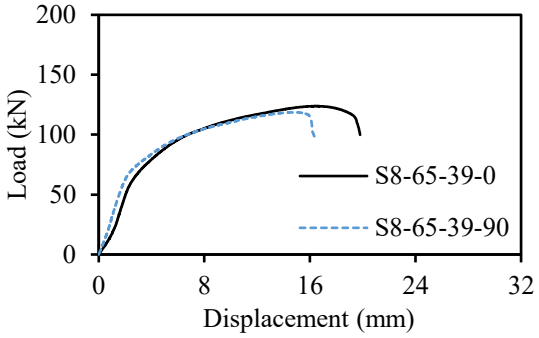


(o) t = 8 mm, θ = 0 or 90°, b = 117 mm and e_1 = 80 or 96 mm

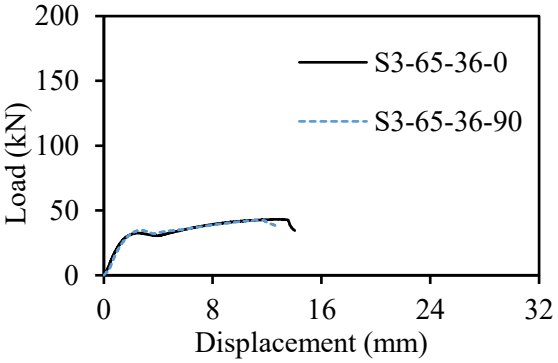
Figure 3.19: Load-displacement curves of lap shear test specimens



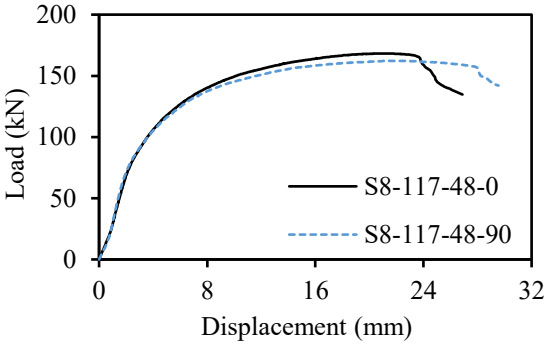
(a) Shear-out failure



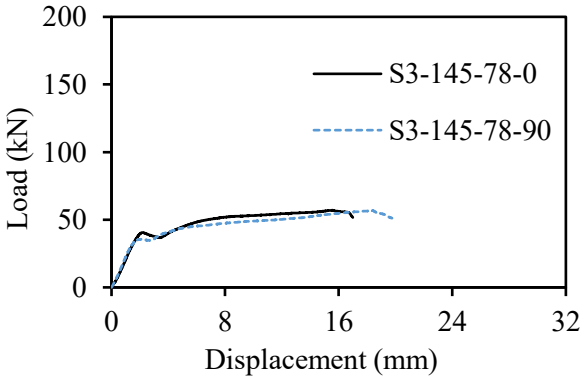
(b) Net section tension failure



(c) Localised tearing failure



(d) Splitting failure

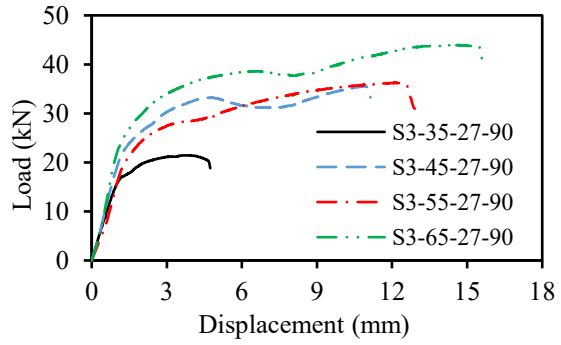


(e) Curl-bearing failure

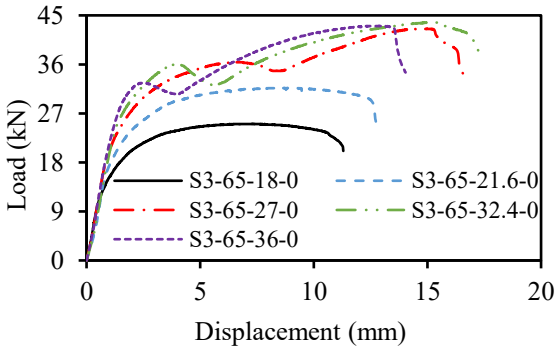
Figure 3.20: Load-displacement curves of pairs of specimens with $\theta = 0°$ and $\theta = 90°$ exhibiting: (a) shear-out, (b) net section tension, (c) localised tearing, (d) end-splitting and (e) curl-bearing failure

The influence of the geometric proportions of the lap plates on the load-displacement curves is presented in Figure 3.21. As expected, increasing the plate width b was found to result in increasing ultimate capacities, as shown in Figures 3.2121 (a) and (c) for the thinner (i.e. 3mm)

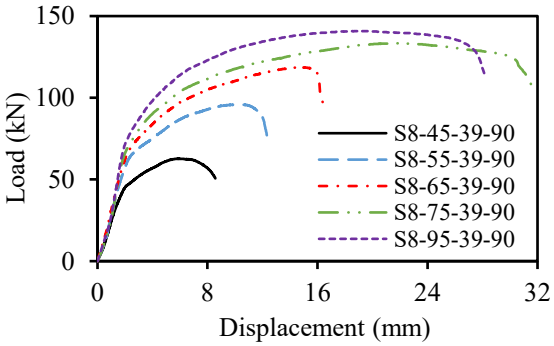
and thicker (i.e. 8 mm) lap shear specimens respectively. Similarly, the influence of the end distance e_1 on the response of the lap shear specimens is illustrated in Figure 3.21 (b) and (d). It can be observed that the ultimate capacity of the specimens increased with increasing end distance, until the load-displacement curves began to exhibit two peaks, reflecting the development of significant curling, eventually leading to failure by localised tearing. It is therefore shown that when localised tearing governs, the influence of further increasing the end distance on the ultimate capacity of lap shear specimens is minimal.



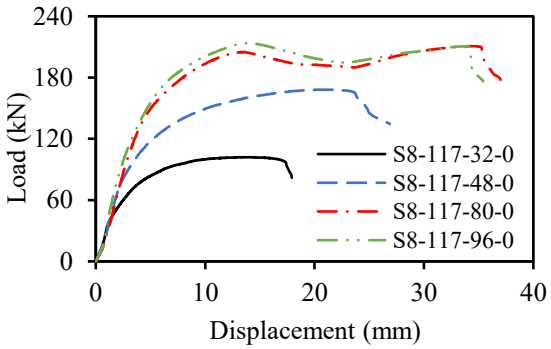
(a) Influence of b on thin plates



(b) Influence of e_1 on thin plates



(c) Influence of b on thick plates



(d) Influence of e_1 on thick plates

Figure 3.21: Influence of width b and end distance e_1 on load-displacement curves of typical test specimens in comparison groups

The influence of the print layer orientation on the response of the lap shear specimens was not found to be significant. In Figure 3.20, where the load-displacement curves plotted in each graph have the same geometry but different print layer orientations, all pairs of curves can be seen to follow similar trends with no significant differences. Comparisons of the ultimate capacities of the specimens with the same nominal geometry but of different print layer orientations (i.e. $P_{u,0}$ and $P_{u,90}$) are presented in Table 3.8. Since the actual plate thickness and ultimate tensile strength varied from their nominal values, the table also provides comparisons

of the ultimate loads normalised by the product of the measured average thickness t and the ultimate tensile strength f_u, confirming the insensitivity of the connection performance to print layer orientation – see Table 3.8.

Table 3.8: Influence of print layer orientation on ultimate capacity of lap shear connections

Specimen pair	$P_{u,90°}/P_{u,0°}$	$\frac{P_{u,90°}}{tf_{u,90°}} \Big/ \frac{P_{u,0°}}{tf_{u,0°}}$
S3-55-27	0.92	0.99
S3-45-27	0.96	1.03
S3-45-36	0.97	1.07
S3-35-27	1.00	1.05
S3-65-18	1.04	1.06
S3-65-21.6	0.98	1.05
S3-65-27	1.03	1.12
S3-65-32.4	1.01	1.04
S3-65-36	0.99	1.04
S3-85-33	0.88	0.94
S3-85-44	0.98	1.04
S3-105-33	1.00	1.02
S3-105-39.6	1.11	1.10
S3-105-44	1.00	1.02
S3-145-44.2	0.94	0.99
S3-145-78	1.00	1.07
S3-145-104	1.03	1.08
S8-45-39	1.04	1.04
S8-55-39	0.95	0.96
S8-65-39	0.96	1.00
S8-75-39	0.91	0.93
S8-95-26	0.95	0.95
S8-95-33.8	0.99	1.01
S8-95-39	1.04	1.03
S8-95-65	1.12	1.09
S8-95-78	0.93	0.93

S8-117-32	1.01	1.02
S8-117-48	0.96	0.98
S8-117-80	1.06	1.07
S8-117-96	0.97	1.00
Mean	0.99	1.02
COV	0.054	0.048

3.6. Existing design equations

The establishment of accurate and reliable design rules is important for the wider use of WAAM in construction. In this section, the resistances of the examined specimens, as determined by physical testing, are compared against the strength predictions given by the design equations set out in current steel design standards, namely AISI S100 (2016), AISC 360 (2016), Eurocode 3 (1-1, 2020; 1-8, 2021) and AS/NZS 4600 (2018), to assess their suitability for application to WAAM lap shear connections. Note that the strength predictions used for the comparisons presented herein were derived using the measured geometric and material properties, while all safety factors were set equal to unity and are hence omitted from the presented formulae.

3.6.1. AISI S100

According to AISI S100-16 (2016), when deformation around the bolt holes is not a design consideration, the bearing capacity $P_{B,AISI}$ of a bolted connection is given by Equation (3.1):

$$P_{B,AISI} = Cm_f dtf_u \tag{3.1}$$

where d is the diameter of the bolt, t is the average thickness of the test plate, f_u is the ultimate tensile strength, C is a bearing factor (equal to 3.0 for the specimens examined herein since $d/t < 10$) and m_f is a modification factor that depends on the type of connection (equal to 0.75 for lap shear connections without washers under single shear).

The nominal resistance of a lap shear connection failing by shear-out $P_{SO,AISI}$ is given by Equation (3.2),

$$P_{\mathrm{SO,AISI}} = 1.2 L_{\mathrm{nv}} t f_{\mathrm{u}} \tag{3.2}$$

while Equation (3.3), introduced in (Teh & Gilbert, 2012b), is adopted for the prediction of the resistance $P_{\mathrm{NS,AISI}}$ of a connection exhibiting net section tension failure.

$$P_{\mathrm{NS,AISI}} = A_{\mathrm{n}} f_{\mathrm{u}} \left(0.9 + \frac{0.1d}{b}\right) \tag{3.3}$$

The variable L_{nv} in Equation (3.2) is the length of the net shear plane, as defined in Figure 3.22. In Equation (3.3), A_{n} is the net cross-section area of the connected plate and b is the width of the plate.

3.6.2. AISC 360

According to AISC 360-16 (2016), when bolt hole deformation is not a concern, the bearing capacity $P_{\mathrm{B,AISC}}$ is given by:

$$P_{\mathrm{B,AISC}} = 3.0 d t f_{\mathrm{u}} \tag{3.4}$$

The shear-out capacity $P_{\mathrm{SO,AISC}}$ is given by:

$$P_{\mathrm{SO,AISC}} = 1.5 L_{\mathrm{nv}} t f_{\mathrm{u}} \tag{3.5}$$

and the net section tension capacity $P_{\mathrm{NS,AISC}}$ of a bolted connection is given by:

$$P_{\mathrm{NS,AISC}} = A_{\mathrm{n}} f_{\mathrm{u}} \tag{3.6}$$

3.6.3. Eurocode 3

According to the new draft EN 1993-1-8 (2021), the ultimate capacity of a lap shear connection, as governed by bearing and shear-out failure, is given by Equation(3.7):

$$P_{\mathrm{B,EC3}} = k_{\mathrm{m}} \alpha_{\mathrm{b}} f_{\mathrm{u}} d t \tag{3.7}$$

in which

$$\alpha_{\mathrm{b}} = \min\left(\frac{e_1}{d_0}; 3\frac{f_{\mathrm{ub}}}{f_{\mathrm{u}}}; 3\right) \tag{3.8}$$

where k_m is a modification factor depending on the steel grade of the connected plate (which is equal to unity for steel grades lower than S460), e_1 is the end distance, as defined in Figure 3.3, d_0 is the bolt hole diameter and f_{ub} is the ultimate tensile strength of the bolts.

In the new draft EN 1993-1-1 (2020), the net section tension resistance $P_{NS,EC3}$ of a lap shear connection is defined as:

$$P_{NS,EC3} = kA_n f_u \tag{3.9}$$

where k is equal to unity for plates with smooth bolt holes (i.e. fabricated by water jet cutting).

3.6.4. AS/NZS 4600

In AS/NZS 4600 (2018), the resistances of lap shear connections to bearing and net section tension failure are predicted using the same equations as in AISI S100 (2016) (i.e. Equations (3.1) and (3.3), respectively). The shear-out capacity $P_{SO,AS/NZS}$ is predicted using Equation (3.10) where, unlike the other specifications, the gross shear plane is employed:

$$P_{SO,AS/NZS} = L_{gv} t f_u \tag{3.10}$$

where L_{gv} is the length of the gross shear plane, as defined in Figure 2.10.

3.6.5. Design equations proposed in the literature

Further design expressions for predicting shear-out failure in lap shear connections have been proposed in the literature (Teh & Uz, 2015; Xing et al., 2020b) and shown to yield accurate capacity predictions. Equation (3.11) was proposed in (Teh & Uz, 2015) for the prediction of the ultimate shear-out resistance $P_{SO,Teh}$:

$$P_{SO,Teh} = 1.2 L_{av} t f_u \tag{3.11}$$

where L_{av} is the length of the active shear plane, assumed to lie between the gross and net shear planes, as illustrated in Figure 2.10 and given by:

$$L_{av} = e_1 - \frac{d_0}{4} \tag{3.12}$$

For cold-reduced sheet steel bolted connections, Equation (3.11) was modified (Xing et al., 2020b) to give Equation (3.13), which accounts for the catenary action that develops in specimens with short end distances:

$$P_{\mathrm{SO,Teh}} = 1.2(\frac{3d}{e_1})^{\mathrm{p}} L_{\mathrm{av}} t f_{\mathrm{u}} \tag{3.13}$$

in which the coefficient p is the catenary power, taken as 1/10 herein for the single-lap connections.

Equation (3.14) was proposed in (Teh & Uz, 2017) for determining the strength P_{TB} of single-lap shear bolted connections failing in tilt-bearing (i.e. the bolt head punching through the connected plate):

$$P_{\mathrm{TB}} = 2.65 d^{1/2} t^{4/3} (b - d_0)^{1/6} f_{\mathrm{u}} \tag{3.14}$$

Although tilt-bearing failure did not occur in the specimens examined herein, Equation (3.14) can be used for predicting localised tearing and curl-bearing failure.

3.7. Comparisons between test results and existing design equations

Comparisons between the test results and the capacity predictions given by the aforementioned design equations are presented in Table 3.9. The measured geometric and material properties shown in Tables 3.4 to 3.6 have been used in predicting the capacities. Note that the value of the tensile strength f_{u} used in the design equations was that determined from the material tests on the as-built coupons in the 0° and 90° directions depending on the print layer orientation of each specimen for both nominal material thicknesses (i.e. 3 mm and 8 mm), as reported in Table 3.6.

Table 3.9: Summary of comparisons between the test results and design equations

Specimen	AISI S100 Eqs. (3.1-3.3)		AISC 360 Eqs. (3.4-3.6)		AS/NZS 4600 Eqs. (3.1,3.3,3.10)		Eurocode 3 Eqs. (3.7,3.9)		Eq. (3.13)	Eq. (3.14)
	$\frac{P_u}{P_{AISI}}$	FM	$\frac{P_u}{P_{AISC}}$	FM	$\frac{P_u}{P_{AS/NZS}}$	FM	$\frac{P_u}{P_{EC3}}$	FM	$\frac{P_u}{P_{SO,Teh}}$	$\frac{P_u}{P_{TB}}$
S3-35-27-90	1.07	NS[1]	1.01	NS	1.07	NS	1.01	NS	N/A	N/A
S3-35-27-0	1.02	NS	0.96	NS	1.02	NS	0.96	NS	N/A	N/A
S3-45-27-90	1.17	(SO)[2]	0.94	NS	1.00	NS	1.06	(SO)	N/A	0.98
S3-45-27-0	1.14	(SO)	0.91	(SO)	0.97	NS	1.02	(SO)	N/A	0.95
S3-45-36-90	1.03	NS	0.96	NS	1.03	NS	0.96	NS	N/A	1.01
S3-45-36-0	0.96	NS	0.90	NS	0.96	NS	0.90	NS	N/A	0.94
S3-55-27-90	1.38	(SO)	1.10	(SO)	1.09	(SO)	1.24	(SO)	N/A	1.10
S3-55-27-0	1.38	(SO)	1.10	(SO)	1.10	(SO)	1.24	(SO)	N/A	1.11
S3-65-18-90	1.67	SO	1.34	SO	1.03	SO	1.15	SO	1.03	N/A
S3-65-18-0	1.59	SO	1.27	SO	0.97	SO	1.08	SO	0.98	N/A
S3-65-21.6-90	1.48	SO	1.19	SO	1.05	SO	1.17	SO	1.02	N/A
S3-65-21.6-0	1.43	SO	1.15	SO	1.01	SO	1.13	SO	0.98	N/A
S3-65-27-90	1.49	(SO)	1.19	(SO)	1.20	(SO)	1.33	(SO)	N/A	1.13
S3-65-27-0	1.33	SO	1.07	SO	1.07	SO	1.19	SO	1.01	N/A
S3-65-32.4-90	1.15	(SO)	0.92	(SO)	1.00	(SO)	1.11	(SO)	N/A	1.13
S3-65-32.4-0	1.10	(SO)	0.88	(SO)	0.96	(SO)	1.07	(SO)	N/A	1.09
S3-65-36-90	0.96	(SO)	0.77	(SO)	0.88	(B)	0.97	(SO)	N/A	1.10
S3-65-36-0	0.92	(SO)	0.74	(SO)	0.84	(B)	0.93	(SO)	N/A	1.06
S3-85-33-90	1.24	(SO)	0.99	(SO)	1.00	(SO)	1.09	(SO)	N/A	1.00
S3-85-33-0	1.32	(SO)	1.05	(SO)	1.06	(SO)	1.16	(SO)	N/A	1.07
S3-85-44-90	0.96	(SO)	0.77	(SO)	0.87	(SO)	0.95	(SO)	N/A	1.16
S3-85-44-0	0.92	(SO)	0.73	(SO)	0.83	(SO)	0.90	(SO)	N/A	1.11
S3-105-33-90	1.41	(SO)	1.13	(SO)	1.12	(SO)	1.25	(SO)	N/A	1.07
S3-105-33-0	1.39	SO	1.11	SO	1.11	SO	1.22	SO	1.04	N/A
S3-105-39.6-90	1.20	(SO)	0.96	(SO)	1.03	(SO)	1.14	(SO)	N/A	1.15
S3-105-39.6-0	1.10	(SO)	0.88	(SO)	0.94	(SO)	1.06	(SO)	N/A	1.08
S3-105-44-90	0.99	(SO)	0.79	(SO)	0.89	(SO)	0.98	(SO)	N/A	1.11
S3-105-44-0	0.96	(SO)	0.77	(SO)	0.86	(SO)	0.95	(SO)	N/A	1.10
S3-145-44.2-90	1.10	(SO)	0.88	(SO)	0.90	(SO)	0.97	(SO)	N/A	0.91
S3-145-44.2-0	1.01	(SO)	0.81	(SO)	0.85	(SO)	0.92	(SO)	N/A	0.93

S3-145-78-90	0.83	(B)	0.62	(B)	0.83	(B)	0.63	(SO)	N/A	1.12
S3-145-78-0	0.77	(B)	0.58	(B)	0.77	(B)	0.59	(SO)	N/A	1.04
S3-145-104-90	0.83	(B)	0.62	(B)	0.83	(B)	0.62	(B)	N/A	1.12
S3-145-104-0	0.77	(B)	0.58	(B)	0.77	(B)	0.58	(B)	N/A	1.05
S8-45-39-90	1.18	NS	1.12	NS	1.18	NS	1.12	NS	N/A	N/A
S8-45-39-0	1.13	NS	1.07	NS	1.13	NS	1.07	NS	N/A	N/A
S8-55-39-90	1.15	NS	1.08	NS	1.15	NS	1.08	NS	N/A	N/A
S8-55-39-0	1.20	NS	1.13	NS	1.20	NS	1.13	NS	N/A	N/A
S8-65-39-90	1.27	(SO)	1.03	NS	1.10	NS	1.11	(SO)	N/A	N/A
S8-65-39-0	1.28	(SO)	1.03	NS	1.10	NS	1.11	(SO)	N/A	N/A
S8-75-39-90	1.39	(SO)	1.12	(SO)	1.11	(SO)	1.21	(SO)	1.05	N/A
S8-75-39-0	1.49	SO	1.19	SO	1.19	SO	1.29	SO	1.12	N/A
S8-95-26-90	1.70	SO	1.36	SO	1.03	SO	1.11	SO	1.03	N/A
S8-95-26-0	1.79	SO	1.43	SO	1.08	SO	1.17	SO	1.08	N/A
S8-95-33.8-90	1.51	SO	1.21	SO	1.12	SO	1.21	SO	1.07	N/A
S8-95-33.8-0	1.51	SO	1.21	SO	1.12	SO	1.21	SO	1.07	N/A
S8-95-39-90	1.42	SO	1.13	SO	1.14	SO	1.23	SO	1.07	N/A
S8-95-39-0	1.38	SO	1.10	SO	1.11	SO	1.19	SO	1.04	N/A
S8-95-65-90	1.14	(B)	0.89	(NS)	1.14	(B)	1.02	(SO)	N/A	1.18
S8-95-65-0	1.05	(B)	0.82	(NS)	1.05	(B)	0.94	(SO)	N/A	1.11
S8-95-78-90	1.07	(B)	0.83	(NS)	1.07	(B)	0.83	(NS)	N/A	1.11
S8-95-78-0	1.14	(B)	0.89	(NS)	1.14	(B)	0.89	(NS)	N/A	1.20
S8-117-32-90	1.73	SO	1.38	SO	1.04	SO	1.11	SO	1.04	N/A
S8-117-32-0	1.70	SO	1.36	SO	1.02	SO	1.09	SO	1.03	N/A
S8-117-48-90	1.35	(SO)	1.08	(SO)	1.09	(SO)	1.16	(SO)	1.02	N/A
S8-117-48-0	1.39	(SO)	1.12	(SO)	1.12	(SO)	1.18	(SO)	1.05	N/A
S8-117-80-90	1.06	(B)	0.84	(NS)	1.06	(B)	0.95	(SO)	N/A	1.20
S8-117-80-0	1.00	(B)	0.79	(NS)	1.00	(B)	0.89	(SO)	N/A	1.13
S8-117-96-90	1.00	(B)	0.79	(NS)	1.00	(B)	0.79	(NS)	N/A	1.13
S8-117-96-0	1.00	(B)	0.79	(NS)	1.00	(B)	0.79	(NS)	N/A	1.12
Mean	1.22		0.99		1.02		1.04		1.04	1.10
COV	0.21		0.22		0.11		0.17		0.03	0.06

[1] SO: Shear-out, NS: net section tension, B: bearing.

[2] In brackets if different from test results.

Among the current steel design standards, overall the most accurate capacity predictions were yielded by AS/NZS 4600 (2018), with an average test-to-predicted capacity ratio of 1.02 in conjunction with a coefficient of variation (COV) of 0.11 – see Table 3.9. Although the equations of AISC 360 (2016) led to an average capacity ratio of 0.99, the resulting COV is double that of the AS/NZS 4600 (2018) equations. Overall, the AISI S100 (2016) equations are the most conservative as they underestimated the capacity of the WAAM connections by 22% on average, with a COV of 0.21. Eurocode 3 (1-1, 2020; 1-8, 2021) is the next most conservative, with an average test-to-predicted capacity ratio of 1.04 and a COV of 0.17.

Comparisons between design equations and test results that focus solely on the average test-to-predicted capacity ratios and the COV values can be misleading; further comparisons, based on failure modes, are therefore presented in the following sub-sections.

3.7.1. Net section tension failure

For the WAAM bolted connection test specimens undergoing net section tension (NS) failure, the four standards generally provide reasonable, if somewhat conservative (especially for the thicker specimens), capacity predictions. As shown in Figure 3.22, where the net section tension stress $f_{NS} = P_u/A_n$, the relevant equations of AISC (2016) and Eurocode 3 (2020), i.e. Equations (3.6) and (3.9), resulted in underestimations of net section tension capacity of up to 12% (1/1.13 = 0.88), while Equation (3.3), specified in AISI (2016) or AS/NZS (2018), led to underestimations of up to 17% (1/1.20 = 0.83). The test-to-predicted capacity ratios of 1.27 and 1.28 shown in Table 3.9 for Specimens S8-65-39-90 and S8-65-39-0, respectively, were calculated using Equation (3.2), since, according to AISI shear-out (SO) was the critical failure mode. This result suggests that Equation (3.2) is excessively conservative for connections failing in shear-out, as discussed in the following subsection.

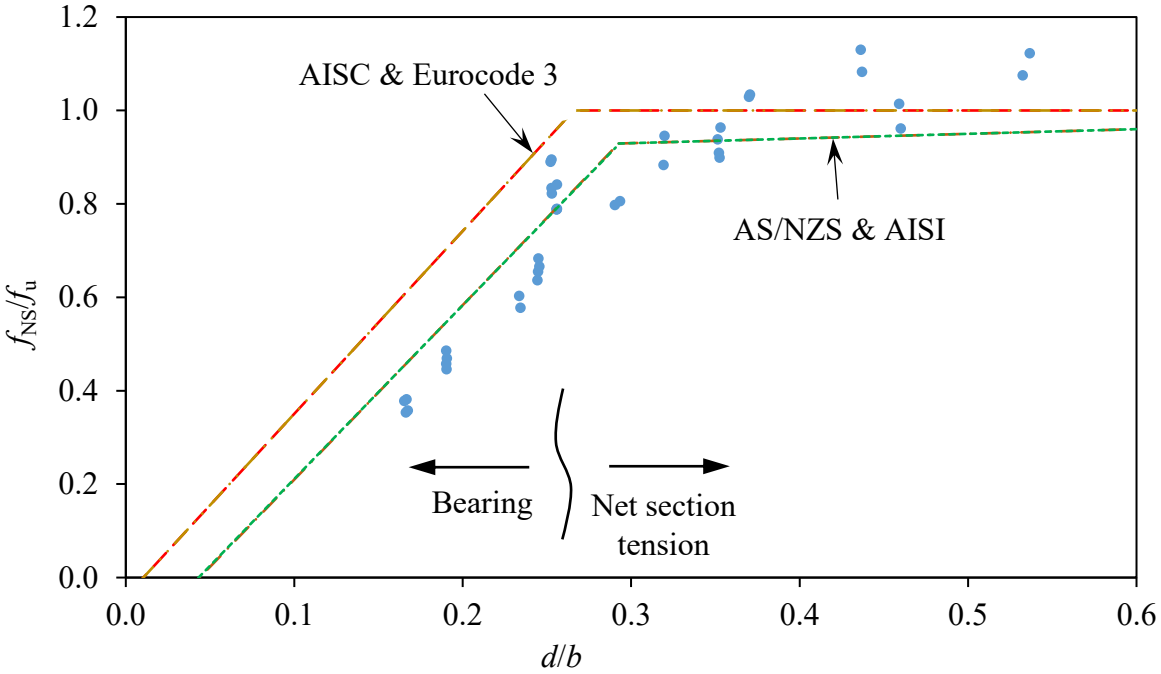


Figure 3.22: Comparison of experimental results and design equations for bearing and net section tension, where net section tension and bearing failure, as described by the considered design codes, are indicated

3.7.2. Shear-out (and end-splitting) failure

Equations (3.2), (3.5) and (3.7), specified in AISI (2016), AISC (2016) and Eurocode 3 (2021), respectively, generally provide overly conservative predictions of shear-out resistance, as evident from the results shown in Table 3.9 and Figure 3.23 where the bearing stress $f_B = P_u/(dt)$. The greatest underestimations by AISI (2016), AISC (2016) and Eurocode (2021) are 44% (1/1.79 = 0.56), 30% (1/1.43 = 0.70) and 25% (1/1.33 = 0.75), respectively. Equation (3.10), specified in AS/NZS (2018), is also conservative, but not to the same extent as the other specifications. The largest underestimation of 17% (1/1.20 = 0.83) is for Specimen S3-65-27-90, which failed in localised tearing.

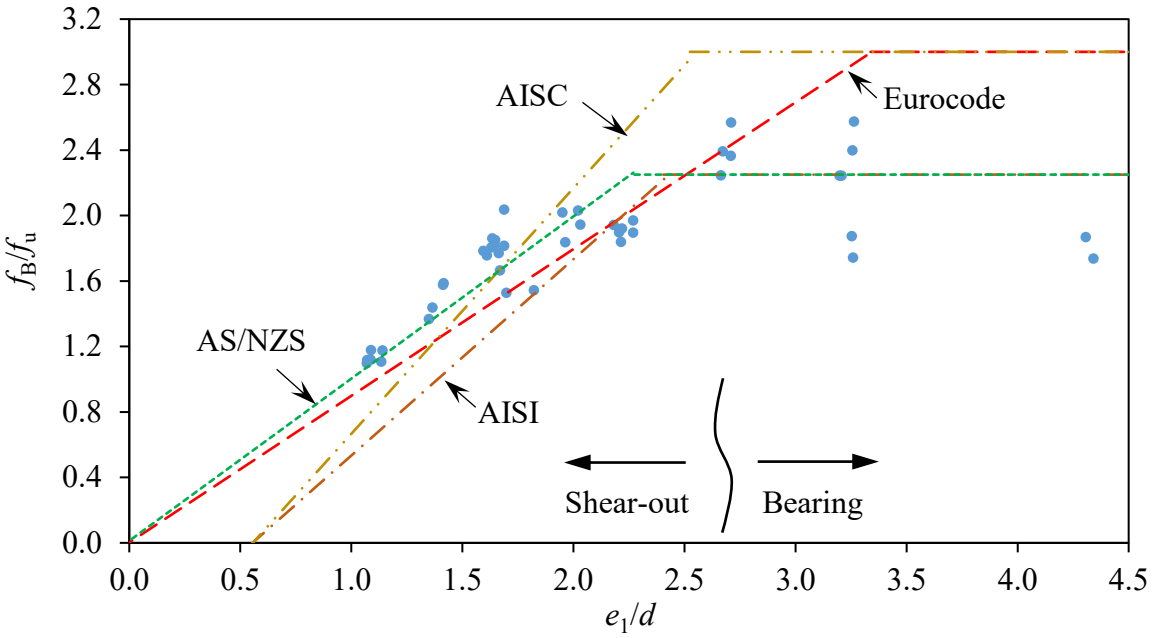


Figure 3.23: Comparison of experimental results and design equations for shear-out and bearing, where shear-out and bearing failure, as described by the considered design codes, are indicated

It should be noted that, while an overestimation of capacity by a set of equations from a given design standard may simply indicate that the governing failure mode is not considered in that standard, any significant underestimation necessarily means that the available equation is too conservative. For example, Eurocode 3 (2021) predicted that Specimen S3-65-27-90 would fail in shear-out (SO), but the specimen actually failed in localised tearing at an ultimate load that was 33% higher than the predicted shear-out capacity. This result means that the actual shear-out capacity must be more than 33% greater than the predicted capacity since the specimen was stronger in shear-out than in localised tearing.

The accuracy of the shear-out capacity predictions of the standards could be improved through the incorporation of Equation (3.13). It can be seen that this equation generally predicted the test shear-out (SO) capacities to within 5%. Using Equation (3.13) for the shear-out capacity prediction of Specimen S3-105-33-0 results in a test-to-predicted capacity ratio of 1.04, instead of 1.39 (AISI S100, 2016), 1.11 (AISC 360, 2016; AS/NZS 4600, 2018) or 1.22 (EN 1993-1-8, 2021) from the considered standards. Similar observations can be made for other specimens failing in shear-out such as Specimens S3-65-18-90 and S8-95-39-90. For practical purposes,

it is also proposed that Equation (3.13) may be used for estimating both shear-out and the end-splitting (ES) capacities, owing to their similarity – see Table 3.9.

3.7.3. Localised tearing and curl-bearing failures

As shown in Table 3.9 and Figures 3.22 and 3.23, AISC (2016), AS/NZS (2018) and Eurocode (1-1, 2020; 1-8, 2021) can either underestimate or overestimate the localised tearing (LT) capacities of the test specimens significantly. The underestimations are generally due to the conservatism of the shear-out design provisions (especially for AISI (2016)), while the overestimations are due to the fact that the localised tearing mode is not properly considered by the standards.

The curl-bearing failure mode is not accounted for in current design standards; hence, all the standards overestimate the curl-bearing (CB) capacities significantly, by at least 20% (1/0.83 = 1.20) and up to 72% (1/0.58 = 1.72). These results demonstrate the need to assess the suitability of a design equation or a set of design equations not only based on the average test-to-predicted capacity ratios, but also considering the performance of particular specimens and failure modes.

The last column of Table 3.9 contains the results of using Equation (3.14) to predict the capacities of the specimens failing in localised tearing or curl-bearing. Although the equation was originally derived for the tilt-bearing failure mode (Teh & Uz, 2017), it has transpired that it can be used to conservatively estimate the localised tearing or curl-bearing failure load of the tested WAAM specimens, mostly within 10% accuracy. The unexpected level of accuracy is due to the fact that both the localised tearing and curl-bearing failure modes involve through-thickness fracture of the connected plate under the bolt head, as in the case of the tilt-bearing failure mode.

If Equation (3.14) were to be incorporated into the sets of equations specified in the considered design standards, then each of the design standards would yield a test-to-predicted capacity ratio of 1.05 for the curl-bearing Specimen S3-145-104-0, instead of 0.77 (AISI S100, 2016; AS/NZS 4600, 2018) or 0.58 (AISC 360, 2016; EN 1993-1-8, 2021). For the localised tearing Specimen S3-65-36-0, the incorporation of Equation (3.14) would lead to a test-to-predicted capacity ratio of 1.06 instead of 0.92 (AISI S100, 2016), 0.74 (AISC 360, 2016), 0.84 (AS/NZS 4600, 2018) or 0.93 (EN 1993-1-8, 2021).

3.8. Conclusions

A total of 60 WAAM steel single-lap shear bolted connections of two different nominal thicknesses, two different print layer orientations and varying dimensions were tested. The measured material properties, geometries, load-deformation characteristics and failure modes, including shear-out, localised tearing, curl-bearing and net section tension fracture, of the test specimens are reported and analysed. The test ultimate loads were compared against the predictions of four major design standards for either structural/hot-rolled (AISC 360 and EN 1993-1-8) or cold-formed (AISI S100 and AS/NZS 4600) steel.

The experimental program revealed that the print layer orientation had little influence on the deformation and load-carrying capacities of the WAAM connections. Although the failure mode sometimes depended on the print layer orientation, the ultimate test loads were essentially unaffected. This finding means that the same structural design equations can be used for different print layer orientations.

The ductility of the WAAM steel enabled the bolt hole of each specimen to elongate to a sufficient extent so that the bolt head avoided punching through the connected plate upstream, i.e. no tilt-bearing failures occurred. Specimens with sufficiently large end distances (to avoid shear-out) and widths (to avoid net section tension fracture) failed predominantly in localised tearing. However, specimens with larger end distances experienced curling which was so severe that the bolt head punched through the connected plate downstream of the bolt hole, as the bolt displaced in the loading direction. To the author's knowledge, this is the first time that this failure mode is identified and is defined as curl-bearing failure.

Current steel design standards were found to not adequately account for the localised tearing and the curl-bearing failure modes; the failure loads of specimens failing in these modes were therefore generally poorly predicted (by up to 72%). However, the localised tearing and curl-bearing failure modes have a similar fracture mechanism to the tilt-bearing failure mode, and the corresponding failure loads are reasonably well predicted by a previously proposed equation (Teh & Uz, 2017) for tilt-bearing failure. If the equation is incorporated, the test-to-predicted capacity ratio of curl-bearing and localised-tearing specimens will be 1.10.

Overall, the WAAM test specimens exhibited the anticipated behavioural trends and, notwithstanding the above shortcomings, their failure loads were generally well predicted by

the existing design standards, with AS/NZS 4600 providing the most accurate capacity predictions.

4. WAAM Double-Lap Shear Bolted Connections

4.1. Introduction

In this chapter, a total of sixty double-lap shear tests on WAAM bolted connections is presented. The production, measurement and testing of the specimens are described, while the test results are analysed and the observed failure modes are discussed. Finally, comparisons are made against the capacity predictions yielded by current design standards.

4.2. Manufacturing and geometric measurements of test specimens

All specimens were extracted by means of waterjet cutting from flat-sided ovals, as described in Section 3.2, and the chemical composition and mechanical properties can be found in Tables 3.1 and 3.2, respectively, as well as the employed printing parameters in Table 3.3. Following their extraction from the parent plates, the specimens were sandblasted with glass beads and laser scanned using a FARO Design ScanArm 2.0 laser scanner, the flow chart of the which is illustrated in Figure 4.1. The obtained point clouds were subsequently processed using Geomagic Wrap (3D Systems, 2017) and inter-connected into 3D CAD models. A typical specimen, along with its scanned point cloud and 3D CAD model, is illustrated in Figure 4.2.

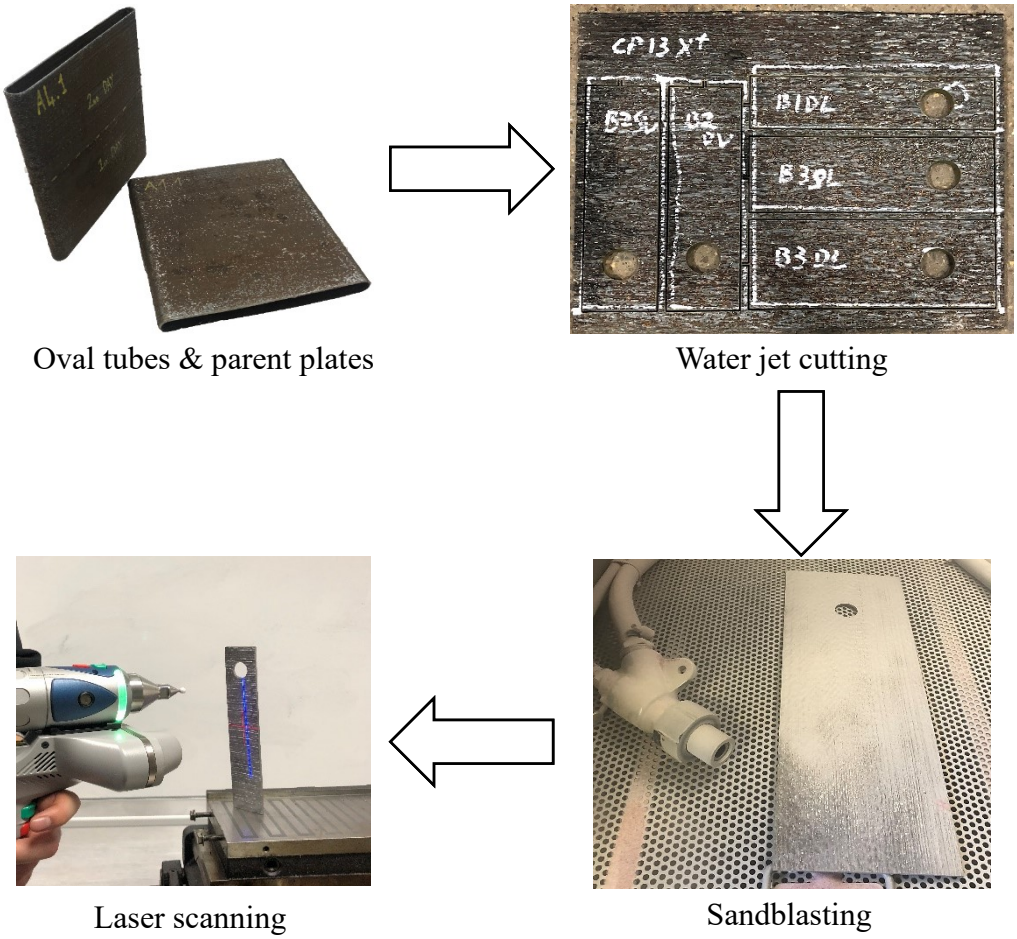
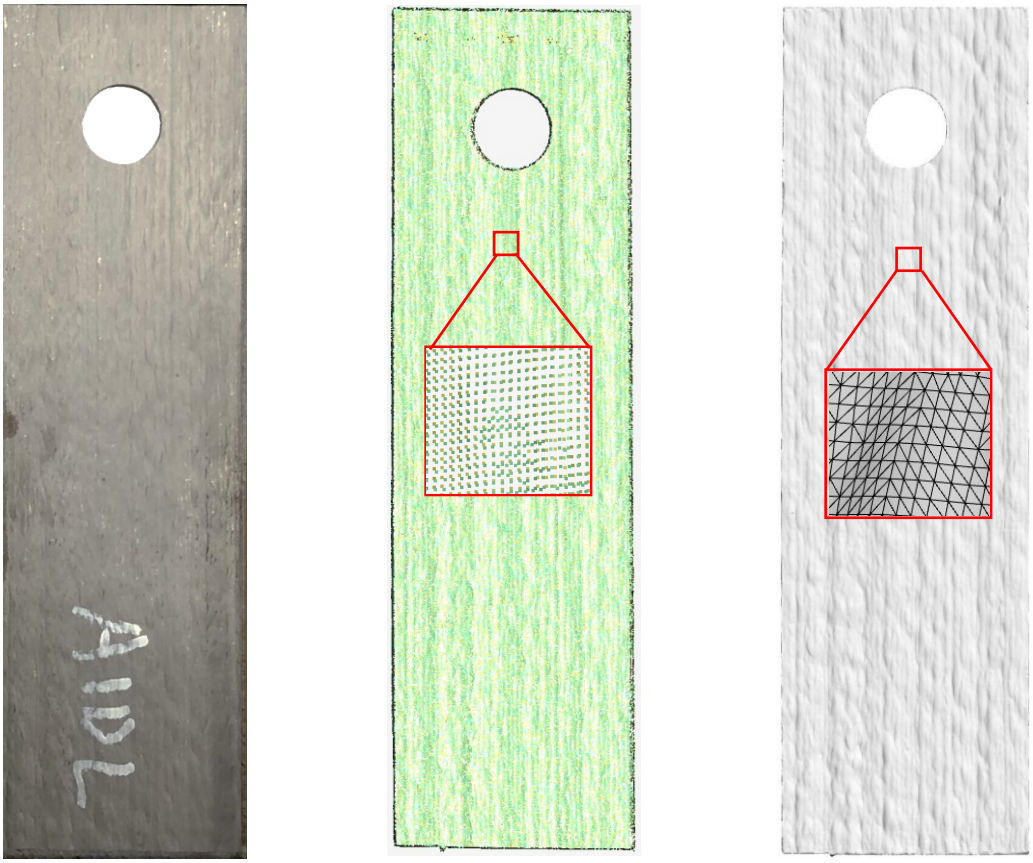


Figure 4.1: Preparation process of typical specimen



(a) Specimen after sandblasting

(b) Point cloud (50% of points displayed)

(c) 3D CAD model (STL file)

Figure 4.2: Real specimen and digital models

The key geometric parameters affecting the structural performance of bolted lap shear connections are the width of the connected plate b, the bolt hole diameter d_0, the distance between the centre of the bolt hole and the end of the plate (termed the end distance) e_1 and the thickness of the plate t – see Figure 3.3 in Chapter 3. The specimens examined herein were suitably proportioned to ensure the occurrence of three different failure modes, namely shear-out, net section tension and bearing.

For each set of dimensions, two specimens were fabricated but with different angles (i.e. 0° and 90°) between the print layer orientation and the loading direction, to investigate the possible influence of material anisotropy and the geometrical undulations inherent to the WAAM process. Sixty specimens were fabricated in total. The labelling system adopted for the test specimens starts with the letter D (for double-shear), followed by the nominal thickness t, nominal width b and nominal end distance e_1 in mm and, finally, by the number 0 or 90 to denote the angle between the print layer orientation and the loading direction (in degrees). For

example, Specimen D3-55-27-90 is a double-shear lap specimen with a 3 mm nominal thickness, a 55 mm nominal width, a 27 mm nominal end distance and a 90° angle between the print layer orientation and the loading direction.

The width b, bolt hole diameter d_0 and end distance e_1 of all specimens were measured using Vernier callipers and averages thicknesses were obtained from the 3D CAD models by using the software Rhino 3D (2017). The obtained geometrical parameters are presented in are reported in Table 4.1. Note that the specimen lengths were about three times their respective widths, varying from 190 mm to 390 mm. The mechanical properties of the WAAM material are as reported in Chapter 3.

Table 4.1: Measured geometric properties of test specimens

Specimen	Bolt type	t (mm)	d_0 (mm)	b (mm)	e_1 (mm)
D3-35-27-0	M16	2.7	18.4	34.7	26.6
D3-45-27-0	M16	2.9	17.8	45.3	27.2
D3-45-36-0	M16	2.9	17.9	45.5	36.2
D3-55-27-0	M16	2.6	18.1	55.2	27.1
D3-65-21.6-0	M16	2.8	17.8	65.4	21.7
D3-65-27-0	M16	2.9	17.9	65.4	27.2
D3-65-32.4-0	M16	2.9	17.8	65.4	32.5
D3-65-36-0	M16	2.8	17.8	65.4	36.0
D3-65-43.2-0	M16	2.8	17.8	65.4	43.5
D3-85-33-0	M20	2.8	21.8	85.4	33.2
D3-85-57.2-0	M20	2.8	21.9	85.5	57.5
D3-105-37.4-0	M20	2.6	22.6	104.8	38.7
D3-105-39.6-0	M20	2.7	22.8	104.5	37.3
D3-105-48.4-0	M20	2.7	22.4	104.4	47.9
D3-145-91-0	M24	2.7	26.1	144.2	90.5
D3-145-104-0	M24	2.7	26.0	142.6	103.3
D3-145-117-0	M24	2.7	26.3	124.0	115.7
D8-45-44.2-0	M24	7.8	26.2	44.9	43.9
D8-55-44.2-0	M24	7.9	26.0	54.9	44.1
D8-75-44.2-0	M24	7.2	26.2	74.9	44.5

D8-80-44.2-0	M24	7.9	25.9	79.9	44.1
D8-90-26-0	M24	7.7	25.8	90.2	25.9
D8-90-39-0	M24	7.7	26.0	90.2	39.0
D8-90-52-0	M24	7.5	25.9	90.2	52.0
D8-90-65-0	M24	7.5	25.9	90.1	65.2
D8-90-91-0	M24	7.6	25.9	90.3	91.3
D8-120-48-0	M30	7.4	31.8	120.1	48.0
D8-120-64-0	M30	7.5	31.8	120.1	64.1
D8-120-80-0	M30	7.5	32.0	120.0	80.0
D8-120-112-0	M30	7.5	32.0	120.0	111.7
D3-35-27-90	M16	2.7	18.0	35.2	27.0
D3-45-27-90	M16	2.9	17.8	45.2	27.3
D3-45-36-90	M16	3.0	17.7	45.4	36.2
D3-55-27-90	M16	2.7	18.2	55.3	27.1
D3-65-21.6-90	M16	2.9	17.8	65.3	21.7
D3-65-27-90	M16	2.9	17.9	65.2	27.2
D3-65-32.4-90	M16	2.9	17.9	65.3	32.6
D3-65-36-90	M16	2.8	17.9	65.6	36.5
D3-65-43.2-90	M16	2.7	17.9	65.3	43.7
D3-85-33-90	M20	2.7	21.9	85.3	33.1
D3-85-57.2-90	M20	2.8	21.9	85.5	57.3
D3-105-37.4-90	M20	2.8	22.1	105.0	37.4
D3-105-39.6-90	M20	2.8	22.2	105.3	39.5
D3-105-48.4-90	M20	2.8	22.2	104.9	48.2
D3-145-91-90	M24	2.7	25.8	143.8	91.0
D3-145-104-90	M24	2.6	26.1	144.3	104.1
D3-145-117-90	M24	2.7	26.4	143.7	118.4
D8-45-44.2-90	M24	7.4	26.0	44.7	43.9
D8-55-44.2-90	M24	7.4	26.2	54.7	43.9
D8-75-44.2-90	M24	7.4	26.0	74.8	44.1
D8-80-44.2-90	M24	7.4	26.2	79.9	44.3
D8-90-26-90	M24	7.7	25.9	90.2	26.0
D8-90-39-90	M24	7.6	25.9	90.3	39.1

D8-90-52-90	M24	7.6	25.9	90.1	52.3
D8-90-65-90	M24	7.7	25.7	90.2	65.0
D8-90-91-90	M24	7.6	25.9	90.2	91.1
D8-120-48-90	M30	7.6	31.8	120.3	48.0
D8-120-64-90	M30	7.6	31.8	120.2	64.0
D8-120-80-90	M30	7.8	31.9	120.1	80.1
D8-120-112-90	M30	7.7	31.9	120.1	112.0

4.3. Double-lap shear lap tests

4.3.1. Test setup

All connection tests were carried out using a 600 kN Instron testing machine. Each WAAM plate was positioned between two grade S700 high-strength steel (HSS) plates, and connected using a fully threaded grade 12.9 bolt in a 2 mm clearance hole. The size of the bolts varied from M16 to M30, depending on the size of the connected plates and the estimated ultimate load, to avoid bolt shear failure. The bolts were finger-tightened to limit the influence of preloading and friction (Lin et al., 2021; Jiang, Zhao & Tan, 2020; Salih, Gardner & Nethercot, 2011). A digital image correlation (DIC) system comprising two pairs of cameras was employed, with each camera pair monitoring one side of the specimen during testing. Prior to the tests, the WAAM specimens, HSS plates and bolts were painted black and then sprayed with a white random speckle pattern, to create contrasting features that would be readily captured by the DIC system, enabling the effective tracking of displacements and strains. For the tests presented herein, the reported displacements of the test specimens extracted from the DIC system (see Section 4.3) were measured over a gauge length of about 150 mm. An overview of the test setup is presented in Figure 4.3.

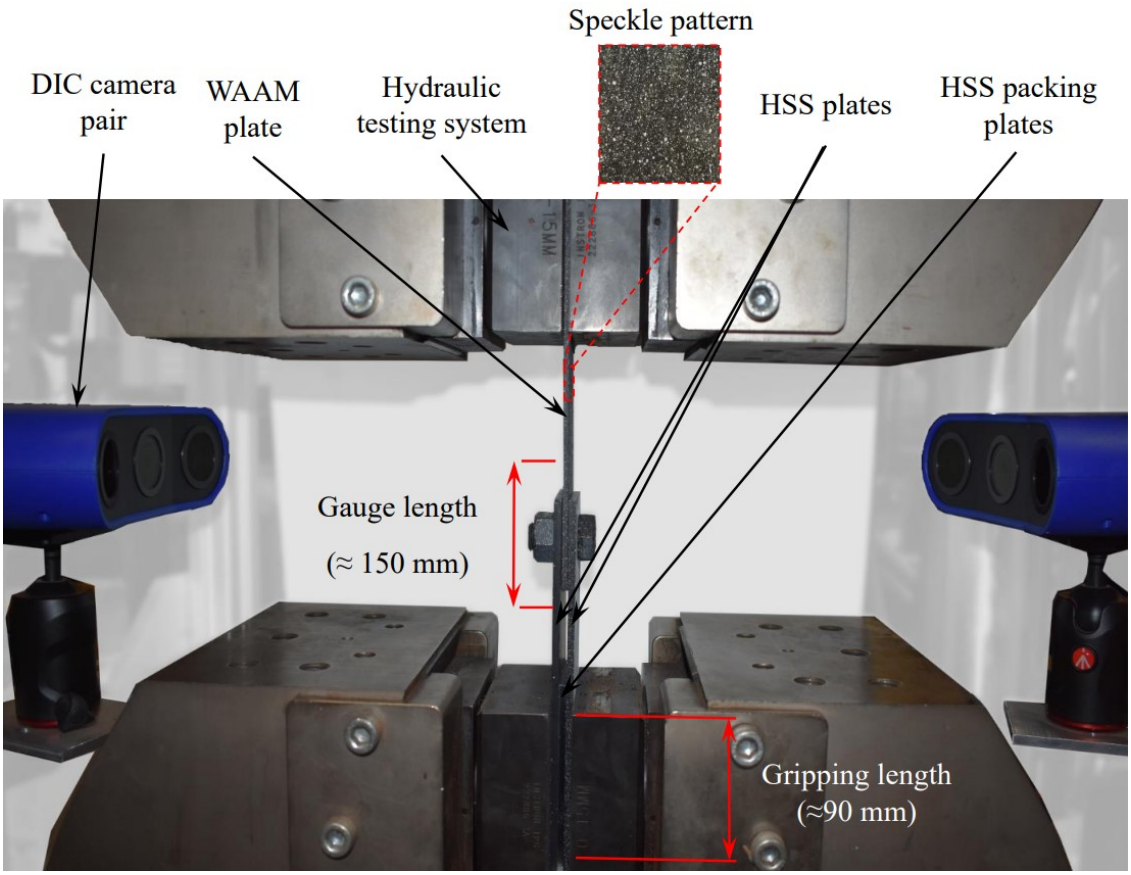


Figure 4.3: Experimental setup for double-lap shear tests

4.3.2. Failure modes

The failure modes observed for all tested specimens are presented in Table 4.2, where SO stands for shear-out, NS for net section tension, B for bearing, IB for incidental block shear and ES for end-splitting. Each failure mode is analysed and discussed in this section.

Table 4.2: Summary of experimental results

Specimen	Test	
	P_u (kN)	FM
D3-35-27-90	23.07	NS[1]
D3-35-27-0	20.83	NS
D3-45-27-90	39.13	NS
D3-45-27-0	39.24	NS
D3-45-36-90	39.03	NS
D3-45-36-0	39.27	NS

D3-55-27-90	34.34	ES
D3-55-27-0	34.27	ES
D3-65-21.6-90	31.04	SO
D3-65-21.6-0	30.24	ES
D3-65-27-90	38.50	ES
D3-65-27-0	38.28	ES
D3-65-32.4-90	46.13	ES
D3-65-32.4-0	46.31	ES
D3-65-36-90	48.42	SO
D3-65-36-0	47.37	ES
D3-65-43.2-90	57.06	IB
D3-65-43.2-0	60.96	IB
D3-85-33-90	44.69	SO
D3-85-33-0	46.86	ES
D3-85-57.2-90	75.67	NS
D3-85-57.2-0	74.42	ES
D3-105-37.4-90	51.87	SO
D3-105-37.4-0	52.31	ES
D3-105-39.6-90	53.89	ES
D3-105-39.6-0	51.96	ES
D3-105-48.4-90	66.90	ES
D3-105-48.4-0	65.66	ES
D3-145-91-90	102.43	B
D3-145-91-0	83.56	B
D3-145-104-90	85.83	B
D3-145-104-0	92.86	B
D3-145-117-90	84.61	B
D3-145-117-0	92.77	B
D8-45-44.2-90	61.85	NS
D8-45-44.2-0	66.32	NS
D8-55-44.2-90	91.79	NS
D8-55-44.2-0	105.33	NS
D8-75-44.2-90	144.85	NS

D8-75-44.2-0	147.67	NS
D8-80-44.2-90	152.07	SO
D8-80-44.2-0	169.12	SO
D8-90-26-90	85.52	SO
D8-90-26-0	87.55	SO
D8-90-39-90	134.02	ES
D8-90-39-0	138.22	ES
D8-90-52-90	182.50	NS
D8-90-52-0	182.68	ES
D8-90-65-90	208.76	NS
D8-90-65-0	208.77	NS
D8-90-91-90	206.40	NS
D8-90-91-0	214.92	NS
D8-120-48-90	162.28	SO
D8-120-48-0	155.10	SO
D8-120-64-90	216.10	SO
D8-120-64-0	207.64	SO
D8-120-80-90	276.15	NS
D8-120-80-0	276.66	SO
D8-120-112-90	267.86	NS
D8-120-112-0	280.28	NS

[1] SO: Shear-out, NS: net section tension, B: bearing, ES: end-splitting, IB: incidental block shear.

4.3.2.1. Shear-out, net section tension and bearing failures

The specimens that failed in shear-out were sized such that their end distance e_1 was short and their width b was relatively large, resulting in the material at the end of the WAAM plate being pulled out – see Figure 4.4(a). For specimens with narrower plate widths, significant necking was observed along the net section, eventually leading to net section tension fracture – see Figure 4.4(b). For specimens with end distances and widths sufficiently large to avoid both shear-out and net section tension failures, the bolt bore into the WAAM plate, piling up the material downstream of the bolt hole and causing bearing failure. It is worth noting that for a failure mode to be classified as bearing, a significant amount of material piling up downstream

of the bolt hole is a prerequisite, with no deformation at the end (parallel to the loading) prior to bearing fracture – see Figure 4.4(c).

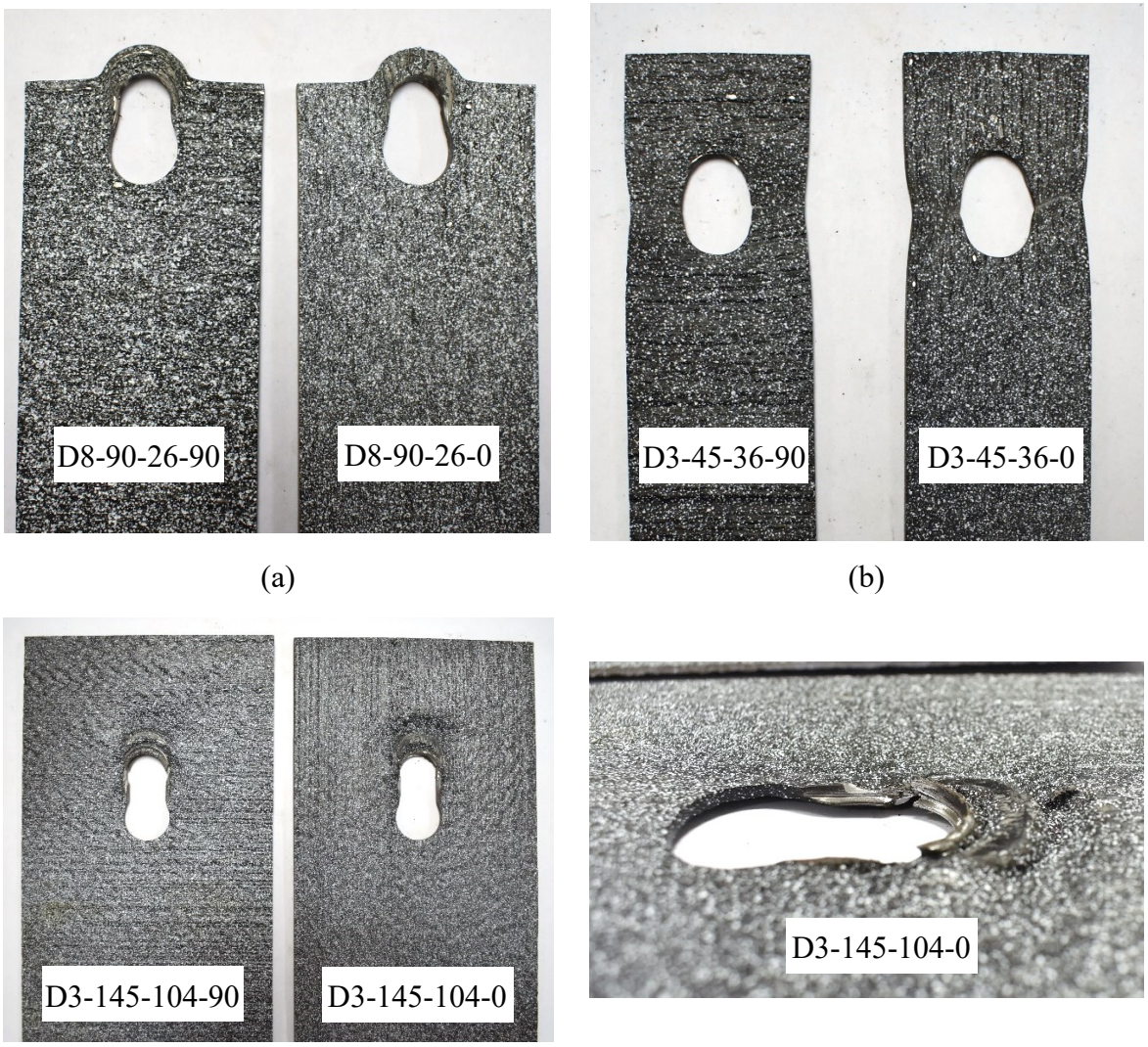


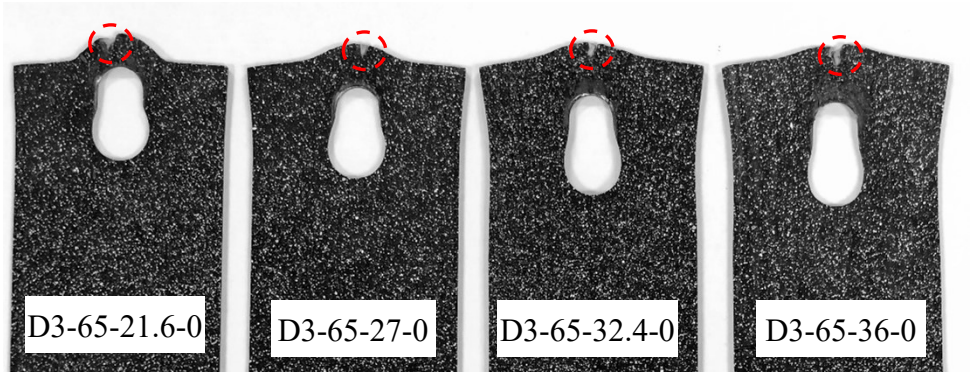
Figure 4.4: Typical failure modes: (a) shear-out, (b) net section tension and (c) bearing failure

4.3.2.2. End-splitting failure

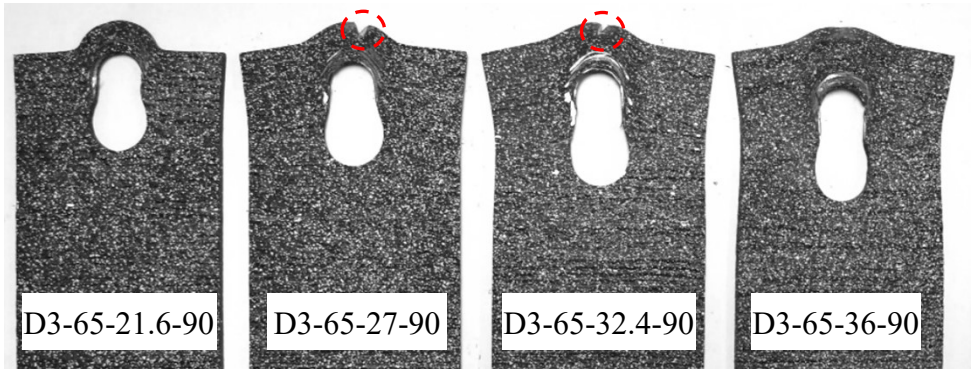
End-splitting is a failure mode characterised by fracture initiated at the free end of the plate, propagating in the loading direction, and is attributed to the development of high transverse tensile stresses (i.e. along the y axis as per Figure 3.3). The earliest description of end-splitting failure was found by the author in a test report on stainless steel bolted connections in 1976 (Owens & Dowling, 1976), where the failure mechanism was described as a "splay", caused by the rotation of the net section, leading to the end of the plate spreading outwards. Since then, end-splitting failure has been observed by several researchers (Može, 2018; Guo et al., 2020; Može & Beg, 2014; Može, 2020; Wang et al., 2017). In (Wang et al., 2017), end-splitting

failure was described as a transition between shear-out and net section tension failure, while in (Može, 2018; Može & Beg, 2014; Može, 2020), end-spitting failure was defined as the lower boundary of the bearing resistance of a lap connection. In all incidents of the failure mode, plastic deformation and rotation of the net section have been observed; some researchers have found the occurrence of end-splitting is related to the cutting and fabrication methods of the connected steel plates (Xing et al., 2020b; Guo et al., 2020).

End-splitting failure was also exhibited by some of the specimens examined herein; typical examples are shown in Figure 4.5, where specimens of the same width (i.e. b = 65 mm) and of increasing end distances e_1 (i.e. from 21.6 to 36 mm) are grouped by their angle θ relative to the print layer orientation (i.e. (a) $\theta = 0°$ and (b) $\theta = 90°$). Note that in the current investigation, a failure was identified as end-splitting if occurrence of fracture at the end was observed to result in load resistance losses. The specimens shown in Figure 4.5(a) have the same dimensions as those shown in Figure 4.5(b), but different print layer orientations.



(a)



(b)

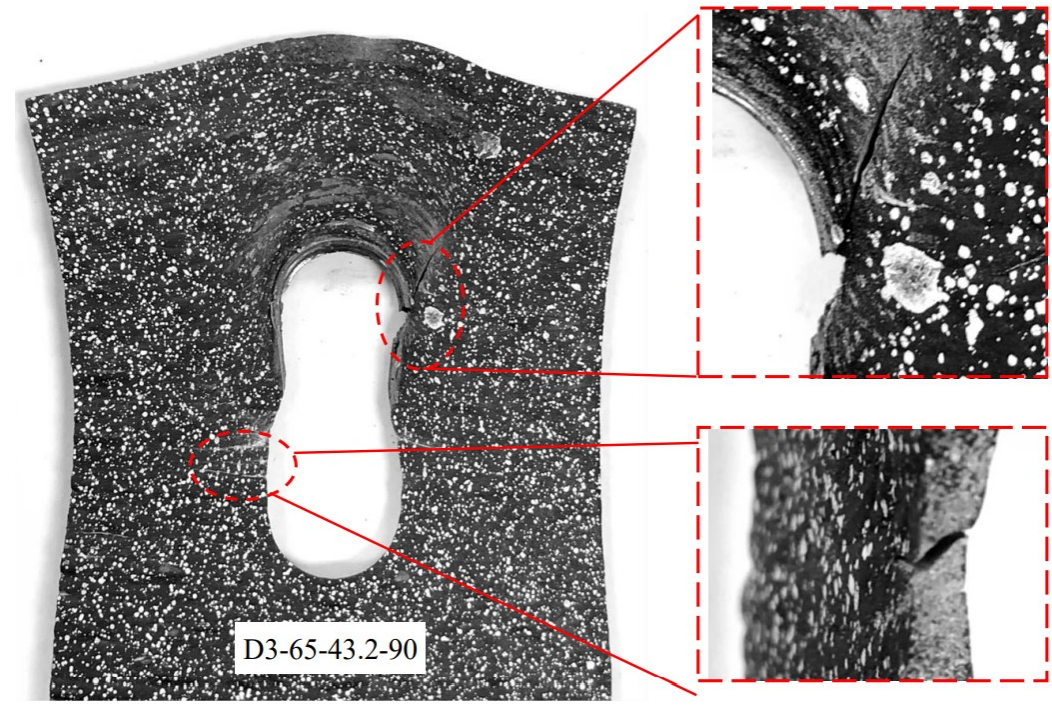
Figure 4.5: Shear-out and end-splitting failures of specimens with b = 65 mm and (a) θ = 0° and (b) θ = 90°

All the $\theta = 0°$ specimens shown in Figure 4.5(a) underwent end-splitting failure irrespective of the ratio e_1/b. Although it was stated in (Može & Beg, 2014) that end-splitting fracture only

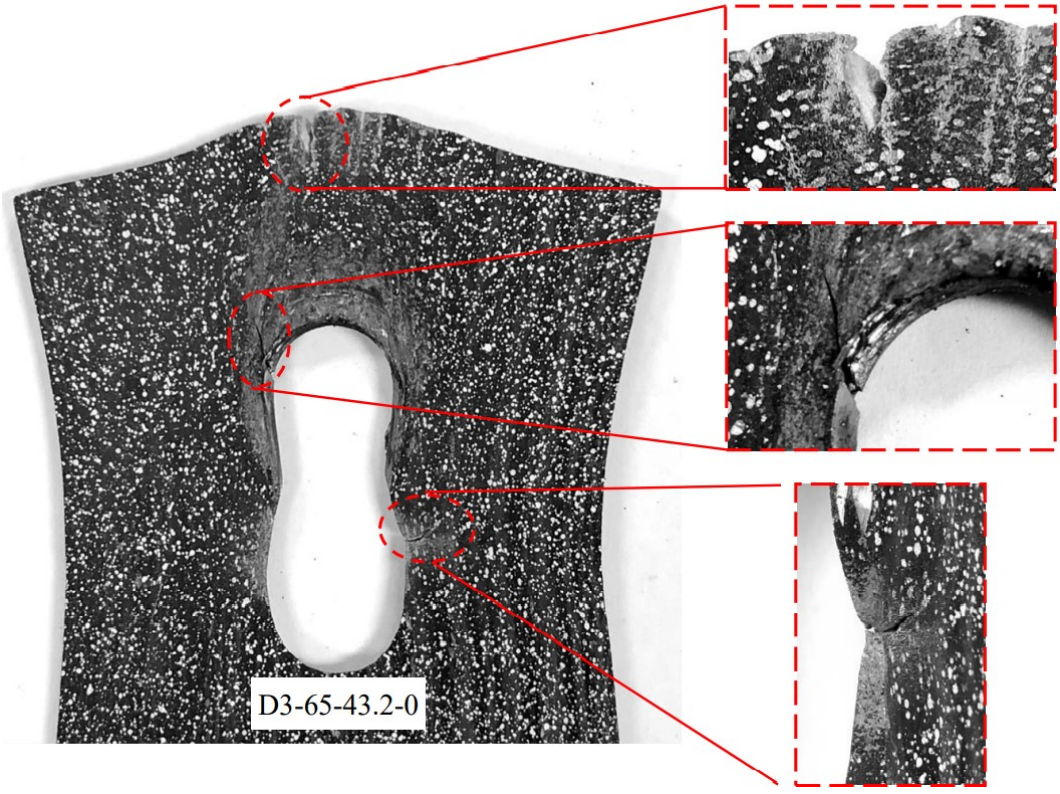
occurs because of partial yielding in the net cross-section thus enabling rotation at this location as well as outward bending at the edge of the plate, which is consistent with the observation on Specimen D3-65-36-0, rotation at the net cross-section of Specimen D3-65-21.6-0 was barely evident. On the other hand, with increasing end distance, the failure mode of the θ = 90° specimens first transitioned from shear-out (Specimen D3-65-21.6-90) to end-splitting (Specimens D3-65-27-90 and D3-65-32.4-90) and then reverted back to shear-out (Specimen D3-65-36-90), indicating that the occurrence of end-splitting failure is more strongly related to the level of material imperfections at the plate end rather than the plate geometry. This indication is supported not only by the fact that all the θ = 0° specimens underwent end-splitting failure while only half of the θ = 90° specimens did, but also by the findings from previous studies that specimens with sheared ends were more prone to end-splitting than those with saw cut ends (Guo et al., 2020; Xing et al., 2020b).

4.3.2.3. Incidental block shear failure

Figures 4.6(a) and 4.6(b) show the "incidental" block shear failures of Specimens D3-65-43.2-90 and D3-65-43.2-0, respectively. An incidental block shear failure may occur in a single bolted connection when the net section tension capacity is nominally the same as the shear-out capacity. In this case, either a net section tension failure, a shear-out failure, or an incidental block shear may take place, depending on the weakest tensile and/or shear planes caused by fabrication or material imperfections. If the two weakest planes are the planes at the net tensile section, then net section tension fractures will govern. Shear-out will govern if the two shear planes are weaker than the two tensile planes on either side of the bolt. If the two weakest planes comprise a shear plane and a tensile plane on the other side of the bolt, then the member will undergo an incidental block shear failure.



(a)



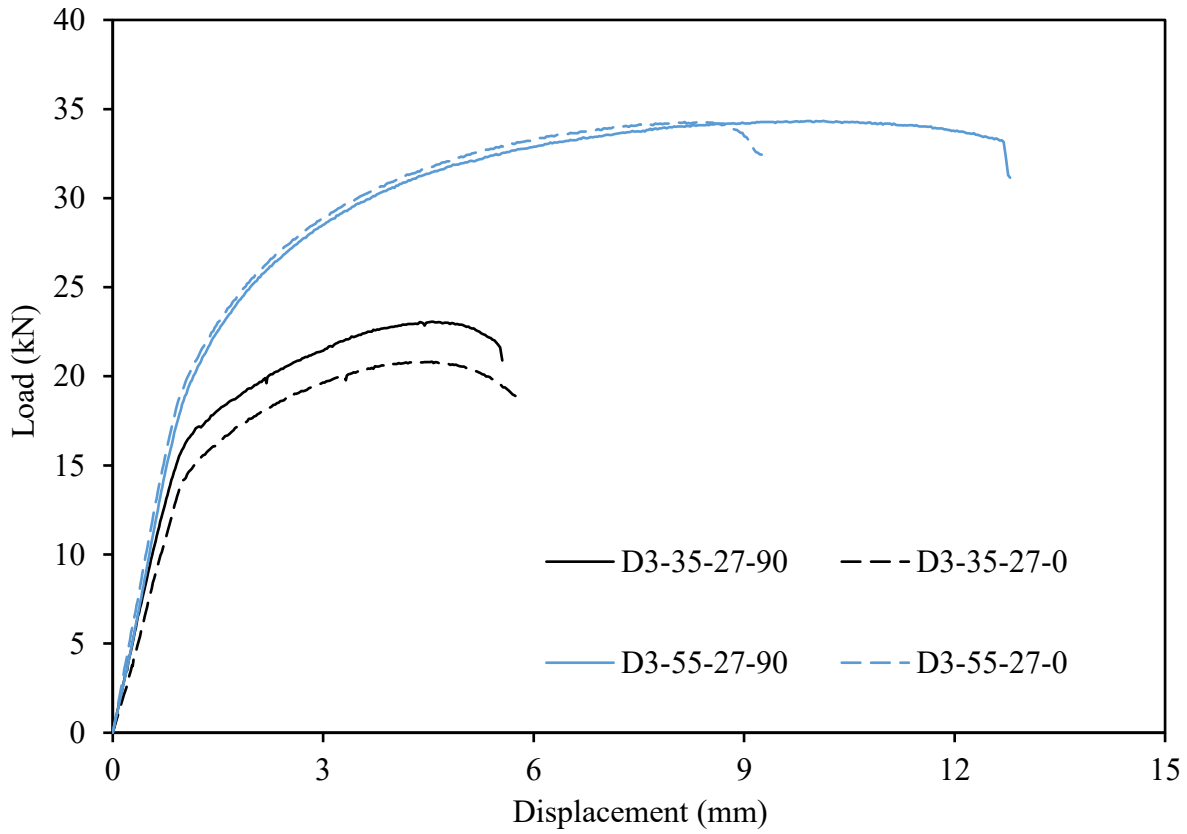
(b)

Figure 4.6: Specimens failing in incidental block shear (a) Specimen D3-65-43.2-90 and (b) Specimen D3-65-43.2-0

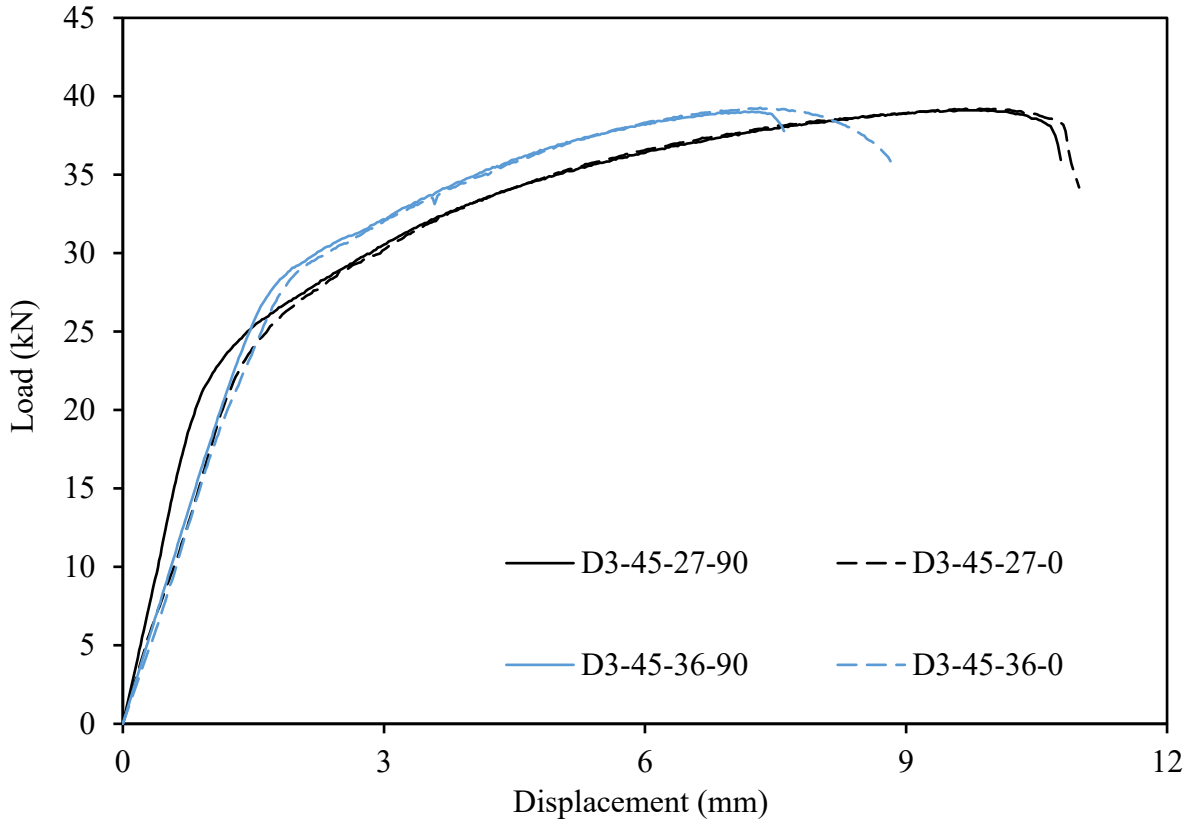
End-splitting failure was observed only for Specimen D3-65-43.2-0, further verifying that this mode of failure is strongly linked to the local conditions at the plate end and, in the context of WAAM connections, is dependent on the print layer orientation rather than the plate geometry.

4.3.3. Ultimate loads and load-deformation responses

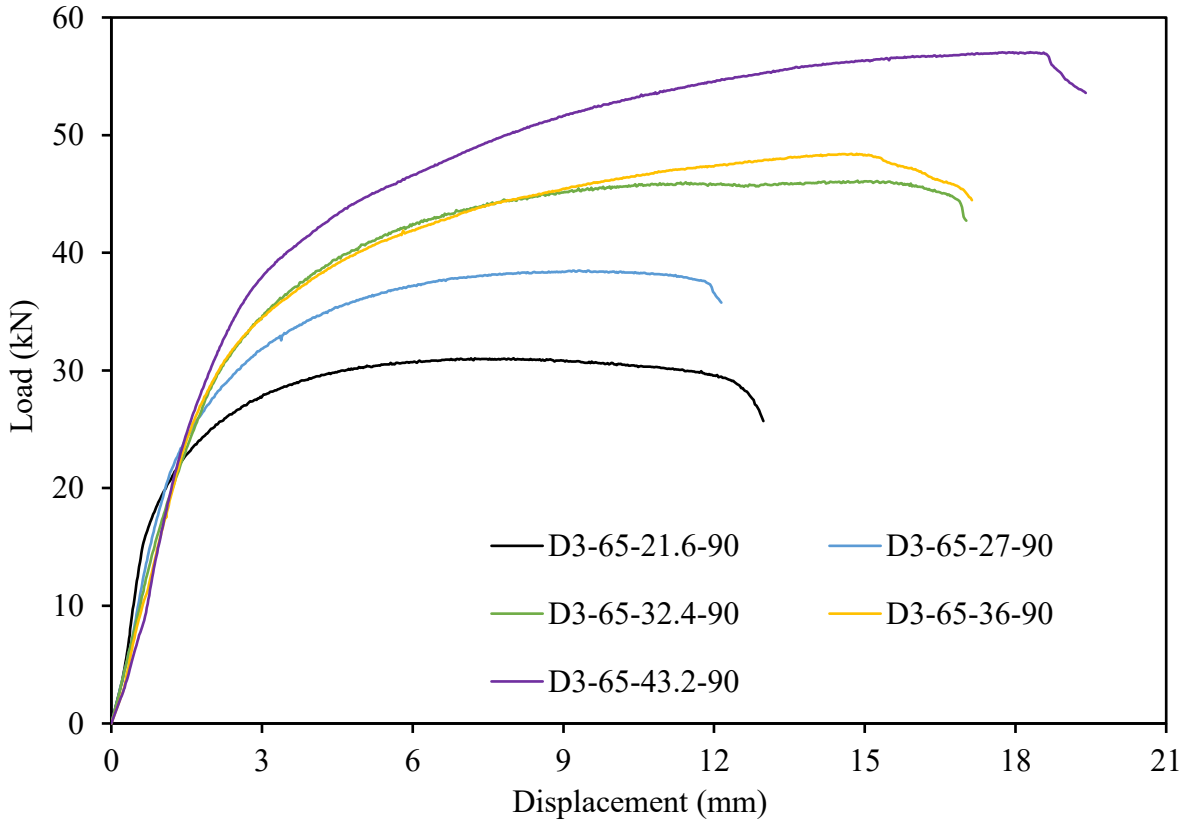
The ultimate loads P_u of all test specimens are reported in Table 4.2, while the load-displacement curves are presented in Figure 4.7, where the displacements were calculated as the average of the measurements from both sides of the specimens, over a gauge length of about 150 mm – see Figure 4.3. Note that some curves in Figures 4.7(h) and 4.7(i), corresponding to the specimens failing in bearing are not as smooth as the others. This is attributed to the material downstream of the bolt hole yielding due to the high bearing stresses and then piling up, resulting in a locally increased plate thickness, subsequently leading to stiffness changes and a more irregular post-yielding behaviour. Typical load-displacement curves of specimens failing in shear-out, net section tension, bearing and splitting are presented in Figure 4.8.



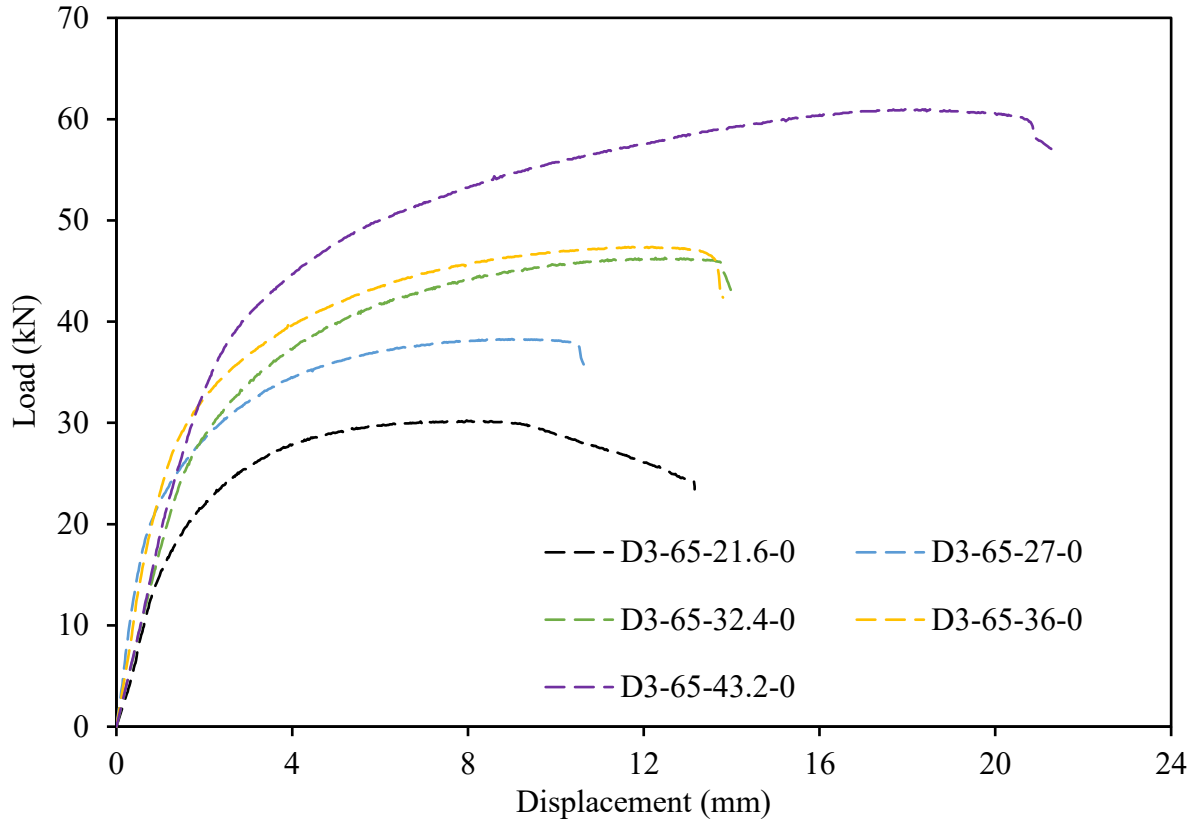
(a) $t = 3$ mm, $\theta = 0°$ or $90°$, $b = 35$ or 55 mm and $e_1 = 27$ mm



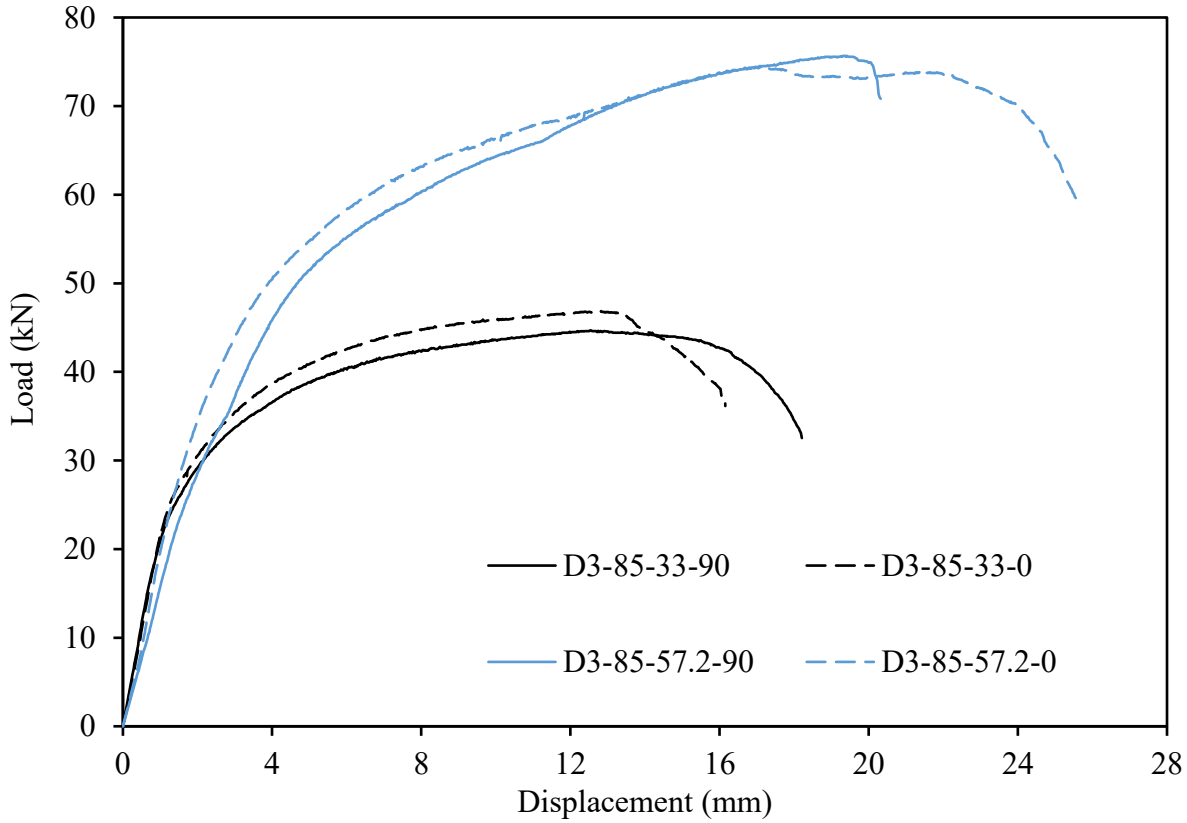
(b) $t = 3$ mm, $\theta = 0°$ or $90°$, $b = 45$ mm and $e_1 = 27$ or 36 mm



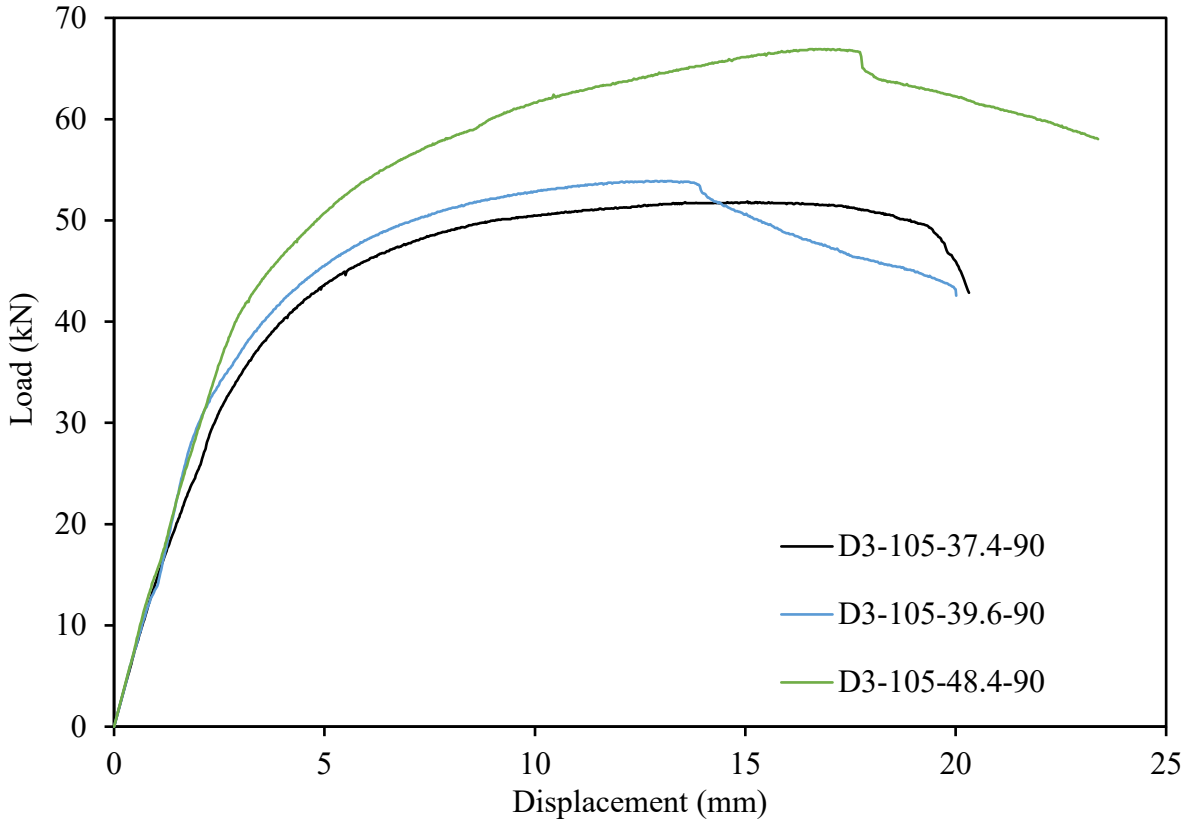
(c) $t = 3$ mm, $\theta = 90°$, $b = 65$ mm and e_1 varying from 21.6 to 43.2 mm



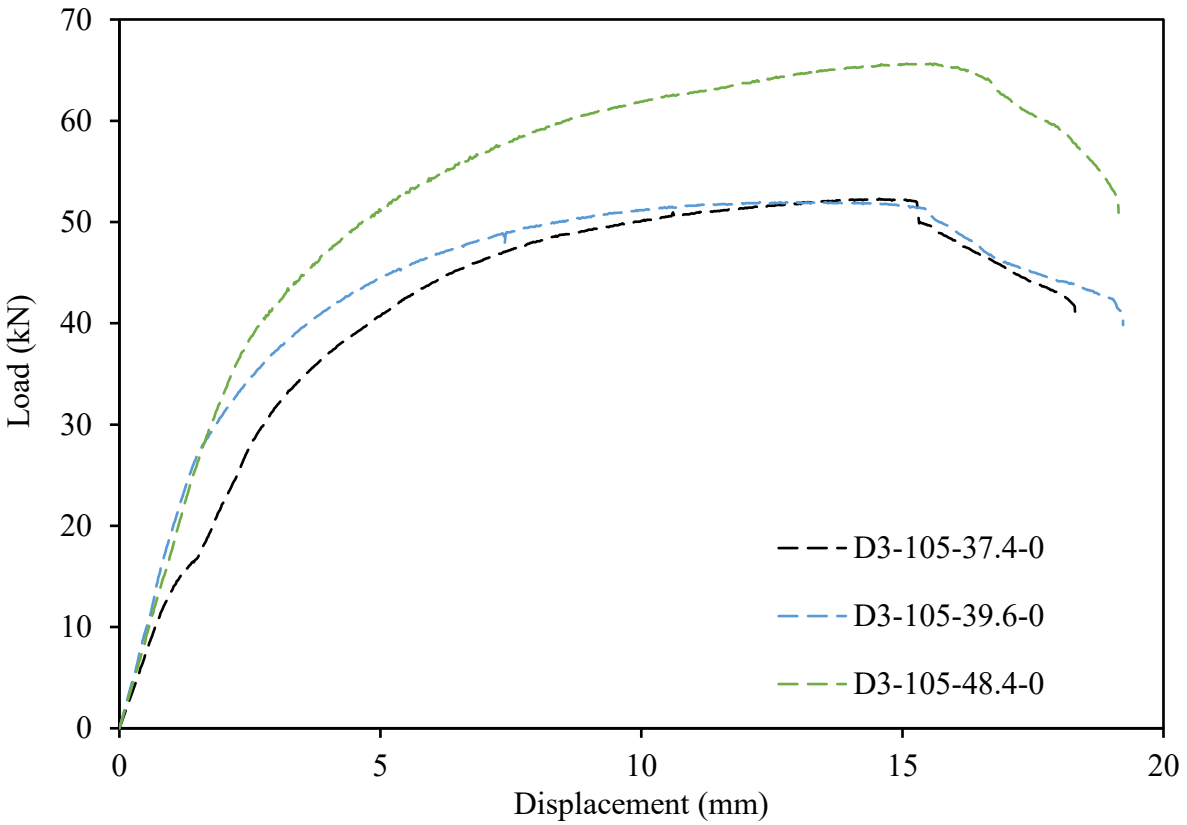
(d) $t = 3$ mm, $\theta = 0°$, $b = 65$ mm and e_1 varying from 21.6 to 43.2 mm



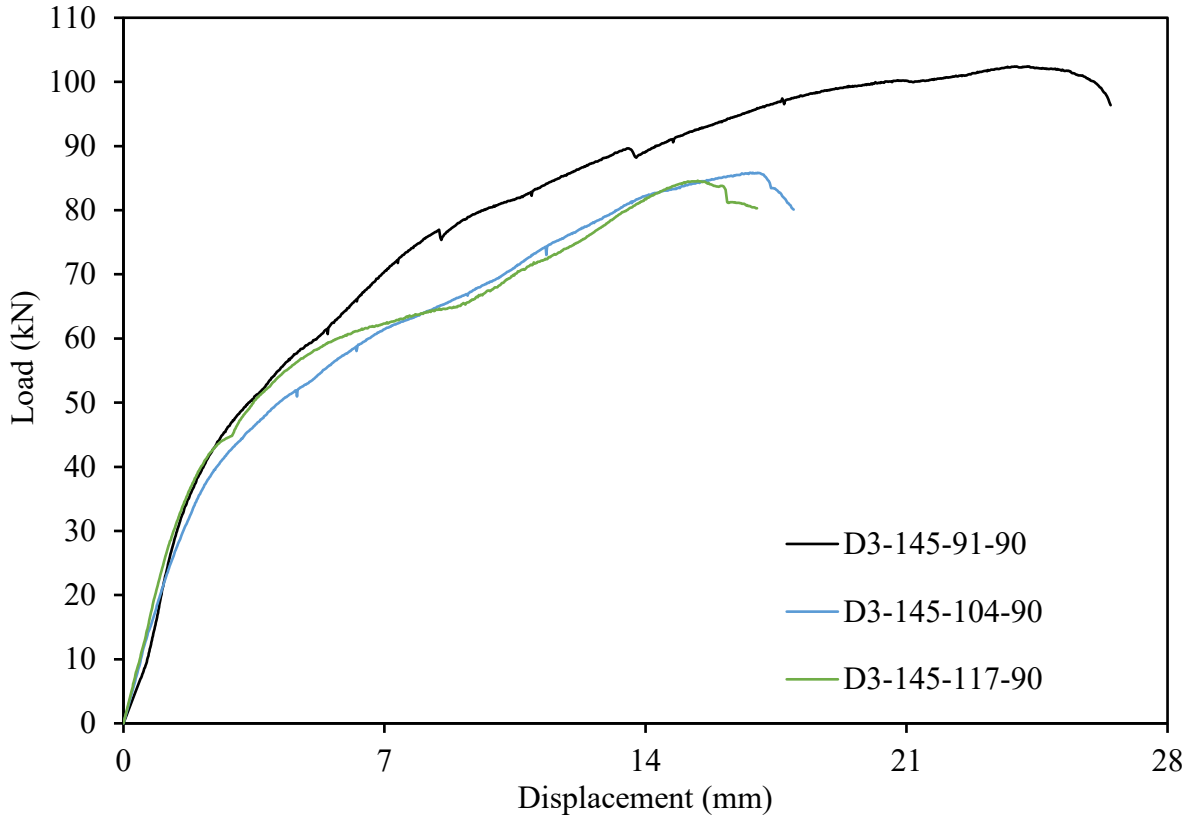
(e) $t = 3$ mm, $\theta = 0°$ or $90°$, $b = 85$ mm and $e_1 = 33$ or 57.2 mm



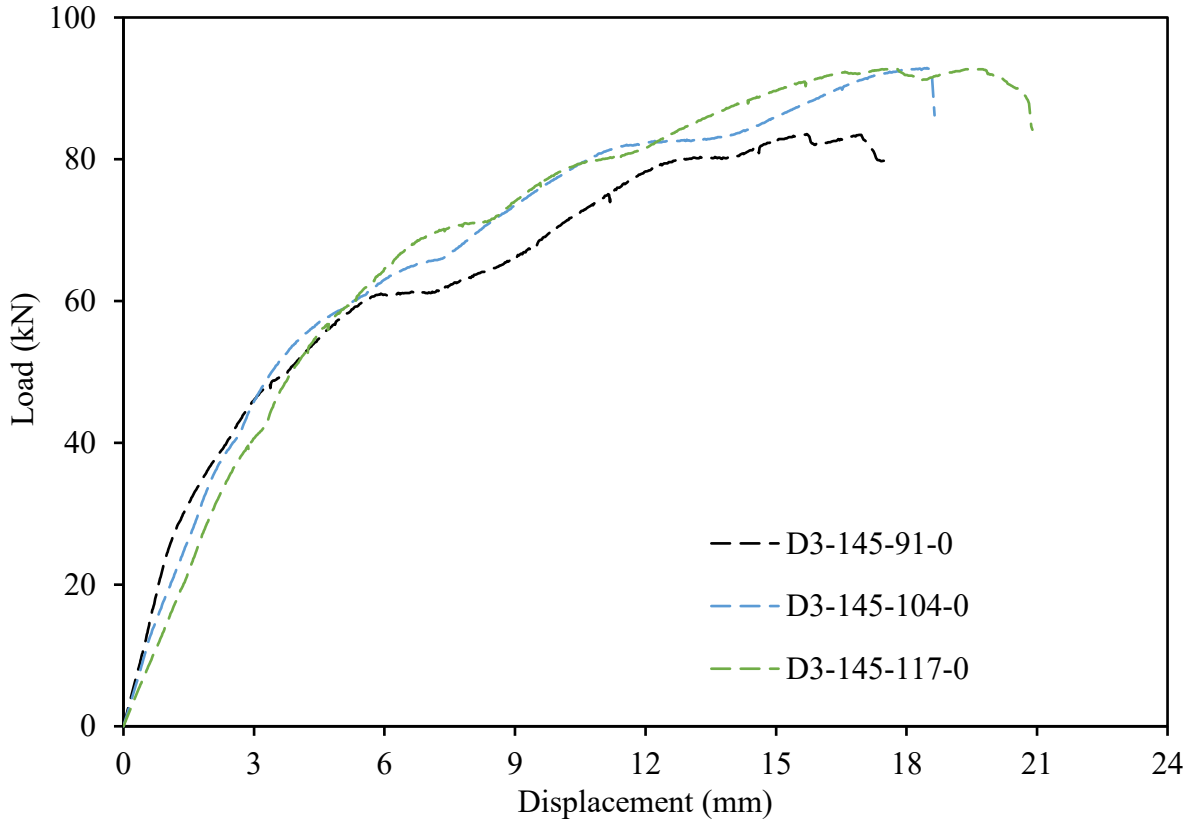
(f) $t = 3$ mm, $\theta = 90°$, $b = 105$ mm and e_1 varying from 37.4 to 48.4 mm



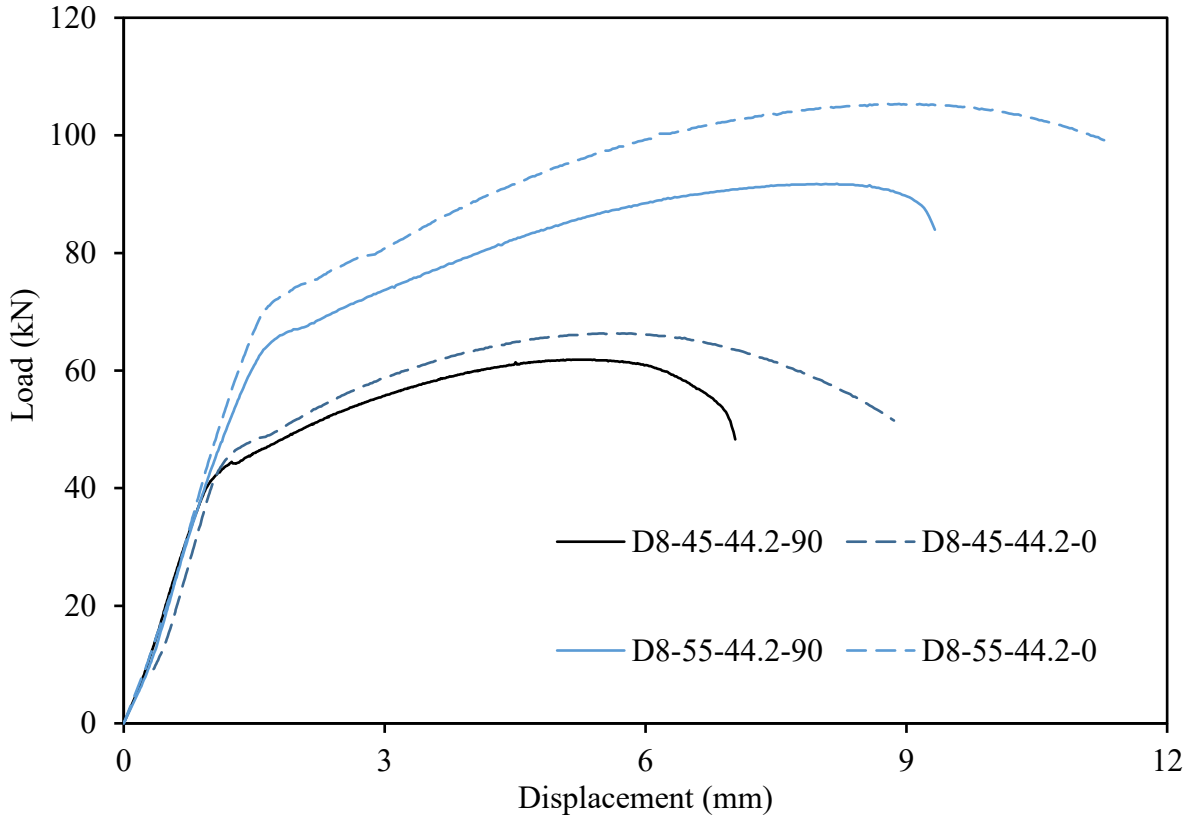
(g) $t = 3$ mm, $\theta = 0°$, $b = 105$ mm and e_1 varying from 37.4 to 48.4 mm



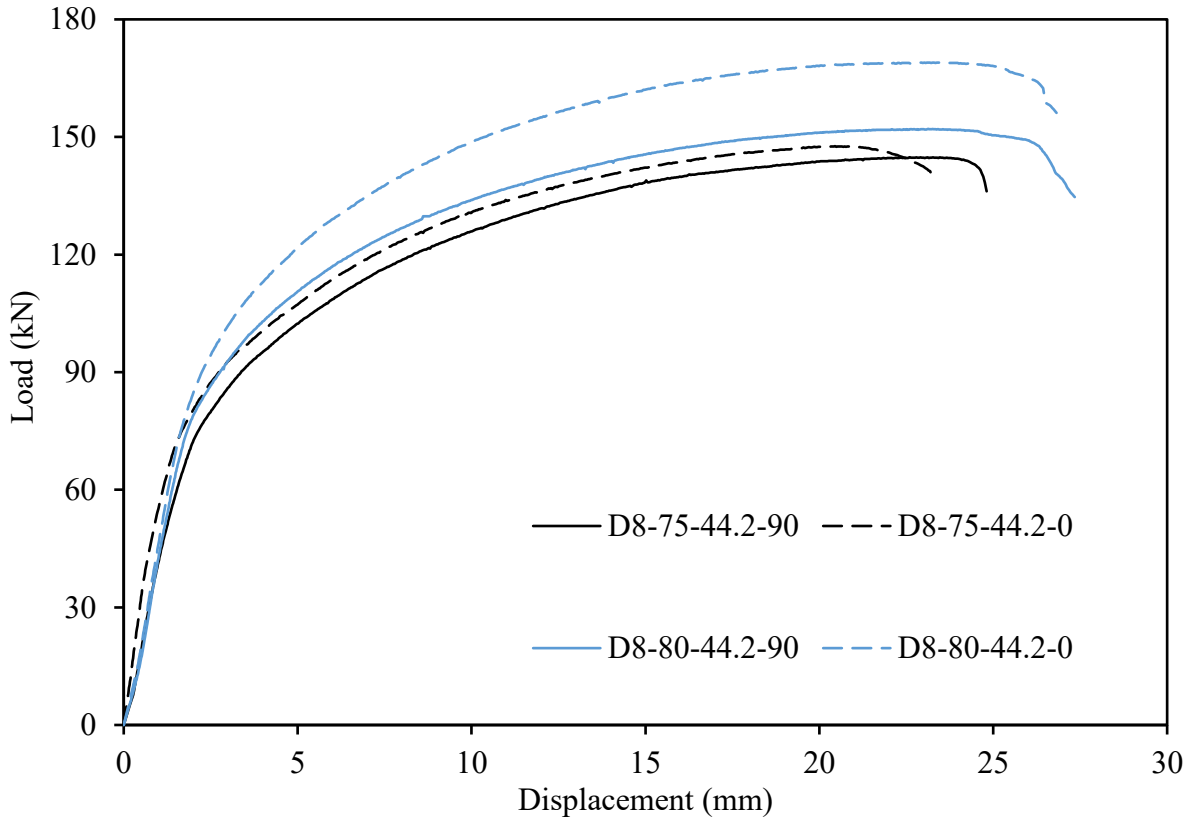
(h) $t = 3$ mm, $\theta = 90°$, $b = 145$ mm and e_1 varying from 91 to 117 mm



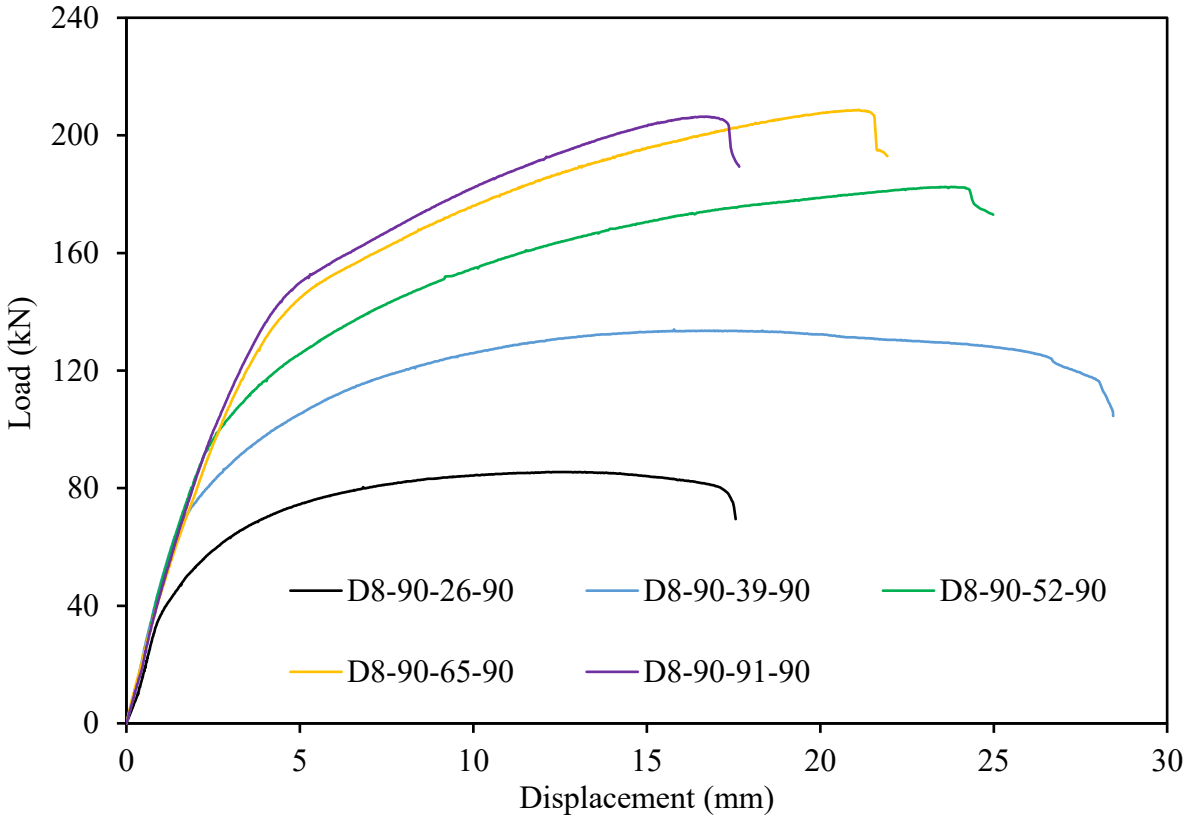
(i) $t = 3$ mm, $\theta = 0°$, $b = 145$ mm and e_1 varying from 91 to 117 mm



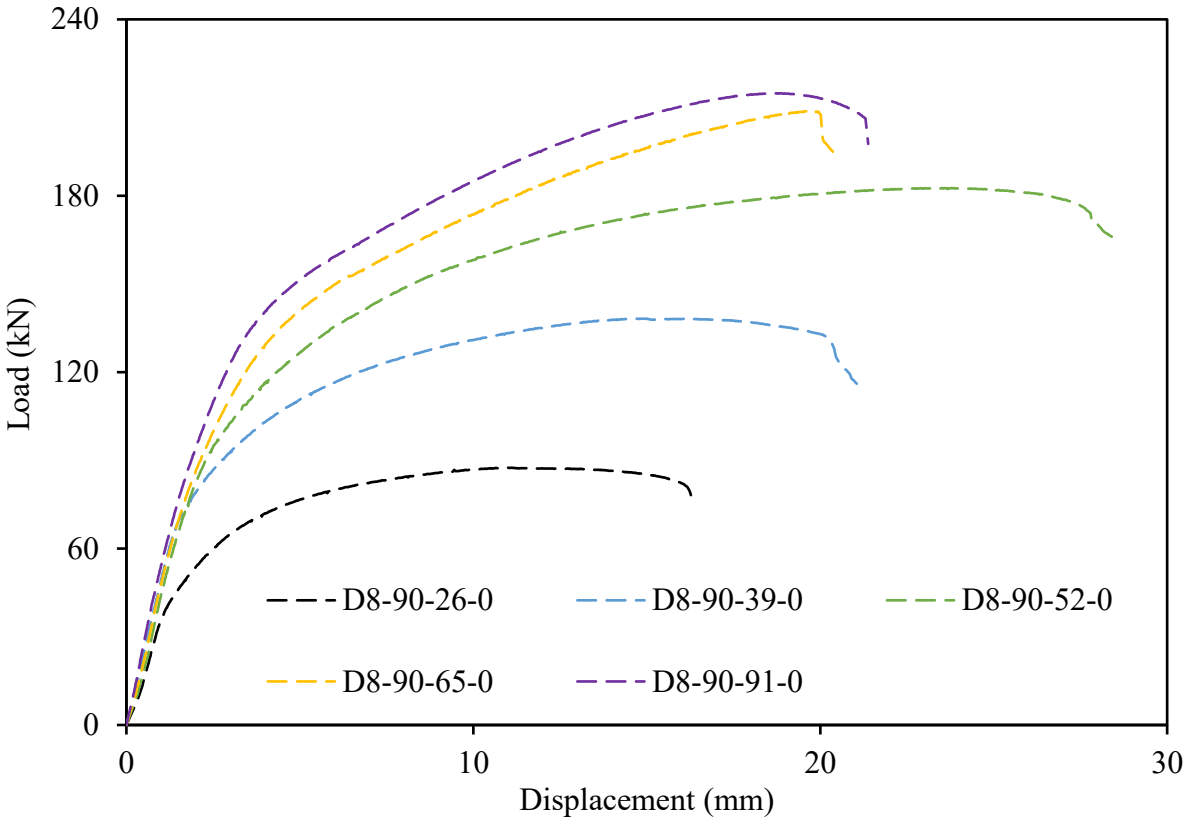
(j) $t = 8$ mm, $\theta = 0°$ and 90°, $b = 45$ or 55 mm and $e_1 = 44.2$ mm



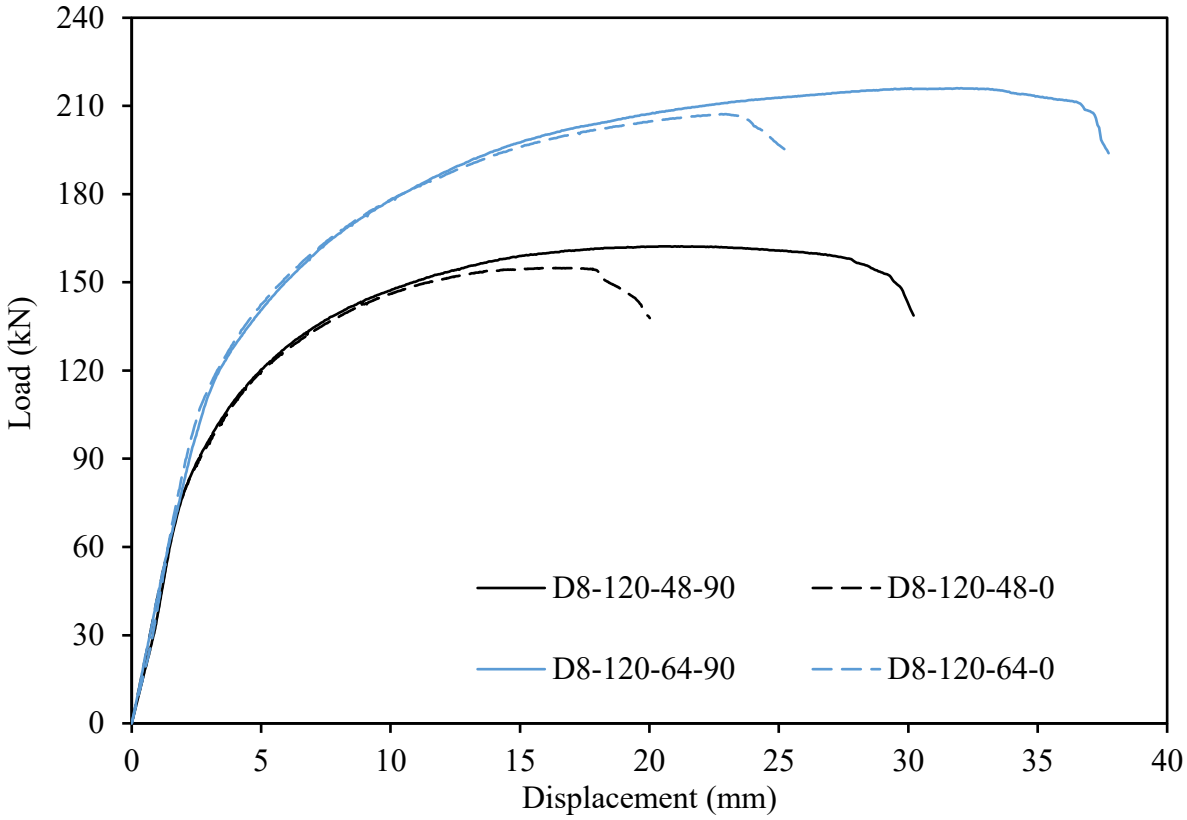
(k) $t = 8$ mm, $\theta = 0°$ and 90°, $b = 75$ or 80 mm and $e_1 = 44.2$ mm



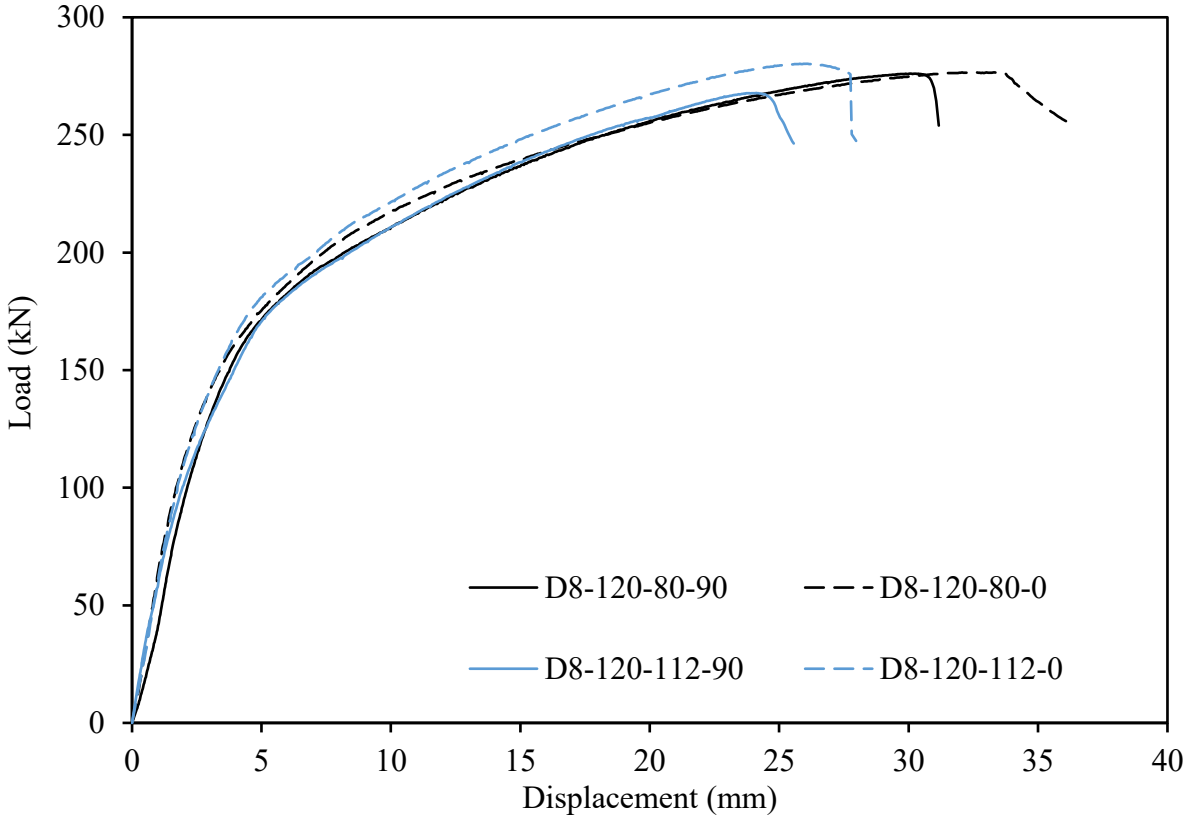
(l) $t = 8$ mm, $\theta = 90°$, $b = 90$ mm and e_1 varying from 26 to 91 mm



(m)$t = 8$ mm, $\theta = 0°$, $b = 90$ mm and e_1 varying from 26 to 91 mm



(n) t = 8 mm, θ = 0 or 90°, b = 120 mm and e_1 = 48 or 64 mm



(o) t = 8 mm, θ = 0 or 90°, b = 120 mm and e_1 = 80 or 120 mm

Figure 4.7: Load-displacement curves of double-lap shear test specimens

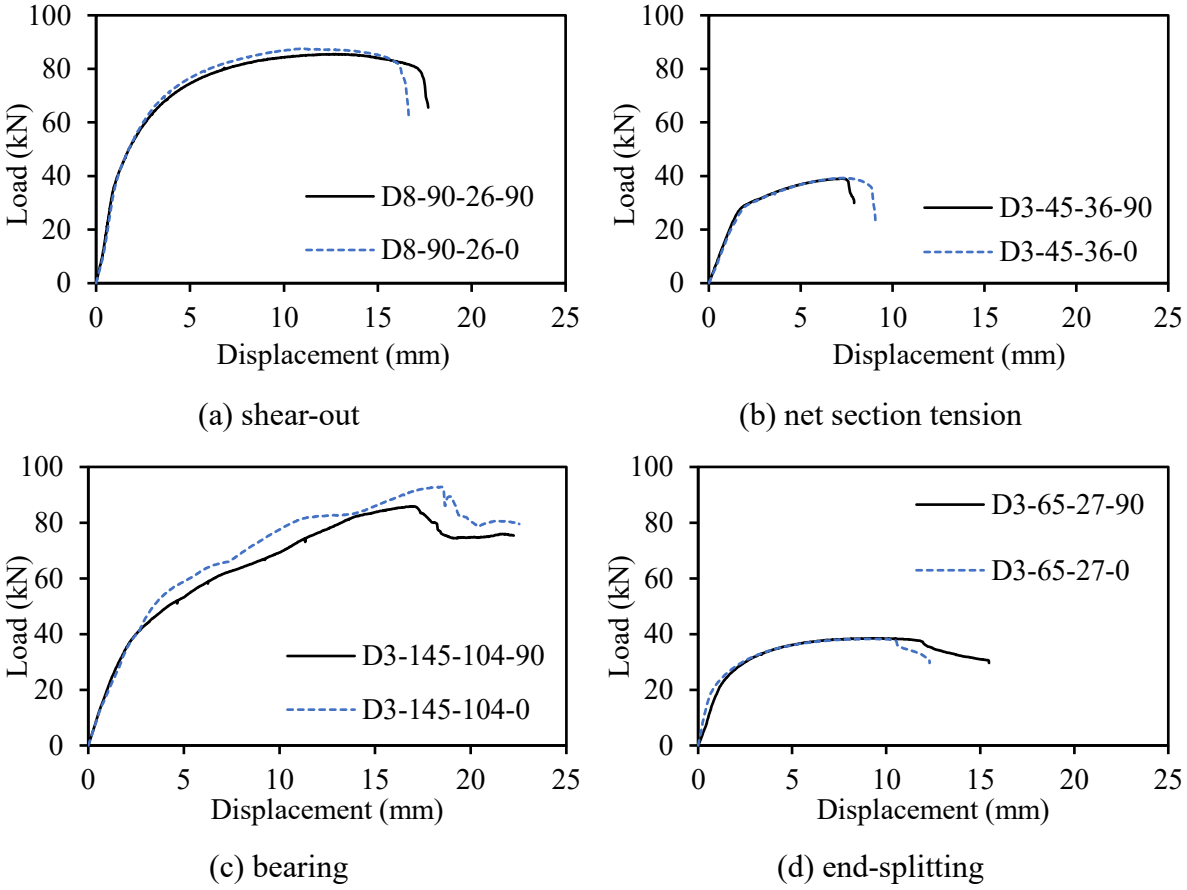


Figure 4.8: Typical load-displacement curves of specimens exhibiting: (a) shear-out, (b) net section tension, (c) bearing and (d) end-splitting failure

The load-displacement curve of Specimen D3-65-21.6-0 is presented in Figure 4.9, where the curve of Specimen D3-65-21.6-90, which failed in shear-out, is also plotted. Unlike the smooth curve of Specimen D3-65-21.6-90, a rather sudden change in gradient can be noticed at the ultimate load point, indicating the occurrence of fracture. Thus, it can be concluded that Specimen D3-65-21.6-0 failed by end-splitting.

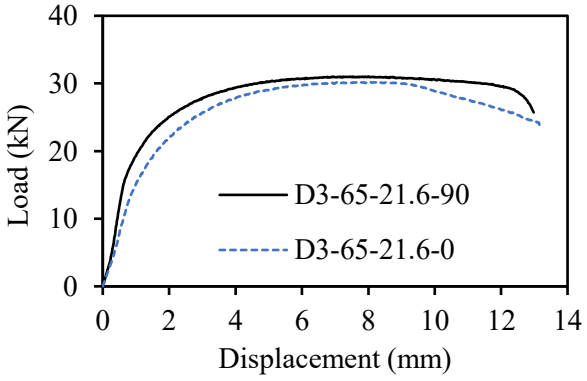


Figure 4.9: Load-displacement curves of specimens failing in shear-out (D3-65-21.6-90) and end-splitting (D3-65-21.6-0)

4.3.4. Influence of print layer orientation

The influence of print layer orientation (i.e. $\theta = 0°$ or 90°) on the ultimate load capacity P_u of the WAAM specimens was not found to be significant, with the average difference in the normalised capacities between comparable specimens of different orientations being 4% – see Table 4.3. However, the failure modes were affected by the print layer orientations, with the $\theta = 90°$ specimens mainly failing in shear-out, while the corresponding 0° specimens tended to fail in end-splitting – see Figures 4.10(a) and 4.10(b). This difference is attributed to more severe imperfections in the transverse direction at the ends of the 0° specimens, resulting in lower resistances to end-splitting.

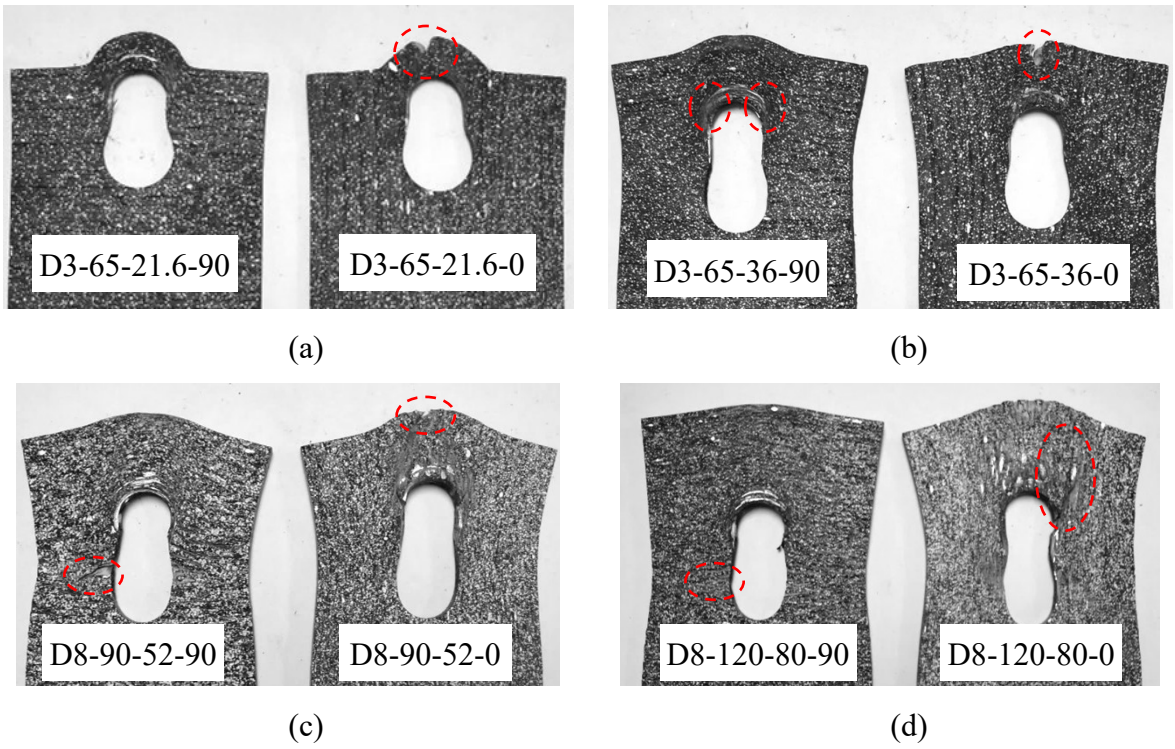


Figure 4.10: Influence of print layer orientation on failure modes for different specimen pairs: (a) D3-65-21.6, (b) D3-65-36, (c) D8-90-52 and (d) D8-120-80

Table 4.3: Influence of print layer orientation on ultimate capacity and failure mode of double-lap shear connections

Specimen pair	$\frac{P_{u,90°}}{tf_{u,90°}} \Big/ \frac{P_{u,0°}}{tf_{u,0°}}$	$FM_{90°}$[1]	$FM_{0°}$[2]
D3-35-27	1.17	NS	NS
D3-45-27	1.06	NS	NS
D3-45-36	1.04	NS	NS

D3-55-27	1.04	ES	ES
D3-65-21.6	1.06	SO	ES
D3-65-27	1.09	ES	ES
D3-65-32.4	1.07	ES	ES
D3-65-36	1.11	SO	ES
D3-65-43.2	1.04	IB	IB
D3-85-33	1.03	SO	ES
D3-85-57.2	1.09	NS	ES
D3-105-37.4	0.98	SO	ES
D3-105-39.6	1.05	ES	ES
D3-105-48.4	1.06	ES	ES
D3-145-91	1.32	B	B
D3-145-104	1.02	B	B
D3-145-117	0.98	B	B
D8-45-44.2	1.00	NS	NS
D8-55-44.2	0.94	NS	NS
D8-75-44.2	0.97	NS	NS
D8-80-44.2	0.98	SO	SO
D8-90-26	1.00	SO	SO
D8-90-39	1.00	ES	ES
D8-90-52	1.00	NS	ES
D8-90-65	1.00	NS	NS
D8-90-91	0.98	NS	NS
D8-120-48	1.04	SO	SO
D8-120-64	1.04	SO	SO
D8-120-80	0.97	NS	SO
D8-120-112	0.95	NS	NS
Mean	1.04		
COV	0.072		

[1]$FM_{90°}$: failure mode of specimens with $\theta = 90°$.

[2]$FM_{0°}$: failure mode of specimens with $\theta = 0°$.

Furthermore, several 90° specimens (i.e. D3-85-57.2-90, D8-90-52-90 and D8-120-80-90) failed in net section tension, while most of their 0° counterparts failed in shear-out or end-splitting (i.e. D8-120-80-0 in shear-out, D8-90-52-0 and D3-85-57.2-0 in end-splitting), indicating that when shear-out and net section tension capacities are of similar magnitude, fracture lines tend to develop along the print layers – see Figures 4.10(c) and 4.10(d).

4.4. Available design equations

4.4.1. Eurocode 3

The bearing capacity $P_{b,EC3}$ of a bolted shear connection is specified in EN 1993-1-8 (2021) as presented in Chapter 3, Equation (3.7). Note that for connections with a sufficiently strong bolt (i.e. $f_{ub}/f_u > 1$), according to the definition of α_b, Eurocode 3 regards the failure mode of shear-out as a special case of bearing failure, occurring when the end distance e_1 is less than 3 times the bolt hole diameter d_0.

The net section tension resistance $P_{n,EC3}$ of a bolted double-lap shear connection defined in EN 1993-1-1(2020) can be obtained by Equation (3.9) in Chapter 3.

4.4.2. AISI S100

In AISI S100-16 (2016), the bearing capacity $P_{b,AISI}$ of a bolted connection, for the cases where the bolt hole deformation is not a design consideration, is given by Equation (3.1). Note that the modification factor m_f is equal to 1.33 for the inner plates of double-shear connections. Meanwhile, the net section tension resistance $P_{n,AISI}$ can be obtained by Equation (3.3).

The shear resistance $P_{s,AISI}$ can be obtained based on Equation (3.2), which can also be expressed as:

$$P_{SO,AISI} = 0.6 A_{nv} f_u \tag{4.1}$$

in which

$$A_{nv} = 2 L_{nv} t \tag{4.2}$$

In Equations (4.1) and (4.2), A_{nv} and L_{nv} are the area and length of the net shear plane respectively, as defined in Figure 2.10.

4.4.3. AISC 360

According to AISC 360-16 (2016), the bearing capacity $P_{b,AISC}$, shear-out capacity $P_{s,AISC}$ and net section tension capacity $P_{n,AISC}$ can be calculated based on Equations (3.4), (3.5) and (3.6).

4.4.4. AS/NZS 4600

In AS/NZS 4600 (2018), the bearing capacity $P_{b,AISC}$, net section tension capacity $P_{n,AISC}$ and shear-out capacity $P_{s,AISC}$ can be calculated based on Equations (3.1),(3.3) and (3.10).

4.4.5. Summary of design specifications

The equations provided in the above-mentioned design standards for the different failure modes of double-lap shear connections can be summarised as follows:

$$P_B = C_B dtf_u \tag{4.3}$$

$$P_{SO} = C_{SO} A_v f_u \tag{4.4}$$

$$P_{NS} = C_{NS} A_n f_u \tag{4.5}$$

where the subscripts *b*, *s* and *n* stand for bearing, shear-out and net section failure respectively, *P* is the capacity prediction, *C* is a modification factor (C_B: bearing factor, C_{SO}: shear factor and C_{NS}: shear lag factor), A_v is the area of the shear plane (net, gross or active shear plane – see Figure 2.10) and A_n is the area of the net section.

4.4.6. Proposed equations in the literature

The equation which was proposed in (Teh & Uz, 2015)and modified in (Xing et al., 2020b) for predicting the shear-out capacity in bolted connections accounting for catenary action, is given by Equations (3.12) and (3.13) in Chapter 3. The catenary power *p* is taken as 1/10 for the WAAM double-lap shear connections examined herein.

4.5. Comparisons between test and predicted capacities

Comparisons between the test results and the nominal capacities and failure modes predicted by the above-mentioned design standards are presented in Table 4.4, where brackets are used

to mark incorrect failure mode predictions. Note that the as-built material properties of the coupons with the same nominal thickness (i.e. 3 mm or 8 mm) and print layer orientation (i.e. 0° and 90°) as the tested specimens were utilised for the predictions. The bearing stress f_B normalised by the corresponding tensile stress f_u, is plotted against e_1/d in Figure 4.11.

Table 4.4: Summary of comparisons between the test results and design equations

Specimen	AISI S100 Eqs. (3.1-3.3)		AISC 360 Eqs. (3.4-3.6)		AS/NZS 4600 Eqs. (3.1,3.3,3.10)		Eurocode 3 Eqs. (3.7,3.9)	
	$\frac{P_u}{P_{EC3}}$	FM	$\frac{P_u}{P_{AISI}}$	FM	$\frac{P_u}{P_{AISC}}$	FM	$\frac{P_u}{P_{AS/NZS}}$	FM
D3-35-27-90	1.07	NS[1]	1.13	NS	1.07	NS	1.13	NS
D3-35-27-0	0.96	NS	1.01	NS	0.96	NS	1.01	NS
D3-45-27-90	1.16	(SO)[2]	1.29	(SO)	1.04	NS	1.12	NS
D3-45-27-0	1.10	(SO)	1.23	(SO)	0.98	(SO)	1.05	NS
D3-45-36-90	1.02	NS	1.09	NS	1.02	NS	1.09	NS
D3-45-36-0	0.98	NS	1.05	NS	0.98	NS	1.05	NS
D3-55-27-90	1.14	(SO)	1.26	(SO)	1.01	(SO)	1.01	(SO)
D3-55-27-0	1.10	(SO)	1.22	(SO)	0.97	(SO)	0.97	(SO)
D3-65-21.6-90	1.18	SO	1.49	SO	1.19	SO	1.06	SO
D3-65-21.6-0	1.11	(SO)	1.40	(SO)	1.12	(SO)	1.00	(SO)
D3-65-27-90	1.17	(SO)	1.30	(SO)	1.04	(SO)	1.05	(SO)
D3-65-27-0	1.08	(SO)	1.20	(SO)	0.96	(SO)	0.96	(SO)
D3-65-32.4-90	1.16	(SO)	1.19	(SO)	0.95	(SO)	1.04	(SO)
D3-65-32.4-0	1.08	(SO)	1.11	(SO)	0.89	(SO)	0.97	(SO)
D3-65-36-90	1.14	SO	1.13	SO	0.90	SO	1.02	SO
D3-65-36-0	1.04	(SO)	1.04	(SO)	0.83	(SO)	0.94	(SO)
D3-65-43.2-90	1.14	(SO)	1.07	(SO)	0.94	(NS)	1.02	(SO)
D3-65-43.2-0	1.10	(SO)	1.03	(SO)	0.90	(NS)	0.98	(SO)
D3-85-33-90	1.15	SO	1.31	SO	1.05	SO	1.05	SO
D3-85-33-0	1.11	(SO)	1.26	(SO)	1.01	(SO)	1.01	(SO)
D3-85-57.2-90	1.12	(SO)	1.05	(SO)	0.98	(B)	1.02	(SO)
D3-85-57.2-0	1.02	(SO)	0.96	(SO)	0.90	(B)	0.94	(SO)

D3-105-37.4-90	1.15	SO	1.23	SO	0.99	SO	1.04	SO
D3-105-37.4-0	1.16	(SO)	1.21	(SO)	0.97	(SO)	1.03	(SO)
D3-105-39.6-90	1.15	(SO)	1.20	(SO)	0.96	(SO)	1.04	(SO)
D3-105-39.6-0	1.20	(SO)	1.26	(SO)	1.01	(SO)	1.05	(SO)
D3-105-48.4-90	1.19	(SO)	1.16	(SO)	0.93	(SO)	1.07	(SO)
D3-105-48.4-0	1.14	(SO)	1.10	(SO)	0.88	(SO)	1.01	(SO)
D3-145-91-90	1.14	B	0.88	(SO)	1.14	B	0.90	(SO)
D3-145-91-0	0.86	B	0.67	(SO)	0.86	B	0.69	(SO)
D3-145-104-90	0.97	B	0.73	B	0.97	B	0.73	B
D3-145-104-0	0.95	B	0.71	B	0.95	B	0.71	B
D3-145-117-90	0.94	B	0.70	B	0.94	B	0.70	B
D3-145-117-0	0.96	B	0.77	(NS)	0.96	B	0.77	(NS)
D8-45-44.2-90	1.09	NS	1.14	NS	1.09	NS	1.14	NS
D8-45-44.2-0	1.08	NS	1.14	NS	1.08	NS	1.14	NS
D8-55-44.2-90	1.06	NS	1.12	NS	1.06	NS	1.12	NS
D8-55-44.2-0	1.11	NS	1.17	NS	1.11	NS	1.17	NS
D8-75-44.2-90	1.18	(SO)	1.28	(SO)	1.03	(SO)	1.09	(SO)
D8-75-44.2-0	1.21	(SO)	1.31	(SO)	1.05	(SO)	1.11	(SO)
D8-80-44.2-90	1.25	SO	1.35	SO	1.08	SO	1.14	SO
D8-80-44.2-0	1.26	SO	1.38	SO	1.10	SO	1.17	SO
D8-90-26-90	1.12	SO	1.73	SO	1.38	SO	1.04	SO
D8-90-26-0	1.13	SO	1.74	SO	1.39	SO	1.05	SO
D8-90-39-90	1.19	(SO)	1.37	(SO)	1.10	(SO)	1.10	(SO)
D8-90-39-0	1.19	(SO)	1.38	(SO)	1.10	(SO)	1.10	(SO)
D8-90-52-90	1.21	(SO)	1.24	(SO)	0.99	(SO)	1.12	(SO)
D8-90-52-0	1.22	(SO)	1.25	(SO)	1.00	(SO)	1.12	(SO)
D8-90-65-90	1.10	(SO)	1.11	NS	1.03	NS	1.11	NS
D8-90-65-0	1.11	(SO)	1.13	NS	1.04	NS	1.13	NS
D8-90-91-90	1.06	NS	1.11	NS	1.03	NS	1.11	NS
D8-90-91-0	1.05	NS	1.13	NS	1.05	NS	1.13	NS
D8-120-48-90	1.15	SO	1.35	SO	1.08	SO	1.09	SO
D8-120-48-0	1.11	SO	1.30	SO	1.04	SO	1.05	SO
D8-120-64-90	1.15	SO	1.20	SO	0.96	SO	1.09	SO

D8-120-64-0	1.10	SO	1.15	SO	0.92	SO	1.04	SO
D8-120-80-90	1.14	(SO)	1.12	(SO)	0.98	NS	1.07	(SO)
D8-120-80-0	1.18	SO	1.15	SO	1.00	(NS)	1.11	SO
D8-120-112-90	1.03	NS	1.04	NS	0.97	NS	1.04	NS
D8-120-112-0	1.03	NS	1.10	NS	1.02	NS	1.10	NS
Mean	1.11		1.17		1.02		1.03	
COV	0.073		0.175		0.099		0.108	

[1] SO: Shear-out, NS: net section tension, B: bearing.

[2] In brackets if different from test results.

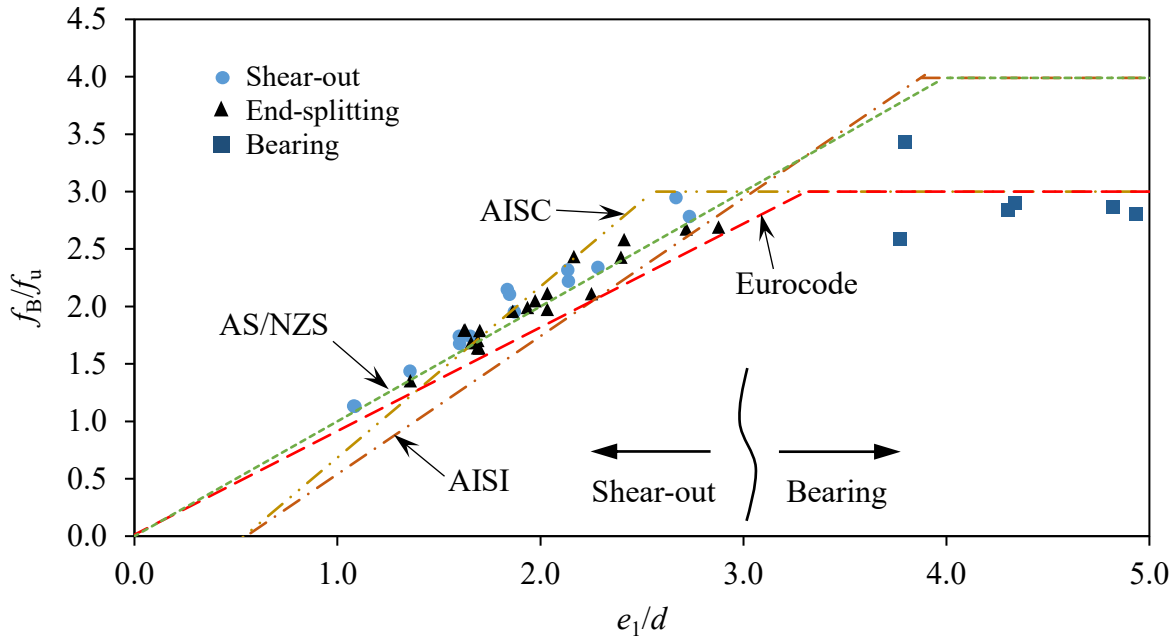


Figure 4.11: Comparison of experimental results and design equations for shear-out and bearing, where shear-out and bearing failure, as described by the considered design codes, are indicated

As shown in Table 4.4, on average the most accurate predictions are given by AISC 360 (2016), with a mean test-to-predicted capacity ratio of 1.02 and a COV of 0.099. The AISC (2016) specification was particularly accurate for the specimens undergoing net section tension failure (see Table 4.5), indicating that no in-plane shear lag factor is required for WAAM bolted connections. However, for specimens failing in shear-out, the capacity predictions were less accurate, with generally overly-conservative estimates of resistance for the specimens with

short end distance (e.g. for Specimens D8-90-26-90 and D8-90-26-90, the ultimate test loads were almost 40% greater than the predicted values) and unconservative estimates for those with relatively long end (e.g. Specimen D8-120-80-0) – see Table 4.6. These findings are consistent with those in the literature for conventional steel connections (Teh & Uz, 2015).

Table 4.5: Assessment of design methods for net section tension failure

Specimen	$\frac{P_u}{P_{NS,EC3}}$	$\frac{P_u}{P_{NS,AISI}}$	$\frac{P_u}{P_{NS,AISC}}$	$\frac{P_u}{P_{NS,AS/NZS}}$
D3-35-27-90	1.07	1.13	1.07	1.13
D3-35-27-0	0.96	1.01	0.96	1.01
D3-45-27-90	1.04	1.12	1.04	1.12
D3-45-27-0	0.98	1.05	0.98	1.05
D3-45-36-90	1.02	1.09	1.02	1.09
D3-45-36-0	0.98	1.05	0.98	1.05
D3-85-57.2-90	0.92	1.00	0.92	1.00
D8-45-44.2-90	1.09	1.14	1.09	1.14
D8-45-44.2-0	1.08	1.14	1.08	1.14
D8-55-44.2-90	1.06	1.12	1.06	1.12
D8-55-44.2-0	1.11	1.17	1.11	1.17
D8-75-44.2-90	0.98	1.05	0.98	1.05
D8-75-44.2-0	1.02	1.09	1.02	1.09
D8-90-52-90	0.91	0.99	0.91	0.99
D8-90-65-90	1.03	1.11	1.03	1.11
D8-90-65-0	1.04	1.13	1.04	1.13
D8-90-91-90	1.03	1.11	1.03	1.11
D8-90-91-0	1.05	1.13	1.05	1.13
D8-120-80-90	0.98	1.06	0.98	1.06
D8-120-112-90	0.97	1.04	0.97	1.04
D8-120-112-0	1.02	1.10	1.02	1.10
Mean	1.02	1.09	1.02	1.09
COV	0.052	0.047	0.052	0.047

Table 4.6: Assessment of design methods for shear-out failure

Specimen	$\frac{P_u}{P_{SO,EC3}}$	$\frac{P_u}{P_{SO,AISI}}$	$\frac{P_u}{P_{SO,AISC}}$	$\frac{P_u}{P_{SO,AS/NZS}}$	$\frac{P_u}{P_{SO,Teh}}$
D3-65-21.6-90	1.18	1.49	1.19	1.06	1.02
D3-65-36-90	1.14	1.13	0.90	1.02	0.95
D3-85-33-90	1.15	1.31	1.05	1.05	0.99
D3-105-37.4-90	1.15	1.23	0.99	1.04	0.97
D8-80-44.2-90	1.25	1.35	1.08	1.14	1.06
D8-80-44.2-0	1.26	1.38	1.10	1.17	1.09
D8-90-26-90	1.12	1.73	1.38	1.04	1.04
D8-90-26-0	1.13	1.74	1.39	1.05	1.05
D8-120-48-90	1.15	1.35	1.08	1.09	1.02
D8-120-48-0	1.11	1.30	1.04	1.05	0.98
D8-120-64-90	1.15	1.20	0.96	1.09	1.00
D8-120-64-0	1.10	1.15	0.92	1.04	0.95
D8-120-80-0	1.18	1.15	0.92	1.11	1.01
Mean	1.16	1.35	1.08	1.07	1.01
COV	0.042	0.149	0.149	0.041	0.042

Among the major design specifications, Eurocode 3 (1-8, 2021) yielded the smallest COV value of 0.073 for all the tested specimens (see Table 4.4), with a reasonable mean test-to-predicted capacity ratio of 1.11. However, the code significantly underestimated the strength of specimens failing in shear-out, as evident from Table 4.6. For Specimens D8-80-44.2-90 and D8-80-44.2-90, the tested strengths were at least 25% higher than the predicted values. Even for the narrower Specimen D8-75-44.2-0, which actually failed in net section tension, the tested strength was over 20% higher than the predicted shear-out strength (see Table 4.4).

As shown in Table 4.4, overall, AS/NZS 4600 (2018) yielded comparable accuracy to AISC 360 (2016), with a mean test-to-predicted capacity ratio of 1.03 and a COV of 0.108. However, the cold-formed steel standard (AISI S100, 2016) severely overestimated the capacities of WAAM specimens failing in bearing, by 37% on average (see Table 4.7 – 1/0.73 = 1.37). The optimistic bearing resistance predictions are "offset" by the conservatism in the predictions for shear-out failure, with the bearing failure specimens D3-145-91-0 and D3-145-91-90 deemed by AS/NZS 4600 (2018) to fail in shear-out (see Tables 4.4 and 4.7).

Table 4.7: Assessment of design methods for bearing failure

Specimen	$\frac{P_u}{P_{B,EC3}}$	$\frac{P_u}{P_{B,AISI}}$	$\frac{P_u}{P_{B,AISC}}$	$\frac{P_u}{P_{B,AS/NZS}}$
D3-145-91-90	1.14	0.86	1.14	0.86
D3-145-91-0	0.86	0.65	0.86	0.65
D3-145-104-90	0.97	0.73	0.97	0.73
D3-145-104-0	0.95	0.71	0.95	0.71
D3-145-117-90	0.94	0.70	0.94	0.70
D3-145-117-0	0.96	0.72	0.96	0.72
Mean	0.97	0.73	0.97	0.73
COV	0.095	0.096	0.095	0.096

The contrast between the optimistic predictions for bearing strengths and the conservative predictions for shear-out strengths is even more stark for the North American cold-formed steel specification AISI S100 (2016). While the specification also overestimates the bearing strength of the WAAM specimens by 37% on average as it uses the same bearing strength equation as AS/NZS 4600 (2018), the actual shear-out strengths of Specimens D8-90-26-90 and D8-90-26-90 were over 70% higher than the predicted values. As shown in Table 4.6, on average the actual shear-out strengths were 35% higher than the predictions of the AISI S100 (2016) specification.

While the net section tension strengths were accurately predicted by the AISC (2016) and Eurocode (1-8, 2021) standards, with some conservatism by the AISI (2016) and AS/NZS (2018) standards (see Table 4.5), the shear-out strengths were often significantly underestimated, as evident from Table 4.6. In light of this, the accuracy of Equation (3.13), which uses the active shear plane and accounts for catenary action (Xing et al., 2020b), was also assessed, giving a mean test-to-predicted capacity ratio of 1.01 and a COV of 0.042 – see Table 4.6.

Although a number of test specimens failed in end-splitting, no design codes currently account for this failure mode, which is mostly predicted as shear-out failure. It is anticipated that since the shear-out capacity increases linearly with the end distance e_1 (see Figure 4.11), and since the specimens failing by end-spitting were found to follow a similar trend, end-splitting capacities could be predicted using the equations for shear-out. In Table 4.8, comparisons between the capacities of the test specimens failing in end-splitting and predictions yielded

using Equation (3.13) are presented, with a mean test-to-predicted capacity ratio of 0.96 and a COV of 0.056. The best overall result is given by Equation (3.10) of AS/NZS 4600 (2018), with a mean test-to-predicted capacity ratio of 1.02 and a COV of 0.053.

Table 4.8: Assessment of design methods for end-splitting failure using shear-out equations

Specimen	$\frac{P_u}{P_{SO,EC3}}$	$\frac{P_u}{P_{SO,AISI}}$	$\frac{P_u}{P_{SO,AISC}}$	$\frac{P_u}{P_{SO,AS/NZS}}$	$\frac{P_u}{P_{SO,Teh}}$
D3-55-27-90	1.14	1.26	1.01	1.01	0.95
D3-55-27-0	1.10	1.22	0.97	0.97	0.92
D3-65-21.6-0	1.11	1.40	1.12	1.00	0.96
D3-65-27-90	1.17	1.30	1.04	1.05	0.99
D3-65-27-0	1.08	1.20	0.96	0.96	0.91
D3-65-32.4-90	1.16	1.19	0.95	1.04	0.96
D3-65-32.4-0	1.08	1.11	0.89	0.97	0.90
D3-65-36-0	1.04	1.04	0.83	0.94	0.87
D3-85-33-0	1.11	1.26	1.01	1.01	0.95
D3-85-57.2-0	1.02	0.96	0.77	0.94	0.86
D3-105-37.4-0	1.16	1.21	0.97	1.03	0.96
D3-105-39.6-90	1.15	1.20	0.96	1.04	0.97
D3-105-39.6-0	1.20	1.26	1.01	1.05	0.99
D3-105-48.4-90	1.19	1.16	0.93	1.07	0.99
D3-105-48.4-0	1.14	1.10	0.88	1.01	0.94
D8-90-39-90	1.19	1.37	1.10	1.10	1.04
D8-90-39-0	1.19	1.38	1.10	1.10	1.04
D8-90-52-0	1.22	1.25	1.00	1.12	1.04
Mean	1.14	1.22	0.97	1.02	0.96
COV	0.050	0.094	0.094	0.053	0.056

4.6. Comparisons with WAAM lap connections in single shear

In this section, the findings from the present chapter on WAAM lap shear connections in double shear are compared to those from Chapter 3 on equivalent connections in single shear.

Note that, for the bearing capacity predictions, a noteworthy difference between the major design specifications is that, in AISC 360 (2016), no distinction is made between single and double shear connections, while in Eurocode 3 (1-8, 2021), AISI S100 (2016) and AS/NZS 4600 (2018), different values of the modification factor are used to account for the two different configurations (e.g. in AISI S100, $m_f = 0.75$ for single shear and $m_f = 1.33$ for double-shear connections). In Chapter 3, WAAM lap specimens of the same dimensions as the ones examined herein but subjected to single shear were tested; their capacities P_u are compared against the capacities of the corresponding double-shear specimens in Table 4.9.

Table 4.9: Comparisons between the single and double shear capacities

Single shear lap tests		Double shear lap tests		$\frac{P_{u,S}}{t_S} \Big/ \frac{P_{u,D}}{t_D}$ [1]
Specimens	FM	Specimens	FM	
S3-55-27-90	LT	D3-55-27-90	ES	1.08
S3-55-27-0	LT	D3-55-27-0	ES	1.13
S3-45-27-90	NS/LT	D3-45-27-90	NS	0.91
S3-45-27-0	NS/LT	D3-45-27-0	NS	0.93
S3-45-36-90	NS/LT	D3-45-36-90	NS	0.93
S3-45-36-0	NS/LT	D3-45-36-0	NS	0.91
S3-35-27-90	NS	D3-35-27-90	NS	0.93
S3-35-27-0	NS	D3-35-27-0	NS	1.04
S3-65-21.6-90	SO	D3-65-21.6-90	SO	1.00
S3-65-21.6-0	SO	D3-65-21.6-0	ES	1.01
S3-65-27-90	LT	D3-65-27-90	ES	1.14
S3-65-27-0	SO	D3-65-27-0	ES	1.11
S3-65-32.4-90	LT	D3-65-32.4-90	ES	0.96
S3-65-32.4-0	LT	D3-65-32.4-0	ES	0.98
S3-65-36-90	LT	D3-65-36-90	SO	0.84
S3-65-36-0	LT	D3-65-36-0	ES	0.90
S3-85-33-90	LT	D3-85-33-90	SO	0.96
S3-85-33-0	LT	D3-85-33-0	ES	1.05
S3-105-39.6-90	LT	D3-105-39.6-90	ES	0.98
S3-105-39.6-0	LT	D3-105-39.6-0	ES	0.94
		Mean		0.99
		COV		0.083
S3-145-104-90	CB	D3-145-104-90	B	0.64
S3-145-104-0	CB	D3-145-104-0	B	0.61
		Mean		0.63
		COV		0.036

[1] $P_{u,S}$: ultimate load of single shear tests; $P_{u,D}$: ultimate load of double shear tests; t_S: measured thickness in single shear tests; t_D: measured thickness in double shear tests

Since curling was restricted for the inner plates of the double-shear connections, localised tearing and curl-bearing failures were eliminated from the present specimens. However, no statistically significant differences were observed between the single and the double-shear capacities except for the single shear specimens failing by curl-bearing vis-a-vis the double-shear counterparts, for which the average single-to-double shear capacity ratio was 0.63. A curl-bearing strength equation was proposed for single-shear bolted connections in Chapter 3.

4.7. Conclusions

Sixty tests on WAAM steel double-lap shear bolted connections of two nominal thicknesses and print layer orientations were carried out, proportioned to trigger different failure modes such as shear-out, net section tension, bearing and end-splitting. The load-deformation responses and observed failure modes were presented and analysed. The print layer orientation was found to have an insignificant effect on the ultimate capacities of the examined double-lap specimens, consistent with the findings for single-lap specimens in Chapter 3. However, the specimens with print layers parallel to the loading direction were more likely to fail by end-splitting.

The test results were used to evaluate the applicability of equations currently used for conventional steel lap connections in design standards, namely Eurocode 3 (1-8, 2021) and AISC 360 (2016) for structural steel and AISI S100 (2016) and AS/NZS 4600 (2018) for cold-formed steel. The net section tension and bearing failure capacity predictions obtained using the structural steel specifications (EN 1993-1-8, 2021; AISC 360, 2016) were more accurate than those determined using the cold-formed steel specifications (AISI S100, 2016; AS/NZS 4600, 2018) (by 7% and 24% respectively).

Shear-out strengths were often overestimated by all specifications. Depending on the end distance, the tested shear-out strengths were higher than the specifications' estimates by up to 26%, 73%, 39% and 17% for Eurocode 3(1-8, 2021), AISI S100 (2016), AISC 360 (2016) and AS/NZS 4600 (2018), respectively. The shear-out strengths were accurately predicted using an equation found in the literature (Xing et al., 2020b), which makes use of the active shear plane in conjunction with the catenary effect.

Interestingly, the end-splitting failure loads could be predicted accurately using the shear-out equation of AS/NZS 4600 (2018), where the end distance is measured from the centre of the

bolt hole. This outcome indicates that the active shear plane has no role in determining the end-splitting strength.

Overall, the structural steel specifications (EN 1993-1-8, 2021; AISC 360, 2016) were found to provide more accurate predictions than the cold-formed steel specifications (AISI S100, 2016; AS/NZS 4600, 2018); this may relate to the ductility of the WAAM steel material being closer to that of the structural (hot-rolled) steel than cold-formed steel.

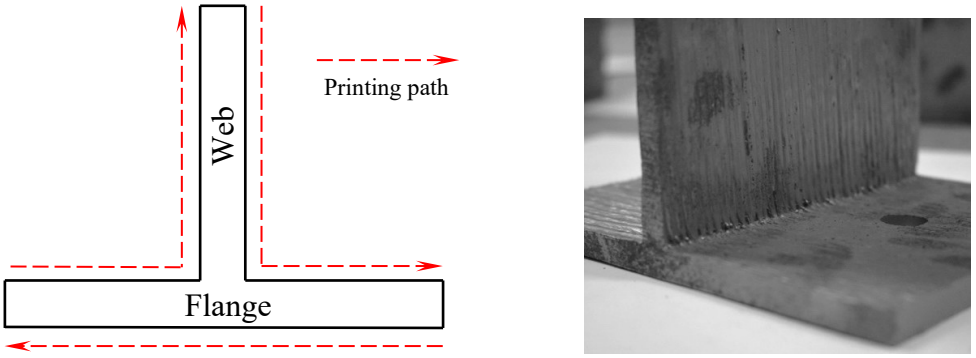
5. WAAM T-Stub Bolted Connections

5.1. Introduction

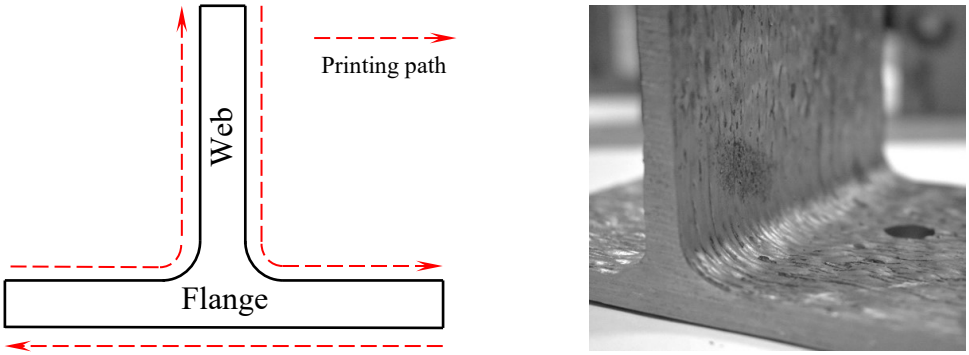
This chapter presents experiments on 52 WAAM T-stubs with two bolts in a row and 28 WAAM T-stubs with four bolts in a row. Advanced experimental techniques, featuring 3D laser scanning and digital image correlation (DIC), have been used to create three-dimensional models of all specimens and to monitor the deformations that developed during testing, respectively. The test results are compared against the design predictions of Eurocode 3 Part 1.8 (EN 1993-1-8, 2021), as well as against the predictions yielded by a method proposed in (Demonceau et al., 2010; Latour et al., 2014) for T-stubs with four bolts in a row. The key findings are presented and discussed.

5.2. Manufacturing and T-stub specimen geometry

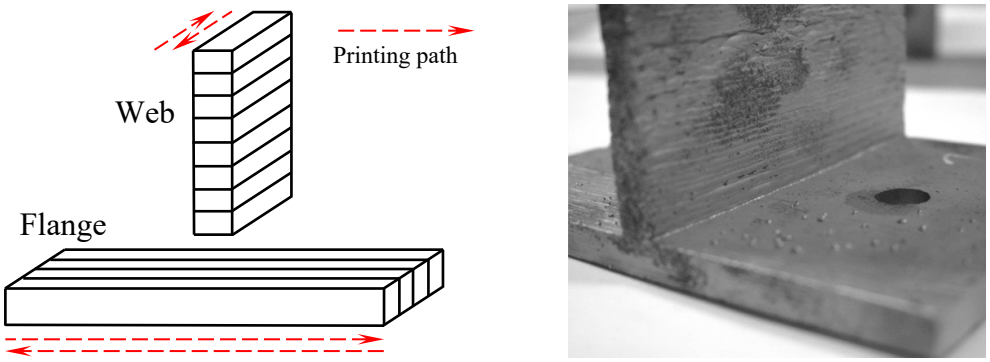
All specimens were manufactured by the Dutch company MX3D (2021), using their multi-axis robotic WAAM technology (2021). The welding wire used for the fabrication of all specimens was ER70S-6 (EN ISO 14341-A G 42 4 M21 3Si1), the chemical composition and mechanical properties of which are given in Tables 3.1 and 3.2 respectively in Chapter 3. All specimens were printed on a 300×300×20 mm S235 steel base plate. The adopted printing parameters are reported in Table 3.3. Figure 5.1 illustrates the different printing strategies that were employed for the examined specimens. Some specimens were printed continuously, as shown in Figure 5.1(a) and (b), while others were printed in two stages, with the flange printed first and the web printed second, directly on the flange – see Figure 5.1(c) and (d). Finally, specimens with both sharp and rounded corners were manufactured – see Figure 5.1. Note that approximately the same amount of time was required for the implementation of the four different printing strategies.



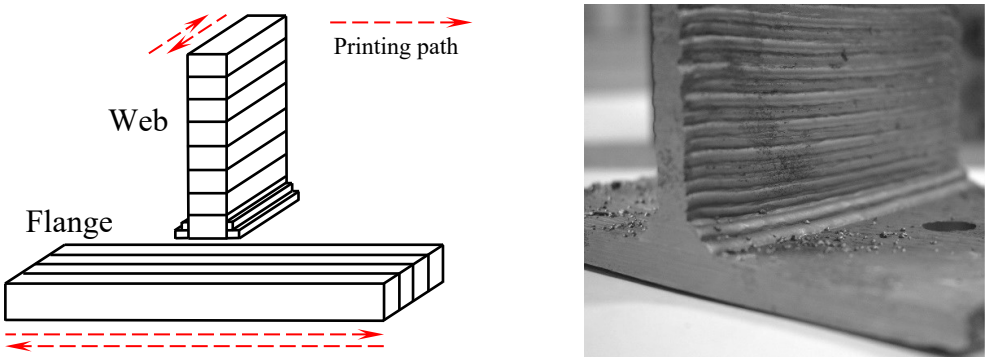
(a) Sharp corners, flanges and web continuously printed



(b) Rounded corners, flanges and web continuously printed



(c) Sharp corners, flanges and web individually printed



(d) Rounded (stepped) corners, flanges and web individually printed

Figure 5.1. Different printing strategies

All T-stubs were first sandblasted to remove any slag or soot from the welding process and then laser scanned using a FARO Design ScanArm 2.0 laser scanner, with a scan rate of 600,000 points/second and an accuracy of 0.075 mm (Faro, 2018). The digital models of all specimens were processed in the software Geomagic Wrap (2017) and then exported as STL files for the determination of their geometric properties.

The examined specimens were of two different geometric configurations; these are shown in Figure 5.2, where t is the thickness of the flanges, d_0 is the bolt hole diameter, m is the distance between the web-to-flange junction and the bolt line (defined as the line across the bolt hole centres parallel to the web) and b is the length of the flange parallel to the web. For the T-stubs with two bolts, e is the distance between the centre of the bolt hole and the tip of the flange, while for the T-stubs with four bolts in a row, e_1 is the distance between the centres of the two bolt holes and e_2 is the distance from the centre of the outer bolt hole to the tip of the flange. Finally, the length of the transition between the web and the flange is denoted as a for the specimens with rounded corners – see Figures 5.2(a) and (b).

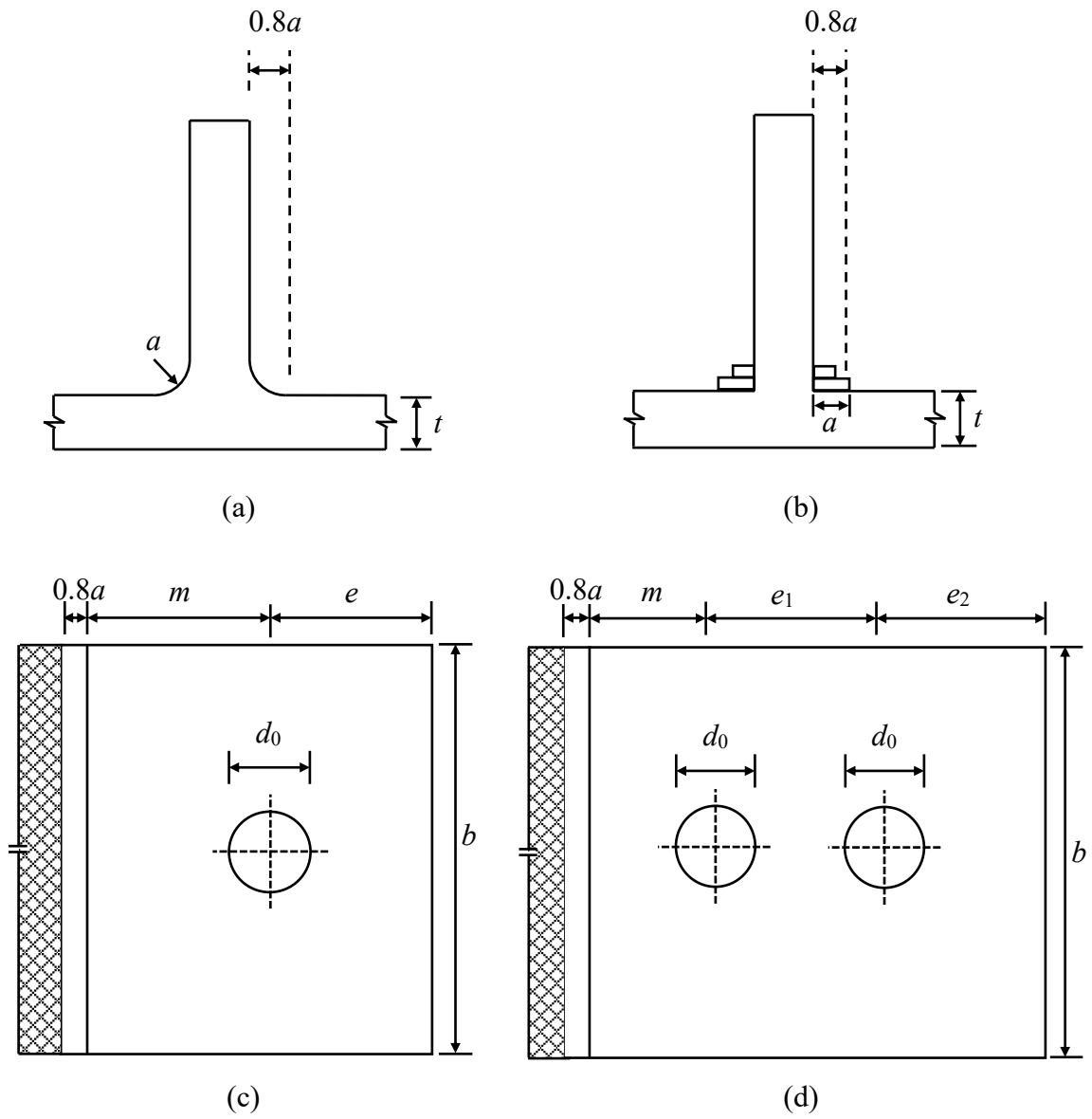


Figure 5.2. Geometrical configuration of different types of T-stub specimens: (a) continuously printed with rounded corners, (b) with web and flange individually printed with rounded (stepped) corners, (c) with two bolts in a row and (d) with four bolts in a row

The adopted specimen labelling system starts with "T1" or "T2" for the T-stubs with one or two bolts per flange outstand respectively, followed by the length of the flange parallel to the web b in mm, the non-dimensional ratio λ ($\lambda = e/m$ for T-stubs with two bolts and $\lambda = (e_1+e_2)/m$ for T-stubs with four bolts in a row), the letter "C" or "I" for the T-stubs with their flanges and web printed continuously or individually respectively – see Figure 5.1, and, finally, the letter "R" or "S" for the T-stubs with rounded or sharp corners respectively. For example, Specimen

T1-40-0.67-C-R is a continuously printed T-stub with rounded corners, one bolt per flange outstand (i.e. 2 in total), a flange length of 40 mm and a λ ratio of 0.67.

The dimensions of all specimens were measured using Vernier callipers and radius gauges, while the average thickness of the flanges, which, due to the surface undulations of the WAAM surface, could not be effectively measured using conventional tools, were determined in Rhino 3D (2017) using the laser scan data, as described in (Kyvelou et al., 2020). A summary of the dimensions of the T-stubs are presented in Tables 5.1 and 5.2 for the specimens with two and four bolts in a row, respectively.

Table 5.1. Measured geometric properties of T-stubs with two bolts in a row

Specimen	Bolt grade	t (mm)	b (mm)	m (mm)	e (mm)
T1-40-0.67-C-R	8.8	8.3	40.7	21.1	20.8
T1-40-0.67-I-R	8.8	9.3	41.1	24.5	20.4
T1-40-0.67-C-S	8.8	8.0	41.0	29.8	20.3
T1-40-0.67-I-S	8.8	9.1	39.5	29.2	20.9
T1-40-2.00-C-R	8.8	8.6	41.7	11.1	40.3
T1-40-2.00-I-R	8.8	9.1	41.0	14.5	40.9
T1-40-2.00-C-S	8.8	8.0	40.2	19.9	40.2
T1-40-2.00-I-S	8.8	8.7	41.8	19.4	40.8
T1-60-0.40-C-R	8.8	8.4	60.5	41.2	20.8
T1-60-0.40-I-R	8.8	8.8	60.0	44.5	20.8
T1-60-0.40-C-S	8.8	8.0	59.5	50.0	20.1
T1-60-0.40-I-S	8.8	8.9	59.1	49.3	20.4
T1-60-0.67-C-R	8.8	8.4	60.5	21.3	20.7
T1-60-0.67-I-R	8.8	8.8	59.7	24.6	21.1
T1-60-0.67-C-S	8.8	8.1	60.9	29.9	20.0
T1-60-0.67-I-S	8.8	8.9	61.1	29.3	20.5
T1-70-0.50-C-R	8.8	8.6	69.2	31.2	20.9
T1-70-0.50-I-R	8.8	8.8	69.8	34.4	20.3
T1-70-0.50-C-S	8.8	8.2	70.1	39.8	20.5
T1-70-0.50-I-S	8.8	8.9	69.8	39.3	21.1
T1-70-0.67-C-R	8.8	8.5	69.6	21.4	20.5
T1-70-0.67-I-R	8.8	8.9	69.0	25.3	21.1
T1-70-0.67-C-S	8.8	8.1	70.0	29.8	20.4
T1-70-0.67-I-S	8.8	9.0	73.0	29.4	20.9
T1-90-0.33-C-R	8.8	7.9	95.7	18.9	11.4
T1-90-0.33-I-R	8.8	8.9	92.1	24.1	11.0
T1-90-0.33-C-S	8.8	8.1	91.1	28.6	11.4
T1-90-0.33-I-S	8.8	8.8	93.4	28.7	11.3
T1-90-0.67-C-R	8.8	8.6	93.9	21.6	23.5

T1-90-0.67-I-R	8.8	8.8	92.4	26.0	22.3
T1-90-0.67-C-S	8.8	8.6	102.5	29.3	22.1
T1-90-0.67-I-S	8.8	9.0	104.3	29.0	22.4
T1-120-0.67-C-R	8.8	7.8	123.6	20.5	19.0
T1-120-0.67-I-R	8.8	8.9	122.2	27.5	21.0
T1-120-0.67-C-S	8.8	8.1	119.4	30.4	19.4
T1-120-0.67-I-S	8.8	8.8	117.4	30.1	19.9
T1-120-1.33-C-R	8.8	7.6	123.0	22.7	39.1
T1-120-1.33-I-R	8.8	8.5	120.2	24.6	41.1
T1-120-1.33-C-S	8.8	7.9	121.1	30.9	39.3
T1-120-1.33-I-S	8.8	8.9	117.2	30.3	38.8
T1-150-0.67-C-R	10.9	7.9	148.1	17.3	18.1
T1-150-0.67-I-R	10.9	8.8	148.6	25.3	19.8
T1-150-0.67-C-S	10.9	7.9	153.4	30.8	19.3
T1-150-0.67-I-S	10.9	9.0	148.3	30.0	19.9
T1-160-0.67-C-R	10.9	8.0	160.5	21.7	19.2
T1-160-0.67-I-R	10.9	8.6	159.9	25.3	19.3
T1-160-0.67-C-S	10.9	8.0	158.1	30.8	19.1
T1-160-0.67-I-S	10.9	8.9	159.8	30.1	19.9
T1-160-1.50-C-R	10.9	8.7	160.1	32.6	59.4
T1-160-1.50-I-R	10.9	8.8	161.3	35.7	59.3
T1-160-1.50-C-S	10.9	8.5	161.6	41.1	58.8
T1-160-1.50-I-S	10.9	8.7	163.0	40.4	59.2

Table 5.2. Measured geometric properties of T-stubs with four bolts in a row

Specimen	Bolt grade	t (mm)	b (mm)	m (mm)	e_1 (mm)	e_2 (mm)
T2-70-1.13-C-R	8.8	8.6	70.8	30.4	35.0	10.4
T2-70-1.13-I-R	8.8	8.9	72.3	34.1	34.9	10.6
T2-70-1.13-C-S	8.8	8.0	69.3	39.6	35.1	10.5
T2-70-1.13-I-S	8.8	8.8	71.9	39.2	35.0	10.3
T2-70-1.83-C-R	8.8	8.6	69.3	20.2	30.0	25.7
T2-70-1.83-I-R	8.8	8.9	70.5	23.9	30.0	26.0
T2-70-1.83-C-S	8.8	8.0	70.8	29.9	30.0	25.3
T2-70-1.83-I-S	8.8	8.8	71.1	29.3	30.0	25.6
T2-90-1.83-C-R	8.8	8.7	89.9	22.3	30.0	24.3
T2-90-1.83-I-R	8.8	9.0	85.6	24.6	30.0	25.8
T2-90-1.83-C-S	8.8	8.7	90.4	30.4	30.0	24.5
T2-90-1.83-I-S	8.8	8.8	95.7	30.4	30.0	24.4
T2-120-2.75-C-R	8.8	8.1	119.2	12.7	30.6	24.4
T2-120-2.75-I-R	8.8	9.0	122.2	14.6	30.3	24.5
T2-120-2.75-C-S	8.8	8.2	120.3	20.6	29.9	24.5
T2-120-2.75-I-S	8.8	8.8	118.2	20.3	30.0	24.6

T2-120-1.83-C-R	8.8	8.6	122.1	20.8	30.0	25.4
T2-120-1.83-I-R	8.8	9.0	121.7	23.6	30.0	25.7
T2-120-1.83-C-S	8.8	8.0	120.7	29.4	30.0	25.3
T2-120-1.83-I-S	8.8	8.9	118.6	29.4	30.0	25.4
T2-140-1.83-C-R	10.9	8.0	139.2	19.7	30.0	24.8
T2-140-1.83-I-R	10.9	8.9	140.4	24.2	30.0	25.0
T2-140-1.83-C-S	10.9	7.8	140.5	29.4	30.0	24.6
T2-140-1.83-I-S	10.9	8.9	142.9	29.2	30.0	24.4
T2-140-2.75-C-R	10.9	8.6	142.0	9.6	30.0	25.8
T2-140-2.75-I-R	10.9	8.8	142.6	13.9	30.0	26.0
T2-140-2.75-C-S	10.9	8.2	140.7	19.8	30.0	25.6
T2-140-2.75-I-S	10.9	8.9	140.9	19.1	30.0	25.8

5.3. Test setup

All specimens were tested in pairs, with each WAAM T-stub connected to a grade S700 high-strength steel (HSS) T-stub, by means of hand-tightened M12 bolts with bolt hole clearances of 2 mm. The bolt grades, which were either 8.8 or 10.9 depending on the specimen, were selected to prevent bolt failure (i.e. Mode 3 failure). A digital image correlation (DIC) system with two pairs of cameras was employed to capture the strain fields during testing, with each camera pair monitoring the upper surface of each flange outstand. Note that despite the cameras being placed at certain angles to the flange outstands, the obtained strain and displacement data were found to be accurate, as demonstrated by comparisons between the DIC displacements and the respective displacements measured by LVDTs. Two Linear Variable Differential Transformers (LVDTs) were also installed on the two sides of each T-stub to monitor the displacements parallel to the T-stub webs. All tests were carried out using a 250 kN Instron testing machine. The tensile load was applied using displacement control at a constant rate of 0.8 mm/min, resulting in failure of the specimens within 30 minutes. An overview of the test setup is presented in Figure 5.3.

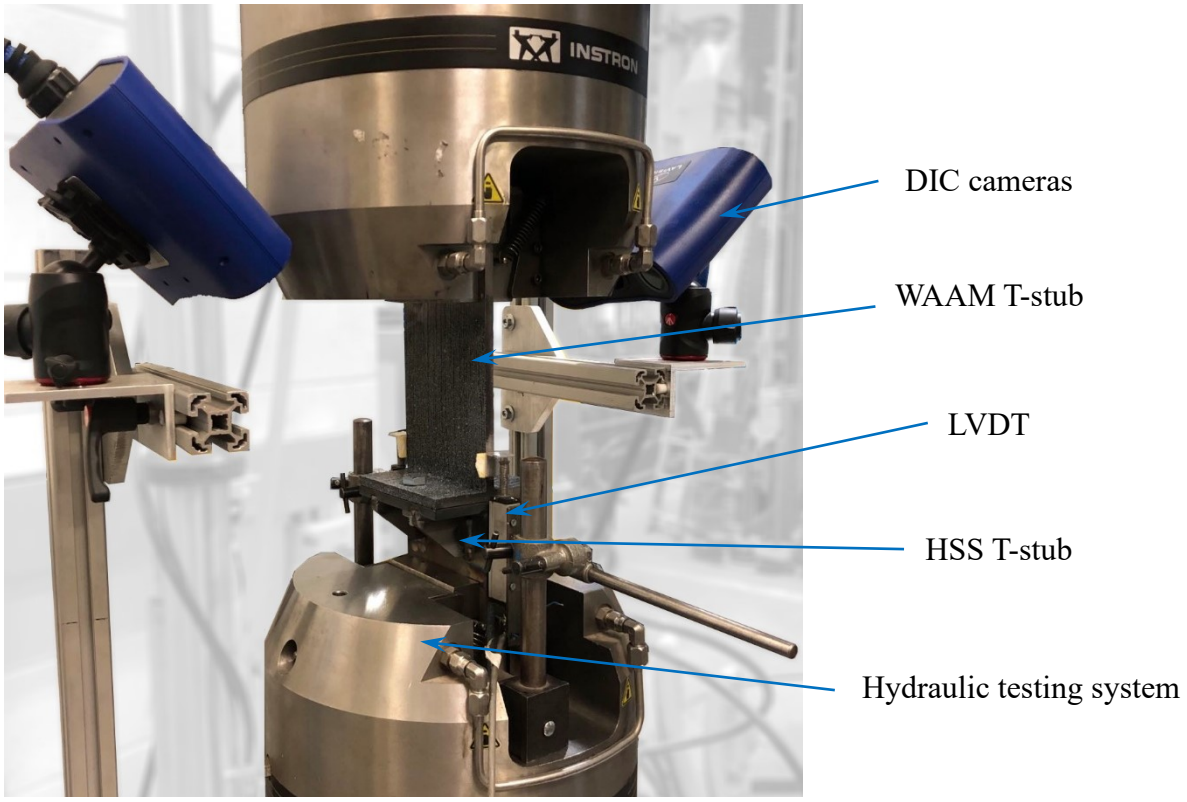


Figure 5.3. T-stub test setup

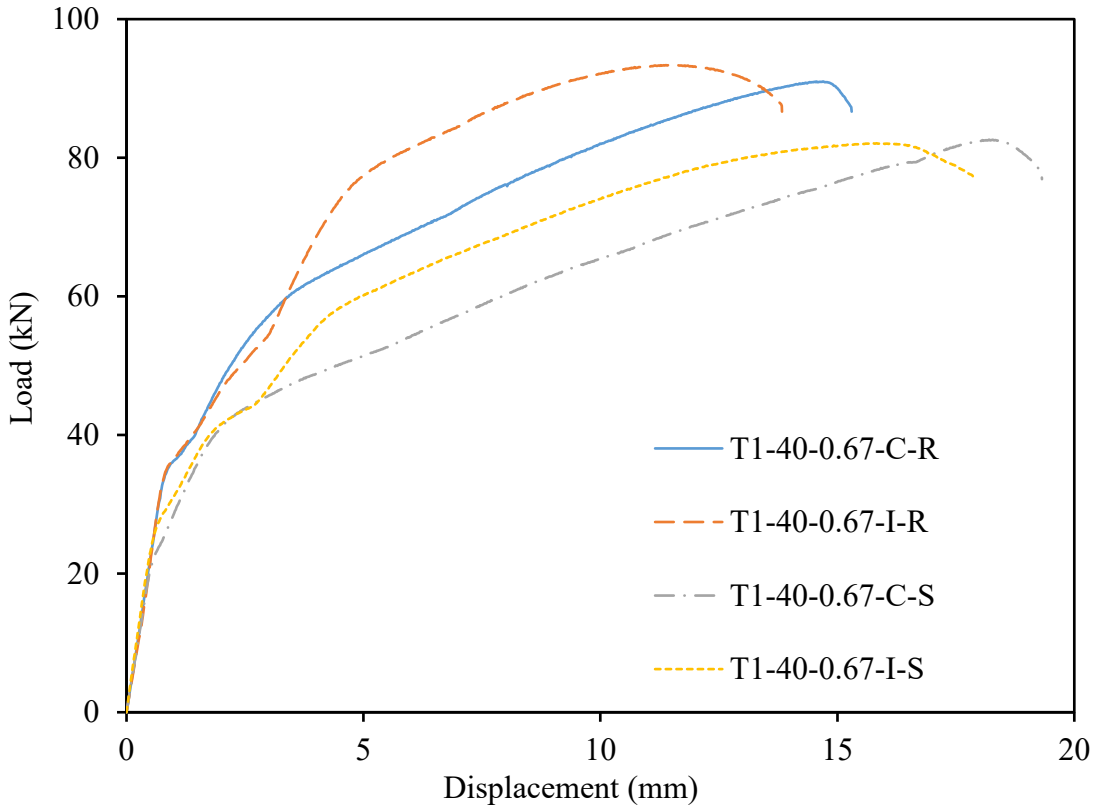
5.4. Test results

5.4.1. Load-displacement curves

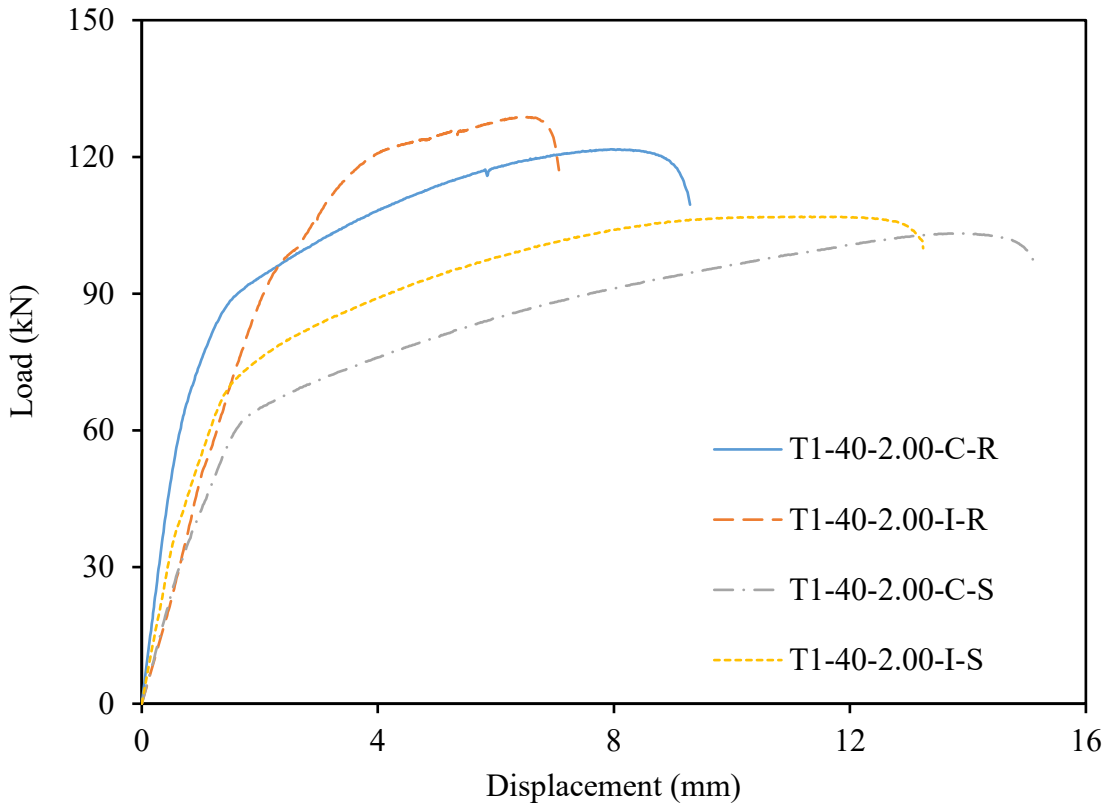
The load-displacement curves of conventionally manufactured T-stubs typically feature two stages – an elastic stage and a plastic stage, with the latter generally exhibiting a plateau followed by strain hardening; the transition point between the two stages defines the yield load of the T-stub i.e. the plastic resistance of the connection (Piluso, Faella & Rizzano, 2001; Coelho et al., 2004; Yuan et al., 2020). In some cases, a third stage, featuring a re-rise in stiffness after large deformations and referred as the "second hardening branch" (Faralli et al., 2021) occurs; this is caused by the development of membrane action in the flange outstands and bearing between the bolt shank and bolt hole (Zhao, Lee & Chiew, 2016; Yapici et al., 2021; Faralli et al., 2021).

The load-displacement curves for the WAAM T-stubs tested herein are presented in Figure 5.4, with the displacement measured on the T-stub web, 30 mm away from the web-to-flange junction. While two-stage and three-stage load-displacement curves were typical – see Figures

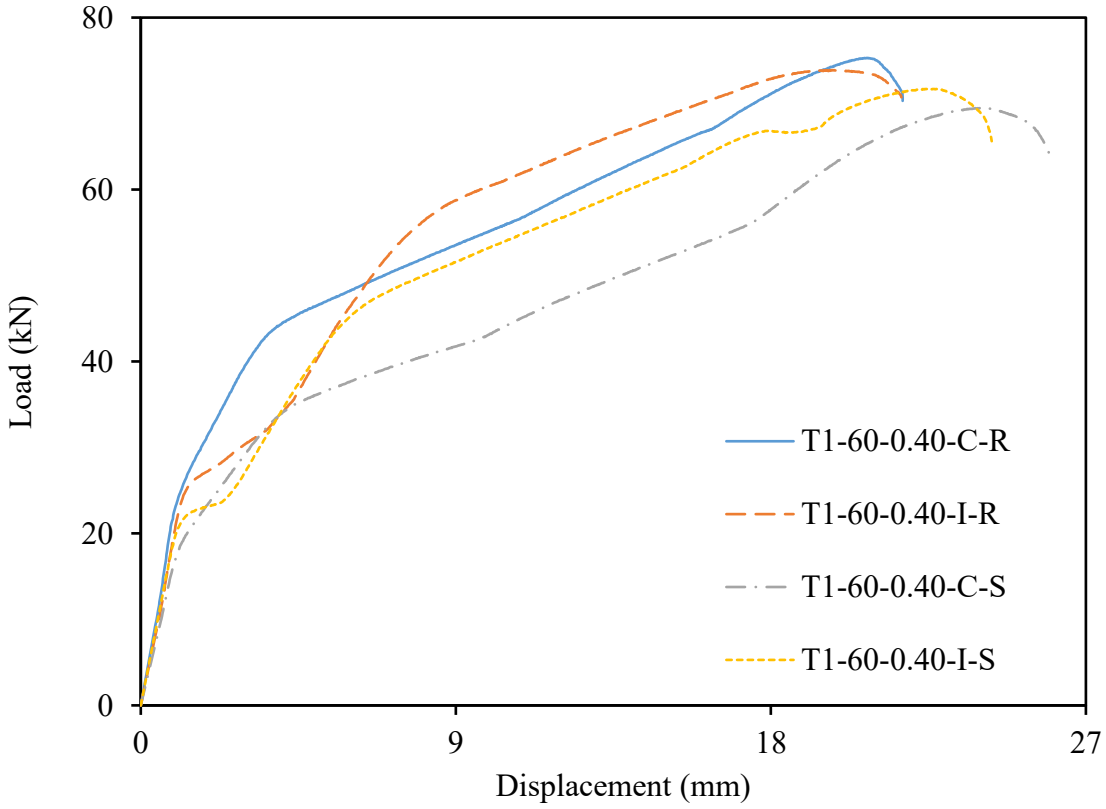
5.5(a) and (b), curves with additional 'kinks' were also evident. Preliminary FE simulations, conducted in Abaqus (2019), indicated that the additional kinks occurred due to gaps between the upper and lower T-stub flanges, caused by surface undulations inherent to the WAAM process or bowing of the WAAM T-stub flange – see Figure 5.6. As shown in Figure 5.7, increasing the gap size between the T-stub flanges in the FE simulations resulted in an increasingly prominent additional kink in the load-displacement curve. The existence of these initial gaps between the T-stub flanges caused a delay in the development of prying forces, the importance of which has been widely recognised (Zhao, He & Yan, 2021; Tartaglia, D'Aniello & Zimbru, 2020; Özkılıç, 2021; Douty & McGuire, 1965; Nair, Birkemoe & Munse, 1974; Couchaux et al., 2017). Once contact between the flanges had been established, prying forces developed, and an increase in stiffness was observed. Determination of the point of this contact was thus considered to be significant.



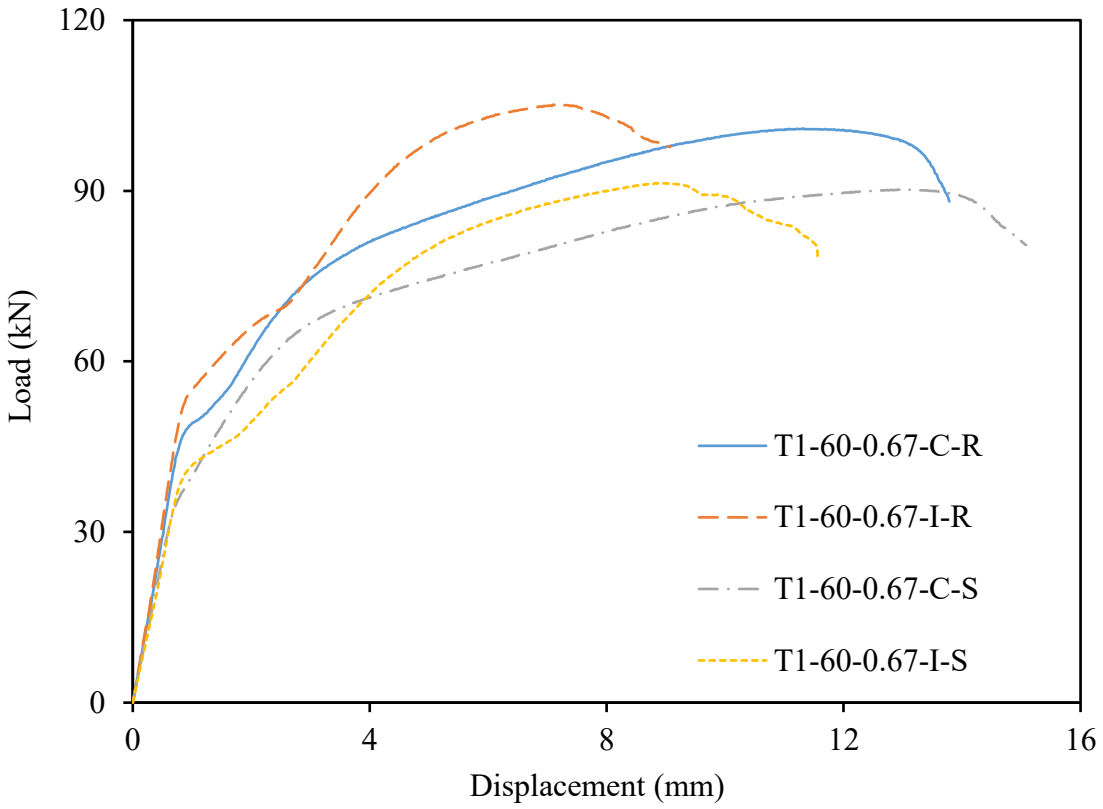
(a) T1-40-0.67



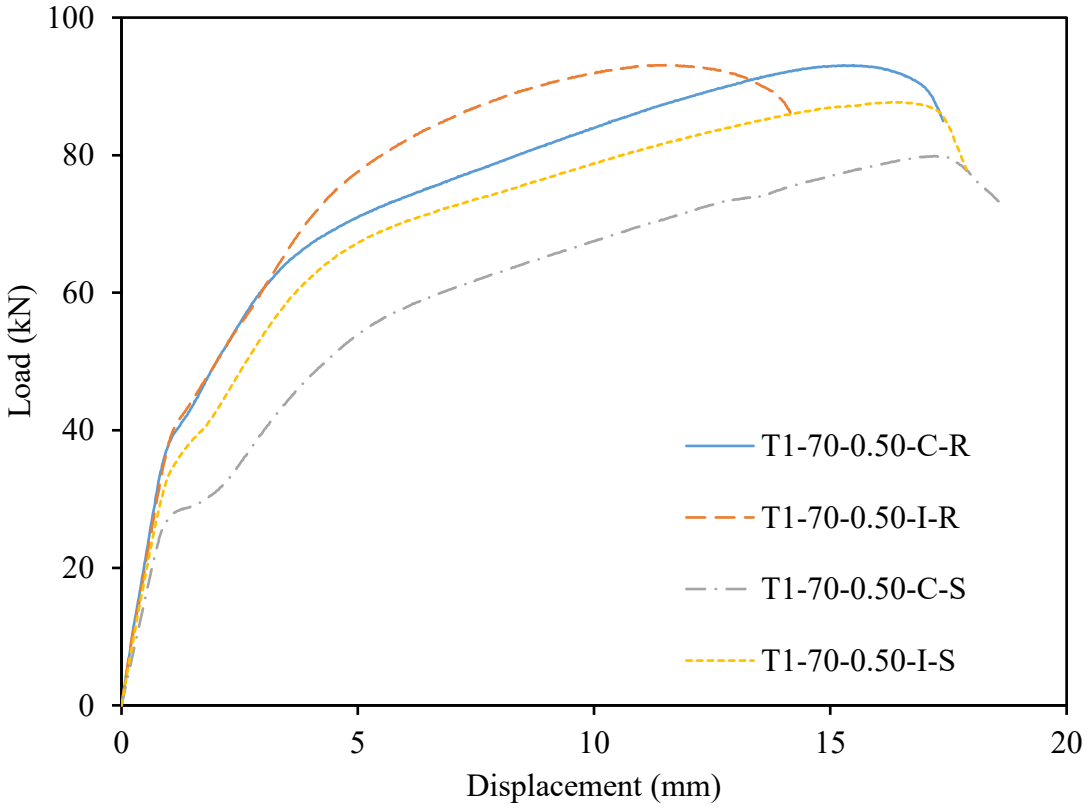
(b) T1-40-2.00



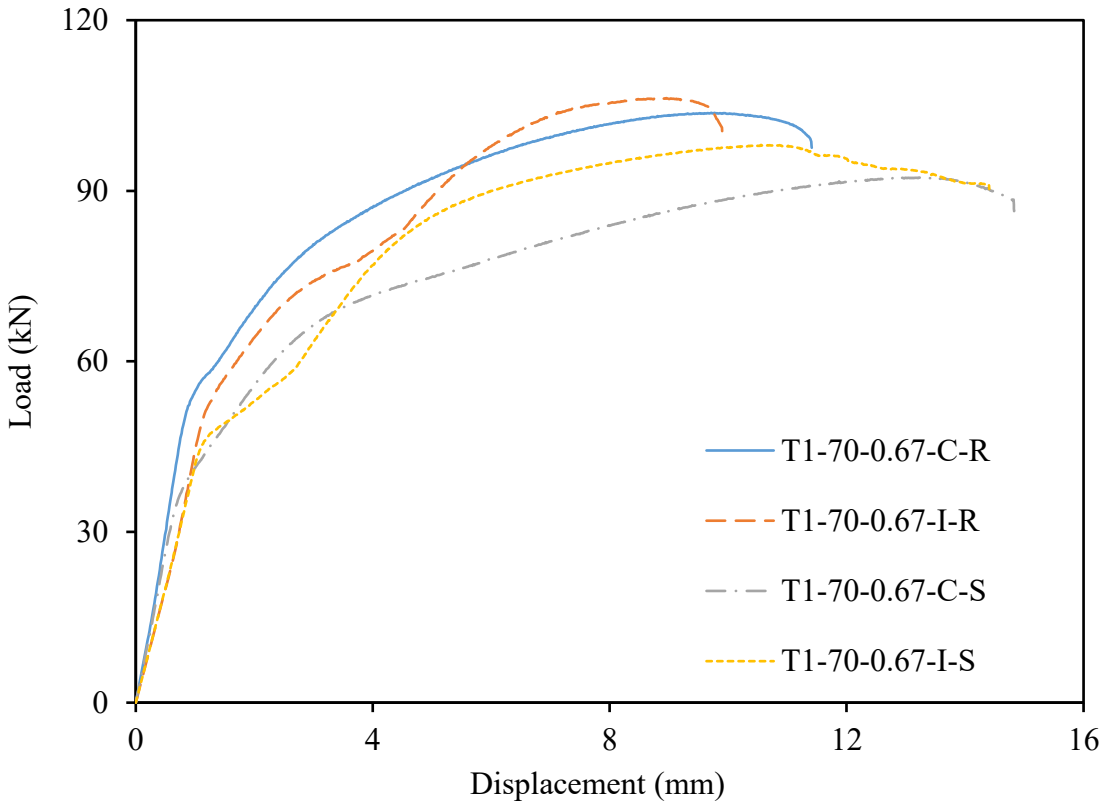
(c) T1-60-0.40



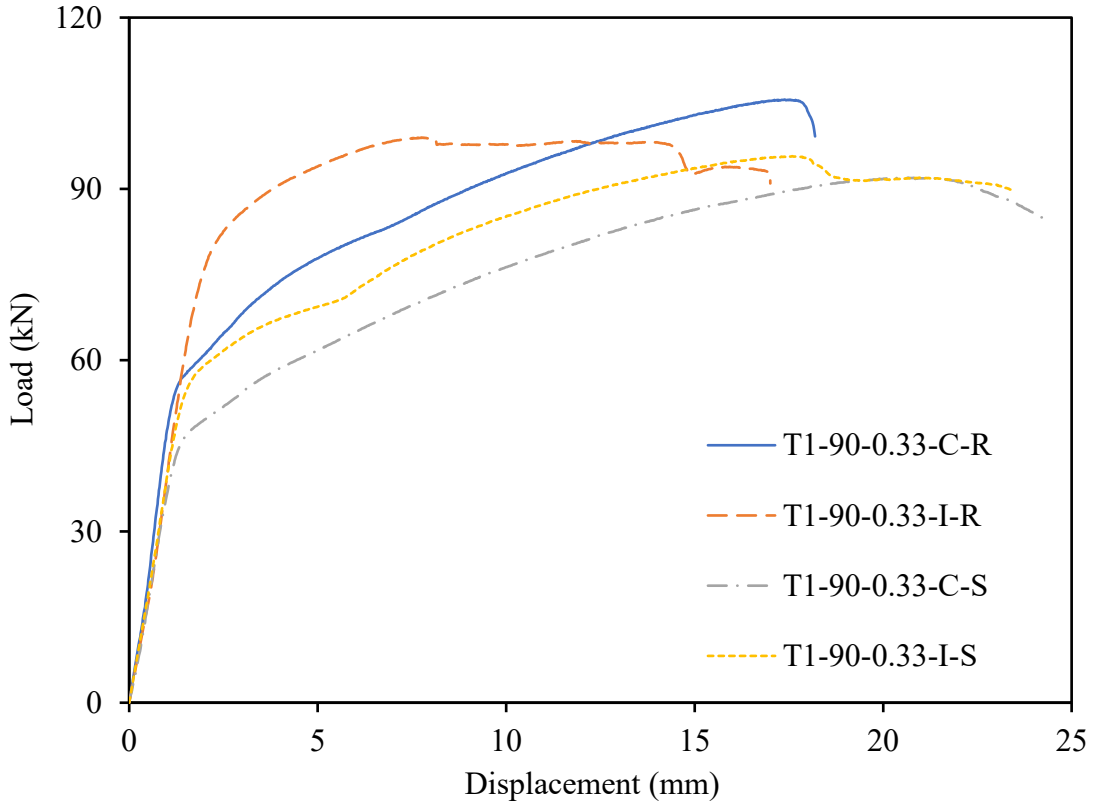
(d) T1-60-0.67



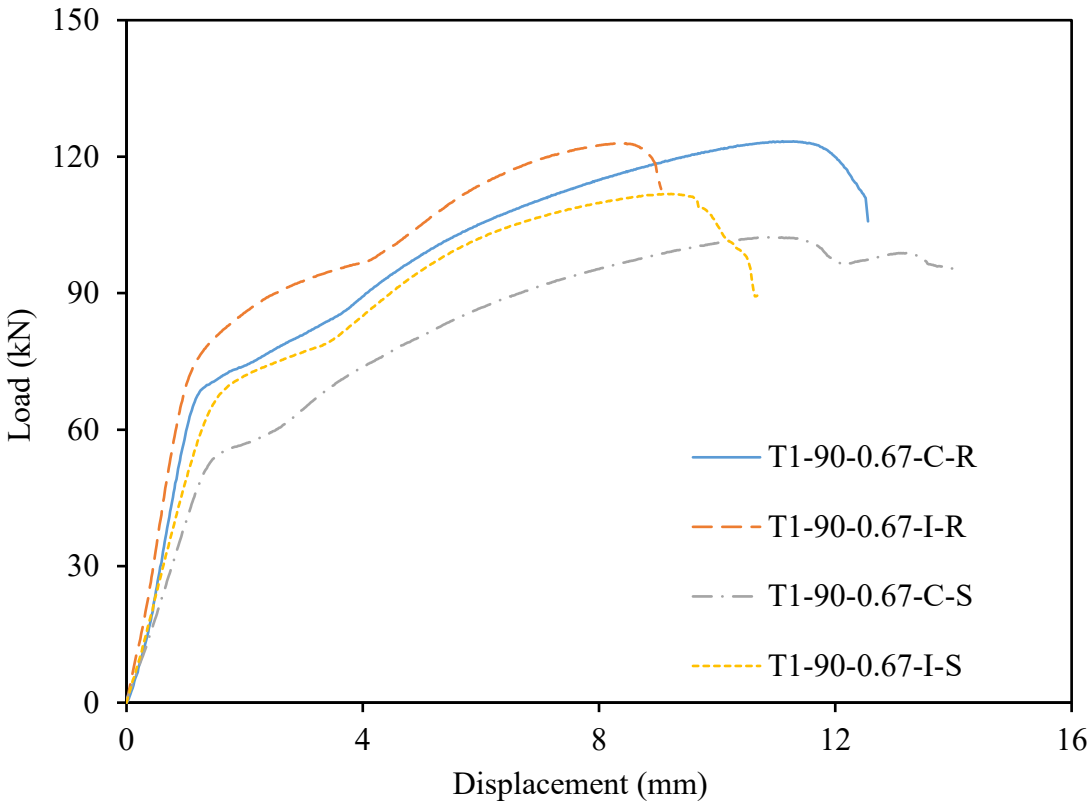
(e) T1-70-0.50



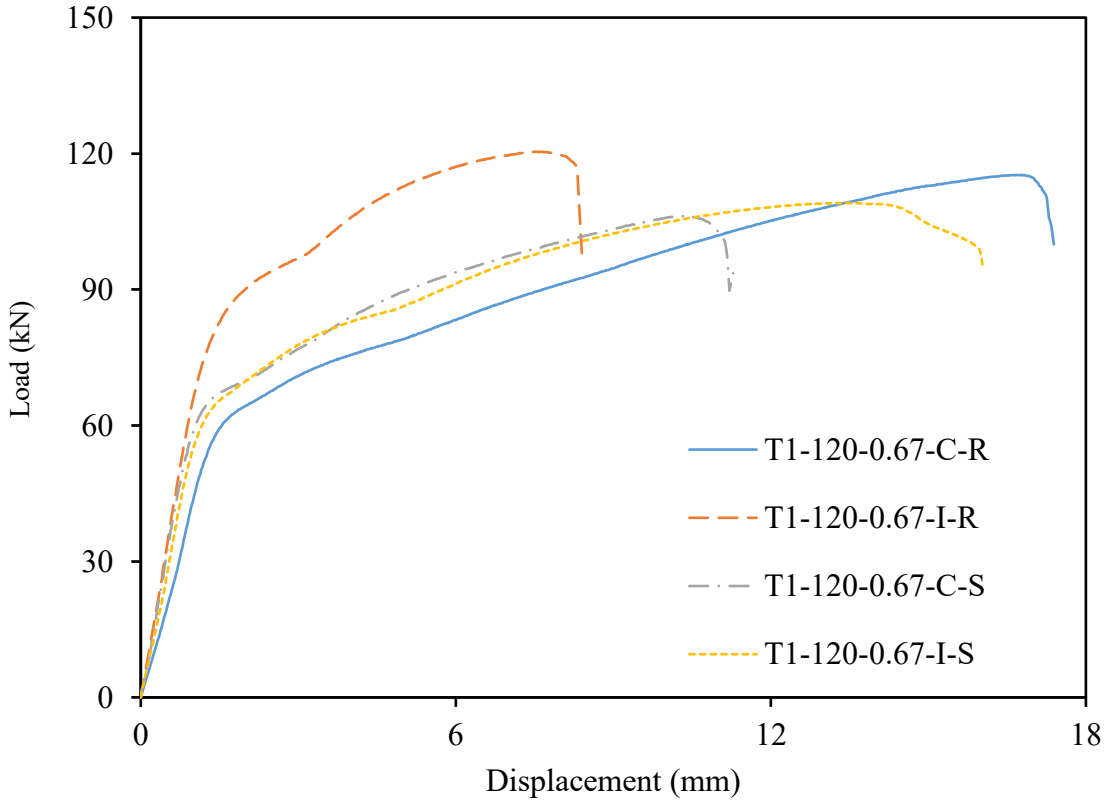
(f) T1-70-0.67



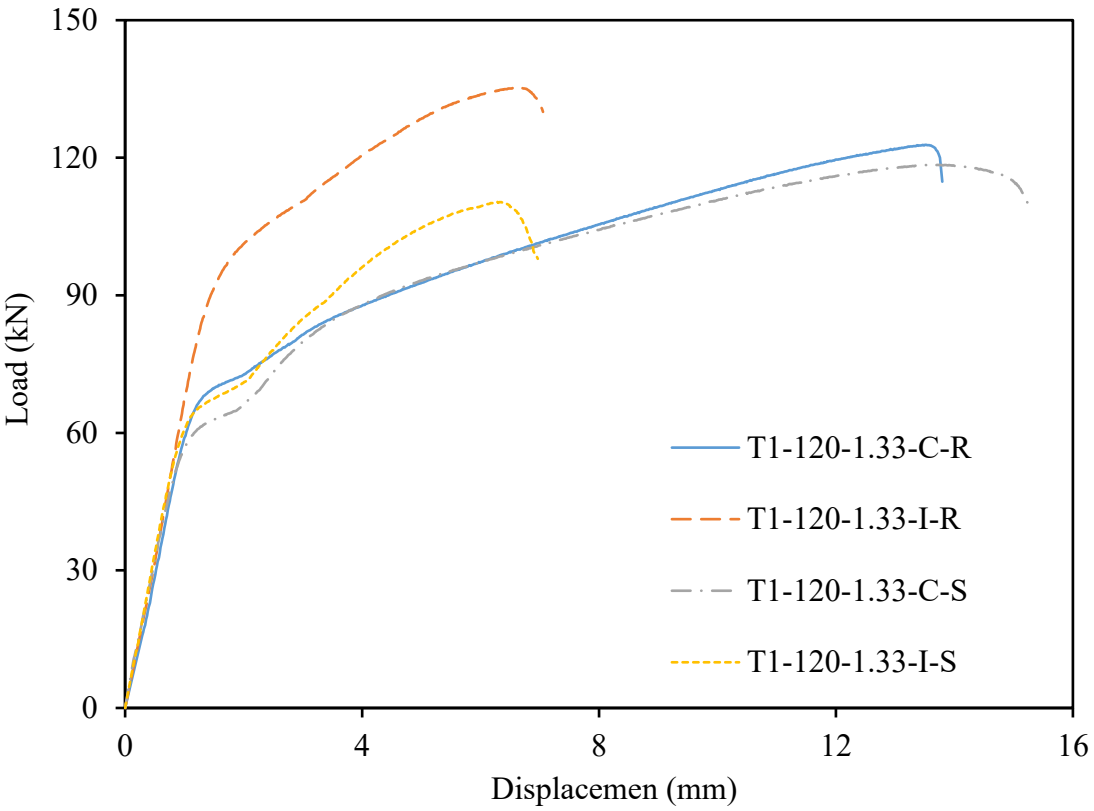
(g) T1-90-0.33



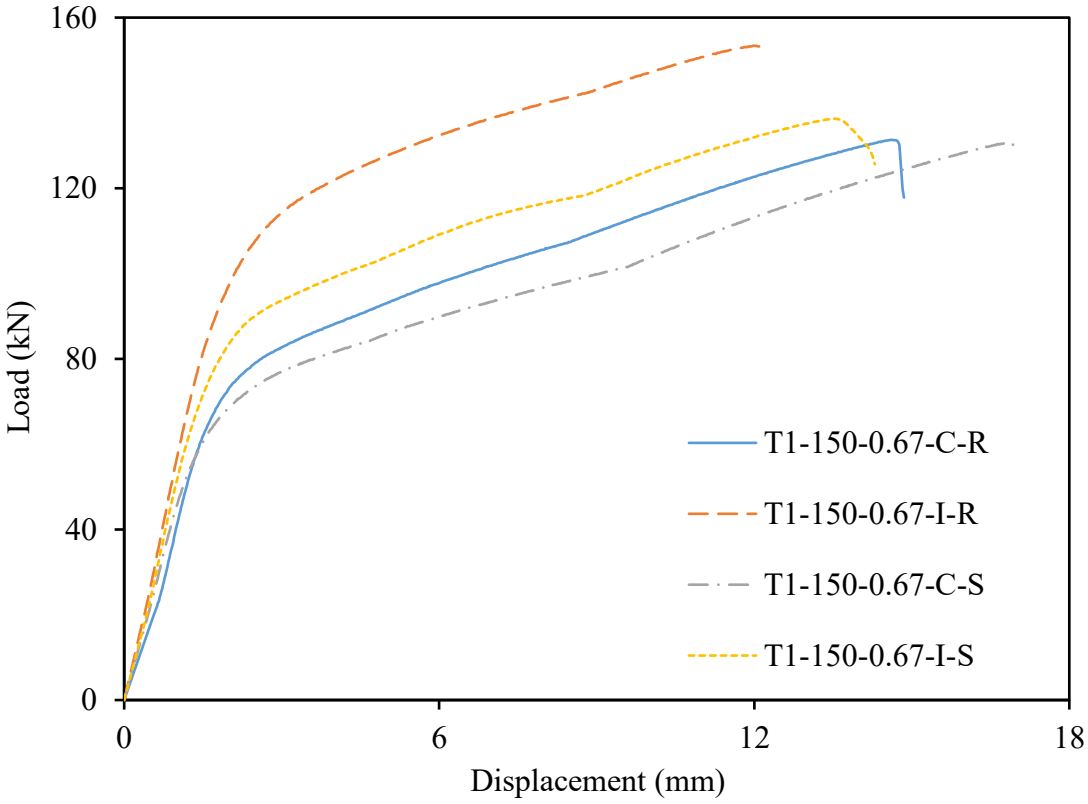
(h) T1-90-0.67



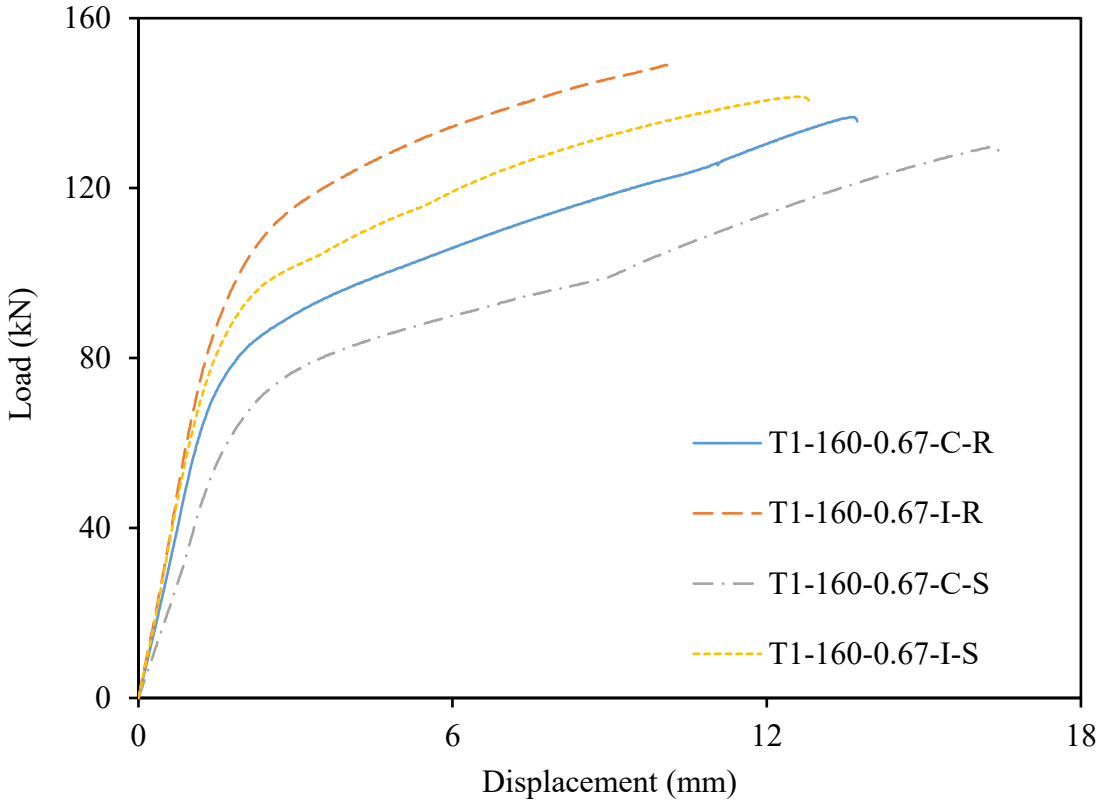
(i) T1-120-0.67



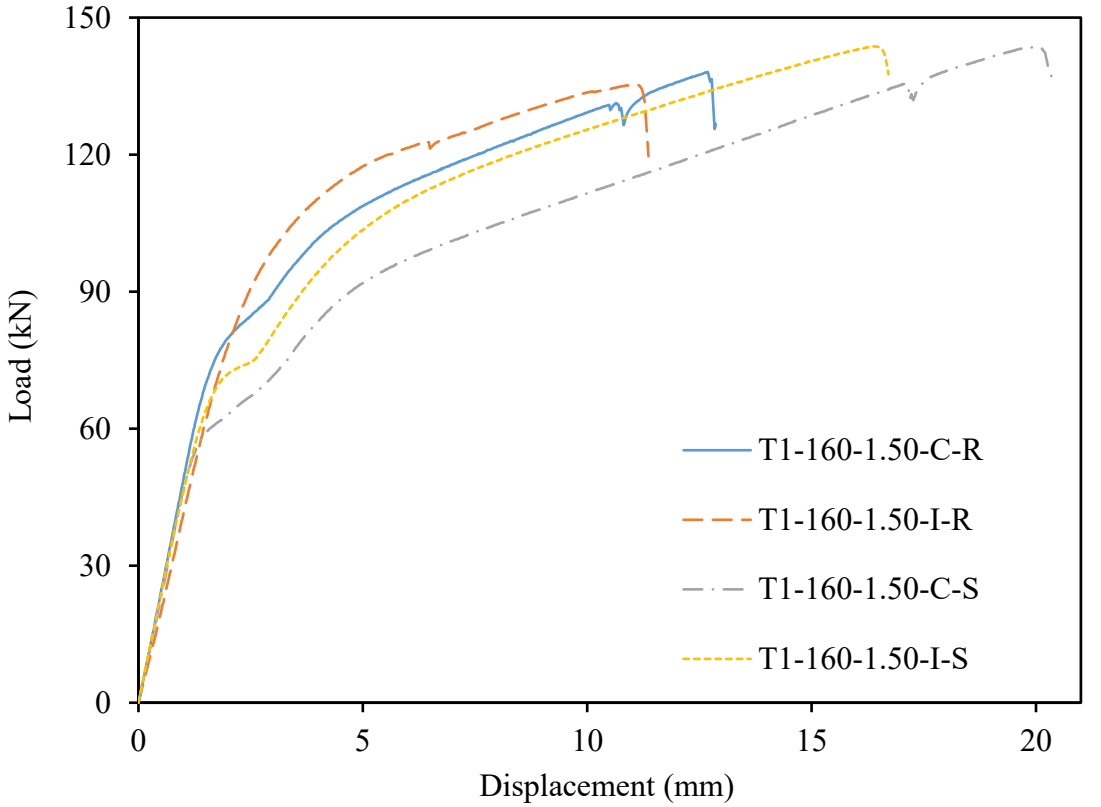
(j) T1-120-1.33



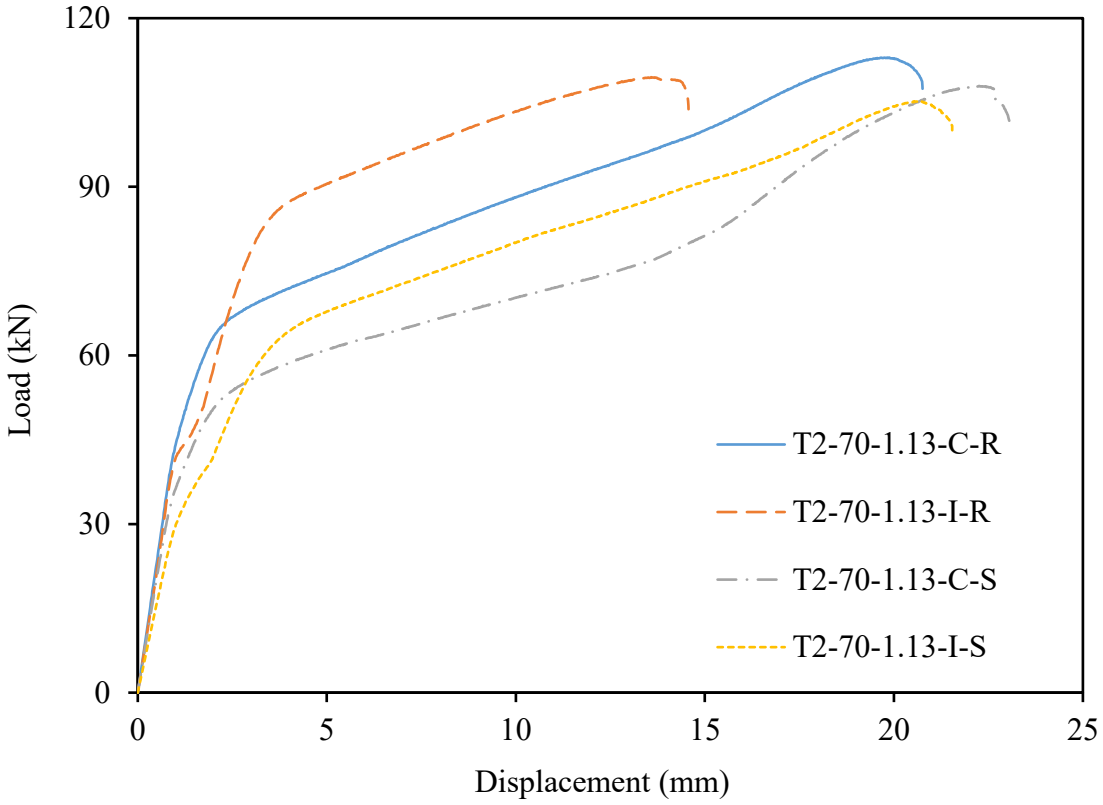
(k) T1-150-0.67



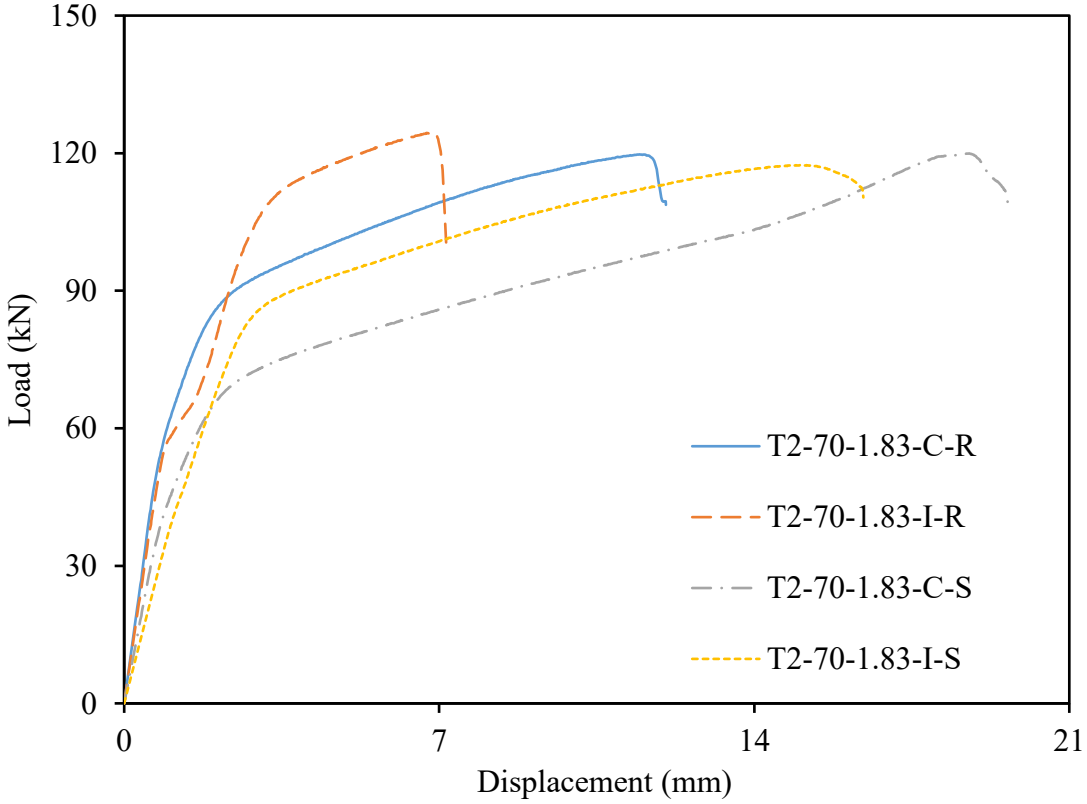
(l) T1-160-0.67



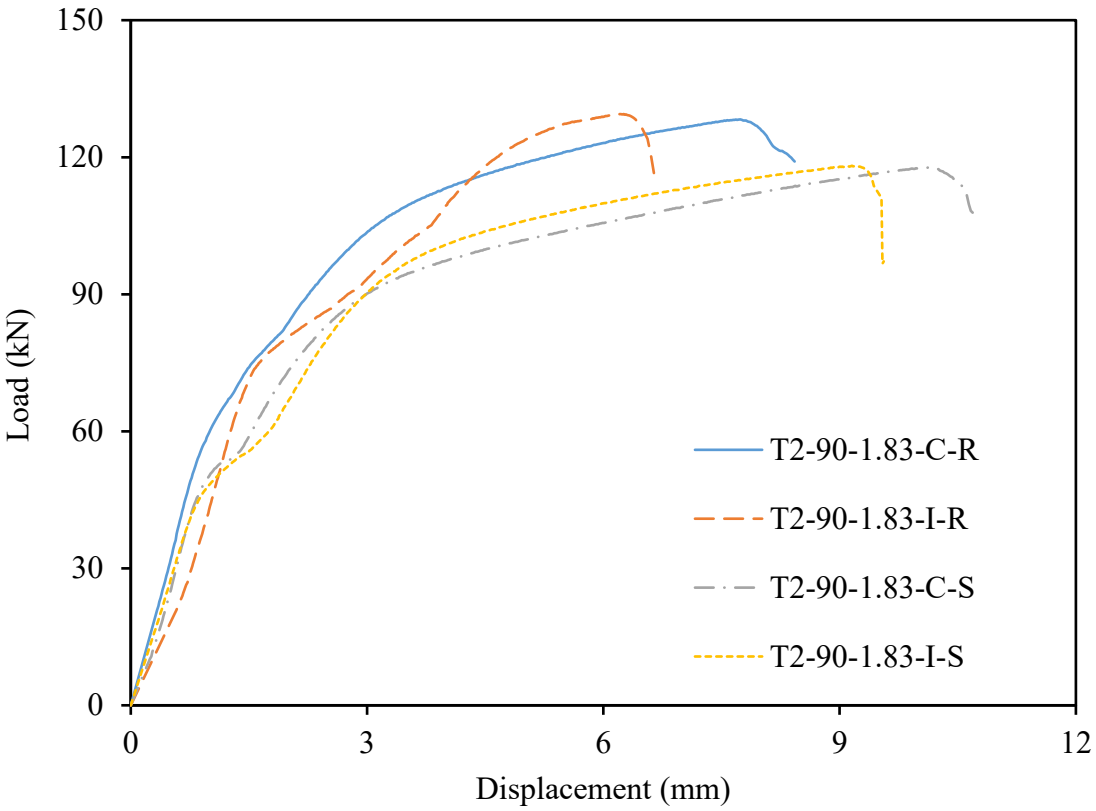
(m)T1-160-1.50



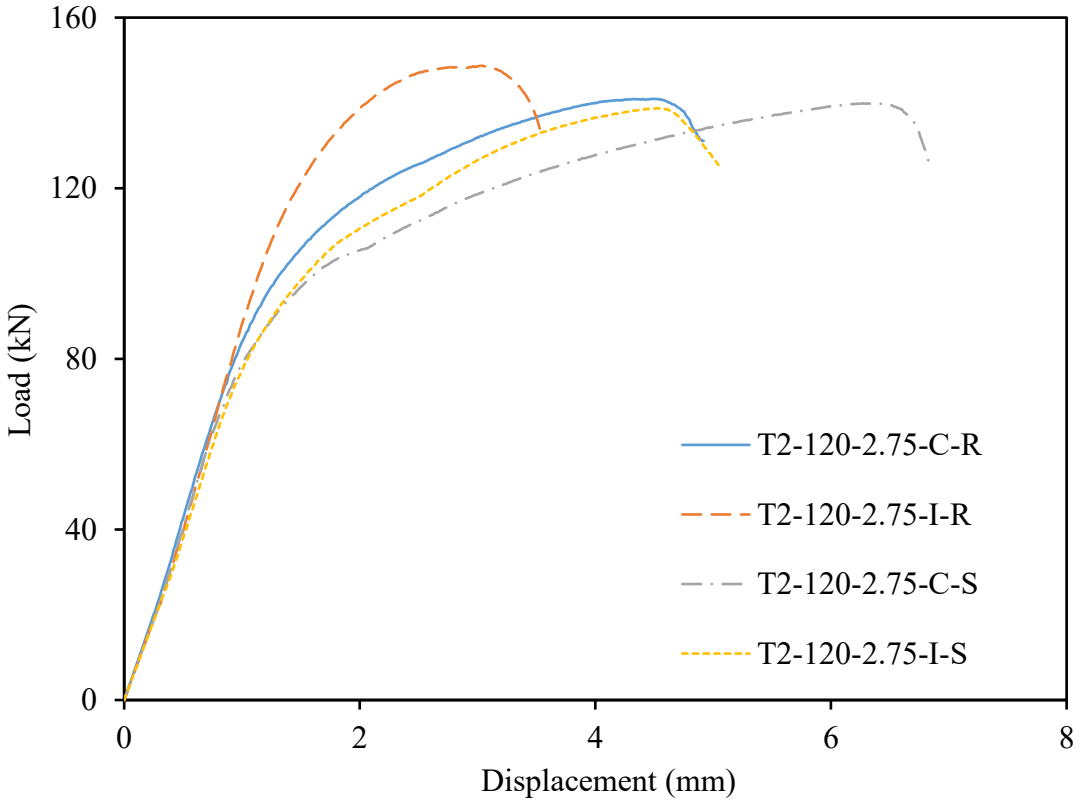
(n) T2-70-1.13



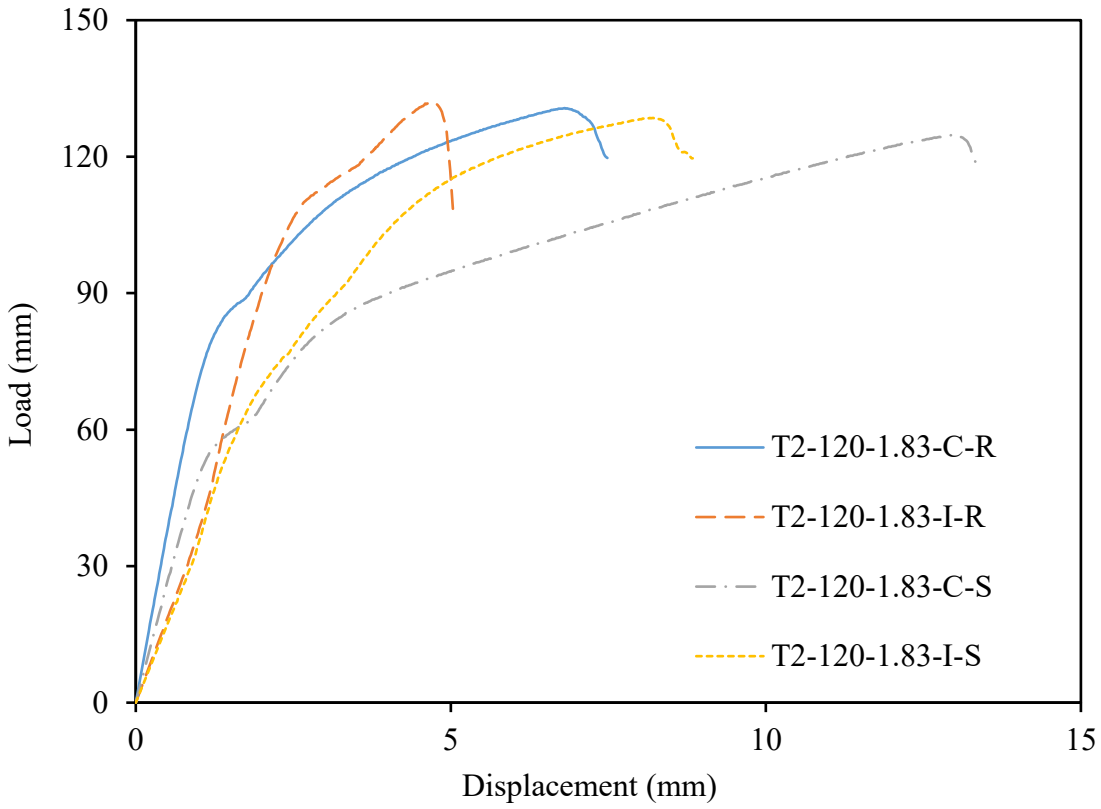
(o) T2-70-1.83



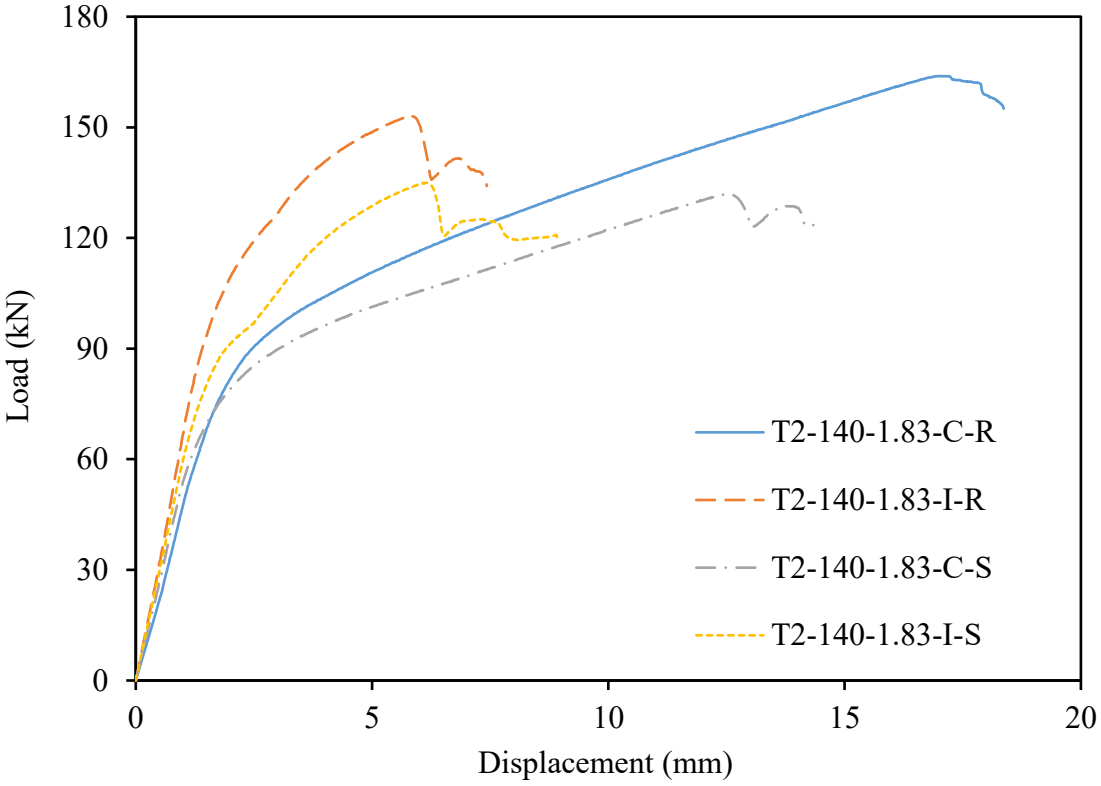
(p) T2-90-1.83



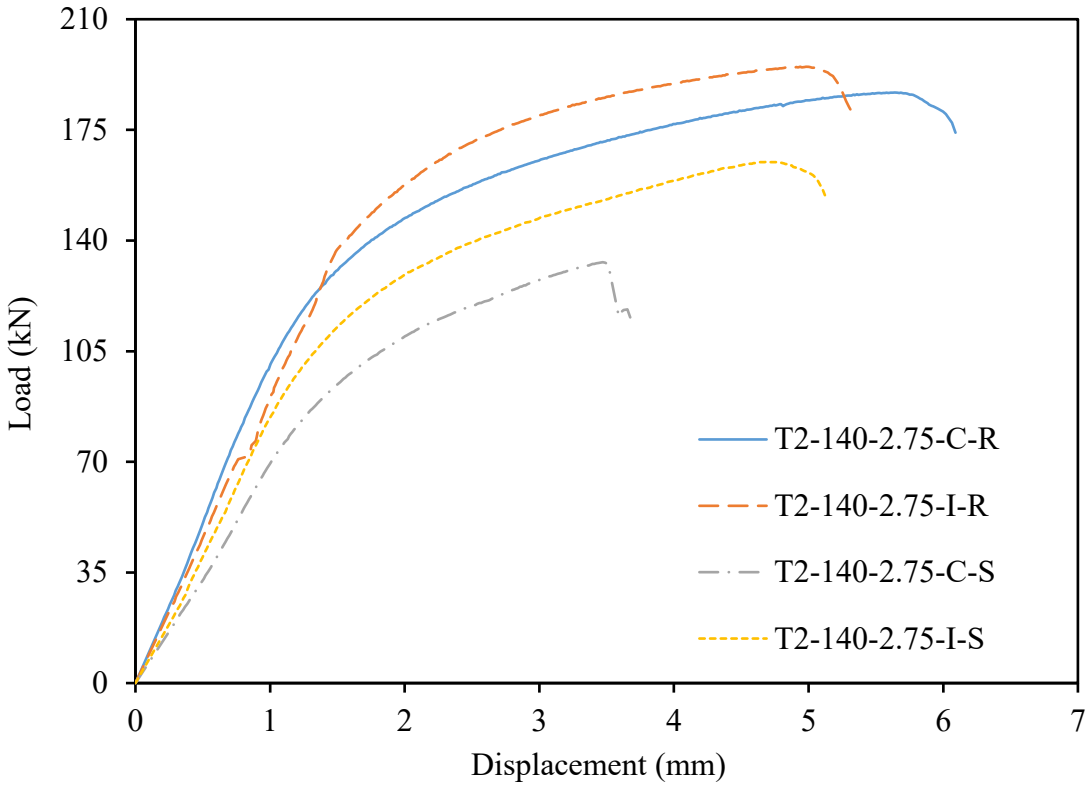
(q) T2-120-2.75



(r) T2-120-1.83

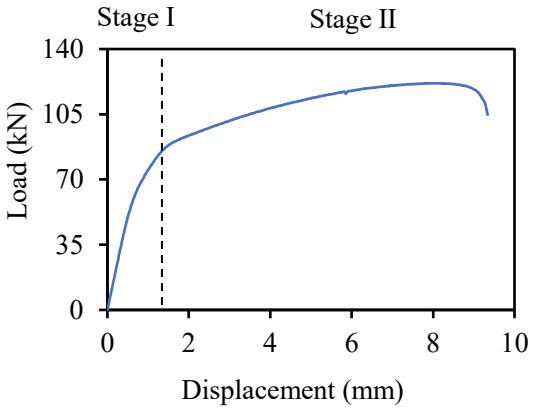


(s) T2-140-1.83

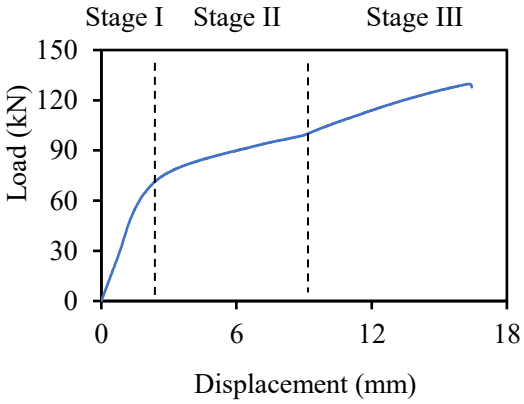


(t) T2-140-2.75

Figure 5.4. Load-displacement curves of tested T-stub specimens

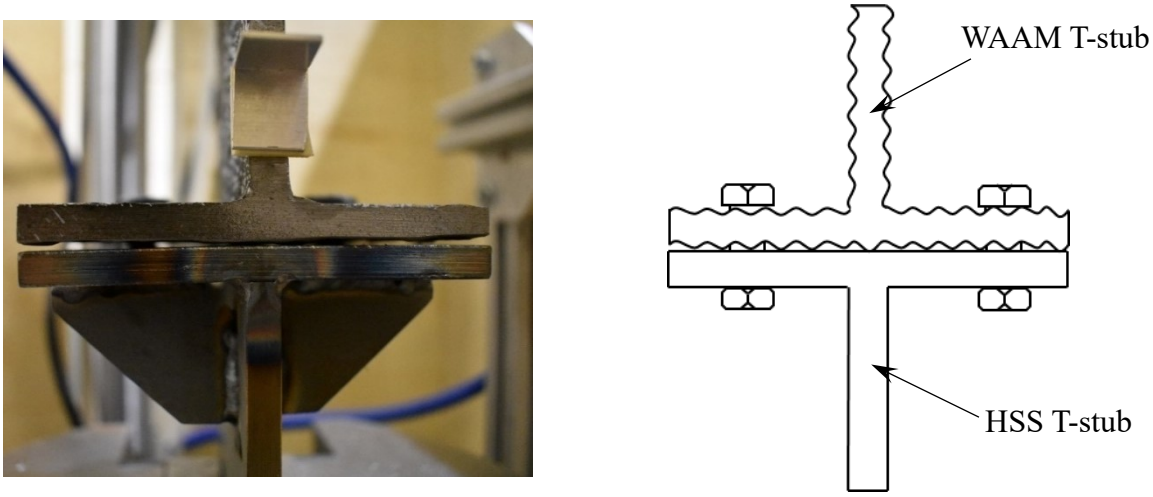


(a) Conventional two-stage behaviour (Specimen T1-40-2.00-C-R)

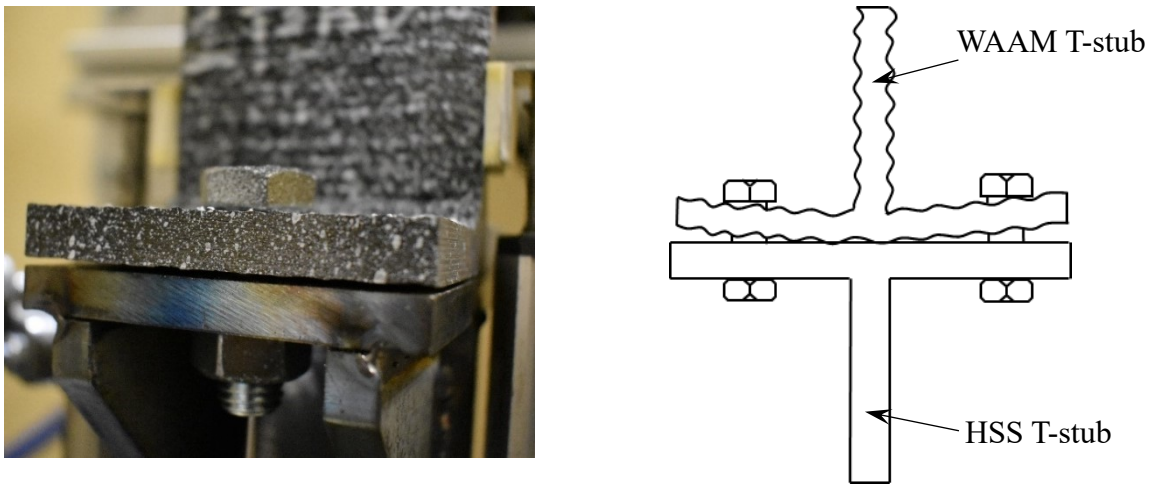


(b) Conventional three-stage behaviour (Specimen T1-160-0.67-C-S)

Figure 5.5. Typical load-displacement curves



(a) Gap caused by surface undulations



(b) Gap caused by flange bowing

Figure 5.6. Gaps between the T-stub flanges

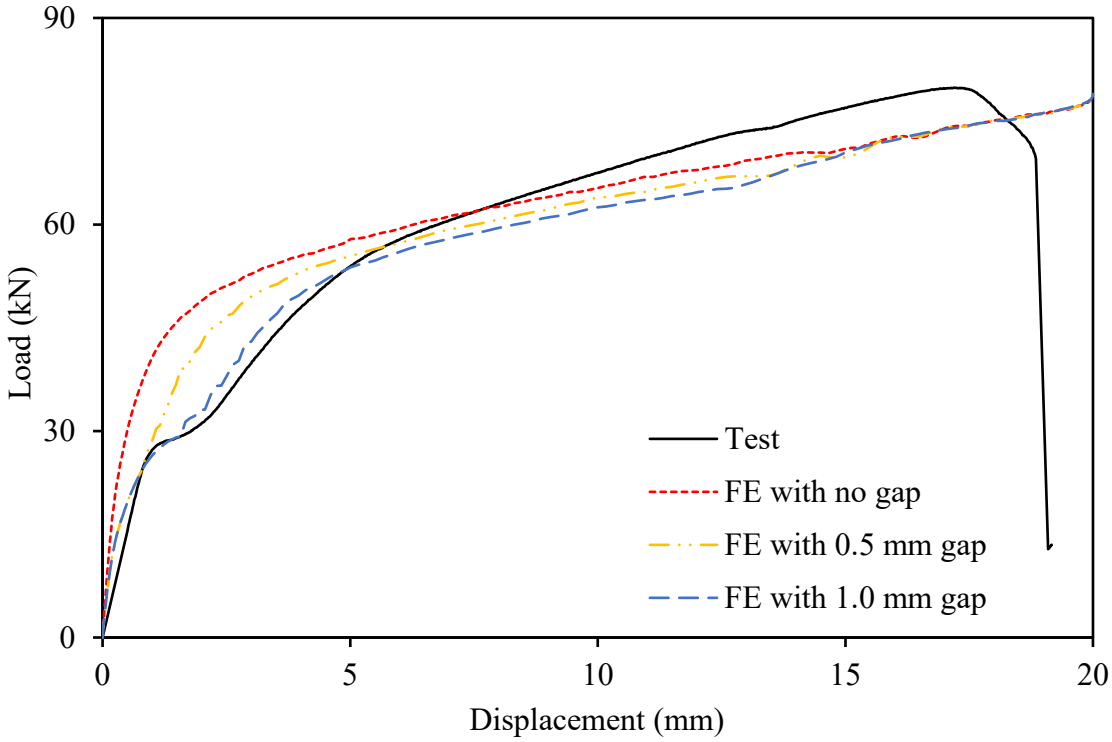
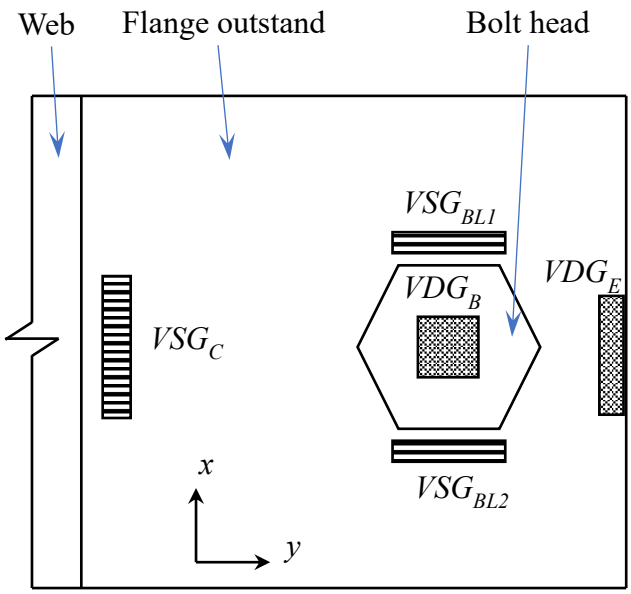
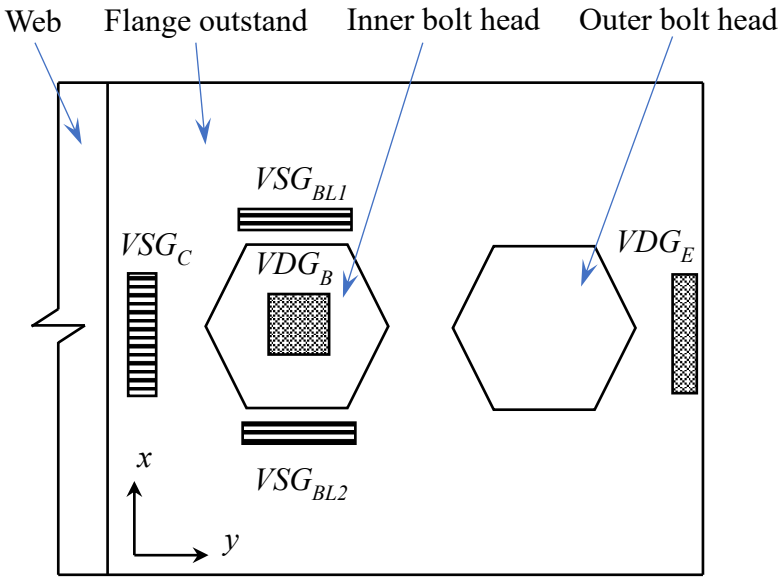


Figure 5.7. Influence of increasing gap size between T-stub flanges on the load-displacement curve of a typical specimen, based on preliminary FE simulations (Specimen T1-70-0.50-C-S)

To determine the point of contact between the flanges in the experiments, the displacement at the tips of the flanges of the WAAM T-stubs was monitored by means of a virtual displacement gauge (VDG_E) through the DIC system, as illustrated in Figure 5.8. In Figure 5.9, the load is plotted against the vertical displacement at the flange tip of a typical specimen, where three stages of behaviour can be observed. In the first stage, the flange rises as the bolt elongates with increasing load, with both the web-to-flange junction and the bolt remaining elastic, until a load level corresponding to yielding at the web-to-flange junction is reached. The second stage is then triggered, characterised by the descent of the flange arising owing to the reduced rotational stiffness following the formation of the plastic hinge at the web-to-flange junction. Finally, in third stage, the descent of the WAAM flange tip is halted as it comes into contact with the flange below, resulting in decreasing displacement with increasing load. A simplified model of the load-vertical displacement curve of the flange tip is also illustrated in Figure 5.9. Hence, the transition from the first to the second stage indicates yielding in the web-to-flange junction, and from the second to the third stage, contact between the upper and lower flanges.



(a) T-stubs with two bolts in a row



(b) T-stubs with four bolts in a row

Figure 5.8. Location of virtual strain and displacement gauges on flange outstands of T-stubs with (a) two bolts in a row and (b) four bolts in a row (VSG: virtual strain gauge, VDG: virtual displacement gauge, C: web-to-flange junction, BL: bolt line, B: bolt and E: flange end)

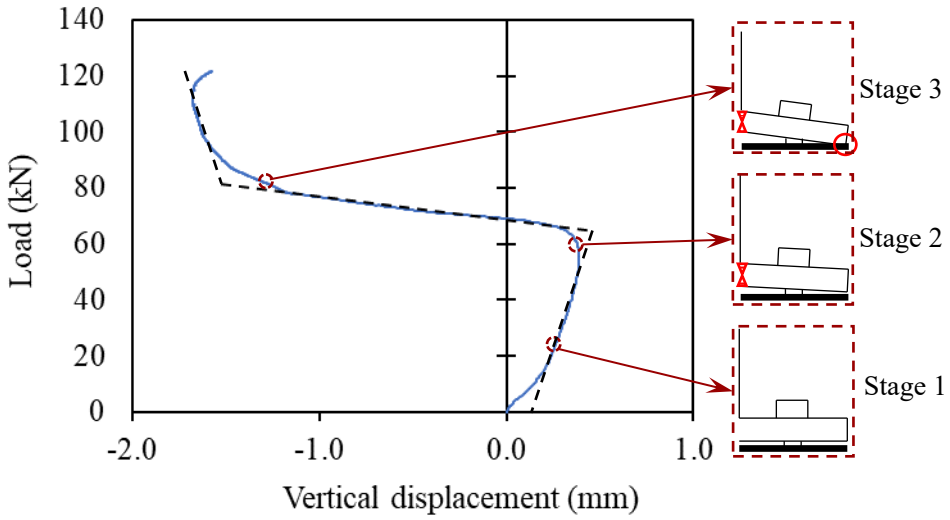


Figure 5.9. Load-vertical displacement of the flange end of Specimen T1-120-1.33-C-R, with illustration of key points

5.4.2. Determination of plastic hinges in the flanges and yielding of bolts

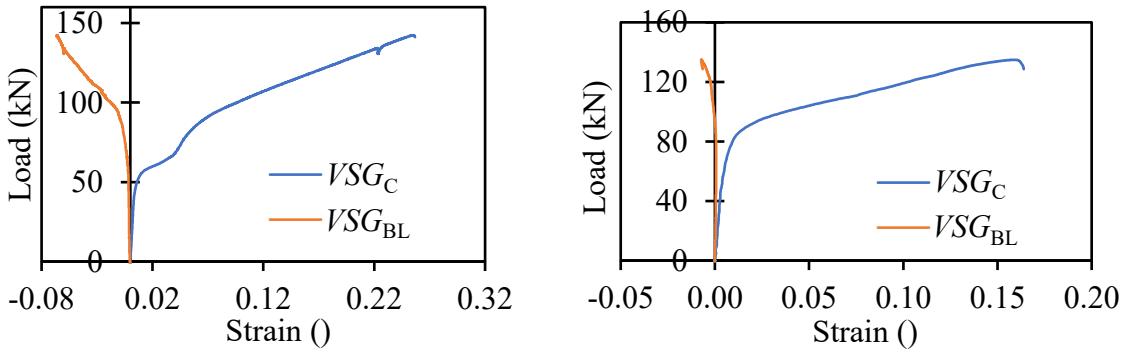
In order to gain a comprehensive understanding of the response of WAAM T-stub connections, a detailed investigation of the development of the plastic hinges in the flanges and yielding of the bolts is required; this is addressed in this section.

Typically, the failure modes of T-stubs have been identified either based on observations of the deformed shape of the flanges, which can be subjective, or by monitoring the strains at critical locations during testing, but often without clear criteria for defining failure modes having been established (Yuan et al., 2019; Yapici et al., 2021; Wang et al., 2019b). In this section, a consistent method to identify the development of the plastic hinges is proposed, whereby the bending moments arising through the thickness of the flanges at critical locations (i.e. at the web-to-flange junction and at the bolt line) are estimated based on the measured strains from virtual strain gauges (VSG), and compared against the theoretical plastic moment resistance of the flanges. Meanwhile, a criterion for the definition of bolt yielding based on the load-elongation response of the bolts is introduced. Note that the mechanical properties of the WAAM T-stubs were taken from Chapter 3, where tensile tests on WAAM coupons, manufactured using the same feedstock material and printing parameters as the T-stubs tested herein, were conducted – see Table 5.3.

Table 5.3. Average mechanical properties obtained from as-built WAAM tensile coupons

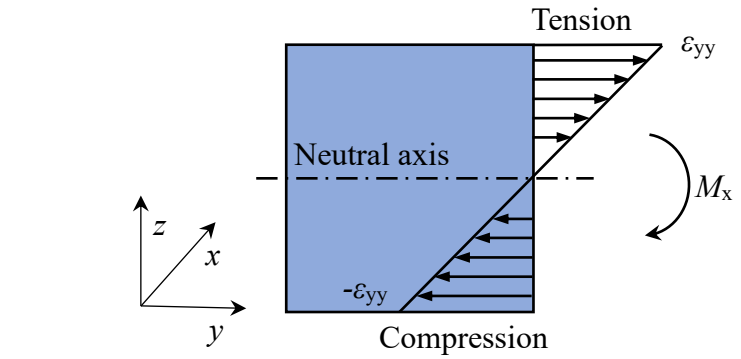
E (GPa)	f_y (MPa)	f_u (MPa)	ε_u	ε_f
215	306	416	0.18	0.36

The first step of the proposed method is to extract the normal strains in the transverse (y) direction ε_{yy} from the DIC data, at the critical locations illustrated in Figures 5.8(a) and (b) for the T-stubs with 2 bolts and 4 bolts in a row respectively. Two typical load-strain responses are presented in Figure 5.10, where the positive strains at the web-to-flange junction (USG_C) indicate tensile deformation on the exposed surface, while negative strains at the bolt line indicate compressive deformation on the exposed surface. Note that the strain at the bolt line is taken as the average of the strains measured on both sides of the bolt hole (VSG_{BL1} and VSG_{BL2}) – see Figure 5.8. Subsequently, the stress distribution across the thickness can be obtained at all load levels based on the average stress-strain curve of the material, assuming a linear strain distribution through the flange thickness, with the maximum strain at the extreme fibre being equal to the DIC strain ε_{yy} – see Figure 5.11(a).

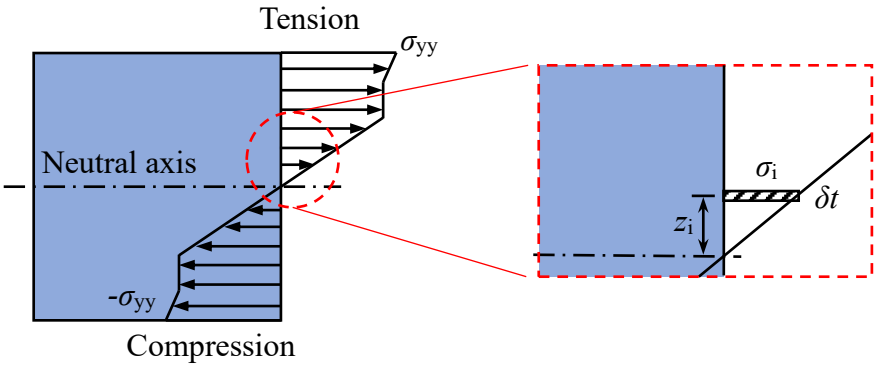


(a) Specimen T1-160-1.50-C-S (b) Specimen T1-120-1.33-I-R

Figure 5.10. Typical load-strain curves at the web-to-flange conjunction and the bolt line



(a) Strain distribution



(b) Stress distribution

Figure 5.11. Strain and stress distributions through flange thickness

Based on the acquired stress distribution, the corresponding bending moment M_x was obtained by discretising the flange thickness into n layers of height δt (taken equal to 0.01 mm) and performing numerical integration thus:

$$M_x = \sum_i^n z_i \sigma_i l_{eff} \delta t \tag{5.1}$$

where l_{eff} is the effective length of the plastic hinge determined according to EN 1993-1-8 (2021), z_i is the distance of layer i from the neutral axis of the flange and σ_i is the stress determined from the stress-strain curve of the WAAM material at layer i, for a value of ε_i equal to:

$$\varepsilon_i = \left(\frac{z_i}{t/2} \right) \varepsilon_{yy} \tag{5.2}$$

where ε_i is the strain in each cross-sectional layer.

The strain required for the formation of a plastic hinge can be chosen by comparing the bending moment M_x obtained by Equation (5.1) against the theoretical plastic moment M_{pl} calculated by Equation (5.3):

$$M_{pl} = \frac{l_{eff} t^2 f_y}{4} \tag{5.3}$$

For the examined specimens, M_x was found to reach 98% of the theoretical plastic moment M_{pl} at a strain of $5\varepsilon_y$, where ε_y is the yield strain taken as $f_y/E = 0.0014$, and f_y and E are the yield stress and Young's modulus – see Table 5.4. The $5\varepsilon_y$ threshold is shown in Figure 5.12, where, for a typical specimen, the bending moment M_x is plotted against the surface strain ε_{yy} at the web-to-flange junction and the bolt line. When the surface strain ε_{yy} reaches $5\varepsilon_y$, the section can be considered to be essentially fully plastic, with the corresponding load applied to the T-stub being the yield load of the section. Based on this criterion, the yield loads for yielding at the web-to-flange conjunction $F_{y,C}$ and at the bolt line $F_{y,BL}$ for the T-stubs with two bolts and four bolts in a row are summarised in Tables 5.5 and 5.6, respectively.

Table 5.4. Evaluation of M_x relative to the theoretical plastic moment M_{pl} for varying multiples of the yield strain ε_y

	M_x/M_{pl}						
ε_{yy}	ε_y	$2\varepsilon_y$	$3\varepsilon_y$	$4\varepsilon_y$	$5\varepsilon_y$	$6\varepsilon_y$	$7\varepsilon_y$
Mean	0.60	0.85	0.94	0.97	0.98	0.99	0.99
COV	0.020	0.009	0.003	0.002	0.002	0.001	0.001

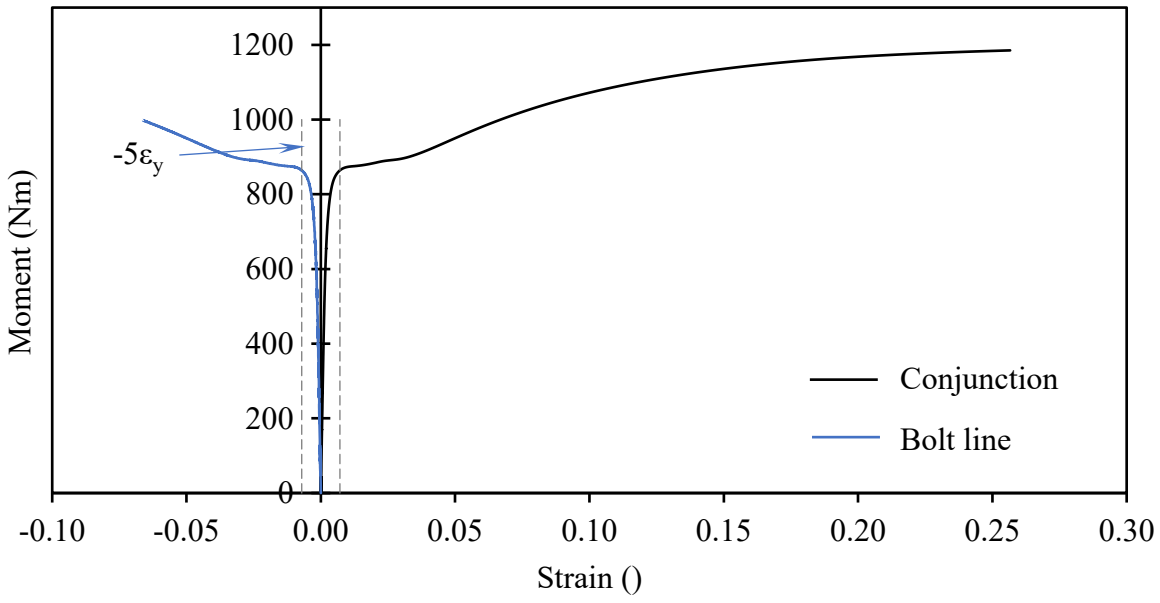


Figure 5.12. Moment-strain curves at critical locations (Specimen T1-160-1.50-C-S)

Table 5.5. Summary of experimental results for T-stubs with two bolts in a row and comparisons with design equations (FM_{Test} = test failure mode and FM_{theo} = theoretical failure mode in brackets if different from the test results)

Specimen	$F_{y,C}$ (kN)	$F_{y,BL}$ (kN)	$F_{y,B}$ (kN)	$F_{coll,test}$ (kN)	F_u (kN)	FM_{Test}	FM_{Theo}	$\frac{F_{y,C}}{F_{Rd,np}}$ Eq.(5.16)	$\frac{F_{y,BL}}{F_{Rd,1}}$ Eq.(5.12)	$\frac{F_{y,B}}{F_{Rd,2}}$ Eq.(5.13)	$\frac{F_{y,C}}{F_{Rd,prop}}$ Eq.(5.18)
T1-40-0.67-C-R	34.21	58.35	41.58	41.58	91.01	2	(1)	1.68	-	0.59	0.89
T1-40-2.00-C-R	61.90	95.09	88.64	88.64	121.67	2	2	1.47	-	1.03	0.16
T1-60-0.40-C-R	28.29	44.82	46.68	44.82	75.30	1	1	1.79	1.23	-	1.36
T1-60-0.67-C-R	52.41	77.29	72.36	72.36	100.95	2	2	1.70	-	0.96	0.91
T1-70-0.50-C-R	40.53	68.51	58.41	58.41	93.06	2	(1)	1.61	-	0.92	1.10
T1-70-0.67-C-R	59.81	98.58	62.47	62.47	103.72	2	2	1.68	-	0.81	0.90
T1-90-0.33-C-R	54.10	60.24	69.08	60.24	105.62	1	(2)	1.29	0.53	-	0.61
T1-90-0.67-C-R	70.33	105.31	71.95	71.95	123.39	2	2	1.42	-	0.83	0.77
T1-120-0.67-C-R	59.52	79.86	70.55	70.55	115.29	2	2	1.27	-	0.84	0.65
T1-120-1.33-C-R	68.07	84.18	68.02	68.02	122.81	2	2	1.29	-	0.77	0.72
T1-150-0.67-C-R	62.62	98.84	75.70	75.70	131.33	2	2	1.24	-	0.74	0.53
T1-160-0.67-C-R	70.41	96.70	92.89	92.89	136.71	2	2	1.46	-	0.95	0.79
T1-160-1.50-C-R	81.22	103.17	105.57	103.17	138.07	1	(2)	1.42	0.80	-	0.99
Mean								1.49	0.85	0.84	0.80
COV								0.13	0.42	0.15	0.37
T1-40-0.67-I-R	34.51	77.65	51.09	51.09	93.36	2	(1)	1.57	-	0.72	0.94
T1-40-2.00-I-R	80.97	101.55	90.05	90.05	128.77	2	2	2.26	-	1.12	0.71
T1-60-0.40-I-R	24.69	58.62	45.68	45.68	73.90	2	(1)	1.53	-	0.96	1.19
T1-60-0.67-I-R	43.49	101.29	63.89	63.89	105.15	2	(1)	1.52	-	1.11	0.91
T1-70-0.50-I-R	38.67	90.44	55.53	55.53	93.10	2	(1)	1.60	-	1.29	1.14
T1-70-0.67-I-R	48.31	103.21	72.44	72.44	106.31	2	2	1.46	-	1.00	0.89

T1-90-0.33-I-R	75.08	97.90	61.14	61.14	98.99	2	2	1.64	-	1.17	0.96
T1-90-0.67-I-R	59.73	98.93	86.37	86.37	122.98	2	2	1.40	-	1.09	0.87
T1-120-0.67-I-R	75.27	116.41	77.96	77.96	120.44	2	2	1.41	-	0.94	0.90
T1-120-1.33-I-R	81.91	131.13	99.60	99.60	135.33	2	2	1.50	-	1.09	0.90
T1-150-0.67-I-R	58.87	120.44	110.80	110.80	153.41	2	2	1.05	-	1.11	0.64
T1-160-0.67-I-R	72.46	115.62	110.78	110.78	149.01	2	2	1.36	-	1.13	0.83
T1-160-1.50-I-R	88.43	108.10	113.63	108.10	135.40	1	(2)	1.67	0.92	-	1.20
Mean								1.54	0.92	1.06	0.93
COV								0.17	-	0.13	0.18
T1-40-0.67-C-S	33.46	41.19	51.03	41.19	82.60	1	1	2.46	1.28	-	1.64
T1-40-2.00-C-S	29.70	63.77	60.50	60.50	103.24	2	(1)	1.51	1.32	-	0.75
T1-60-0.40-C-S	19.55	35.52	42.26	35.52	69.50	1	1	1.69	1.35	-	1.35
T1-60-0.67-C-S	34.89	48.52	51.30	48.52	90.22	1	1	1.71	1.49	-	1.14
T1-70-0.50-C-S	28.19	57.80	56.29	56.29	79.88	2	(1)	1.57	-	1.01	1.18
T1-70-0.67-C-S	39.54	71.50	45.10	45.10	92.33	2	(1)	1.68	-	1.01	1.12
T1-90-0.33-C-S	42.50	71.82	55.18	55.18	91.95	2	2	1.33	-	0.99	0.87
T1-90-0.67-C-S	52.58	95.45	66.23	66.23	102.32	2	2	1.31	-	0.97	0.87
T1-120-0.67-C-S	57.77	89.17	67.01	67.01	106.21	2	2	1.47	-	1.09	0.99
T1-120-1.33-C-S	55.90	83.60	67.07	67.07	118.44	2	2	1.50	-	0.92	1.02
T1-150-0.67-C-S	53.49	78.65	78.38	78.38	130.63	2	2	1.27	-	0.79	0.86
T1-160-0.67-C-S	51.50	81.85	79.64	79.64	129.71	2	2	1.20	-	0.92	0.81
T1-160-1.50-C-S	52.01	95.42	81.88	81.88	143.58	2	(1)	1.21	0.91	-	0.92
Mean								1.53	1.27	0.96	1.04
COV								0.22	0.17	0.09	0.24
T1-40-0.67-I-S	26.50	42.62	54.73	42.62	82.08	1	1	1.56	1.06	-	1.03
T1-40-2.00-I-S	33.05	72.35	80.13	72.35	106.90	1	1	1.31	1.17	-	0.64
T1-60-0.40-I-S	22.78	46.28	57.23	46.28	71.72	1	1	1.58	1.41	-	1.26
T1-60-0.67-I-S	38.88	86.67	42.93	42.93	91.40	2	(1)	1.54	-	0.92	1.02

T1-70-0.50-I-S	33.95	63.48	48.03	48.03	87.71	2	(1)	1.59	1.29	-	1.19
T1-70-0.67-I-S	43.84	95.19	57.49	57.49	98.07	2	2	1.44	-	1.15	0.95
T1-90-0.33-I-S	54.50	83.77	66.23	66.23	95.72	2	2	1.41	-	1.05	0.92
T1-90-0.67-I-S	65.75	111.96	68.76	68.76	111.81	2	2	1.48	-	1.19	0.97
T1-120-0.67-I-S	60.33	84.92	70.46	70.46	109.14	2	2	1.30	-	1.06	0.87
T1-120-1.33-I-S	62.73	108.88	77.19	77.19	110.36	2	2	1.33	-	0.97	0.89
T1-150-0.67-I-S	67.99	105.91	95.03	95.03	136.30	2	2	1.23	-	0.99	0.82
T1-160-0.67-I-S	73.08	104.04	99.37	99.37	141.53	2	2	1.34	-	1.07	0.90
T1-160-1.50-I-S	70.71	100.94	95.29	95.29	143.71	2	(1)	1.50	0.98	-	1.13
Mean								1.43	1.18	1.05	0.97
COV								0.08	0.15	0.09	0.17
Mean								1.50	1.12	0.98	0.93
COV								0.16	0.24	0.15	0.25

Table 5.6. Summary of experimental results for T-stubs with four bolts in a row and comparisons with design equations (FM_{Test} = test failure mode and FM_{theo} = theoretical failure mode in brackets if different from the test results)

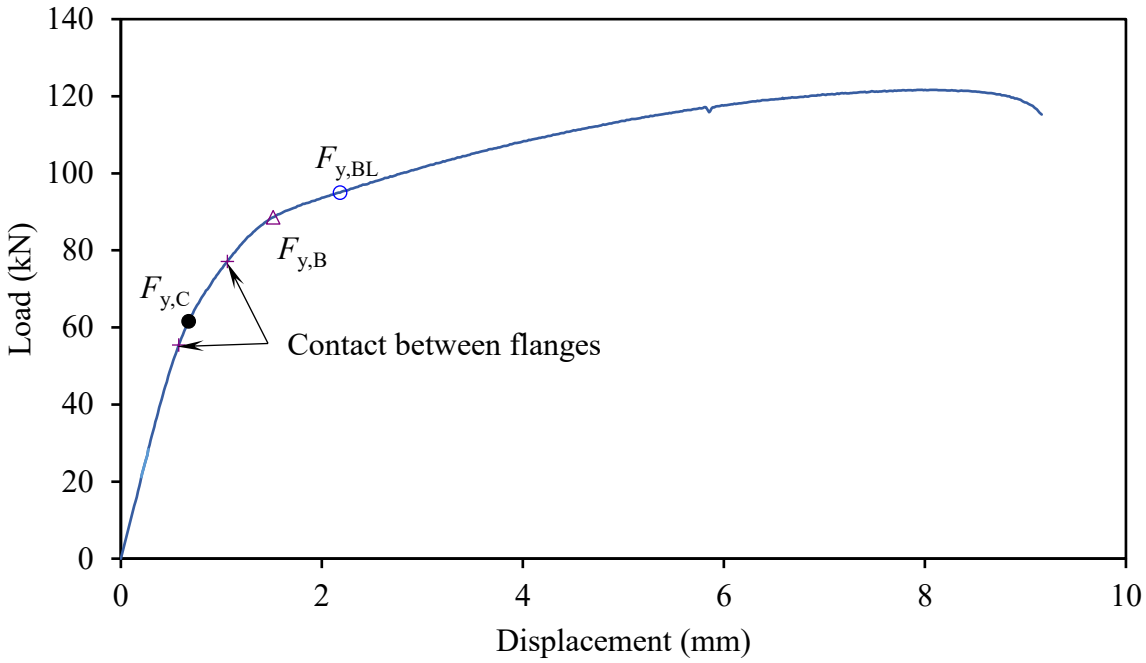
Specimen	$F_{y,C}$ (kN)	$F_{y,BL}$ (kN)	$F_{y,B}$ (kN)	$F_{coll,test}$ (kN)	F_u (kN)	FM_{Test}	FM_{Theo}	$\frac{F_{y,C}}{F_{Rd,np}}$ Eq.(5.16)	$\frac{F_{y,BL}}{F_{Rd,1}}$ Eq.(5.12)	$\frac{F_{y,B}}{F_{Rd,2}}$ Eq.(5.17)	$\frac{F_{y,C}}{F_{Rd,prop}}$ Eq.(5.18)
T2-70-1.13-C-R	43.64	62.22	73.31	62.22	112.99	1	1	1.67	1.05	-	1.17
T2-70-1.83-C-R	53.68	87.21	79.37	79.37	119.73	2	2	1.38	-	0.90	0.97
T2-90-1.83-C-R	60.85	103.49	88.21	88.21	128.28	2	2	1.32	-	0.99	0.92
T2-120-2.75-C-R	90.84	140.40	114.31	114.31	140.96	2	2	1.62	-	1.12	1.14
T2-120-1.83-C-R	88.02	110.86	88.88	88.88	130.68	2	2	1.41	-	0.91	0.99
T2-140-1.83-C-R	86.69	96.44	93.59	93.59	164.59	2	2	1.59	-	0.83	1.11
T2-140-2.75-C-R	116.07	148.65	122.86	122.86	186.83	2	2	1.85	-	0.95	1.29
Mean								1.55	-	0.95	1.08
COV								0.12	-	0.10	0.12
T2-70-1.13-I-R	50.42	80.24	80.33	80.24	109.51	1	1	1.95	1.39	-	1.36
T2-70-1.83-I-R	46.21	101.38	80.83	80.83	124.41	2	2	1.30	-	0.97	0.91
T2-90-1.83-I-R	60.28	103.64	84.87	84.87	129.45	2	2	1.40	-	0.99	0.98
T2-120-2.75-I-R	92.27		110.84	110.84	148.72	2	2	1.35	-	1.06	0.95
T2-120-1.83-I-R	71.16		97.20	97.20	131.95	2	2	1.10	-	1.01	0.77
T2-140-1.83-I-R	60.37	135.87	115.57	115.57	153.11	2	2	0.89	-	1.01	0.63
T2-140-2.75-I-R	69.18	185.16	116.08	116.08	194.96	2	2	1.04	-	0.93	0.73
Mean								1.29	-	1.00	0.90
COV								0.27	-	0.05	0.27
T2-70-1.13-C-S	42.18	51.45	58.00	51.45	107.93	1	1	2.46	1.36	-	1.72
T2-70-1.83-C-S	40.99	65.20	70.31	65.20	119.94	1	1	1.77	1.24	-	1.24
T2-90-1.83-C-S	48.83	81.65	77.61	77.61	117.73	2	2	1.42	-	1.00	0.99
T2-120-2.75-C-S	69.10	102.98	87.48	87.48	139.89	2	2	1.21	-	0.92	0.85
T2-120-1.83-C-S	53.40	81.45	81.81	81.45	124.77	1	(2)	1.33	0.89	-	0.93

T2-140-1.83-C-S	56.14	80.59	86.10	80.59	131.99	1	(2)	1.25	0.79	-	0.87
T2-140-2.75-C-S	69.53	141.28	121.61	121.61	133.14	2	2	1.21	-	1.06	0.84
Mean								1.52	1.07	0.99	1.06
COV								0.30	0.26	0.07	0.30
T2-70-1.13-I-S	31.07	57.37	62.98	57.37	105.19	1	1	1.43	1.20	-	1.00
T2-70-1.83-I-S	37.17	84.95	96.54	84.95	117.39	1	1	1.28	1.29	-	0.90
T2-90-1.83-I-S	52.58	99.06	80.30	80.30	118.13	2	2	1.40	-	1.01	0.98
T2-120-2.75-I-S	79.36	120.27	86.19	86.19	138.81	2	2	1.21	-	0.87	0.85
T2-120-1.83-I-S	54.38	110.22	85.67	85.67	128.49	2	2	1.11	-	1.00	0.77
T2-140-1.83-I-S	75.68	113.08	80.40	80.40	134.97	2	2	1.28	-	0.76	0.89
T2-140-2.75-I-S	94.36	152.42	118.90	118.90	164.91	2	2	1.40	-	1.00	0.98
Mean								1.30	1.24	0.93	0.91
COV								0.09	0.05	0.12	0.09
Mean								1.42	1.15	0.96	0.99
COV								0.22	0.19	0.09	0.22

Regarding the point at which yielding of the bolt occurs, this can be determined by monitoring the bolt elongation (of the inner bolt for T-stubs with four bolts in a row), measured by means of a virtual displacement gauge (provided by the DIC system) positioned at the top of the bolt head, as illustrated in Figure 5.8. Bolt yielding was identified as the point on the load-elongation curve where a marked drop in stiffness occurs; the corresponding load is denoted $F_{y,B}$. The loads corresponding to yielding of the bolts $F_{y,B}$ for the examined T-stubs with two bolts and four bolts in a row are summarised in Tables 5.5 and 5.6, respectively.

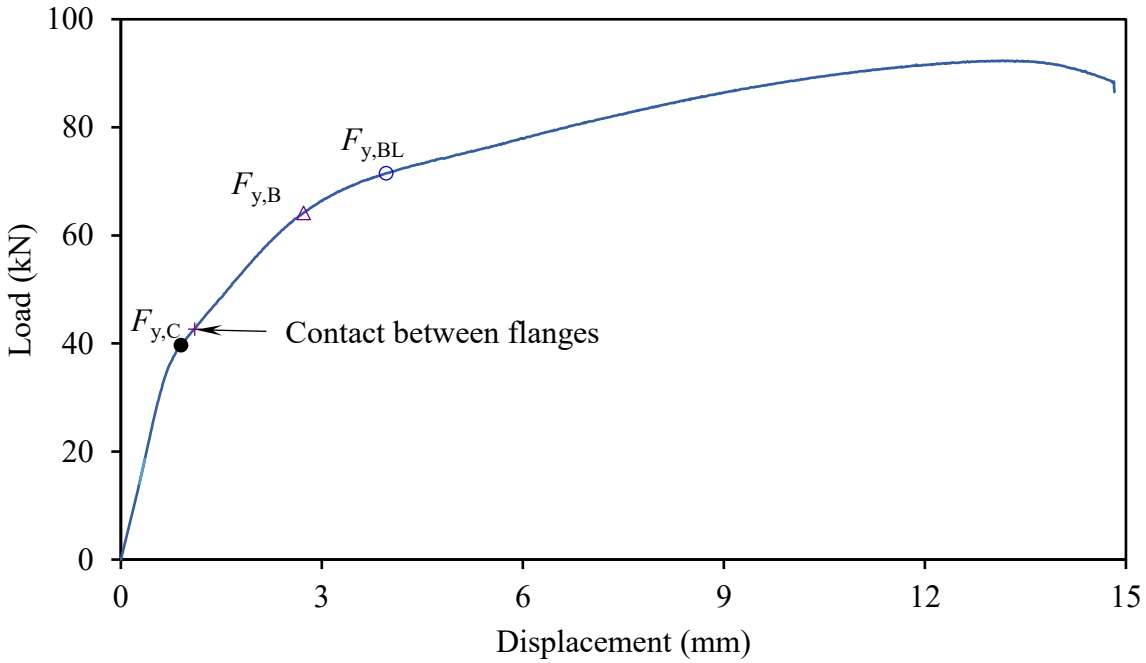
5.4.3. Determination of plastic resistance and identification of failure mode

The load-displacement curves of four typical T-stub specimens are plotted in Figure 5.13, where the different stages of the behaviour and key points, namely the yield points of the web-to-flange junction, bolt line and bolt and when the upper and lower flange outstands (left and right) come in contact, are marked. Following the development of yielding at two of the three key locations, a pronounced drop in stiffness can be observed, corresponding to the formation of a plastic mechanism in the T-stub, after which complete failure eventually occurs. The load corresponding to the occurrence of yielding at the second location is therefore defined as the collapse load $F_{coll,test}$ of the T-stub. Note that if yielding at the web-to-flange conjunction develops prior to the establishment of contact between the upper and lower flanges, a plastic mechanism is formed, accompanied by a loss in stiffness, up until the point that the two flanges come into contact, after which a recovery in stiffness takes place.



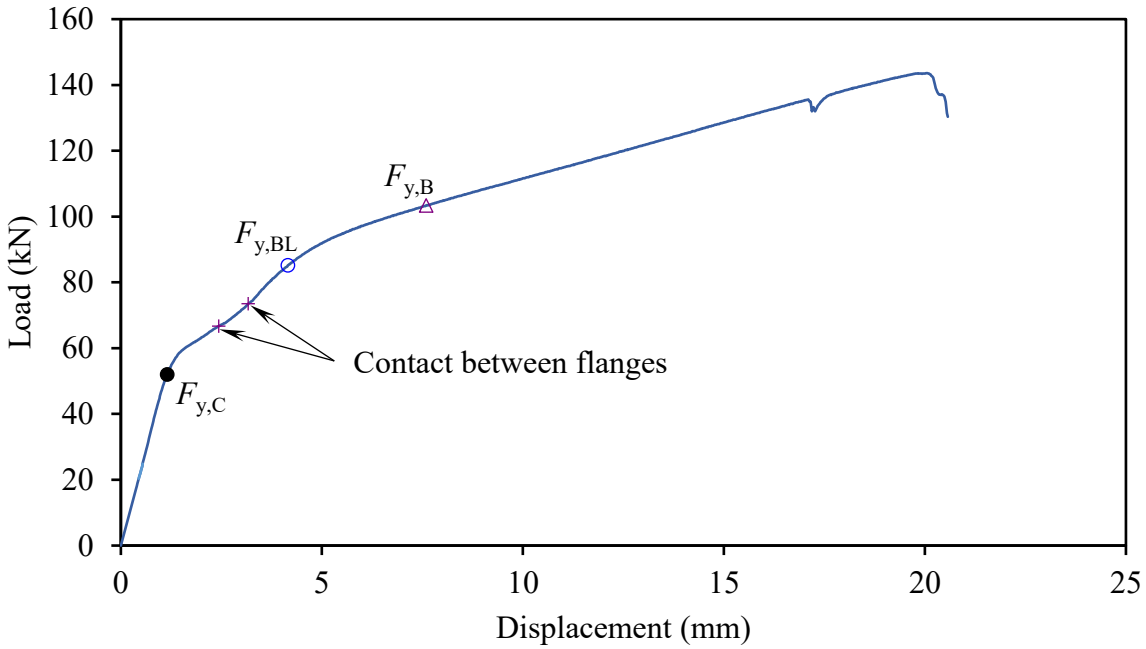
(a) Two-stage behaviour – Mode 2

(Specimen T1-40-2.00-C-R)



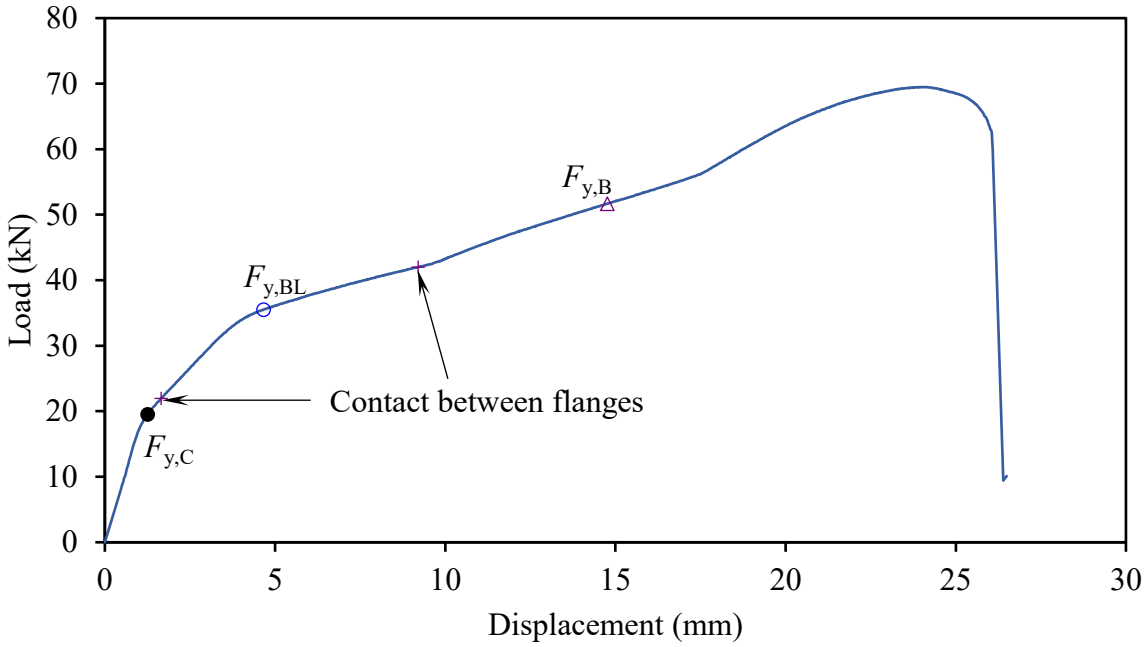
(b) Two-stage behaviour with an additional kink – Mode 2

(Specimen T1-70-0.67-C-S)



(c) Two-stage behaviour with two additional kinks – Mode 1

(Specimen T1-160-1.50-C-S)



(d) Three-stage behaviour with an additional kink – Mode 1

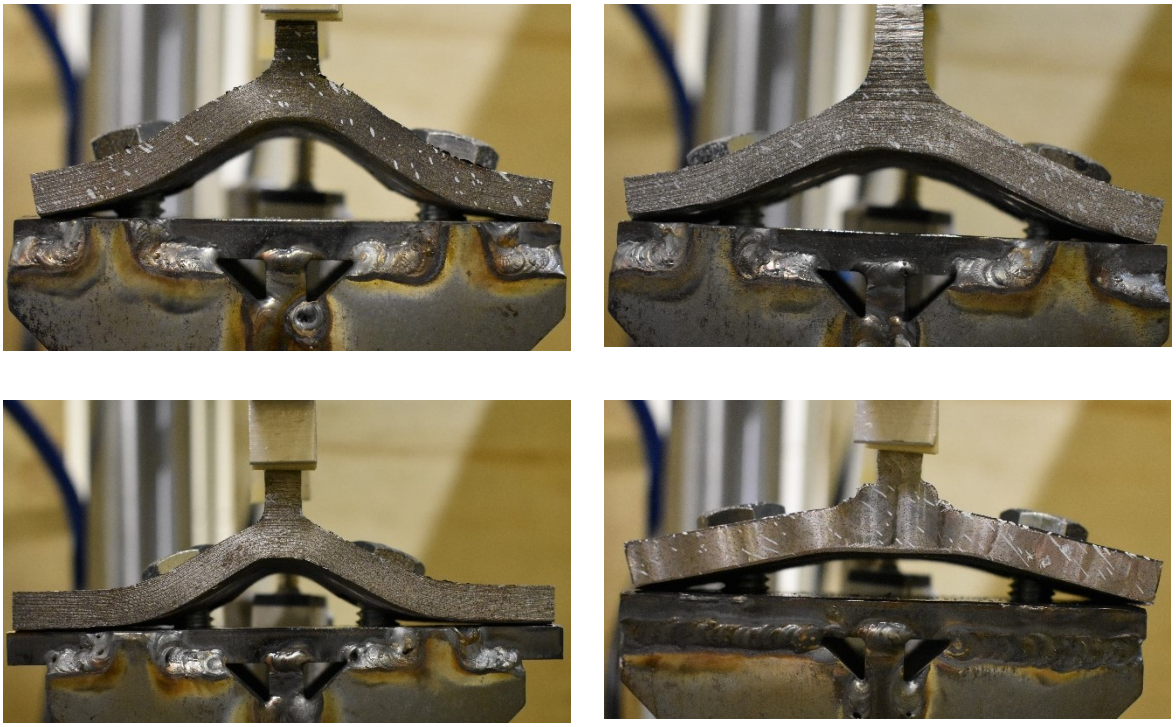
(Specimen T1-60-0.40-C-S)

Figure 5.13. Typical load-displacement curves with critical points marked

The failure mode of the T-stub can be identified based on the location of the second point of yielding. According to Eurocode 3 Part 1.8 (2021) and the literature (Demonceau et al., 2010),

Mode 1 involves the formation of plastic hinges at the web-to-flange junction and at the bolt line (the inner bolt line for the T-stubs with four bolts in a row), while for Mode 2, plasticity develops at the web-to-flange junction and in the bolt. Thus, since yielding at the web-to-flange junction was always found to precede either yielding of the bolt or of the flange at the bolt line, the collapse load $F_{\text{coll,test}}$ of the specimens failing in Mode 1 was equal to the load at which yielding of the bolt line $F_{\text{y,BL}}$ occurred, while that of specimens failing in Mode 2 was equal to the bolt yield load $F_{\text{y,B}}$. The collapse loads and failure modes of the T-stubs with two bolts and four bolts in a row examined herein are summarised in Tables 5.5 and 5.6, respectively.

Typical deformed specimens, grouped by failure mode, are presented in Figure 5.14, where it can be observed that identification of the failure mode by inspection would have been challenging. Conversely, the proposed approach provides a consistent and accurate way to determine both the collapse loads and failure modes.



(a) Specimens T1-40-0.67-C-S (top) and T1-40-2.00-C-S (bottom)

(b) Specimens T1-40-0.67-C-R (top) and T1-60-0.67-I-R (bottom)

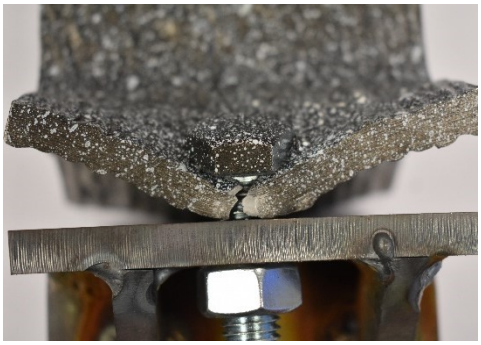
Figure 5.14. Typical specimens failing in (a) Mode 1 and (b) Mode 2

In certain cases, the load applied to the T-stubs was found to keep rising even after the collapse load had been attained, and even after yielding had occurred at three locations – see Figure 5.13(d). This additional capacity is attributed to strain hardening of the material and the

development of membrane action in the flanges, with contact between the bolt shank and the bolt hole (Faralli et al., 2021). The eventual ultimate loads $F_{u,test}$, including this additional capacity, obtained for the T-stubs with 2 bolts and with 4 bolts in a row are presented in Tables 5.5 and 5.6, respectively. It is worth noting that the ultimate loads $F_{u,test}$ obtained in the current test programme were governed by ultimate (inner) tensile bolt failure for most specimens – see Figure 5.15(a), while shear-out and punching failure (i.e. the bolt head punching through the flange) were also observed for two specimens – see Figures 5.15(a) and (b), respectively.



(a) Ultimate bolt failures



(b) Shear-out failure (Specimen T1-90-0.33-C-R)



(c) Punching failure (Specimen T2-140-1.83-C-R)

Figure 5.15. Ultimate failure of tested T-stubs

5.5. Influence of printing strategy

The loads corresponding to yielding at the web-to-flange junction $F_{y,C}$, bolt line $F_{y,BL}$ and bolt $F_{y,B}$, as well as plastic collapse $F_{coll,test}$, taken as the lower value of $F_{y,BL}$ and $F_{y,B}$ (see Section 4.2), obtained from the test results are used in this section to evaluate the influence of the

different printing strategies on the structural performance of the examined T-stub connections. The specimens with rounded corners that were continuously printed, labelled C-R, were chosen as the benchmark against which the other specimens were compared. Furthermore, in order to eliminate the influence of the geometrical variability between specimens, the aforementioned loads were normalised by the thickness t and width b of each flange. The mean and COV values of the comparative load ratios, grouped by printing strategy, are presented in Table 5.7.

Table 5.7. Comparisons between the yield loads of the four different printing strategies

Printing strategy i		$\frac{F_{y,C,i}}{tb} \Big/ \frac{F_{y,C,C\text{-}R}}{tb}$	$\frac{F_{y,BL,i}}{tb} \Big/ \frac{F_{y,BL,C\text{-}R}}{tb}$	$\frac{F_{y,B,i}}{tb} \Big/ \frac{F_{y,B,C\text{-}R}}{tb}$	$\frac{F_{coll,test,i}}{tb} \Big/ \frac{F_{coll,\,test,C\text{-}R}}{tb}$
C-R	Mean	1.00	1.00	1.00	1.00
	COV	-	-	-	-
I-R	Mean	0.93	1.18	1.07	1.09
	COV	0.21	0.13	0.12	0.12
C-S	Mean	0.77	0.87	0.99	0.94
	COV	0.17	0.15	0.16	0.11
I-S	Mean	0.78	0.95	1.01	0.96
	COV	0.15	0.14	0.20	0.14

Key: C-R = Continuously printed with rounded corners, I-R = Flanges and web individually printed with rounded corners, C-S = Continuously printed with sharp corners, I-S= Flanges and web individually printed with sharp corners

The plastic resistances $F_{coll,test}$ of the T-stubs with rounded corners were found to be higher than those with sharp corners, due to the length of the lever between the bolt hole and the web-to-flange conjunction (i.e. the distance between the two plastic hinges, marked as m in Figure 5.2) being reduced because of the gradual flange-to-web transition. Furthermore, the T-stubs printed in two steps (first the flange and then the web) exhibited higher plastic resistances than the continuously printed ones, regardless of the type of corner. Overall, the I-R type specimens exhibited the strongest performance, with their plastic resistances being up to 15% higher than the weakest specimen type (i.e. C-S type).

Similarly, given that the loads corresponding to the formation of plastic hinges at the web-to-flange junctions and at the bolt lines are closely related to the distance m, the highest values of $F_{y,C}$ and $F_{y,BL}$ were attained by the specimens with rounded corners. Furthermore, the bolt line yield loads $F_{y,BL}$ were higher for the specimens printed in two steps (rather than continuously), with the values of $F_{y,BL}$ for the I-R type specimens being 18% higher on average than the C-R

type specimens, and for the I-S type specimens being 8% higher on average than the C-S type specimens.

The yield loads at the web-to-flange junction $F_{y,C}$ of the I-R type specimens were found to be 7% lower on average than the C-R type specimens. This is attributed to the more pronounced flange bowing that arose in the specimens printed in two steps, leading to a delay in the development of prying action and, thus, to premature yielding at the conjunction.

Finally, the loads corresponding to bolt yield $F_{y,B}$ of the I-R type specimens were noticeably higher (about 7% on average) than of all other specimens, while almost similar bolt yield loads were obtained for the C-R, C-S and I-S type specimens. This is attributed to the higher levels of bending that developed as a result of the flange rotation for all specimen types apart from the I-R type, where the least rotation arose due to the high rotational stiffness of the conjunction, leading to the bolt being mainly subjected to tension.

5.6. Design equations

Design equations for T-stubs with two bolts in a row are provided in Eurocode 3 Part 1.8 (2021), along with the definition of the effective length, which depends on the yield line mechanism that develops in the T-stub flange. For T-stubs with four bolts in a row, design equations have been provided by Demonceau et al. in (Demonceau et al., 2010), while the recommended effective length can be found in (Latour et al., 2014).

5.6.1. Yield line pattern and effective length

According to Eurocode 3 Part 1-8 (2021), three main types of yield line pattern can occur in T-stub flanges, namely beam, circular and non-circular patterns – see Figure 5.16. The effective length of the yield line depends on the considered pattern and can be calculated as a function of the geometrical properties. For T-stubs with two bolts in a row, the effective length l_{eff} of the beam, non-circular and circular patterns are given by Equations (5.4), (5.5) and (5.6) respectively.

$$l_{eff,bp} = b \tag{5.4}$$

$$l_{eff,np} = 4m + 1.25n \tag{5.5}$$

$$l_{eff,cp} = \min(2\pi m; \pi m + 2e) \tag{5.6}$$

where

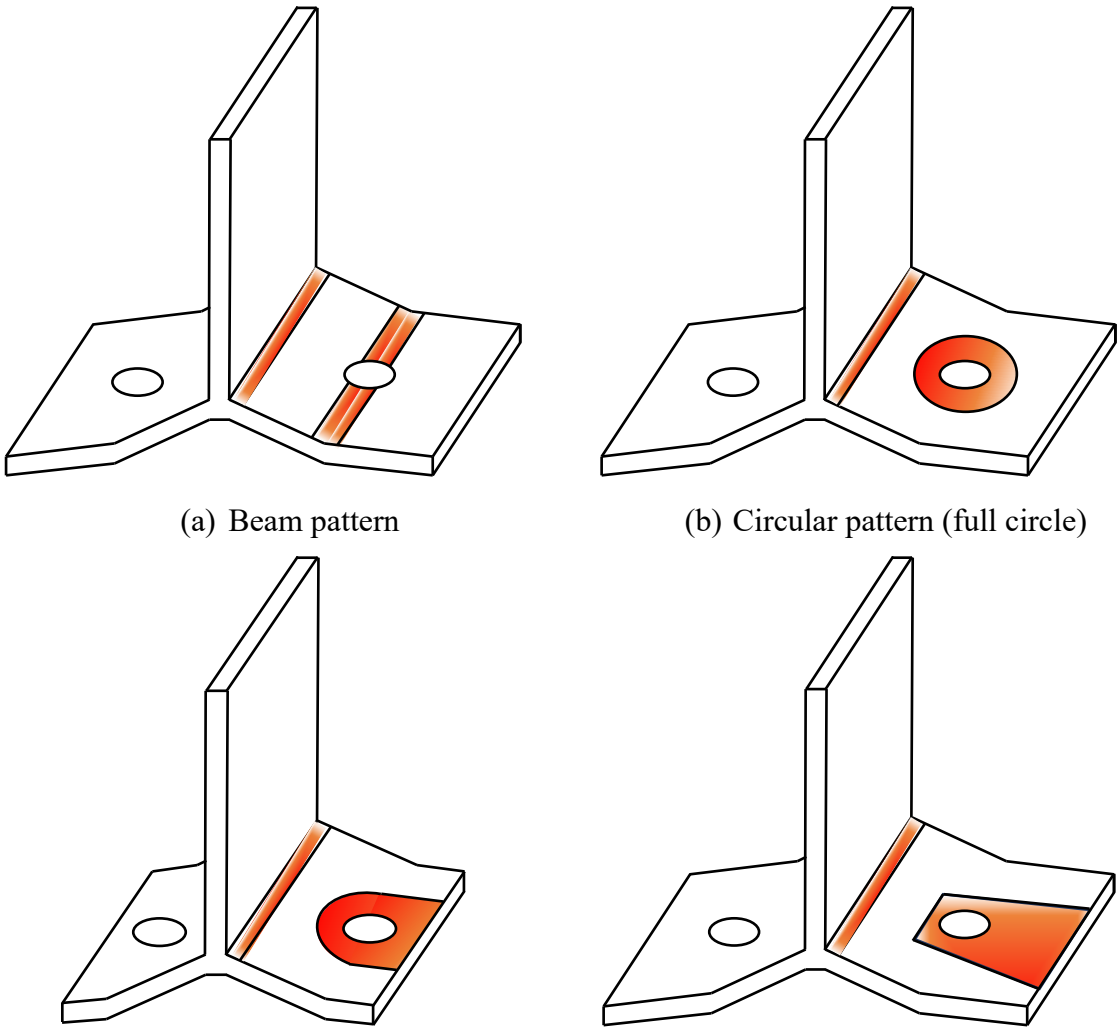
$$n = \min(e; 1.25m) \tag{5.7}$$

The subscripts *bp*, *np* and *cp* denote the beam, non-circular and circular yield line mechanisms, respectively, and n is the distance between the bolt hole centre and the position of the prying force (which is normally at the flange tip), but with $n < 1.25m$. Yielding in a beam or non-circular yield pattern usually indicates a Mode 1 or 2 failure, while a circular yield line pattern can only be observed in Mode 1 failure. Thus:

$$l_{\text{eff},1} = \min(l_{\text{eff,bp}}; l_{\text{eff,np}}; l_{\text{eff,cp}}) \tag{5.8}$$

$$l_{\text{eff},2} = \min(l_{\text{eff,bp}}; l_{\text{eff,np}}) \tag{5.9}$$

where $l_{\text{eff},1}$ and $l_{\text{eff},2}$ are the effective lengths that can potentially cause Mode 1 or 2 failure, respectively.



(a) Beam pattern (b) Circular pattern (full circle)

(c) Circular pattern (circular individual end) (d) Non-circluar

Figure 5.16. Theoretical yield line patterns: (a) beam, (b) circular with full circle, (c) circular individual end and (d) non-circular

In (Latour et al., 2014), it was concluded that Equations (5.4) and (5.6) remain applicable to T-stubs with four bolts in a row, while Equation (5.5) can only be used for the determination of the effective length corresponding to Mode 1. For Mode 2, the effective length for non-circular patterns is given by:

$$l_{\text{eff,np}} = 5.685m + 5.867n \tag{5.10}$$

in which

$$n = \min(e_1 + e_2; 1.25m) \tag{5.11}$$

5.6.2. Plastic collapse load predictions

In line with EN 1993-1-8 (2021), for T-stubs with two bolts in a row, the design plastic resistances F_{Rd} for the three modes illustrated in Figure 2.13 in Chapter 2 are defined as:

Mode 1: $$F_{Rd,1} = \frac{(8n - 2e_w)M_{pl,1}}{2mn - e_w(m+n)} \tag{5.12}$$

Mode 2: $$F_{Rd,2} = \frac{2M_{pl,2} + n\sum F_{T,Rd}}{m+n} \tag{5.13}$$

Mode 3: $$F_{Rd,3} = \sum F_{T,Rd} \tag{5.14}$$

in which

$$e_w = \frac{d_w}{4} \tag{5.15}$$

where $M_{pl,1}$ and $M_{pl,2}$ can be calculated by Equation (5.3) using $L_{eff,1}$ and $L_{eff,2}$, respectively, $\sum F_{T,Rd}$ is the design resistance of all of the bolts in tension and d_w is the diameter of the bolt head.

Additionally, for the special case where no prying forces develop, the design resistance $F_{Rd,np}$ can be calculated using Equation(5.16):

$$F_{Rd,2} = \frac{2M_{pl,1}}{m} \tag{5.16}$$

For T-stubs with four bolts in a row, Equation(5.12), which should be used in conjunction with Equation(5.11), remains applicable for Mode 1, since the location of the plastic hinges is essentially unchanged – see Figure 2.14(a) in Chapter 2. Similarly, Equation (5.14) can be used for Mode 3, with a reduction factor of 0.9.

Finally, the equation accounting for the contribution of the outer bolts for Mode 2 is:

$$F_{Rd,2} = \frac{2M_{pl,2} + \frac{\sum F_{T,Rd}}{2}\left(\frac{n_1^2 + 2n_2^2 + 2n_1n_2}{n_1+n_2}\right)}{m + n_1 + n_2} \tag{5.17}$$

where $n_1 = e_1$ and $n_2 = e_2$ with $n_2 \leq 1.25m + n_1$.

5.7. Comparisons between test results and design equations

Comparisons are now made between the test results and the plastic resistance predictions determined using the equations introduced in Section 5.6, based on the measured geometric

and material properties. The obtained test-to-prediction resistance ratios are presented in Tables 5.5 and 5.6 for the T-stubs with two bolts and four bolts in a row, respectively. Note that since the design plastic resistances for Mode 1 ($F_{Rd,1}$) and Mode 2 ($F_{Rd,2}$) correspond to yielding at the bolt line and in the bolt respectively, the value of $F_{Rd,1}$, obtained from Equation (5.12), are compared against $F_{y,BL}$ (see Section 4.2), while $F_{Rd,2}$, calculated using Equations (5.13) or (5.17) for the T-stubs with two bolts or four bolts in a row, respectively, are compared against $F_{y,B}$ (see Section 4.2). Meanwhile, the design resistance $F_{Rd,np}$, obtained from Equation (5.16), is evaluated against $F_{y,C}$ (corresponding to yielding at the web-to-flange conjunctions – see Section 4.2), due to the absence of prying forces at the early stages of loading.

5.7.1. T-stubs with two bolts in a row

The plastic resistances associated with yielding at the bolt lines for the examined T-stubs with two bolts in a row were generally underestimated by Equation (5.12), with a mean test-to-prediction ratio of 1.12 and a COV of 0.24. On the contrary, the plastic resistances associated with yielding of the bolts were accurately predicted by Equation (5.13), with a slight overestimation of only 2% on average and a COV of 0.15.

Only a limited number of specimens failed in Mode 1, the majority of which were the T-stubs with sharp corners, due to the larger values of m, as discussed in Section 5.5. Generally, the specimen capacities were found to be underestimated by Equation (5.12) when the failure mode was correctly predicted, but overestimated when the failure mode was wrongly predicted. The variability in the prediction accuracy is believed to relate primarily to the value of the distance m, which is the distance between the two plastic hinges (i.e. at the web-to-flange conjunction and the bolt line). Eurocode 3 assumes that the plastic hinge at the bolt line always lies across the centre of the bolt hole, while, in reality, its location is also dependent on the strength of the bolt. In addition, the plastic hinge at the web-to-flange conjunction is assumed to be located at a distance of $0.8a$ from the web, as illustrated in Figure 5.2, while this location can vary depending on the specimen geometry. Note also that equations for T-stubs with sharp corners are not explicitly included in Eurocode 3.

For Mode 2, Equation (5.13) generally overestimated the capacities of the T-stubs that were printed continuously, with a mean test-to-prediction ratio of 0.84 and 0.96 and COVs of 0.15 and 0.09 for the T-stubs with rounded and sharp corners respectively. Conversely, Equation (5.13) yielded conservative predictions for the T-stubs that were printed in two steps

(individually), underestimating the capacity of the specimens with rounded and sharp corners by 6% and 5% on average, respectively, with COVs of 0.13 and 0.09, respectively.

5.7.2. T-stubs with four bolts in a row

Comparisons between the capacity predictions given by Equations (5.12) and (5.17) for the yield loads at the bolt line and the bolt, respectively, are presented in Table 5.6. It can be seen that the failure modes were generally accurately predicted. As also observed for the T-stubs with two bolts, Equation (5.12) provided conservative capacity predictions, except when the failure modes were not correctly predicted. Meanwhile, Equation (5.17), which has been specifically devised for T-stubs with four bolts in a row, yielded accurate predictions with only very few exceptions.

5.7.3. Yielding at the web-to-flange conjunction

The test-to-predicted capacity ratios presented in Tables 5.5 and 5.6 show that Equation (5.16) significantly underestimated the yield load at the web-to-flange junction, by 50% and 42% on average for the T-stubs with two bolts and four bolts in a row, respectively. This underestimation is attributed to the fact that Equation (5.16) simplifies the force applied to the flange by the bolt head as a point load applied at the centre of the bolt hole.

An improved model, replicating the force from the bolt head as a point load applied at the bolt head edge (closer to the T-stub web) as shown in Figure 5.17, is thus proposed for the determination of the load $F_{\mathrm{Rd,prop}}$ corresponding to yielding at the conjunction:

$$F_{\mathrm{Rd,prop}} = \frac{2M_{\mathrm{pl}}}{m - d_{\mathrm{w}}/2} \tag{5.18}$$

The test-to-prediction ratios yielded by Equation (5.18) are presented in Tables 5.5 and 5.6. It can be observed that, despite the slightly larger scatter, Equation (5.18) yields considerably more accurate results than Equation (5.16), with a mean ratio of 0.93 for the T-stubs with two bolts in a row, and with a mean ratio of 0.99 for the T-stubs with four bolts in a row.

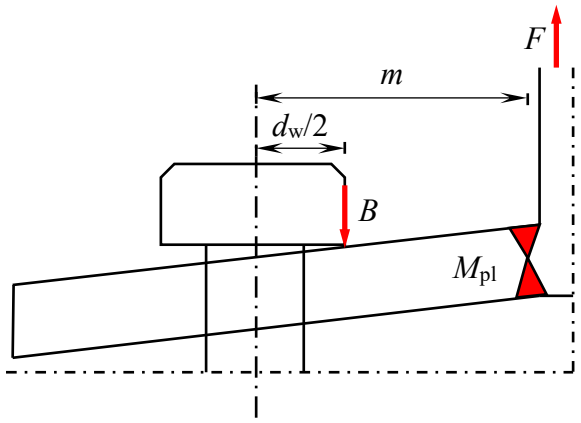


Figure 5.17. Improved model recognising the influence of the bolt head size

F = applied load, B = force at the bolt head.

5.8. Conclusions

Eighty tests on WAAM T-stub connections of different printing strategies, bolt configurations and dimensions have been carried out. The development of plastic hinges at critical locations on the T-stub flanges was thoroughly analysed, and a method for the identification of their occurrence has been established. It was found that the first plastic hinge always forms at web-to-flange junction, followed by yielding of either the bolt line or the bolt, with the first to occur determining the failure mode and collapse load of the connection.

Initial gaps between the T-stub flanges, occurring due to the WAAM surface undulations and bowing of the flanges, were found to lead to a reduction in stiffness and premature yielding at the web-to-flange conjunctions due to the absence of prying forces. Following yielding at the web-to-flange conjunction, contact between the flanges was established, leading to a recovery in stiffness until yielding at the second location took place.

It was found that the printing strategy can have a significant influence on the load-carrying capacity of WAAM T-stub connections. The T-stubs with rounded corners were generally stronger than those with sharp corners, while the specimens printed in two steps, rather than continuously, exhibited the highest plastic resistances due to their higher cooling rate.

Finally, the test results were used to evaluate the applicability of current design equations for conventionally manufactured T-stub connections. For the T-stubs with two bolts in a row, the plastic resistance of Mode 1 was found to be underestimated by Eurocode 3, while rather

accurate predictions were yielded for Mode 2. Similarly, for the T-stubs with four bolts in a row, conservative capacity predictions were obtained for Mode 1 when the equations of Eurocode 3 were used, while an equation proposed in the literature, specifically devised for T-stubs with 4 bolts, provided slightly unconservative results. The yield load at the web-to-flange conjunction calculated using the Eurocode 3 equation not accounting for prying actions was found to lead to overly conservative predictions. Thus, a new equation has been proposed, accounting for the bolt head size, resulting in more accurate capacity predictions.

Overall, this chapter illustrates the feasibility of producing structural steel connections using WAAM and demonstrates that sound structural performance can be achieved. This paves the way for the establishment of more optimised connections that can fully exploit the geometric freedom afforded by WAAM.

6. Conclusions and Future Research

6.1. Conclusions

WAAM bolted connections, in conjunction with conventionally manufactured structural members in structural steel frames, have the potential to enable more automated construction and repair, thanks to their versatility and ease of fabrication while reducing the material consumption and wastage. Despite the promising potential demonstrated by metal WAAM and its growing use in many sectors, it has only recently begun to gain traction in the construction industry and started to receive attentions from researchers. The primary objective of this thesis was to investigate experimentally the structural behaviour of WAAM bolted connections and evaluate the applicability of currently design standards.

Single-lap shear bolted connections are one of the most common type of joints applied in steel structures. Their structural behaviour was first investigated through a series of destructive tests where a total of 60 specimens were tested to failure, which were described in detail in Chapter 3. Conventional failure modes such as net section tension and shear-out were identified and discussed. Bearing failure, on the other hand, was found to be less likely to develop in single-lap shear connections due to the curling effect. Instead, localised tearing would develop when the connected plate was dimensioned to avoid net section tension and shear-out failure. Curl-bearing failure was a newly identified type of failure mode that featured the bolt head penetrating the plate downstream of the bolt hole, which could occur on the specimens with long end distance. Severe curling was evidenced on most of the specimens. It was assumed that the inherent surface undulation of the WAAM specimens additionally fuelled the occurrence of curling. Generally, the ultimate load-carrying capacity of the tested specimens was well predicted by the current design standards for structural/hot-rolled (AISC 360 and EN 1993-1-8) and cold-formed (AISI S100 and AS/NZS 4600), among which AS/NZS 4600 yielded the

most accurate capacity predictions. However, noticeable shortcomings still exist in the design standards, since the localised tearing and curl-bearing failure are not included, resulting in poorly predicted failure loads for some specimens. In addition, print layer orientations showed little influence on the failure load, which indicates that the same structural design equations can be applied for both print layer orientations.

Chapter 4 presented an experimental investigation into WAAM double-lap shear bolted connections. A total of 60 specimens were tested to failure. Conventional failure modes such as shear-out, net section tension and bearing were evidenced and discussed in detail. End-splitting failure was also evidenced, and the print layer orientation was found to promote the occurrence of this failure mode. Otherwise, the print layer orientation showed an insignificant effect on the ultimate capacities of the specimens. Meanwhile, unlike in the single-lap shear tests, out-of-plane deformation of the plates (i.e. curling) was restricted. The failures such as localised tearing and curl-bearing could therefore not develop. As for the failure load predictions yielded by the design standards, the structural/hot-rolled steel specifications (AISC 360 and EN 1993-1-8) were found to be more accurate than the cold-formed steel specifications (AISI S100 and AS/NZS 4600). This is because that while all specifications significantly overestimated the shear-out strengths, net section tension and bearing strengths were more accurately predicted by the structural/hot-rolled steel specifications. Also, while the end-splitting failure has not yet been included in any specifications, the failure load could be accurately predicted by AS/NZS 4600 – a cold-formed steel specification, using the shear-out equation.

An experimental investigation into WAAM T-stub bolted connections was presented in Chapter 5. A total of 80 T-stub connections, including 52 T-stub with two bolts and 28 T-stubs with four bolts in a row, manufactured using four different printing strategies, were tested to failure. A new analysis approach, based on the moment-strain response at critical locations on the flanges and the load-elongation responses of bolts, was used for the investigation of the development of failure mechanisms, namely complete flange yield and combined flange and bolt yield. It was found that the prying force played an important role on the development of the plastic hinges in the flanges. Initial gaps between the flanges occurring due to WAAM surface undulations and flange bowing could result in the absence of prying forces at the early stages of loading, leading to the premature yield of the T-stubs. Meanwhile, it was found that the printing strategies significantly influenced the performance of the T-stub connections, while the webs and flanges that were separately printed with rounded web-to-flange transitions

demonstrated the best structural performances. Overall, the structural behaviour of the examined WAAM T-stubs, analysed using the proposed methods, were generally in line with the predictions yielded by Eurocode 3 Part 1-8 and by the literature.

6.2. Suggestions for future research

Although the findings of the thesis have demonstrated that WAAM bolted connections generally exhibit the anticipated behavioural trends, and the current design standards were able to provide relatively accurate capacity predictions, to ensure the safety of the design and applications, further research is required to assess reliability and to derive suitable safety factors.

6.2.1. Different steel grade and type

The current test programme employed EN ISO 14341-A (2010): G 42 4 M21 3Si1 steel welding wire (grade S235). In order to expand the use of WAAM connections into different loading scenarios and to develop comprehensive design guidance, tests on different steel grades are suggested. Meanwhile, tests on WAAM stainless steel bolted connections are also suggested since the great ductility and pronounced strain hardening provided by stainless steel can result in rather different structural behaviour. Also, unlike the carbon steel examined herein, WAAM stainless steel has been found to exhibit high anisotropy, which could result in substantial differences in behaviour between the printing strategies. Relevant experiments are required.

6.2.2. Dynamic tests on WAAM bolted connections

A comprehensive understanding of the structural response of WAAM bolted connections under dynamic loading is essential for wider use. While the behaviour of connections under static loading was thoroughly investigated, dynamic tests were not covered by the current test programme. Therefore, tests on WAAM bolted connections under dynamic loading are suggested for the future investigations.

6.2.3. Numerical analysis and parametric study

Although a great number of physical tests on WAAM connections has been conducted, numerical simulations are suggested to further expand the data pool. Meanwhile, in order to investigate the fracture mechanism in lap shear connections, fracture simulation is recommended to be included in the finite element analysis.

6.2.4. Topological optimisation

Finally, the potential of topological optimisation provided by WAAM can be further explored through both numerical simulations and experiments. By optimising the shape of bolted connections, potentially less material will be used while more uniform stress distributions can be obtained, and ultimately higher load-carrying capacities can be reached.

References

3D Systems (2017) *Geomagic Wrap*.

Aalberg, A. & Larsen, P.K. (2001) Bearing strength of bolted connections in high strength steel. In: *Construction Conference*. 2001 Helsinki: Helsinki University of Technology. pp. 859–866.

Aalberg, A. & Larsen, P.K. (2002) The effect of steel strength and ductility on bearing failure of bolted connections. In: *European Conference on Steel Structures*. 2002 pp. 869–878.

AISC 360 (2016) *Specification for structural steel buildings*. American Institute of Steel Construction, Chicago.

AISI S100 (2016) *North American Specification for the Design of Cold-Formed Steel Structural Members*. American Iron and Steel Institue, Washington DC.

Alonso, U., Veiga, F., Suárez, A. & Artaza, T. (2020) Experimental investigation of the influence of wire arc additive manufacturing on the machinability of titanium parts. *Metals*. 10 (1).

Arana, M., Ukar, E., Rodriguez, I., Aguilar, D. & Álvarez, P. (2022) Influence of deposition strategy and heat treatment on mechanical properties and microstructure of 2319 aluminium WAAM components. *Materials and Design*. 221.

AS/NZS 4600 (2018) *Cold-formed steel structures*. Australian/New Zealand Standard, Sydney.

Attar, H., Bermingham, M.J., Ehtemam-Haghighi, S., Dehghan-Manshadi, A., Kent, D. & Dargusch, M.S. (2019) Evaluation of the mechanical and wear properties of titanium produced by three different additive manufacturing methods for biomedical application. *Materials Science and Engineering A*. 760, 339–345.

Berrospi Aquino, G.J., Gómez Amador, A.M., Alencastre Miranda, J.H. & Jiménez de Cisneros Fonfría, J.J. (2021) A review of the t-stub components for the analysis of bolted moment joints. *Applied Sciences (Switzerland)*. 11 (22).

Buchanan, C. & Gardner, L. (2019) Metal 3D printing in construction: A review of methods, research, applications, opportunities and challenges. *Engineering Structures*.180 pp.332–348.

Chi, J., Cai, Z., Wan, Z., Zhang, H., Chen, Z., Li, L., Li, Y., Peng, P. & Guo, W. (2020) Effects of heat treatment combined with laser shock peening on wire and arc additive manufactured Ti17 titanium alloy: Microstructures, residual stress and mechanical properties. *Surface and Coatings Technology*. 396.

Cho, Y.H., Teh, L.H. & Young, B. (2021) Effects of material ductility and cooling methods on the bearing strength of steel bolted connections. *Journal of Constructional Steel Research*. 181.

Coelho, A.M.G., Bijlaard, F.S.K., Gresnigt, N. & da Silva, L.S. (2004) Experimental assessment of the behaviour of bolted T-stub connections made up of welded plates. *Journal of Constructional Steel Research*. 60 (2), 269–311.

Couchaux, M., Hjiaj, M., Ryan, I. & Bureau, A. (2017) Effect of contact on the elastic behaviour of tensile bolted connections. *Journal of Constructional Steel Research*. 133, 459–474.

Dassault Systèmes Corp. (2019) *Abaqus*.

Demonceau, J.F., Weynand, K., Jaspart, J.P. & Müller, C. (2010) Application of eurocode 3 to steel connections with four bolts per horizontal row. *Proceedings of SDSS' Rio 2010: International Colloquium Stability and Ductility of Steel Structures*. 1, 199–206.

Derekar, K., Lawrence, J., Melton, G., Addison, A., Zhang, X. & Xu, L. (2019) Influence of Interpass Temperature on Wire Arc Additive Manufacturing (WAAM) of Aluminium Alloy Components. *MATEC Web of Conferences*. 269, 05001.

Dhalla, A.K., Errera, S.J. & Winter, G. (1971) Connections in thin low-ductility steels. *Journal of Structural Engineering, ASCE*. 97 (10), 2549–2566.

Dörrie, R., Laghi, V., Arrè, L., Kienbaum, G., Babovic, N., Hack, N. & Kloft, H. (2022) Combined Additive Manufacturing Techniques for Adaptive Coastline Protection Structures. *Buildings*. 12 (11), 1806.

Douty, R. & McGuire, W. (1965) High strength bolted moment connections. *J. Struct. Div. ASCE*. 91, 101–128.

EN 1993-1-1 (2020) *Eurocode 3. Design of steel structures. Part 1-1: General rules and rules for buildings*. In: European Committe for Standardization, Brussels. p.

EN 1993-1-8 (2021) *Eurocode 3. Design of steel structures. Part 1-8: Design of joints*. In: European Committe for Standardization, Brussels. p.

EN ISO 6892-1: 2019 (2019) *Metallic materials – tensile testing, part 1: Method of test at room temperature*. In: International Organization for Standardization. p.

Faella, C., Piluso, V. & Rizzano, G. (1998) Experimental Analysis of Bolted Connections: Snug versus Preloaded Bolts. *Journal of Structural Engineering*. 124 (7), 765–774.

Faralli, A.C., Latour, M., Tan, P.J., Rizzano, G. & Wrobel, P. (2021) Experimental investigation and modelling of T-stubs undergoing large displacements. *Journal of Constructional Steel Research*. 180.

Faro (2018) *FARO Design ScanArm 2.0 ®*.

Feucht, T., Lange, J., Waldschmitt, B., Schudlich, A.K., Klein, M. & Oechsner, M. (2020) Welding process for the additive manufacturing of cantilevered components with the WAAM. In: *Advanced Structured Materials*. Springer. pp. 67–78.

Feucht, T., Waldschmitt, B., Lange, J. & Erven, M. (2022) Additive manufacturing of a bridge in situ. *Steel Construction*. 15 (2), 100–110.

Fisher, J.W. & Struik, J.H. (1974) *Guide to design criteria for boltede and riveted joints*.

Galjaard, S., Hofman, S., Perry, N. & Ren, S. (2015) Optimizing Structural Building Elements in Metal by using Additive Manufacturing. In: *IASS Future Visions 2015*. 2015 Amsterdam. p.

Galjaard, S., Hofman, S. & Ren, S. (2015) New Opportunities to Optimize Structural Designs in Metal by Using Additive Manufacturing. In: *Advances in Architectural Geometry 2014*. Springer International Publishing. pp. 79–93.

Gao, W., Zhang, Y., Ramanujan, D., Ramani, K., Chen, Y., Williams, C.B., Wang, C.C.L., Shin, Y.C., Zhang, S. & Zavattieri, P.D. (2015) The status, challenges, and future of additive manufacturing in engineering. *CAD Computer Aided Design*. 69, 65–89.

Gardner, L. (2023) Metal additive manufacturing in structural engineering – review, advances, opportunities and outlook. *Structures*. 47, 2178–2193.

Gardner, L., Kyvelou, P., Herbert, G. & Buchanan, C. (2020) Testing and initial verification of the world's first metal 3D printed bridge. *Journal of Constructional Steel Research*. 172.

Goverdhan, A.V. (1984) *A Collection of Experimental Moment-rotation Curves and Evaluation of Prediction Equations for Semi-rigid Connections*. Vanderbilt University, Nashville.

Gradl, P.R., Greene, S.E., Protz, C., Bullard, B., Buzzell, J., Garcia, C., Wood, J., Cooper, K., Hulka, J. & Osborne, R. (2018) Additive manufacturing of liquid rocket engine combustion devices: A summary of process developments and hot-fire testing results. In: *2018 Joint Propulsion Conference*. 2018 American Institute of Aeronautics and Astronautics Inc, AIAA. p.

Grand View Research, Inc. (2022) *Additive Manufacturing Market Size, Share & Trends Analysis Report By Component, By Printer Type, By Technology, By Software, By Application, By Vertical, By Material, By Region, And Segment Forecasts, 2022 - 2030*.

Guo, H., Xie, Y., Liu, Y. & Yang, D. (2020) Study on mechanical behavior of Q690D high strength steel bearing-type bolted connections. *Structures*. 23, 588–601.

Guo, N. & Leu, M.C. (2013) Additive manufacturing: Technology, applications and research needs. *Frontiers of Mechanical Engineering*.8 (3) pp.215–243.

Hadjipantelis, N., Weber, B., Buchanan, C. & Gardner, L. (2022) Description of anisotropic material response of wire and arc additively manufactured thin-walled stainless steel elements. *Thin-Walled Structures*. 171.

Horgar, A., Fostervoll, H., Nyhus, B., Ren, X., Eriksson, M. & Akselsen, O.M. (2018) Additive manufacturing using WAAM with AA5183 wire. *Journal of Materials Processing Technology*. 259, 68–74.

Huang, C., Kyvelou, P., Zhang, R., ben Britton, T. & Gardner, L. (2022a) Mechanical testing and microstructural analysis of wire arc additively manufactured steels. *Materials and Design*. 216.

Huang, C., Meng, X., Buchanan, C. & Gardner, L. (2022b) Flexural Buckling of Wire Arc Additively Manufactured Tubular Columns. *Journal of Structural Engineering*. 148 (9).

Huang, C., Meng, X. & Gardner, L. (2022) Cross-sectional behaviour of wire arc additively manufactured tubular beams. *Engineering Structures*. 272, 114922.

ISO 14341: 2010 (2010) *Welding consumables - Wire electrodes and weld deposits for gas shielded metal arc welding of non alloy and fine grain steels - Classification*. In: International Organization for Standardization. p.

ISO/ASTM (2017) *ISO/ASTM 52900:2017. Additive manufacturing -- General principles -- Terminology*. In: ISO/ASTM International. p.

Jiang, K., Zhao, O. & Tan, K.H. (2020) Experimental and numerical study of S700 high strength steel double shear bolted connections in tension. *Engineering Structures*. 225, 111175.

Kamtekar, A.G. (2012) On the bearing strength of bolts in clearance holes. *Journal of Constructional Steel Research*. 79, 48–55.

Kanyilmaz, A., Demir, A.G., Chierici, M., Berto, F., Gardner, L., Kandukuri, S.Y., Kassabian, P., Kinoshita, T., Laurenti, A., Paoletti, I., du Plessis, A. & Razavi, S.M.J. (2022) Role of metal 3D printing to increase quality and resource-efficiency in the construction sector. *Additive Manufacturing*.50.

Kim, H.J. & Yura, J.A. (1999) The effect of ultimate-to-yield ratio on the bearing strength of bolted connections. *Journal of Constructional Steel Research*. 49, 255–269.

Kulak, G.L., Fisher, J.W., Struik, J.H.A. & Fisher, J.W. (1987) *Guide to design criteria for bolted and riveted joints*. Wiley.

Kumar, S.P.K., Elangovan, S., Mohanraj, R. & Ramakrishna, J.R. (2021) A review on properties of Inconel 625 and Inconel 718 fabricated using direct energy deposition. In: *Materials Today: Proceedings*. 2021 Elsevier Ltd. pp. 7892–7906.

Kyvelou, P., Huang; Cheng, Gardner; Leroy, Asce, M. & Buchanan, C. (2021) *Structural Testing and Design of Wire Arc Additively Manufactured Square Hollow Sections*.

Kyvelou, P., Slack, H., Daskalaki Mountanou, D., Wadee, M.A., Britton, T. ben, Buchanan, C. & Gardner, L. (2020) Mechanical and microstructural testing of wire and arc additively manufactured sheet material. *Materials and Design*. 192.

LaBoube, R.A. (1988) Strength of Bolted Connections: Is It Bearing Or Net Section? In: *9th International Specialty Conference on Cold-Formed Steel Strcutres*. 1988 pp. 589–601.

Laghi, V., Palermo, M., Gasparini, G., Girelli, V.A. & Trombetti, T. (2020) Experimental results for structural design of Wire-and-Arc Additive Manufactured stainless steel members. *Journal of Constructional Steel Research*. 167.

Laghi, V., Tonelli, L., Palermo, M., Bruggi, M., Sola, R., Ceschini, L. & Trombetti, T. (2021) Experimentally-validated orthotropic elastic model for Wire-and-Arc Additively Manufactured stainless steel. *Additive Manufacturing*. 42.

Lange, J., Feucht, T. & Erven, M. (2020) 3D printing with steel: Additive Manufacturing for connections and structures. *Steel Construction*. 13 (3), 144–153.

Latour, M., Rizzano, G., Santiago, A. & Simoes, D.S.L. (2014) Experimental analysis and mechanical modeling of T-stubs with four bolts per row. *Journal of Constructional Steel Research*. 101, 158–174.

LaVision (2017) *DaVis*.

Leal, R., Barreiros, F.M., Alves, L., Romeiro, F., Vasco, J.C., Santos, M. & Marto, C. (2017) Additive manufacturing tooling for the automotive industry. *International Journal of Advanced Manufacturing Technology*. 92 (5–8), 1671–1676.

Lin, X.M., Yam, M.C.H., Chung, K.F. & Lam, A.C.C. (2021) A study of net-section resistance of high strength steel bolted connections. *Thin-Walled Structures*. 159, 107284.

Liu, J., Xu, Y., Ge, Y., Hou, Z. & Chen, S. (2020) Wire and arc additive manufacturing of metal components: a review of recent research developments. *The International Journal of Advanced Manufacturing Technology*. 111, 149–198.

Liu, M., Zhu, X., Wang, P., Tuoya, W. & Hu, S. (2017) Tension strength and design method for thread-fixed one-side bolted T-stub. *Engineering Structures*. 150, 918–933.

Može, P. (2018) Bearing strength at bolt holes in connections with large end distance and bolt pitch. *Journal of Constructional Steel Research*. 147, 132–144.

Može, P. (2020) Statistical evaluation of bearing resistance and related strength functions for bolted connections. *Journal of Constructional Steel Research*. 171, 106128.

Može, P. & Beg, D. (2014) A complete study of bearing stress in single bolt connections. *Journal of Constructional Steel Research*. 95, 126–140.

Može, P. & Beg, D. (2010) High strength steel tension splices with one or two bolts. *Journal of Constructional Steel Research*. 66 (8–9), 1000–1010.

MX3D (2021) *About – MX3D*. 15 March 2021. https://mx3d.com.

Nair, R.S., Birkemoe, P.C. & Munse, W.H. (1974) High strength bolts subject to tension and prying. *Journal of the Structural Division*. 100 (2), 351–372.

Nethercot, D.A. & Zandonini, R. (1989) Methods of prediction of joint behaviour: Beam-to-column connections. In: R. Narayanan (ed.). *Structural connections Stability and Strength*. Elsevier Science Pubilishers Ltd, Essex. p.

Ng, C.H., Bermingham, M.J., Kent, D. & Dargusch, M.S. (2021) High stability and high strength β-titanium alloys for additive manufacturing. *Materials Science and Engineering A*. 816.

Onuike, B. & Bandyopadhyay, A. (2019) Additive manufacturing in repair: Influence of processing parameters on properties of Inconel 718. *Materials Letters*. 252, 256–259.

Owens, G.W. & Cheal, B.D. (1989) *Structural steelwork connections*. Courier International Ltd, Tiptree, Essex.

Owens, G.W. & Dowling, P.J. (1976) *Bearing stresses in connections using grade 8.8 bolts, unpublished test report*.

Özkılıç, Y.O. (2021) The capacities of unstiffened T-stubs with thin plates and large bolts. *Journal of Constructional Steel Research*. 186.

Packer, J.A. & Morris, L.J. (1977) A limite state design method for the tension region of bolted beam-column connections. *Struct. Eng.* 55, 446–458.

Piluso, V., Faella, C. & Rizzano, G. (2001) ULTIMATE BEHAVIOR OF BOLTED T-STUBS. II: MODEL VALIDATION. *Journal of Structural Engineering*. 127 (6), 694–704.

du Plessis, A. & Macdonald, E. (2020) Hot isostatic pressing in metal additive manufacturing: X-ray tomography reveals details of pore closure. *Additive Manufacturing*. 34.

du Plessis, A., Yadroitsava, I. & Yadroitsev, I. (2020) Effects of defects on mechanical properties in metal additive manufacturing: A review focusing on X-ray tomography insights. *Materials and Design*.187.

Pragana, J.P.M., Sampaio, R.F.V., Bragança, I.M.F., Silva, C.M.A. & Martins, P.A.F. (2021) Hybrid metal additive manufacturing: A state–of–the-art review. *Advances in Industrial and Manufacturing Engineering*.2.

Rex, C.O. & Easterling, W.S. (2003) Behavior and Modeling of a Bolt Bearing on a Single Plate. *Journal of Structural Engineering*. 129 (6), 792–800.

Rhino 3D (2017) *Rhino 3D computer-aided design software* .

Rogers, C.A. & Hancock, G.J. (1999) Bolted connection design for sheet steels less than 1.0 mm thick. *Journal of Constructional Steel Research*.51.

Rogers, C.A. & Hancock, G.J. (2000) Failure modes of bolted-sheet-steel connections loaded in shear. *Journal of Structural Engineering*. 126 (2), 288–296.

Salih, E.L., Gardner, L. & Nethercot, D.A. (2011) Bearing failure in stainless steel bolted connections. *Engineering Structures*. 33 (2), 549–562.

Schuh, G., Bergweiler, G., Lichtenthäler, K., Fiedler, F. & de La Puente Rebollo, S. (2020) Topology optimisation and metal based additive manufacturing of welding jig elements. In: *Procedia CIRP*. 2020 Elsevier B.V. pp. 62–67.

Shah, I.H., Hadjipantelis, N., Walter, L., Myers, R.J. & Gardner, L. (2023) Environmental life cycle assessment of wire arc additively manufactured steel structural components. *Journal of Cleaner Production*. 389, 136071.

Soltani-Tehrani, A., Chen, P., Katsarelis, C., Gradl, P., Shao, S. & Shamsaei, N. (2022) Laser powder directed energy deposition (LP-DED) NASA HR-1 alloy: Laser power and heat treatment effects on microstructure and mechanical properties. *Additive Manufacturing Letters*. 3, 100097.

Talja, A. & Torkar, M. (2014) Lap shear tests of bolted and screwed ferritic stainless steel connections. *Thin-Walled Structures*. 83, 157–168.

Tanvir, A.N.M., Ahsan, M.R.U., Ji, C., Hawkins, W., Bates, B. & Kim, D.B. (2019) Heat treatment effects on Inconel 625 components fabricated by wire + arc additive manufacturing (WAAM)—part 1: microstructural characterization. *International Journal of Advanced Manufacturing Technology*.

Tartaglia, R., D'Aniello, M. & Zimbru, M. (2020) Experimental and numerical study on the T-Stub behaviour with preloaded bolts under large deformations. *Structures*. 27, 2137–2155.

Teh, L.H. & Gilbert, B.P. (2012a) Net Section Tension Capacity of Bolted Connections in Cold-Reduced Steel Sheets. *Journal of Structural Engineering*. 138 (3), 337–344.

Teh, L.H. & Gilbert, B.P. (2012b) Net Section Tension Capacity of Bolted Connections in Cold-Reduced Steel Sheets. *Journal of Structural Engineering*. 138 (3), 337–344.

Teh, L.H. & Uz, M.E. (2015) Ultimate Shear-Out Capacities of Structural-Steel Bolted Connections. *Journal of Structural Engineering*. 141 (6), 04014152.

Teh, L.H. & Uz, M.E. (2017) Ultimate Tilt-Bearing Capacity of Bolted Connections in Cold-Reduced Steel Sheets. *Journal of Structural Engineering*. 143 (4), 04016206.

Uriondo, A., Esperon-Miguez, M. & Perinpanayagam, S. (2015) The present and future of additive manufacturing in the aerospace sector: A review of important aspects. In: *Proceedings of the Institution of Mechanical Engineers, Part G: Journal of Aerospace Engineering*. 18 September 2015 SAGE Publications Ltd. pp. 2132–2147.

Veiga, F., del Val, A.G., Suárez, A. & Alonso, U. (2020) Analysis of the machining process of titanium Ti6Al-4V parts manufactured by wire arc additive manufacturing (WAAM). *Materials*. 13 (3).

Waller, J., Parker, B., Hodges, K., Walker, J. & Burke, E. (2014) *Nondestructive Evaluation of Additive Manufacturing State-of-the-Discipline Report: Tech. Rep. NASA/TM-2014-218560*.

Wang, L., Suo, Y., Liang, Z., Wang, D. & Wang, Q. (2019a) Effect of titanium powder on microstructure and mechanical properties of wire + arc additively manufactured Al-Mg alloy. *Materials Letters*. 241, 231–234.

Wang, Y., Lyu, Y. & Li, G. (2018) Experimental investigation of two-bolt connections for high strength steel members. In: *12th International Conference on Advances in Steel-Concrete Composite Structures*. 2018 Universitat Politecnica de Valencia, València, Spain. pp. 595–600.

Wang, Y.B., Lyu, Y.F., Li, G.Q. & Liew, J.Y.R. (2017) Behavior of single bolt bearing on high strength steel plate. *Journal of Constructional Steel Research*. 137, 19–30.

Wang, Z., Wang, Y., Zhang, Y., Gardner, L. & Ouyang, Y. (2019b) Experimental investigation and design of extruded aluminium alloy T-stubs connected by swage-locking pins. *Engineering Structures*. 200 (August), 109675.

Weynand, K., Jaspart, J.-P. & Steenhuis, M. (1995) The stiffness model of revised Annex J of Eurocode 3. In: *Int. Workshop on Connection in Steel Struct.* 1995 Pergamon. pp. 115–126.

Winter, G. (1956) Tests on Bolted connections in light gage steel. *Journal of the Structural Division*. 82 (2), 1–25.

Wohlers, T. & Gornet, T. (2015) *Wohlers Report 2015*.

World Economic Forum (2016) *Winsun - Demonstrating the Viability of 3D Printing at Construction Scale*.

Wynne, Z., Buchanan, C., Kyvelou, P., Gardner, L., Kromanis, R., Stratford, T. & Reynolds, T.P.S. (2022) Dynamic testing and analysis of the world's first metal 3D printed bridge. *Case Studies in Construction Materials*. 17, e01541.

Xing, H., Teh, L.H., Jiang, Z. & Ahmed, A. (2020a) Shear-Out Capacity of Bolted Connections in Cold-Reduced Steel Sheets. *Journal of Structural Engineering*. 146 (4).

Xing, H., Teh, L.H., Jiang, Z. & Ahmed, A. (2020b) Shear-Out Capacity of Bolted Connections in Cold-Reduced Steel Sheets. *Journal of Structural Engineering*. 146 (4), 04020018.

Xiong, J., Li, Y.J., Yin, Z.Q. & Chen, H. (2018) Determination of surface roughness in wire and arc additive manufacturing based on laser vision sensing. *Chinese Journal of Mechanical Engineering (English Edition)*. 31 (4).

Yapici, O., Theofanous, M., Dirar, S. & Yuan, H. (2021) Behaviour of Ferritic Stainless Steel Bolted T-stubs Under Tension-Part 1: Experimental Investigations. *ce/papers*. 4, 866–875.

Ye, J., Kyvelou, P., Gilardi, F., Lu, H., Gilbert, M. & Gardner, L. (2021) An End-to-End Framework for the Additive Manufacture of Optimized Tubular Structures. *IEEE Access*. 9, 165476–165489.

Yuan, H.X., Gao, J.D., Theofanous, M., Yang, L. & Schafer, B.W. (2020) Initial stiffness and plastic resistance of bolted stainless steel T-stubs in tension. *Journal of Constructional Steel Research*. 173 (July).

Yuan, H.X., Hu, S., Du, X.X., Yang, L., Cheng, X.Y. & Theofanous, M. (2019) Experimental behaviour of stainless steel bolted T-stub connections under monotonic loading. *Journal of Constructional Steel Research*. 152, 213–224.

Zhang, R., Buchanan, C., Matilainen, V.P., Daskalaki-Mountanou, D., Britton, T. ben, Piili, H., Salminen, A. & Gardner, L. (2021) Mechanical properties and microstructure of additively manufactured stainless steel with laser welded joints. *Materials and Design*. 208.

Zhang, R., Gardner, L., Amraei, M., Buchanan, C. & Piili, H. (2022) Testing and analysis of additively manufactured stainless steel corrugated cylindrical shells in compression. *Journal of Engineering Mechanics [Accepted]*.

Zhang, R., Meng, X. & Gardner, L. (2022) Shape optimisation of stainless steel corrugated cylindrical shells for additive manufacturing. *Engineering Structures*. 270.

Zhang, Y., Liu, M., Ma, Q., Liu, Z., Wang, P., Ma, C. & Sun, L. (2020) Yield line patterns of T-stubs connected by thread-fixed one-side bolts under tension. *Journal of Constructional Steel Research*. 166.

Zhao, M.S., Lee, C.K. & Chiew, S.P. (2016) Tensile behavior of high performance structural steel T-stub joints. *Journal of Constructional Steel Research*. 122, 316–325.

Zhao, X., He, S. & Yan, S. (2021) Full-range behaviour of T-stubs with various yield line patterns. *Journal of Constructional Steel Research*. 186.

Zoetemeijer, P. (1974) A design method for the tension side of statically loaded, bolted beam-to-column connections. *Heron*. 20.